REPORT DOCUMENTATION PAGE

Form Approved
OMB No. 0704-0188

AD-A253 670

2. REPORT DATE	3. REPORT TYPE AND DATES COVERED
	FINAL 15 Jan 91 TO 14 Jan 92

4. TITLE AND SUBTITLE
AUTOMATIC CLOUD CLASSIFICATION FROM MULTI-SPECTRAL SATELLITE DATA OVER OCEANIC REGIONS

5. FUNDING NUMBERS
G AFOSR-91-0143
PE 61102F
PR 2310
TA A1

6. AUTHOR(S)
Professor Catherine Gautier

7. PERFORMING ORGANIZATION NAME(S) AND ADDRESS(ES)
University of California
Santa Barbara, CA 93106

8. PERFORMING ORGANIZATION REPORT NUMBER
AFOSR-TR- 92 0726

9. SPONSORING/MONITORING AGENCY NAME(S) AND ADDRESS(ES)
Lt Col Stobie
AFOSR/NL
Building 410
Bolling AFB DC 20332-6448

DTIC
ELECTE
JUL 29 1992
S C D

10. SPONSORING/MONITORING AGENCY REPORT NUMBER

11. SUPPLEMENTARY NOTES

12a. DISTRIBUTION/AVAILABILITY STATEMENT

12b. DISTRIBUTION CODE

13. ABSTRACT *(Maximum 200 words)*

This project was aimed at developing an operational "expert" system to perform the classification of satellite images into cloud types. The approach we have used is based on a number of number of assumptions. The first one is that such a classification is possible with satellite images of 1 km (or more) resolution. A second assumption, which lays the foundations for all classifications, is that there exists a parameter space wherein some clustering of the data occurs, so the task is to identify this parameter space from the data. An additional assumption necessary to physically interpret the results, but not necessary for the classification itself, is that the clusters found in this parameter space can be related to cloud types or physical features. We chose a Bayesian classifier for our classification. We believe that this type of classifier is best suited for the task because clouds are fuzzy objects which have overlapping characteristics. Also, with a Bayesian classifier, each point in the parameter space has a probability to belong to each class, although this probability may be anywhere between zero and one.

14. SUBJECT TERMS

15. NUMBER OF PAGES

16. PRICE CODE

17. SECURITY CLASSIFICATION OF REPORT	18. SECURITY CLASSIFICATION OF THIS PAGE	19. SECURITY CLASSIFICATION OF ABSTRACT	20. LIMITATION OF ABSTRACT
(U)	(U)	(U)	(U)

Final Report

Air Force Contract # AFOSR-91-0143

AUTOMATIC CLOUD CLASSIFICATION FROM MULTISPECTRAL SATELLITE DATA

C. Gautier, D. Lavallée, P. Peterson and D. Schweizer

I. INTRODUCTION

This report presents experiments made and results obtained in the course of executing the Air Force contract # AFOSR-91-0143 entitled: "Automatic Cloud Classification from Multispectral Satellite Data". This project was aimed at developing an operational "expert" system to perform the classification of satellite images into cloud types.

The availability of an accurate cloud classification scheme is important for developing a climatology of clouds and cloud systems (ensemble of clouds that have particular characteristics). While this is, in part, being addressed by the ISCCP project, we believe that more information about cloud and cloud system type could be extracted from higher resolution satellite data than those obtained through the present ISCCP algorithm. Another important application of cloud classification is the ability to relate different cloud types to physical processes occurring in the atmosphere or at the surface. An accurate cloud classification would help relate changes in the global radiation budget observed by such instruments as the Earth Radiation Budget Experiment to changes in horizontal or vertical extent of different cloud types or changes in observed cloud radiative forcing (e.g., Harrison *et al.*(1990) and Cess *et al.* (1992)). Such estimates of cloud changes can also be used to check current numerical model predictions with regards to changes in earth radiation budget, for instance. Once physical processes are well understood, then conceptual models can be developed that include these relationships in the form of parameterizations for numerical climate prediction models . Additional use of cloud classification is the development of angular distribution models (ADM) that relate radiances to fluxes, as those used to interpret the radiances measured by ERBE in terms of fluxes for earth radiation budget studies.

The conceptual expert system we originally had in mind was a system whose results would be rather insensitive to input data resolution. This is an important feature for any classification since the next generation of sensors (i.e., Earth Observing System) will have higher spatial resolution. The current concept of this system has, however, evolved towards an initial version capable of **classifying multispectral data from AVHRR at about 1 km resolution over water**. This evolution results from difficulties encountered in designing and implementing a multi-purpose system, as will be reported below.

Cloud classification can be partitioned into two phases: (1) classification into clear, partly cloudy and overcast conditions, and (2) cloud typing (or properties extraction) for both overcast and partly cloudy conditions. We believe that the first phase defines the quality of the rest of the classification. The cloud typing will be addressed in this report as they relate to radiation budget studies (i.e., through altitude and thickness properties). Such classifications appear to be more important to physical climate understanding than classical descriptions[1] (e.g., stratus, cumulus, cirrus).

The approach we have used is based on a number of assumptions. The first one is that such a classification is possible with satellite images of 1 km (or more) resolution. A second assumption, which lays the foundations for all classifications, is that there exists a parameter space wherein some clustering of the data occurs, so the task is to identify this parameter space from the data. An additional assumption necessary to physically interpret the results, but not necessary for the classification itself, is that the clusters found in this parameter space can be related to cloud types or physical features.

The actual implementation of such a classification scheme is an extremely complex practical problem. This is due to several facts: (1) the objects we are trying to classify (clouds) are defined in terms of parameters (radiances) which cannot be directly

---

[1] However, correspondence or equivalence between both classifications may be suggested for some classes.

interpreted in terms of cloud properties, (2) cloud radiances at different wavelengths are generally correlated, (3) clouds are complex objects whose definition varies with the application for which they are used and, (4) clouds have no well defined boundaries in any space (geometrical, radiance etc.). As an example, it can be very difficult to delineate cloud/no cloud regions or define the boundaries of each individual cloud class.

It is because of some of these difficulties that we decided to first focus on clouds over water. This situation is, to some degree, less difficult to analyze, but nevertheless an important feature to implement (see Chapter II). The analysis simplification is principally due to the homogeneity (in radiance space) of the ocean surface and to the difference in reflectance signature between ocean water and overlying atmosphere. It is important to note, however, that recent results suggest that when looking at detailed changes in reflectance around edges of small clouds (e.g., cumulus), the reflectance difference is smaller than earlier assumed (e.g., Wiliecki and Parker (1992)). This results from the fact that cloud thickness is smaller at the edge of clouds that in the center. We don't expect, however, that this will affect our classification based on larger clouds for which the aspect ratio (width over height) is rather large.

As a result of the above assumptions and the nature of the problem investigated, we have chosen a Bayesian classifier for our classification. We believe that this type of classifier is best suited for the task because clouds are fuzzy objects which have overlapping characteristics. Also, with a Bayesian classifier, each point in the parameter space has a probability to belong to each class, although this probability may be anywhere between zero and one. The idea is to find the class for which this probability is maximum and to regroup all pixels that have a strong probability to belong to one class into the same class. Under some conditions, it is possible that pixels have similar probabilities to belong to different classes. Furthermore, we have selected an unsupervised rather than a supervised classifier mostly because clouds are still rather poorly defined and have differences too large between one another to be able to select characteristic clouds for

training an expert, be it human or computer. Other investigators have chosen supervised classifications when dealing with specific applications for which a few specific cloud conditions were known (e.g., Welsh *et al.* (1992)) .

The main contention of our work is that the set of all cloud types (or radiances) forms a continuum and not a disjoint collection of objects. However, some cloud types may have a stronger occurrence than others or may have the same interesting properties with regard to a particular application. The goal is to find the appropriate parameters to use in the extraction of these properties. Under this assumption, clear conditions are at one end of the continuum. This contention has important implications that will be discussed below.

The remainder of this report is organized as follows. Chapter II presents a brief review of existing classification methods. Chapter III presents the data set and parameters used in our analysis. Chapter IV addresses the method we originally investigated, based on Typical Shape Function analysis (Jalickee and Ronolewski, 1979), and discusses its successes and drawbacks and the rationale for changing to a new classifier. Chapter V continues with Autoclass, the Bayesian approach later selected, and presents the results obtained with this approach. Results from experiments using an increasing number of parameters for classification are presented. Chapter VI describes how we have attempted to include multifractal concepts to improve our classification and experiments performed with that approach. Finally, Chapter VII summarizes the most important results obtained in this reported work and discusses the next steps necessary to arrive at a full-fledged, operational classification.

II. BACKGROUND AND CONTEXT

Different attempts have been made to classify clouds during the last few years. A brief review of those methods is presented and some of their basic ideas are discussed. We also indicate the way in which our classification method (discussed in Chapter IV) differs from previous methods and how our approach will hopefully improve the classification.

II.A. REVIEW OF METHODS

One major difficulty with cloud analysis and classification deals with the data used to perform such tasks. The quantities observed are radiance fields at different wavelengths which need to be related to physical (or optical) properties of clouds. There are two general types of approaches with many variations in-between. The first type of approach extracts physical (or optical) parameters from the data and uses these parameters to classify the clouds. This approach can be validated with physical observations but has one major drawback: the extraction of the physical parameters necessarily relies on a number of simplifying assumptions. If the retrieval is physically based (e.g., based on radiative transfer principles), these assumptions are included in the forward solution of the radiative transfer but also in the inverse (retrieval) solution. The assumptions in the forward model include plane parallelism for the clouds and discrete phase function representation for the radiance field, for instance. The assumptions for the retrievals include selection of some governing parameters or constraints in order to limit the number of solutions. When computed, the physical parameters are only rough estimates and their accuracy depends on the quality of the radiative transfer models used and the retrieval technique applied. The second type of approach is one that analyzes the data in a non-physical parameter space to differentiate between different cloud types. The difficulty with this approach, which is the one we have chosen, is its validation, since it is not explicitly based on physical characteristics. This issue will be discussed in Chapter IV.

The first type of classifications is typically represented by the ISCCP cloud algorithm with some modifications, as noted in the text. It begins with a cloud detection stage but, contrary to initial appearances, this task is not trivial. The existence of difficulties can be seen by the abundant literature on this topic and the number of recent studies proposing new ways of addressing this issue. It is becoming clear that cloud cover estimation requires great care and that results will depend on satellite sensor resolution and algorithm applied. The ISCCP algorithm uses two pre-assigned thresholds (visible and infrared) based on a clear scene type already known. Once clear pixels have been eliminated, a typical algorithm analyzes the remaining pixels and assigns a cloud fraction to each of them. Most of the algorithms, including the ISCCP algorithm, assign a fraction of 1 to the non-clear pixel for lack of information. Only a few of the algorithms attempt to assign a variable fractional cloud cover (e.g., Coakley and Bretherton (1982) and Arking and Child (1986)). The fractional coverage computation requires an assumption about the number of cloud types present and the origin of the cloud field radiance variability. In particular, all algorithms assume that observed variations in cloud radiance result only from changes in fractional cloud coverage, therefore cloud radiance is constant for each cloud. This hypothesis appears to be in some disagreement with recent observations made from high resolution visible sensors which suggest that the optical thickness for a cloud may vary within the cloud (e.g., Welsh and Wielicki (1986) and Wielicki and Parker (1991)). This limitation is eliminated if cloud fraction is treated as an effective cloud fraction which includes both cloud coverage and cloud optical thickness effects (in the visible) and cloud top temperature (in the infrared). Once a region has been assigned a cloud cover, the cloudy data is used under some assumptions to provide cloud properties, such as optical thickness, or physical properties, such as cloud top temperature. In the ISCCP algorithm, two limiting assumptions are made: (1) the effective particle radius is fixed at 10 μm, and (2) the cloud phase is chosen as water. Once computed, the optical and physical parameters are, in turn, used to classify clouds by type. We believe that this

approach is rather limiting for precise studies of cloud properties because of the assumptions it is based on. Also, since textural parameters are not included, important structural and directional properties, which can be helpful for the classification, are omitted.

The second type of classification contains the following general features. First, it consists of choosing a set of parameters which summarizes cloud properties. The parameters can be the values of the data or parameters that result from mathematical operations[2] on the data. Two types of parameters are usually considered: spectral and textural parameters. Spectral parameters are associated with physical properties of clouds (e.g., altitude, liquid water content), whereas textural parameters provide information about cloud structure (e.g., broken, homogeneous, anisotropic). A parameter space is then constructed, the dimension of which equals the number of parameters. Each point in this space has its coordinates determined by the values the different parameters take when evaluated over a superpixel (see Fig. II.1). The goal is to develop a technique to identify regions of the parameter space with a high density of points (clusters) and partition the parameter space according to these regions. To each region corresponds a class. The accuracy of image classification depends on, first the appropriate choice of the set of parameters, and second, the algorithm used to explore the parameter space.

A simple example of this approach is the spatial coherence method (Coakley and Bretherton (1982)). In their approach two parameters are selected: mean and standard deviation of infrared radiances for super pixels. These two parameters are plotted one versus the other, and if a cloud field has one cloud deck and some clear pixels, the plot will have an arch shape (see Fig. II.1), with each foot of the arch (or equivalently cluster) representing clear and cloud conditions since they are associated with spatially

---

[2] In this case many parameters can be extracted from a given configuration of pixels, called superpixels.

homogeneous (very small standard deviation) super pixels. The arch itself represents mixed super pixels. The average radiance values associated with the feet of the arch (below a given threshold standard deviation) is used to deduce the fractional cloud coverage of each mixed super pixel.

To our knowledge, only two classes of all-purpose algorithms following the second type of approaches have been developed. The first one was initiated by Garrand and collaborators (e.g., Garrand and Weinman (1986) and Garrand (1986)) and applied by Ebert (1987, 1989 and 1992) for classifying clouds over snow. This classification is based on defining a large number of spectral and textural parameters characterizing the cloud field and classifying clouds based on a maximum likelihood estimation method or other pattern recognition techniques. The second type of algorithms has been recently developed by Welsh *et al.* (1992), and builds upon Welsh's and collaborators previous work, but also on that of Garrand (1988). In earlier work Welsh and collaborators have looked in detail at using spatial as well as spectral descriptions of cloud fields in order to investigate the structural and textural properties dependence on cloud types. For this purpose, they have analyzed marine stratus, cumulus and cirrus clouds over the ocean using high resolution Landsat images to characterize cloud structural properties - such as cloud size, cloud inhomogeneity (hole), monofractal dimensions, clustering scales, etc. Cloud textural measures such as Contrast, Correlation, etc. (see Chapter III) have been used to discriminate cloud fields structures. It is difficult to directly use that body of work for the analysis of AVHRR data because it is based on high resolution (~30 m) data from the Thematic Mapper (TM) on Landsat satellites. Their more recent cloud analysis work, however, is based on AVHRR data but is limited to snow and ice surfaces. The parameter space chosen is composed of spectral and textural parameters and the classification methods investigated are: a stepwise discriminate analysis and two neural networks (Welch, *et al.* (1992)). A comparison of the results from the three classification methods does not favor the neural network approach but they claim that the information contained

in the network nodes is not fully tapped. Both classes of classifications are based on a supervised classification, that is, an a-priori classification is performed in a few cases and used to train the classification scheme (e.g., neural networks).

Another issue that raises questions is that of the effect of clouds spatial variability at resolution smaller than the resolution of the sensor. In our case, the observations are made with 1km resolution sensor but we know that the spatial variability of some clouds (e.g., cumulus marine stratus) is of the order 100m. The analysis of the scale invariance properties of the clouds, discussed in Chapter VI, will provide some clues on how to handle these issues.

II.B. ORIGINALITY OF OUR APPROACH

The approach we developed has several features that differentiates it from the methods discussed above. First, it does not depend on fixed thresholds as the ISCCP algorithm does. The threshold is obtained from the data themselves. The thresholds are not assumed to have any particular geometry (i.e., straight lines parallel to axis as in spatial coherence method). We explore non-linear spaces which may be more appropriate for investigating natural geophysical phenomenon, especially if multiscaling is at work.

In the case of the cloud coverage issue, a given value of the temperature (or of reflectance) is chosen as the threshold and then every pixel with a smaller value (or a higher value) is identified as being part of a cloud. The main difficulty with the threshold approach is the arbitrariness of the chosen threshold values. An alternative approach, which this document explores, is to study the probability distribution[3] of a given parameter and determine the threshold for cloud coverage from a large change in the probability distribution. Of course this requires the search of the appropriate parameters (and the

---

[3] In general, any typical functions that characterize the behavior of the parameters can be used.

assumption that such parameters exist), but when such parameter space is found, the method should work with images at different resolutions. An illustration of this improvement and its consequences is discussed in Chapter V, where classifications obtained with Autoclass III are compared with those obtained with the spatial coherence method.

Another important feature that differentiates our approach from those of the second kind mentioned above (e.g., Welsh *et al.* (1992)) is that it is unsupervised. We do not use experts to give us answers to use in the training of the classifier (i.e., pattern recognition), nevertheless we use expert knowledge to evaluate the quality of our classifications. The difficulty associated with that approach is its validation since there is no "truth" to compare it with.

III. DATA AND PARMETERS

In the following sections, the data used to performed the classifications are described. As discussed in previous sections, parameters and parameter spaces are required for this task. The definition of the spectral and textural parameters used is also given.

III.A. THE DATA SET

The data analyzed were obtained from the Nimbus-9 satellite. The 12 AVHRR (Advanced Very High Resolution Radiometer) images, illustrated in Figure III.1, were selected from the FASINEX experiment in February 1986 (the exact date are the 10^{th}, the 11^{th}, the 12^{th}, the 14^{th}, the 15^{th}, the 16^{th}, the 17^{th}, the 18^{th}, the 19^{th}, the 20^{th}, the 24^{th} and the 25^{th}). These pictures were obtained with the sensor centered at a longitude of 70^{o} west and a latitude of 27.5^{o} north . This point is situated over the Atlantic Ocean, east of Florida. The resolution of the sensor is 1.1km at nadir. Each image scene is made of 512×512 pixels. These images are not remapped so the pixels size varies slightly from image to image due to small change of the satellite nadir point. The pixel digital number will be used for all the subsequent analysis and calculation. When required, normalization or transformation will be specified.

For each day, AVHRR data are available in five channels. Histograms of the values for the 5 channels are illustrated in Figure III.2 for two different days. Notice that in both case, the behavior of channel 1 and 2 are very close and that curve of channel 4 is similar, within an horizontal translation, to the one of channel 5. This behavior is consistent for all 12 days. Histogram of channel 3 includes both reflectance and emittance signal. Channel 3 is the noisiest and hardest to deconvolve into physical interpretations.

However, it is well known that except for channel 3, the AVHRR data are nearly noise-free.

For these reasons, only channel 1 and 4 have been used in a first phase. Channel 1 is in the visible (0.5 - 0.75μm) and provides information about total cloud liquid water content and visible optical thickness. Channel 4 is in the infrared (10.4 - 11.1 μm) and provides information about cloud top temperature which is related to its altitude.

III.B. SPECTRAL AND TEXTURAL PARAMETERS

Each image is subdivided into non-overlapping adjacent windows, called superpixels. Superpixel is formed by $n \times n$ pixels. For the classification discussed in chapters IV and V $n = 8$, in chapter VI n is variable. Spectral and textural parameters are computed in each superpixel. Discussions on spectral and textural parameters can be found in Haralick *et al.* (1973), Parikh (1977), Ebert (1987, 1989), Welch *et al.* (1988a, b), Tournadre and Gautier (1989), Sengupta *et al.* (1990), Wielicki and Parker (1991) and Welch *et al.* (1992).

Selected spectral parameters are related to physical properties of clouds (e.g. altitude, reflectance, liquid water content). They are computed on both visible and infrared images. They are the *mean*, *minimum*, and *maximum* value within a superpixel.

The textural parameters give information on cloud structures. They are related to broken pattern, coarseness and local variability within clouds. Directional properties of the structures can be also extract. The latter feature will not be used in the classification schemes, but their scaling properties will be discussed in chapter VI . In this study, textural parameters have been estimated only for channel 1 since structures are more easily characterized in the visible.

The textural parameters are related to the statistical property (the joint density function) of neighboring pairs of pixel. Their evaluations are based on the Gray Level Difference Method - GLDM (Parikh (1977)). Defining the gray level intensity $g(\mathbf{x})$ at the

position **x** on the image, the (absolute value of) gray level difference $-g$ is given by the following relation:

$$-g(\rho,\theta) = |g(\mathbf{x} + \mathbf{r}) - g(\mathbf{x})| \qquad \text{(III.1)}$$

where ρ is a vector between two pixels with magnitude $\rho \equiv |\rho|$ and direction θ. The magnitude ρ takes integer values between 1 and (l-1), where l is the size of the superpixel, and the 4 following values of θ are considered (0º, 45º, 90º, 135º). Let $f_\theta(\rho,-g)$ be the number of occurrence[4] of pixel pairs, for a given ρ and θ, such that their gray level difference is $-g$ within a superpixel. The following textural parameters can then be estimated:

$$Difference = \frac{1}{256} \sum_{-g=0}^{255} -g \left(\frac{f_\theta(\rho,-g)}{N} \right) \qquad \text{(III.2)}$$

$$Contrast = \sum_{-g=0}^{255} (-g)^2 \left(\frac{f_\theta(\rho,-g)}{N} \right) \qquad \text{(III.3)}$$

$$Entropy = - \sum_{-g=0}^{255} \left(\frac{f_\theta(\rho,-g)}{N} \right) \ln \left(\frac{f_\theta(\rho,-g)}{N} \right) \qquad \text{(III.4)}$$

$$Angular\ Second\ Moment = \sum_{-g=0}^{255} \left(\frac{f_\theta(\rho,-g)}{N} \right)^2 \qquad \text{(III.5)}$$

where N is the total number of pairs of points separated by a distance ρ in direction θ within a superpixel. The expression $f_\theta(\rho,-g)/N$ approximate the probability, for a given ρ and θ, that a given value of $-g$ will be observed within a superpilel. Notice that the

---

[4] This is also called a frequency histogram.

expression for *difference* is commonly referred to as *mean* in the literature. It is renamed *difference* to avoid confusion with the spectral parameter called *mean.* It is also important to point out that the textural parameters considered in the classification discussed in chapter IV and V have been averaged over the 4 directions and estimated with $\rho = 1$.

Two additional parameters are examined for the classification discussed in chapter V. They are the IR and visible *standard deviation*[5] within a superpixel.

[5] The *standard deviation* is also a spectral parameter.

IV. CLASSIFICATION WITH TYPICAL SHAPE FUNCTION (TSF)

A brief discussion of the properties of the typical shape function (TSF) methods is given. Then the difficulties encountered in the resulting classification are enumerated. The TSF method was found to be unreliable with respect to cloud classification.

IV.A. DESCRIPTION OF THE TYPICAL SHAPE FUNCTION (TSF)

The idea behind the Typical Shape Function analysis is to generalize an unsupervised classification scheme developed by Jalickee and Ropolewski (1979) to classify temperature and humidity profiles. The classification methods follow a three step procedure.

In the first step, cloud parameters are identified to characterize cloud features. The parameters correspond to the coordinates of a vector, called the "cloud profile", in the parameter space. The cloud profile vectors are then organized in an array, where each column coincides with a vector.

In the second step, the array of data is expressed as a series of terms using the singular value decomposition theorem. Those terms are Empirical Orthogonal Functions (EOFs), which define the best fitting subspace that can represent the higher dimensional feature space of the cloud profiles. The terms are ordered according to decreasing importance. Practically, this is obtained from the singular values (or eigenvalues) of the covariance matrix of the array . The leading terms contain much of the important features of the data, since the variance of each term is proportional to the respective singular value (or eigenvalue). This operation consist mainly in the decomposition of the matrix data into an orthogonal basis.

The last step consists in keeping only those terms in the series that will account for more than a given (high) percentage of the variance (e.g., in this study 99% of the

variance). All the steps of the procedure just described are quite similar to a Principal Component Analysis (see e.g., Richards (1986)). The leading terms of the approximation are then recombined to obtain the typical shape functions (TSF). This procedure corresponds to a rotation in the parameter space. The rearrangement is performed in such a way to maintain the approximation. In general, the new typical shape functions will neither be independent nor orthogonal. These functions are intended to characterize features in mutually exclusive subgroups of the data. The subgroups are then identified as classes when they includes a number of profile larger than 2% of the total number of profiles. Details of the mathematical formulation of the classification method is discussed elsewhere (see Jalickee and Ropolewski (1979) and Tournadre and Gautier (1989)).

IV.B. TYPICAL SHAPE FUNCTION ANALYSIS & RESULTS

The Typical Shape Function classification has been applied to pairs of AVHRR satellite images discussed in section III.A and also to MILDEX (Mixed Layer Dynamics experiments) discussed in Tournadre and Gautier (1989). Channel 1 (visible) and channel 4 (infrared) data are used to extract 10 first parameters (6 spectral, 4 textural) presented in section III.B. To avoid computational bias it is necessary to perform a normalization of the data set Tournadre and Gautier (1989).. To normalize the data, each parameter value is expressed in standard units. Illustration of the cloud profile for clear sky conditions is given in Figure IV.1.

The results of all the analysis led to the same conclusions. In many instances, it appeared possible to partition cloud scenes in what appeared to be reasonable cloud classes. However, counter examples were found for which the classification was not possible. In those cases, the approach showed some limitations. These instances were associated with rather complex cloud systems that had clouds organized in such a way that parts of the field appeared to be the "contrast negative" of other parts. Or, in another way, some clouds cells in one part of the image were very similar to open cells. In this case, the

basis of the method, which is an EOF analysis, created problems because the EOF analysis does not provide the signs of the basis vector (or the direction of the axis of the basis vector). While it was relatively straight forward to decide the TSFs were reversed in the clear conditions, it was not possible to for cloudy conditions.

The TSF classification scheme has another important limitation. The number of classes that can be extracted from a pair of image has an upper bound. The latter is independent of the data analyzed. It is given by the maximum numbers of parameters used in the EOF analysis (see also, Jalickee and Ropolewski, 1979). Nevertheless, the classification scheme may have some applications when the partitioning of the data does not require a large number of classes. A good example is the determination of the cloud cover for which, in a first step, two classes only - cloud/clear- need to be identified[6].

The difficulties and insufficiency mentioned above led us to look for another approach to the classification. The one selected, Autoclass III, based on Bayesian statistics, is the topic of the next chapter.

---

[6] Even for this particular example, the classification schemes discussed in the next chapter will be found to be more powerful and efficient.

V. CLASSIFICATION WITH AUTOCLASS III

V.A. AUTOCLASS III

V.a.1 Description and Features:

Our selected classifier is Autoclass III, a program for automatically discovering classes from a data base. This Bayesian Statistical technique automatically determines: (1) the most probable number of classes present, (2) their probabilistic description and, (3) the probability that each point in the parameter space is a member of each class (Cheeseman *et. al.* (1988 a, b and 1989) and Cheeseman (1990)).

Autoclass has some important features for our application. The number of classes is not limited by the number of parameters, as was the case with EOF's. It is dynamically dependent on the density of points in the constructed parameter space. However an upper bound in the number of classes can also be imposed by the user. When the number of classes is found, Autoclass determines the probability of each point belonging to each class. In this sense, it represents a fuzzy rather than a hard classification. A point (or superpixel) is usually assigned to the class for which its probability is maximum. The latter is important since it allows Autoclass to give a weight, or measure of confidence, that a point (or superpixel) belongs to a given class. The second best weighted class can also give pertinent information for subsequent classifications within a given class.

V.a.2 Bayesian Classification:

The purpose of this section is to briefly outline the theory involved in the Bayesian method also referred to as the maximum likelihood method. In a parameter space, where dimension D equals the number of parameters, each point is identified by a D-dimensional vector $\mathbf{x}$. The assumption is that the parameter space may be partitioned into clusters which could be associated with distinct classes C_i. The objective is to associate a point $\mathbf{x}$ to

the class C_i whose center exerts the greatest influence with respect to likelihood. (see Fig. V.1).

Conditional probability is the probability of an event occurring conditional upon some other event or circumstance. So the conditional probability $p(\mathbf{x}|C_i)$ is the probability of finding a point at position **x** considering only the class C_i (or the probability to find an event of class C_i at the position **x**). The probability $p(C_i)$ is the relative weight associated with each class C_i in the parameter space (it indicates the probability that a point randomly chosen will come from class C_i). The $p(C_i)$ are called *a priori* or prior probability. Their product is the probability that a point positioned at **x** in the parameter space belongs to the C_i. The classification rule is then given by the following relation:

$$\mathbf{x} \in C_i \quad \text{if} \quad p(\mathbf{x}|C_i)\, p(C_i) > p(\mathbf{x}|C_j)\, p(C_j) \quad \text{for all } [i\ ,j\ i \neq j\ ] \qquad \text{(V.1)}$$

which indicates that **x** belongs to C_i when the product $p(\mathbf{x}|C_i)\, p(C_i)$ is maximized.

The probability $p(\mathbf{x}|C_i)$ is either a binomial distribution when the position **x** takes on discrete values or normal or lognormal distributions when **x** has continuous values. The probability distribution assigned to $p(\mathbf{x}|C_i)$ can be chosen prior to the classification or determined by Autoclass III[7] itself. The prior probability $p(C_i)$ has initial values which are iteratively modified until eq. (V.1) is satisfied.

V.B. METHODOLOGY

Our general approach is to investigate different parameter spaces for some measure which consistently identifies clearly distinct clusters that relate to physical attributes of the

---

[7] For all the parameter spaces studied and discussed below, AC determined that the log-normal distribution was the most appropriate probability distribution to describe the point density.

satellite image field. That way combinations of parameters can be used to infer the physical characteristics of clouds. As with TSF, two types of parameters are used to characterize clouds: spectral and textural.

V. C. EXPERIMENTS & RESULTS

Initial experiments with Autoclass II used all 10 parameters (see section III.2) used at that time[8] (two standard deviation parameters have since been added). The output of these runs often had over 20 classes which made the classification difficult to interpret. By comparison with the TSF approach, a Baysian classifier can use any number of parameters to produce a classification without imposing any restriction on the number of classes determined. Since it was very difficult to relate 20 or more classes with physical features it was decided to systematically look at the classification results of each parameter individually. Another difficulty with classification performed with a large number of parameters is the stability of their classes. Our study also indicated that when the maximum numbers of classes allowed is changed, even by one class, the resulting classifications could be quite different, especially for the less populated classes. For these reasons a new strategy was adopted. It starts by exploring a single parameter space with Autoclass. (Over the course of our investigation a new version of Autoclass has become available. Autoclass II was being used when we tried 10 parameters and fixed the class number. All the work presented in this report is the product of Autoclass III. The next version, Autoclass IV, will add the ability to impose probability density function information for each parameter, allow for a hierarchical classification of categories and use knowledge about the correlation. For the remainder of this report, AC will refer to Autoclass III.)

---

[8] This was done in the spirit of the original TSF experiments for which the maximum number of classes was limited to 10 as discussed in section III.

A summary of the number of classes obtained as a function of the dimension[9] of the parameter space is presented in Table V.1. There exists a systematic increase in the number of classes found as the number of parameters increases. Single textural parameters generally result in a higher number of classes than single spectral parameters with standard deviation falling between these two. For more than one parameter, standard deviation is considered a spectral parameter. This observation is clear from looking at the 1, 2, and 3 parameter line totals. Note that only with one parameter runs do we get one as the best number of classes, and overwhelmingly this occurs with a visible spectral parameter. A result of one for the best number of classes implies that Autoclass found no obvious clustering in the parameter space. It is interesting to note that while visible minimum and visible maximum each result in one class for 2-14, the combination of visible minimum and maximum results in a three class classification. Therefore while a single parameter may not produce obvious clustering, it may still induce clusters when combined with other parameters.

v.c.1 Analysis in a single parameter space

In a single parameter space, the number of classes found is relatively small, typically 2 or 3, (in this study, the maximum found was 4 which occurs ~4% of the time.) The frequency of the number of classes found for spectral parameters, standard deviation, textural parameters and for all the parameters are given in Table V.1 (see also Tables V.2a, b and c for more details). When using single spectral parameters, it is typical for Autoclass to find only two classes, 60/72 or 72/96 with standard deviations. A detailed account of the first and second choices for the number of classes found for each day and each parameter is presented in Table V.2a. From this, the different classifications obtained

---

[9] The dimension of the parameter space is implied by the number of parameters used to construct it.

were compared one to the other and also to the original images. These comparisons allow us to determine their relative usefulness in producing a reasonable classification. From this analysis it has been possible to eliminate some parameters because of their redundancy with other parameters or due to their poor performance in highlighting physical features. The classifications obtained for each of the twelve parameters for the 12 images are given in Figures V.2 and V.3. In what follows, we will discuss the classes found by AC and their corresponding physical properties.

The colors in Figure V.2 and V.3 may be interpreted as follows. For single spectral parameters the first two colors used are, blue for low values and dark green for high parameter values. If a third class is identified, the intermediate values are colored yellow. In three instances a fourth class is identified. This fourth class is colored light green and is located between the intermediate yellow and high dark green classes. The color sequence blue-yellow-light green-dark green, then characterizes the low to high parameter value classes for single spectral parameter classification.

For textural parameters, a different set of colors is used. When only two classes exist, tan denotes the low textural values and purple corresponds to the high texture class. When a third intermediate class is found, it is colored red. When a fourth class is detected it is colored pink and is located between the intermediate red class and the high purple class. The coloring of a single textural classification from low to high is then characterized by the sequence tan-red-pink-purple. Table V.3 contains a summary of the one parameter coloring assignments along with their physical interpretation.

An important result from the single parameter experiments was the identification of the most appropriate parameters to identify cloudy regions and distinguish it from clear regions. They are the following spectral parameters: minimum, mean and maximum for the infrared channel (see Fig. V.2). Our experiments indicate that the variation in channel 4 (temperature) is more consistent for making this distinction than the variation in channel

1.[10] The temperature measured is related to the altitude of the observations, with water representing the warmest pixels at sea level and cloud tops being cooler as their altitude increases.

An interesting example is given for the IR minimum classification obtained for 2-10-86 (see Figure V.2). In this example, 4 classes of approximately the same weight were found by AC as its first and second best classification (see also Table V.2a). In this case three distinct cloud altitude classes are found. Notice that the yellow class, identified in the IR minimum classification, is difficult to see on the IR image (see Fig. III.1) and did not appear at all on the visible image, (Figure III.1). This class may be a light marine layer, due to a warm water front from the Gulf Stream.

There is a consistent trend when going from minimum IR to mean IR and to maximum IR consisting of an increase in the number of superpixels classified as cloudy and a complementary reduction in the number of clear superpixels. It is the mixed superpixels composed of clear and cloudy that have their classification modified when switching between the IR minimum, mean, and maximum parameter. With the IR maximum, a single high pixel value will bias the entire superpixel to be in the cloud class which includes superpixels that are partially or totally cloud covered. With the IR minimum, a single low value will bias the superpixel in a similar way towards the clear class and the mean IR will have behavior somewhere in between these two extremes. The difference in the number of cloudy superpixels between the min. IR and max. IR

---

[10] Often, the classification obtained for channel 1 using the maximum, mean or minimum parameter is similar to the one obtained with channel 4 for the corresponding parameters, (see Figures V.2 and V.3).

classification indicates the number of mixed superpixels[11]. These superpixels are made up of clouds mixed with clouds of different altitudes or/and clear pixels. From this, a minimal definition[12] of clear superpixels is given by the maximum IR parameter. A minimal definition of cloudy superpixels is given by the minimum IR parameter. The remaining pixels are considered as partly cloudy.

Occasionally a single spectral parameter will produce more than two classes (see Table V.2a). When this happens the third class is usually relatively small[13] and if necessary could be regrouped into the other two classes or simply disregarded. This reclassification is possible using AC information about each points second most likely class to reassign the points of a small third class into the other two.

Consider now the classification obtained with IR standard deviation parameter (middle right image in Figure V.2). Most of the time, 2 or 3 classes are found. They are related to the variability of the altitude measured inside a given superpixel. The light blue corresponds to super pixel of uniform altitude, and going from yellow to light green then to dark green correspond to superpixels of increasing (from low to high) variability in their altitude, (see Table V.3). When the standard deviation classification gives two classes (6 out of 12) or a weak third classes (3 out of 6), another feature can be associated to each superpixel already classify as cloudy or clear. Since cloudy superpixels of (almost)

---

[11] Mixed with respect to the feature associated with the IR minimum, mean and maximum parameters, i.e. the altitude. Superpixel can be mixed with respect with other features, as will be discussed below.

[12] Practically this definition is equivalent to considering a Superpixel as being clear or cloudy when classified as clear or cloudy in the IR maximum, mean and minimum parameter space (see fig. V.2). Otherwise the superpixel is said to be partially cloudy.

[13] An interesting exception to this dominant behavior, already discussed above, is IR minimum classification for 2-10-86 (see figure V.2).

constant altitude and clear superpixels will have low values for their standard deviation, they will therefore be associated with the same class. Cloudy superpixel with uniform altitude can be differentiated from clear by comparing the coincident minimum IR classification (see Table V.4). The superpixels with variable altitude represent a mixed class. This occurs at cloud boundaries, when clouds of different altitudes coexist in the same single superpixel.

Classifications of the visible (channel 1) spectral parameters and standard deviation are given in Figure V.3. The choice of colors corresponds to those of the IR spectral parameters. The visible data are more sensitive to the thickness of the clouds and the feature associated with the visible minimum, mean and maximum classification is cloud optical thickness. Following this, the visible standard deviation classifications indicates large region of variable thickness for the case 2-14-86, 2-16-86, 2-17-86, 2-19-86 and 2-24-86 and regions of uniform thickness (light blue and yellow) for the cases 2-12-86 and 2-20-86 (compare Fig. V.3 with left hand side of Fig. III.1)

The analysis of the single textural parameters allowed us to draw some conclusion about their utility and their reliability in detecting associated features (see the last row in Figure V.2 for visible Contrast and Difference and Figure V.3 for visible Entropy and Angular Second Moment).

Analysis of the classification obtained for second moment indicated that it tends to enhance the differences between low pixel values and bunch together high pixel values, (see Figure V.3, in the low right corner). In other words, the second moment focuses on differentiating the clear superpixels, a feature not so important for the classification of clouds. Therefore, it was eliminated from further consideration. The classification given with the entropy parameter (see Fig. V.3 in the lower left corner) did not provide significant additional information when compared to classification performed with spectral parameters. It was also observed that the classification obtained with entropy and second moment is often similar with an inversion of the class associated with high values (color

purple) to the one associated to the low values (color tan) of the textural parameter. These particular behavior is mostly evident when only two classes (and also with a third weak class) are found by AC (see Fig. V.3 for the following cases: 2-10-86, 2-16-86, 2-17-86, 2-19-86, 2-20-86 and 2-24-86).

Contrast and difference are the two most promising textural parameters. The classifications obtained for the single difference parameter are illustrated in Figure V.2 in the lower left corner. Most of the time the class identified by the tan colored regions corresponds to the regions that are light blue on both the IR minimum and standard deviation and thus corresponds to the clear sky (see Fig. V.2 and the Table V.3). The other class found with the visible parameter corresponds to superpixels that are identified as clouds when using IR minimum and standard deviation parameters. So they provide additional information for these clouds. It was also noted that when the IR standard deviation has a strong intermediate class (color yellow) only two classes are found with the visible difference parameter (see Fig. V.2 for 2-14-86, 2-19-86, and the 2-24-86 cases).

Contrast measures factor such as the amount of local variation within the cloud and the overall homogeneity -with respect to the presence of structures- within the superpixel. The classifications obtained for the single contrast parameters are illustrated in Figure V.2 in the lower left corner. When contrast is compared to the classification obtained for the IR minimum spectral parameter, some additional information is found. The pixels colored tan are this time either clear (when the IR minimum is light blue) or structure-free clouds (when the IR minimum is dark green). Most of the time the red pixels seem to be related to the boundary between different clouds or between superpixels of water and cloud. For 2-24 (Figure V.2) where most of the scene is red, this description is not obvious. In this case most of the superpixels have a similar value of intermediate contrast with a small number of superpixels at the two extremes. Here the red class is a boundary of extreme thickness. Superpixels classified purple may indicate clouds with structure if they are

classified as cloud when using IR minimum and standard deviation parameters (see Fig. V.2 for 2-12-86 and 2-17-86 cases).

The previous information given by the single parameter classification can be used to attribute to each superpixels a set of physical features (see Table V.5). These sets can become signatures for identifying different "superclasses". Such a combined classification can be more easily applied to single parameter spaces with a low number (2 or 3) of classes . This type of procedure could be automated without any major difficulty.

An example of a combined classification using Table V.5 is discussed for image 2-11-86. Using the IR minimum classification (Figure V.2) allows us to identify two regions with clouds, in the upper left corner and in the lower right corner. The IR standard deviation parameter indicates that the cloud in the upper left corner has a variable altitude, the one in the lower right corner is partially (in its center) uniform in altitude. Between the two clouds smaller clouds are detected. From the visible minimum classification, (Figure V.3) we can deduce that the cloud in the upper left is thin and the other one is thicker. Finally the visible contrast classification shows that the only structure is in the lower right part of the image. From this we can say that the clouds in the upper left corner are thin with a variable altitude and no apparent structures, on the other hand the one in the lower right corner is thick with spatial structures but rather uniform altitude. This description is in agreement with the visible and IR images given in Figure III.1.

v.c.2 Secondary analysis from single parameter classification:

The above describes a technique for combining multiple single parameter classifications into superclasses. We describe here a method to extract additional information from a single classification expanding two classes into a number of subclasses. In particular, a single IR spectral parameter will be used to estimate the cloud fraction within a superpixel. Previously in this report, the IR spectral parameters were shown to provide a means for estimating an upper and lower bound for cloud cover.

Summing the number of superpixels assigned to the cloud class provides an estimate of cloud cover. In this way superpixels have one of two values, zero for clear and one for cloudy. The different estimates between parameters arises from whole superpixels being reassigned to new classes.

Autoclass makes it possible to infer a greater range of values for the cloud fraction, in fact 91 values instead of just two. This is achieved by using the percentage likelihood of a pixel's membership in a given class. The percentage likelihood value recorded by Autoclass is in the range 10 through 100, an unrecorded value for a class is assumed to be zero. This gives 91 different degrees of membership in a particular class. For a two class spectrally-based derived classification, this is interpreted as a clear/cloud fraction scale. This scale has some interesting qualities such as an inverse relationship with a point's percentage likelihood between the two classes. As a superpixel's likelihood for one class increases its likelihood for the other class decreases. Figure V.4 shows this relationship graphically for the three parameters IR min, max and mean. This characteristic behavior of the function assigning percentage likelihoods to pixel values is consistent over the FASINEX data set. At the low pixel values (which represents high temperature), the probability of belonging to the water class is highest, typically 99-100%. As the pixel value increases the graph reaches a point where the probability starts to decline steadily. When this probability hits 90% the probability of belonging to the cloud class is introduced at 10%. From this point the blue curve (water) continues to fall as the red curve (cloud) rises until they cross. The two curves cross at the 50% likelihood level where the parameter value denotes the class boundary. These two curves continue in a symmetric fashion with the blue curve dropping out when the red curve reaches 90%. The red curve then continues until it reaches it peak where it stays until the maximum parameter value is reached.

Along with the breakpoint between class boundaries we define two other points characteristic to these V diagrams[14], the SUP_{90} and the INF_{90}. The SUP_{90} is the largest pixel value where the water curve is no longer above 90%. This is also the first nonzero point of the cloud curve. The INF_{90} point is the lowest pixel value on the other side of the breakpoint where all subsequent cloud values are > 90% and the water curve vanishes. What is interesting is the stability of these points for different days and across the three parameters for a single day. Table V.6 gives the pixel values for these three points for all IR spectral parameters which resulted in two classes along with the range in pixel values for each parameter. The average range for SUP_{90}, class boundary and INF_{90}, for each day, is given as the last number in these columns. With respect to clear/cloud fraction estimates, all pixel values < SUP_{90} are 100% clear, all pixel values > INF_{90} are 100% cloudy, and the remaining values have clear/cloud fraction somewhere between zero and one.

This analysis is useful even without knowing the exact relationship between the clear/cloud fraction and the pixels location in the mixed interval. The fact that this relationship, as shown in Figure V.4 is smooth, well behaved, symmetric and predictable, indicates that even a simplistic interpretation should serve well for improving our clear fraction estimates. A natural way to use this probabilistic information would be to assume that a pixel value with X percentage likelihood membership in the water (cloud) class has a clear (cloudy) fraction of X percentage. Let the index i be the pixel value for one of the three IR parameters. Then the equation:

---

[14] When the percentage likelihood curves were first graphed only the values for the most probable (expressed) classes were included. This produced a "V" shape whose vertex occured at the class boundary with a likelihood value of 50 percent. The diagram has sinced been extended to show all values greater than 10 percent. This has the effect of adding the unseen roots to the original "V".

$$\sum_{i \in \text{parameter range}} \text{likelihood}(i) \times \text{histogram}(i) = \text{clear/cloud fraction} \qquad \text{(V.2)}$$

evaluates the cloud/clear fraction for the satellite scene. This could be done using either the blue (water) or tan (cloud) percent likelihood function or a weighted average of the two.

The percentage likelihood(i) function could be convolved with the histogram of the original AVHRR image. This would give a clear fraction estimate which captures the variability of the data at the scale at which it was measured. This would be an improvement over the coarser resolution estimate made at the superpixel scale using only zeros and ones. Another original aspect of this technique is it's lack of externally set thresholds. The appropriate points for conducting the analysis are derived from the data themselves and are therefore not biased by any human introduced assumptions. Finally this technique suggests that clouds can be treated as a continuum of liquid water content, whose classification is by nature fuzzy.

v.c.3 Analysis in a two parameter space

The next step was to investigate two parameter spaces with AC. The pairs of parameters combined were either one spectral and one textural parameter, or two spectral parameters. As indicated in Table V.1 the number of classes found using 2 parameters is typically larger than those found with the single parameter analysis. The parameter pairs were selected with respect to the results obtained in the single parameter experiments, or as to mimic other known classification schemes (i.e., spatial coherence method of Coakley and Bretherton (1982)). A summary of the number of classes found for the different combination of two spectral parameters or one spectral with one textural parameter is presented in Table V.1.

Expanding into two parameter spaces motivated an increase use of color to reflect the increased number of classes and their relative location in the parameter space/scattreplot. To help make this section clear a color guide is now introduced. The general basis on this scheme is expressed in Figure V.5 where the axis are labeled first parameter and second parameter. The first parameter is always an IR spectral parameter (mean) and the second parameter may be either spectral or textural, both are graphed on a log scale. Setting this orientation avoids ambiguity when using relative phrases like left-right, lower-upper.

Color choices are intended to consistently relate to the same cloud types throughout this section. These choices are based on a classes relative location on the two parameter scatterplot. The easiest color to assign was pale blue to the scatterplot's lower left corner. This class, representing clear superpixels, is always present and typically very dense. Next, light green is assigned to the highest, left-middle values. This class is typically associated with superpixels containing a wide range of values, where no single description applies to all the pixels inside it. Assigning tan to the lower far right values produces a triangle which spans the scatterplot. This tan class is associated with homogeneous middle to high clouds. In Figure V.5 these three colors, pale blue, green and tan, are printed in the largest letters. This is meant to indicate that they are typically the most consistent and reliable colors used in the classified image. These first three colors define an internal reference for describing the locations of additional classes/colors. The next three most consistent colors are red, purple and dark green. These colors appear regularly and are generally consistent with the interpretation found in Table V.7. Adding yellow and dark blue completes the set of colors used for two parameter classifications. This gives the following set of colors used for two parameter classifications: pale blue, light green, tan, red, purple, dark green, yellow, and dark blue.

In this study the blue and green class is always separated by an intervening class assigned the color red. The red class is made up of superpixels containing water/cloud

boundaries or sometimes very low clouds. Occasionally a fourth class will be present along the blue-green line below the red class. The color yellow is assigned to this region which represents low clouds or their boundaries. Yellow indicates enough separation with respect to the second parameter to produce four classes along with a small value for the first parameter. The most dramatic use of yellow occurs for 2-10-86 (see Figures V.2 and III.1). For this day the water class is made up of two distinct homogeneous regions which differ only slightly with respect to IR spectral intensity.

If a class exists between the light green and tan classes it is denoted by the color purple. This class is made up of middle to high clouds with moderate to high structure, or superpixels on the boundary between low and high structure cloud classes. As with the blue-green line the green-tan line may intercept a fourth class. In this case the class is colored dark blue denoting superpixels similar to the yellow superpixels with higher first parameter values (altitude). The dark blue class is an intermediate class between tan and any number of other cloud types.

The final color used in this section in dark green. It is assigned to the class which would separate the pale blue and tan classes along the tan-blue line. This class color is rarely used and implies the absence of a tan class. It is the lowest, right most class, indicating a low altitude cloud with little variation in structure or temperature. This description introduces a basis for color interpretation for two parameter classifications presented in this section. The text is then free to focus on the unique attributes of the discussion at hand. When no reference to color is made, the above interpretation is assumed. Table V.7 summarizes the relationship between class location on scatterplot, assigned color and physical interpretation.

A comparison between classification obtained by Autoclass and the spatial coherence method (Coakley and Bretherton (1982)) was performed for two days, the 2-18-86 and 2-24-86. (see Fig. III.1). The spatial coherence method uses two IR parameters. The mean and the standard deviation of each superpixel are evaluated and

then plotted in a parameters space where the standard deviation corresponds to the vertical axis and the mean value to the horizontal axis. At the top of the scatterplots, the points spread out without any characteristic shape, while arches can be identified at the bottom of the scatterplot. A threshold value is chosen for the standard deviation, separating the top from the bottom of the graph. In the bottom, each foot of the arc can then be identified with clear or different cloud heights[15]. Using the spatial coherence methods[16] four feet were found in both case 2-18-86 and 2-24-86. Classifications obtained for different values of the standards deviation threshold are illustrated in Figure V.6 for both cases. Note the classification's sensitivity to the choice of standard deviation threshold. A threshold value of six was judged to give the best classification and kept for comparison with AC in the same parameter space. These comparisons are illustrated in Figure V.7. along with each methods working parameter space.

Scatter plot of the parameters space, on a log-log graph[17], classified with Autoclass III and the resulting image are in the upper half. Scatter plots used with the spatial coherence method and its classification are shown in the lower half. Unlike the spatial coherence methods, Autoclass will not necessary assign a different class to each foot (see discussion below). However in both cases, the two extreme feet were recognized as two different classes. The upper part of the scatter plot, considered as a uniform class with the

---

[15] Some improvements of the spatial coherence method have been proposed since its introduction (see Ebert (1989) among others).

[16] The spatial coherence method is generally applied to single arch scatterplots. Applying this method to a four arch scatterplot weakens the exact interpretation while maintaining the spirit of the spatial coherence method.

[17] The classifier Autoclass III assigns a log-normal probability distribution to the point density in this parameter space. It is then more appropriate to usea log-log representation to illustrate the parameter space in which the classification occurred.

spatial coherence method, is divided in different classes by Autoclass. The consequence of the two classifications can be compared on Figure V.7 (for 2-18-86 and 2-24-86). For the two cases studied, the two methods give similar classifications for the superpixels assigned to the water (light blue), the cloud tops at high altitude (tan) and the mixed class (green). In both case, Autoclass underestimate the number of superpixels classified as cloud tops at low altitude (red) or cloud tops at middle altitude (purple)[18] with the spatial coherence method.

Using the same two IR parameters, the resulting classifications and scatter plot of the parameters spaces (on a log-log graph[17]) are given for each day in Figure V.8. The resulting classification is related to cloud altitude and variability (see also discussion in v.d.1). The number of classes found vary between 3 and 5. The following observations can be drawn from the scatter plots (right hand side in Fig. V.8). The feet of the arches are identified as distinct classes when:

1) they have a high density of points (cases 2-11-86 and 2-17-86),

2) the distance between the feet is large enough (2-15-86 case),

3) the two previous features are simultaneously coupled (cases 2-12-86, 2-18-86, 2-19-86, 2-20-86, 2-24-86 and 2-25-86).

Intermediate feet are found to sometimes have their superpixels classified in the same class as a neighboring foot (cases 2-15-86, 2-18-86 and 2-25-86) or other times are partitioned into different classes (cases 2-12-86 and 2-24-86). The difficulty in recognizing different feet as different classes seems to be a consequence of the closeness between the feet or when a foot is consist of a weak density of events. It should also be noted that the upper half of the scatter plot is often divided in different classes (case 2-10-86, 2-11-86, 2-12-86, 2-15-86, 2-17-86, 2-18-86 and 2-19-86). The resulting

---

[18] In the second case 2-24-86, any of the superpixels were identified as cloud at middle altitude with AC.

classifications (left hand side in Fig. V.8) have the following characteristics. The superpixels that belong to the water class are well identified, except in the case 2-10-86 (see Fig. V.2 for IR min. classification of the same day), 2-11-86 and 2-15-86. With respect to the altitude features (see Fig. III.1), different clouds have been assigned with coherence to different classes (case 2-10-86, 2-12-86, 2-18-86, 2-19-86, 2-20-86 and 2-24-86).

A second two dimensional parameter space is presented composed of one spectral parameter, the IR mean and one textural parameter, the visible contrast. The resulting classifications and scatter plot of the parameters space (on a log-log graph[17]) are given for each case in Figure V.9. The number of classes vary between three and seven. The shapes of different scatter plots (right hand side in Fig. V.9) have no characteristic shapes as for IR mean and standard deviation discussed above. However, one arch with two feet can be identified in several scatter plot (case 2-12-86, 2-1686, 2-20-86, 2-24-86 and 2-25-86), while the scatterplot for 2-11-86 is unique.

The region colored light blue correctly corresponds to the water, except in the case 2-10-86 (see Fig. V.2 for IR min. classification of the same day) and 2-25-86. In the later case, the water seems to have been separated into two classes (light blue and yellow). For this parameter space the color assignment and interpretation is well respected.

v.c.4 Analysis in a three parameter space

A typical analysis in a 3 dimensional space is presented in Figures V.10 and V.11. The scatter plots (on a log-log graph[17]) are the projections of the parameter space onto three orthogonal planes (each one having two parameters as vertical and horizontal axis). They are illustrated with the resulting classifications (in the lower right corner). In both studies, the analysis was performed for the day 2-18-86 and the spectral parameters used are IR min. and max. In the first example, (Fig. V.10), the textural parameter is the visible difference, for the second case, (Fig. V.11), the third parameter used was the visible

contrast. Using visible difference, five classes were found, with visible contrast ,seven distinct classes were recognized.

The upper left scatterplots in Figure V.10 and V.11 may be interpreted as described in Table V.7 and Figure V.5 where IR maximum is the first parameter and visible difference is the second parameter. The two other scatter plots (that include the textural parameter in the vertical axis) indicate little or no structures for the tan cluster and more structure for the clouds associated with the green and yellow cluster. The classifications is in agreement with the raw image (see Fig. III.1), except for the red class that correspond in this case to a mixed class (superpixels at the border of clouds).

When the two Figures are compared (especially the scatterplots), it is easy to observe that the superpixels included in the green and red cluster of Figure V.10 are separated into four different classes in Figure V.11. The two scatter plots with textural parameter indicate that red and dark blue have the same value for their contrast but the *later is at a higher altitude.* The yellow and green superpixels are similar in altitude but differ significantly in structure. When compared with the raw data (see Fig. III.1), the dark blue cluster identify correctly a low or middle cloud in the lower right corner of the image (in the lower right corner of Fig. V.11).

The resulting classification for each day is given in Figure V.12 for the 3 dimensional parameter space made of the IR maximum and minimum and the visible contrast[19] . The number of classes varies between four and seven (see Table V.2c). The water, represented by light blue color, is well identified in each case. We note that water and cloud at low altitude, represented with yellow color, are correctly separated for 2-10-86 case. This feature is also observed for the three dimensional parameter space with

---

[19] The classification obtained with the visible difference parameter, replacing the visible contrast, is similar for large classes but with a lesser number of class (see table V2.c)

the visible difference, rather than the visible contrast, and for the three dimensional parameters space composed of IR max., min. and mean. This result stresses the importance of the IR minimum parameter for distinguishing cloud at low altitude from water[20]. Small holes in the clouds are also correctly found (cases 2-14-86, 2-16-86, 2-18-86, 2-20-86 and 2-20-86).

With the help of scatter plots (see also discussion at the beginning of this section and Figures V.10 and V.11), features can be associated with some classes. Corrections to the feature and class association can be verified by comparing the classification with the raw image (see Fig. III.1). The yellow superpixels are correctly identified as homogeneous (few structures) clouds at low altitude for cases 2-10-86, 2-11-86, 2-12-86 and 2-16-86. The purple superpixels identify clouds at intermediate altitude but with structures for cases 2-11-86, 2-15-86, 2-17-86, 2-18-86, 2-20-86 and 2-25-86. Homogeneous clouds at medium and high altitudes (tan colored class) are well identified for the cases 2-10-86, 2-12-86, 2-18-86, 2-20-86 and 2-25-86. The basic correspondence between class and features used so far is difficult to apply to the day 2-14-86. This is understandable considering 2-14-86 produced only one class (i.e. random) for four different parameters.

The other classes, green, red and dark blue colors, usually appears with a weaker density of superpixels and are dispersed over all the images (exceptions are the case 2-14-86 and 2-24-86 for the red class and 2-16-86 for the green). This causes some difficulty to assess the resulting classification.

v.c.5 Summary:

The main difficulty with multiparameter classifications is to identify the physical features associated with each class. This identification is more complicated when the

[20] As already indicated in section v.c.1.

number of classes increases, especially with classes that include few occurrences. The use of the scatterplot is particularly useful for assigning and understanding physical features corresponding to a given class. As illustrated in the two previous sections this can be done by analyzing the shape and the distribution of the points density in scatter plots. However the multiparameter classification may generate new classes, that correspond to features difficult to identify or underlying processes, or even represent a features that have no logical physical interpretation.

Single parameter classifications find classes that are more easily associated with physical features. However fewer classes are found and these classes are only obtained with respect to a single feature. This constraint can be easily removed when using combination of single[21] parameter classification. Each superpixels is assigned to different classes, with each class obtained from a particular single parameter classification. Each class is also associated to a physical feature. So each superpixel (or region) is identified by a collection of classes or features (e.g. high, thick, no flat structure, ..., etc.). A resulting combination of features is synthesized into a superclass.

[21] Sequential classification is not restricted to single parameter space.

Table V.1: Summary of the number of classes found for different dimensional parameter spaces grouped by type of parameters used.

Number Of Parameters	Number Of Classes Found							TOTALS
	1	2	3	4	5	6	7	
1 spectral	8	60	3	1	.	.	.	72
1 STD	.	12	10	2	.	.	.	24
1 textural	1	22	22	3	.	.	.	48
1 Parameter Totals	9	94	35	6	.	.	.	144
1 spectral and 1 textural	.	3	12	31	27	7	4	84
2 spectral	.	8	36	15	10	2	1	72
2 Parameter Totals	.	11	48	46	37	9	5	156
3 spectral	.	.	4	8	.	.	.	12
2 spectral and 1 textural	.	.	.	6	6	7	5	24
3 Parameter Totals	.	.	4	14	6	7	5	36
Total TOTALS	9	105	87	66	43	16	10	336

Table V.2a: Number of classes found for each single parameter run of Autoclass.

	Visible Parameters								IR Parameters			
Date	MIN	MAX	MEAN	STD	DIFF	CONT	ENTR	SECM	MIN	MAX	MEAN	STD
2-10	1,2	2,2	2,3	3,3	3,3	4,3	2,3	3,3	4,4	2,2	2,3	2,2
2-11	2,4	2,3	2,3	4,4	3,3	2,3	2,3	3,3	2,3	2,2	2,3	4,4
2-12	2,3	2,3	2,3	3,3	3,3	3,3	2,2	2,2	2,3	3,3	2,3	3,3
2-14	1,2	1,2	1,2	2,2	2,2	3,3	1,2	2,5	2,3	2,3	2,3	3,3
2-15	3,3	2,3	2,3	3,3	3,3	3,3	2,3	3,5	2,3	2,2	2,3	2,3
2-16	1,2	2,3	1,2	3,3	3,3	3,3	2,3	2,3	1,2	2,2	1,2	2,2
2-17	2,3	2,3	2,3	2,3	3,3	3,3	2,3	3,2	2,3	2,2	2,4	2,2
2-18	2,3	2,2	2,3	2,2	3,4	3,3	3,4	2,2	2,3	2,3	3,3	2,2
2-19	2,3	2,3	2,3	2,3	2,3	4,4	2,3	2,3	2,3	2,3	2,3	3,3
2-20	2,3	2,3	2,3	3,4	4,5	3,3	3,3	2,3	2,3	2,3	2,3	3,4
2-24	2,3	2,3	2,3	2,2	2,3	3,3	2,2	2,3	2,3	2,3	2,3	3,2
2-25	2,3	2,3	2,3	2,2	2,2	3,3	2,2	2,3	2,3	2,3	2,3	2,2

Table V.2b: Number of classes found for each two parameter run of Autoclass.

	1 Spectral and 1 Textural Parameter							2 Spectral Parameters					
Date	Vis Max & Cont	Vis Max & Entr.	Vis Std & Cont	Vis Std & Diff	Vis Std & Entr	IR Mean & Cont	IR Mean & Diff	Vis Min & Max	Vis Mean & Std	Vis Max & IR Min	Vis Std & IR Std	IR Min & Max	IR Mean & Std
2-10	5,5	3,3	6,6	5,5	4,5	5,6	4,4	2,4	4,4	3,3	4,4	4,4	3,4
2-11	4,4	4,5	6,6	5,5	5,5	4,4	4,4	3,4	4,3	3,3	6,7	2,3	5,6
2-12	4,4	2,3	5,6	5,4	4,4	7,7	5,5	3,3	5,5	3,3	5,5	3,3	5,4
2-14	4,4	2,3	5,5	5,5	3,3	5,5	4,4	2,2	3,3	2,3	3,3	2,3	3,3
2-15	4,4	3,3	5,5	4,4	5,5	5,4	4,4	3,4	3,3	3,4	4,5	3,3	5,5
2-16	4,4	3,3	4,4	4,5	4,4	3,3	3,3	2,3	3,3	2,2	3,3	2,2	3,2
2-17	4,4	3,3	5,5	4,5	4,4	5,5	3,3	3,3	3,3	3,3	4,4	3,3	5,5
2-18	5,6	3,3	7,5	6,6	5,5	5,5	5,5	3,3	4,5	3,3	7,6	4,4	5,4
2-19	4,5	3,4	6,5	4,4	4,4	6,4	4,5	3,3	4,5	3,4	4,5	3,3	5,5
2-20	5,6	3,3	5,6	4,5	4,4	5,7	5,7	3,4	4,4	3,3	6,5	3,3	5,5
2-24	4,3	2,3	6,5	5,5	4,4	5,5	4,4	3,4	3,3	3,3	4,4	3,3	4,4
2-25	7,7	3,4	6,5	4,4	4,4	7,7	5,5	3,4	4,5	3,4	5,5	3,3	4,6

Table V.2c: Number of classes found for each three parameter run of Autoclass.

	3 Spectral Parameters	2 Spectral and 1 Textural Parameter	
Date	IR Min, Max & Mean	IR Min, Max & Contrast	IR Min, Max & Difference
2-10	4,4	7,8	6,6
2-11	3,3	6,7	5,7
2-12	4,4	6,8	6,6
2-14	3,3	5,6	4,4
2-15	4,4	7,6	4,4
2-16	3,3	4,4	4,3
2-17	4,5	6,5	4,5
2-18	4,4	7,7	5,5
2-19	4,4	6,6	5,5
2-10	4,4	7,8	5,5
2-24	3,3	5,5	4,4
2-25	4,4	7,8	6,6

Table V.3 : Color assignment summary for single parameter classifications with associated physical interpretation.

Spectral Parameters				
			Physical Interpretation	
Color	Value	Description	IR	Visible
Blue	low	highest temperature	water	water
Yellow	low to middle	high to middle temperature	low clouds	thin clouds
			↓	↓
Light Green	middle to high	middle to low temperature	↓	↓
Dark Green	high	coolest temperature	high clouds	thick clouds
Standard Deviation Parameters				
			Physical Interpretation	
Color	Value	Description	IR	Visible
Blue	low	lowest variability	small variability in altitude	small variability in optical thickness
Yellow	low to middle	intermediate variability	↓	↓
Light Green	middle to high	intermediate variability	↓	↓
Dark Green	high	highest variability	high variability in altitude	high variability in optical thickness
Visible Textural Parameters				
			Physical Interpretation	
Color	Value	Description	Difference, Contrast, or Entropy	Angular Second Moment
Tan	low	least structure	little structure	high structure
Red	low to middle	low structure	↓	↓
Pink	middle to high	moderate structure	↓	↓
Purple	high	most structure	high structure	little structure

Table V.4: Examples of the physical features that are associated with superpixels that have been classified in two different single parameter spaces. The resulting combination of the two classifications is in good agreement with the original image for the 2-12-86 case (see Figures III.1 and V.2). The low number of classes and their physical interpretation allow this easy identification of the physical properties of each superpixel.

IR minimum classification	IR standard deviation classification	Resulting features associated to the superpixels
blue/clear	blue/uniform altitude	water
green/cloudy	blue/uniform altitude	clouds at the same altitude
blue/clear	green/variable altitude	mixed cloud/water or clouds at different altitudes
green/cloudy	green/variable altitude	clouds at different altitudes

Table V.5: Example of combining 4 single parameter classifications (the four left handed columns into superclasses) and the resulting diagnostics (the last column). In the later, 7 superclasses can be identify. The superclass "no diagnostic" indicates contradictory information from different single parameter classifications (e.g., a superpixel identified as water by one parameter classification but as having a spatial structure by another one). Few superpixels are expected to belong to the "no diagnostic" superclass. The superpixels belonging to the superclass "mixed cloud/water or clouds at different altitudes" will require additional analysis to be more precisely identified.

IR minimum classification	IR standard deviation classification	Visible minimum classification	Visible contrast classification	Diagnostic
blue/clear	blue/uniform altitude	blue/thin	tan/no structure	water
green/cloudy	blue/uniform altitude	blue/thin	tan/no structure	thin clouds at the same altitude with no structure
green/cloudy	blue/uniform altitude	green/thick	tan/no structure	thick clouds at the same altitude with no structure
green/cloudy	blue/uniform altitude	blue/thin	purple/structure	thin clouds at the same altitude with structure
green/cloudy	blue/uniform altitude	green/thick	purple/structure	thick clouds at the same altitude with structure
blue/clear	green/variable altitude	blue/thin	tan/no structure	mixed cloud/water or clouds with different features
green/cloudy	green/variable altitude	blue/thin	tan/no structure	
blue/clear	green/variable altitude	green/thick	tan/no structure	
green/cloudy	green/variable altitude	green/thick	tan/no structure	
blue/clear	green/variable altitude	blue/thin	purple/structure	
green/cloudy	green/variable altitude	blue/thin	purple/structure	
blue/clear	green/variable altitude	green/thick	purple/structure	
green/cloudy	green/variable altitude	green/thick	purple/structure	
blue/clear	blue/uniform altitude	green/thick	tan/no structure	No diagnostic
blue/clear	blue/uniform altitude	blue/thin	purple/structure	
blue/clear	blue/uniform altitude	green/thick	purple/structure	

Table V.6: V-diagram summary of key points for all twelve days.

Day	IR Parameter	$Sup._{90}$	Class Boundary	$Inf._{90}$	Parameter Range
2-10	min @				96
	max	94	100.5	110	127
	mean	94.4	102.5	115.2	106.1
2-11	min	93	102.5	117	86
	max	93	101.5	116	101
	mean	93.7	102.0	115.8	90.3
2-12	min	106	114.5	126	126
	max #				127
	mean	106.5	115.7	128.3	126.1
2-14	min	97	106.5	121	118
	max	98	107.5	123	119
	mean	97.7	107.1	121.3	118.2
2-15	min	107	118.5	133	124
	max	105	117.5	136	135
	mean	106.7	118.5	135.2	129.1
2-16	min *				51
	max %				87
	mean *				68.5
2-17	min	95	104.5	118	102
	max	92	100.5	114	113
	mean	94	103.0	117.7	108.7
2-18	min	105	113.5	125	130
	max	103	113.5	128	136
	mean #				131.8
2-19	min	103	110.5	120	137
	max	106	114.5	126	141
	mean	105	112.8	123	139
2-20	min	107	117.5	130	130 (?)
	max	106	116.5	132	132
	mean	107.4	118.4	133.3	129.5
2-24	min	104	114.5	129	104
	max	103	114.5	133	110
	mean	104.3	115.6	132.2	106.8
2-25	min	104	112.5	123	125
	max #				127
	mean	102.5	110.6	121.9	125
Ave range/day over min, max, & mean		1.53	1.78	3.19	

* Classification produced 1 class
\# Classification produced 3 classes
@ Classification produced 4 classes
% Range of % likelihood values insufficient for this analysis

Table V.7 : Two parameter color assignments summary with associated physical interpretation.

Color	Value for		Physical interpretation with First Parameter = IR Mean and,	
	First Parameter	Second Parameter	Second Parameter = visible contrast	Second Parameter = IR Standard deviation
Pale Blue	low	low	Water	Water
Light Green	middle	high	high variability/mixed class	highly inhomogeneous clouds, mixed cloud-water boundaries
Tan	high	low	solid middle→high clouds with low structure	homogeneous middle→high clouds
Red	low→middle	middle	cloud-water boundary, low clouds	cloud-water boundary, low clouds
Purple	middle→high	middle	middle-high clouds with moderate→high structure	moderately inhomogeneous middle→high clouds
Yellow	low→middle	low→middle	very low clouds, low cloud-water boundary	very low clouds, low cloud-water boundary
Dark Blue	middle→high	low→middle	cloud-cloud boundary, low→moderate structure	No examples of using this color
Dark Green	middle	low	low→middle clouds with low structure	homogeneous low→middle clouds

VI. MULTIFRACTAL PROPERTIES OF THE CLOUDS AND OF THE TEXTURAL PARAMETERS

The classification issue was questioned in relation with the scale invariance properties of the clouds. Or, as indicated in the original proposal, how fractal notions could be used to support classification? The following sections are an attempt to partially answer this question.

VI.A. INTRODUCTION

The simplest fractals are those that are self similar with respect to their geometry. The microstructure is indistinguishable, within a magnification or dilatation, from the macrostructure. Fractals dimensions can also be characterized by the statistical properties of a set. In this case, it is no more the geometry, but rather the probability distribution (or statistical moments) of the set that are scale invariant.

Fractals are limited in their applications since they can only used with sets. Typical geophysical quantities, e.g. satellite cloud radiance, are best described by fields. Multifractals[22] become more appropriate since they are measures of field properties: they characterize the scaling behavior of the statistical properties of the field over a range of scales. If clouds are geophysical processes which fall into the category of universal multifractal (Tessier *et al.* (1992)), then there is a great deal that can be infered from existing satellite measurements. Most important would be the ability to relate measurements taken at different resolutions.

---

[22] Multifractal can be seen as a collection of sets, with their fractal dimensions varying continuously, embedded one into the other. They are complex nonlinear superposition of singularities of various order and thus involve coherent structures of all size.

VI.B. MULTIFRACTAL ANALYSIS OF SATELLITE CLOUD RADIANCES

The scaling properties of fields can be investigated in different way. A first indication of scale invariance is given by the energy (or power) spectra $E(k)$, which have the following behavior when scaling is observed:

$$E(k) \approx k^{-\beta} \tag{VI.1}$$

where the wavenumber magnitude is given by $k \equiv |\mathbf{k}|$ and β is the scaling exponent. Recall that the energy spectrum is both the ensemble average and angle integrated squared modulus of the Fourier transform of the image.

The curves[23] of the power spectrum for each image are illustrated for both the visible in fig. VI.1 and the infrared in fig. VI.2. A more accurate estimate of the scaling behavior of the data is obtained by performing a spectral analysis on the ensemble average spectra of the 15 images[23]. This is shown in fig. VI.3 for both channels. A more detailed discussion of these results can be found in Lovejoy *et al.* (1992).

The scaling properties of any field can also be studied by analyzing their statistical behavior at different scale lengths. The field intensity is denoted by the symbol ε_λ at a scale ratio λ ($\lambda = L/l$ where L is the size of the largest structure and l is the averaging length scale). The q^{th} statistical moments of ε_λ also exhibit multiscaling properties when they have the following behavior:

---

[23] In figures VI.1 and VI.2, 16 curves are illustrated that correspond to 15 different days. In these studies, three additional days (the 13th, the 22th and the 27th) were considered that were not used in the classification discussed in chapter V. See also section III.A for more details on the data.

$$\langle \varepsilon_\lambda{}^q \rangle \propto \int \lambda^{q\gamma} \lambda^{-c(\gamma)} d\gamma \approx \lambda^{K(q)} \qquad \text{(VI.2)}$$

The bracket in eq. (VI.2) indicates the statistical ensemble average where $K(q)$ is the scaling exponent associated with the statistical moment of the field intensities (e.g., β is the one associated with the energy spectrum). Without any *a priori* hypothesis, $K(q)$ could be any convex function. However, for the most general process to generate multifractals -the (canonical) multiplicative cascade process- it has been shown that stable (attractive) universality classes[24] exist (see Schertzer and Lovejoy (1987a, b, 1991). Brax and Peshanski (1991) and Kida (1991)). The latter imply that the scaling exponents have their functional behavior specified by two parameters, α and C_1.

The Lévy index, α , indicates the class to which the probability distribution belongs. It takes values[25] between 0 and 2 (e.g. $\alpha = 0$ corresponds to monofractal, $\alpha = 1$ to logCauchy and $\alpha = 2$ to lognormal). The second parameter, C_1 is the codimension which characterizes the sparseness/inhomogeneity of the mean of the process ($C_1 = 0$ is space filling). In general a third parameter, H, is needed to complete the scaling description of empirical data. H is the Kolmogorov scaling exponent and can be estimated through energy spectra analysis when the values of α and C_1 are known. The estimate of these three parameters leads to a complete characterization of the multiscaling properties of geophysical fields (see table VI.1).

---

[24] This result for multiplicative cascade corresponds to the central limit theorem for the addition of random variables. The latter guaranties that stable distributions (e.g. the Gaussian) will appear in many situation independently of the detail of the generating process.

[25] An important result is the estimated value $\alpha \approx 1.3$ for turbulent velocity fields (Schmitt *et al.* (1991a, b)).

IV.C. SCALING PROPERTIES OF THE TEXTURAL PARAMETER

As indicated in the previous section, strong evidence of the scaling properties of the satellite cloud radiances have been found. The question is whether or not textural parmeters are also scale invariant and under which conditions. Scale invariance is fundamental for the generalization of their applications. Textural parameters are the result of specific transformations or operations which involve scale-lengths that are performed on the data fields. Analyzing the behavior of the q^{th} statistical moment of the fields as a function of the scale length may provide the information[26] needed. Curves of q vs. length on a log-log graph which produce a straight line, may suggest that scaling is respected by the transformation. Recall that scaling properties of the data were deduced by observing the same behavior for the power spectrum $E(k)$ (see fig. VI.1) or statistical moments (see Tessier *et al.* (1992)) as indicated by equations VI.1 and VI.2.

The textural parameters have a double dependence on the scale length. One can study the variation of the textural parameters as a function of ρ, the distance between two pixels (see eq. III.1), keeping the size of the superpixel, l, constant (and in the case discussed below, equal to the size of the field). Or one can study the variation of the textural parameters as a function of l, keeping ρ fixed (and equal to 1 in the analysis given below).

Additionally, the dependence on θ (see chapter III) of the scaling properties was studied. If the scaling properties are not modified with θ, the field may be isotropic with respect to the given textural parameter.

The scaling properties of $\nabla g(\rho,\theta)$ (see eq. III.1) with respect to a change in ρ are investigated. For a given θ, the values of $\nabla g(\rho,\theta)$ are estimated for ρ values increasing

---

[26] Notice that the method proposed is not the only one.

from 1 to 256 by a factor of 2, for all the pixels in the scene[27]. For each value of ρ, the q^{th} order of the statistical moment of $\nabla g(\rho,\theta)$, denoted by $\langle[\nabla g(\rho,\theta)]^q\rangle$, are estimated over the whole image. Statistical moments have been evaluated with $q = 0.2$, 0.4, 0.6, 0.8, 1.00, 1.25, 1.50, 1.75, 2.00, 3.00, 4.00 and 5.00. This procedure is repeated for the four values of θ.

Although scaling will not hold exactly on any finite number of samples, two individual cases have been investigated, 2-14-86 and 2-24-86 (see fig. III.1). Curves of statistical moments are mapped as a function of ρ on a log-log graph for each of the four angles in both cases. These results are respectively reported in figures VI.4 and VI.5. A more accurate estimate of the scaling can be obtained when the statistical averages are performed over the 13 scenes. Curves of statistical moments are given for each of the four angles in fig. VI.6. Each curve corresponds to different values of q. Straightness of the curves indicates that scaling is well observed in every situation. This linear relationship indicates the same power law behavior across all scales.

The scaling exponent for a given q is given by the slope of the regression line of $\log(\langle[\nabla g(\rho,\theta)]^q\rangle)$ vs. $\log(\rho)$. This operation is performed for different values of q to obtain the behavior of the scaling exponent as a function of q. For the three analyses described above, the curves of the scaling exponents as a function of q are illustrated in figures VI.7, VI.8 and VI.9. In each figure, four curves are given which correspond to the four values of θ to compare how the scaling properties change relative to each other as a function of direction. If the curves lie on top of each other, the scaling is direction independent. Although the plots for all four angles are relatively close together for all values of q, the curves are closer together for low values of q and spread further apart as q increases. The

---

[27] Recall that in the first part, superpixel size is held constant at 512 pixels, corresponding to the image size.

increasing gap between the curves indicates angle is a factor in determining the degree of scale change and thus the field may be weakly anisotropic.

In the second part, the scaling properties of each individual textural parameter with respect to modification of the superpixel size l is investigated. The four textural parameters described by eq. III.2 to eq. III.5 are evaluated for a fixed value of $\rho = 1$ over superpixel of size that ranges from $l = 4$ to $l = 256$ by a factor of two. For each value of l, the q^{th} order[28] of the statistical moment of the textural parameter is estimated over the whole image. This procedure is carried out for each angle individually as well as for an average over all four angles. An average of the four angles combined provides a larger data set.

The same two individual cases have been investigated, 2-14-86 and 2-24-86. For each direction and the average over the four directions, the statistical moments are mapped as a function of l on a log-log graph. The results for *Difference*, *Contrast*, *Entropy* and *Angular Second Moment* are respectively reported in fig. VI.10 to fig. VI.13 for the case 2-14-86 and in fig. VI.14 to fig. VI.17 for the case 2-24-86. Each curve corresponds to a different value of q. Plots which return a straight line denote scaling or scale invariance. The results suggest that scaling is preserved for the textural parameters *Difference* (see figures VI.10 and VI.14) and *Contrast* (see figures VI.11 and VI.15) for each individual angle and for an average over all angles. However, the parameters *Entropy* and *Second Angular Moment* do not appear to exhibit a linear relationship (see figures VI.12 and VI.16 and figures VI.13 and VI.17 respectively) and thus scaling is not preserved. The same analysis have been performed over a simulated multifractal field generated by cascade processes (see section VI.B). The simulations is with $\alpha = 2$ (corresponding to lognormal) and $C_1 = .18$. For a direction $\theta = 0$, the results for *Difference*, *Contrast*, *Entropy* and

[28] The values of q are the same as in part 1.

Angular Second Moment are given in fig. VI.18. As from the image for 2-14-86 and 2-24-86, only the two first textural parameters scale.

Table VI.1. The values of 3 universal parameters have been estimated for the set of 15 images[23], both for channel 1 and 4 (see Tessier *et al.* (1992) for details).

	α	C_1	H
Channel 1 (visible)	1.15	0.1	0.4
Channel 4 (infrared)	1.45	0.1	0.5

VII. CONCLUSION AND PERSPECTIVES

Building an expert system for the automatic interpretation of clouds and cloud systems is a complicated and difficult task. The first two attempts discussed used Typical Shape Function (EOF) analysis (see chapter IV) and Autoclass II (see section V.C) with a large parameter space (ten or more parameters). Both methods were either unsuccessful or leading to complicated partitioning of the parameter space with a high number of classes[29]. Another difficulty was related to the interpretation of those classes.

Parameter spaces of one, two or three dimensions were studied with Autoclass III . For one and two parameter spaces, classes can be associated with physical features. The results obtained and described in section V.C are promising and suggest new avenues of investigation. First, the analysis in single parameter space is used to evaluate parameters usefulness and eliminate those that are useless. In this study, only channel 1 and 4 have been considered, it will be important to performed the same kind of analysis with other sensor channels and also with microwave data. Ultimately a bank of classifications that results from various single parameter space can be constructed.

Also a new methods of classification was developed and is essentially based on the analysis of many single parameter spaces. Each superpixel is characterized by a collection of classes, and then physical features, obtained from independent analysis of the image with single parameter spaces. Classifications related to single parameter space, avoids the non trivial problems of correlated parameters. Problems related to the choice of units (specially when nonlinear transformation are needed) is less dramatic in single parameter space.

---

[29] Analysis performed with Autoclass III suggest that increasing the dimension of the parameter space usually lead to a larger number of classes found.

A basic feature of Autoclass III is that each point in the parameter space has a given weight to belong to each class. Using this attribute of Autoclass allows the determination of the clouds and clear cover which is independent of an *a priori* threshold. We also point out that cloud/clear cover is best handled by considering a continuum of intermediate state, from completely clear to completely cloudy.

The classification performed in three dimensional space, with two spectral and one textural parameter, was very good for almost all the images analyzed. These results stress the importance of the textural parameter. However the classification obtained in two dimensional space was less impressive. When compare to the spatial coherence method, the classification obtained with Autoclass III using the same parameter spaces was less appropriate in several images. However the spatial coherence method is quite limited and suffers from its own drawbacks as well.

An interesting point is that an automated version of the method discussed above can be implemented for cloud classification from satellite data. Nevertheless, after all the various experiments and analysis performed with Autoclass III, we believe that finding the appropriate set of parameters is the most difficult aspect of this problem. This may be more important than the classifier used. This is very important for further applications of classifications in domain such as the weather forecasting or climate studies. However, the set of parameters and the resulting classification may vary with the domain of application. The effort spent in understanding the performance of difficult parameter space, or their combinations, is the most likely to significantly improve the classification results.

Scaling and multifactal properties of satellite cloud radiance are features that can hardly be ignored. Illustration of those properties were discussed in section VI.B for the same data set used for classification. The scaling properties of the textural parameters were also investigated. The fact that the textural parameters are scale independent indicates that classification performed with them will be independent of the resolution of the data. Scaling analysis indicate also that the probability distribution of the satellite

cloud radiances (channels 1 and 2) are not exactly lognormal. An improvement to implement on classifiers will be to used the appropriate probability distribution.

Acknowledgment. The authors would like to acknowledge colleagues and collaborators , B. Anderson, P. Collar, T. Figel, H. Gartner, M. Landsfeld, E. Morrow, J. Paddon, Y. Shiren and R. van der Leeden who gave valuable help during various stages of this project.

VIII. REFERENCES

Arking, A., and Child, J. D., 1986: Retrieval of cloud cover parameters from multi-spectral satellite measurements. J. Clim. and Appl. Meteor., 24, pp. 322-333.

Brax P. and Peshanski, R., 1991: Levy stable law description of intermittent behavior and quark-gluon plasma phase transitions. Phys. Lett. B, 253, pp. 225-230.

Cess, R. D., Harrison, J. D., Minnis, P., Barkstrom, B.R., 1992: Interactions using interp. of seasonal cloud climate: earth radiation budget experiment data. J. Geophys Res.-Atmos., 97, pp. 7613-7617.

Cheeseman, P., Freeman, D., Kelly, J., Self, M., Stutz, J., and Taylor, W., 1988a: Autoclass: a Bayesian classification system. *Proceedings of the Fifth International Conference on Machine Learning* . pp. 54-64. Ann Arbor, MI: Morgan Kaufmann.

Cheeseman P., Freeman, D., Kelly, J., Self, M., Stutz, J., and Taylor, W., 1988b: Bayesian classification. *Proceedings of the Seventh National Conference of Artificial Intelligence* pp. 607-611. St. Paul, MN: Morgan Kaufmann.

Cheeseman, P., Goebel, J., Self, M., Stutz, M., Volk, K., Taylor, W., and Walker, H., 1989: Automatic classification of the spectra from the infrared astronomical satellite (IRAS). (Reference Publication 1217). Washington, DC: National Aeronautics and Space Administration.

Cheeseman, P., 1990: On finding the most probable model. In Jeff Shrager and Pat Langley, editors, Computational Models of Discovery and Theory Formation, pp. 73-96. Morgan Kaufmann, Palo Alto, 1990.

Coakley, J. A., Jr. and F. P. Bretherton, 1982: Cloud cover from high-resolution scanner data: Detecting and allowing for partially filled field of view. J. Geophys Res., 87, 4917-4932.

Ebert, E., 1987: A pattern recognition technique for distinguishing surface and cloud types in the polar regions, J. Climate Appl. Meteor., 26, 1412-1427.

Ebert , E., 1989: Analysis of polar clouds from satellite imagery using pattern recognition and a statistical cloud analysis scheme, J. Appl. Meteor., 28, 382-399.

Ebert, E., 1992: Pattern recognition analysis of polar clouds during summer and winter, Int. J. Remote Sensing, 13, 97-109.

Garrand, L., 1986: Automated recognition of oceanic cloud patterns and its application to remote sensing of meteorological parameters, Ph.D. Thesis, University of Wisconsin, 231 pp.

Garrand, L., 1988: Automated recognition of oceanic cloud patterns. Part I: Methodology and application to cloud climatology, J. Climate, 1, 20-39.

Garand, L., and Weinman, J. A., 1986: A structural-stochastic model for the analysis and synthesis of cloud images, J. Climate and Appl. Meteor., 25 1052-1068.

Haralick , R. M., Shanmugam, K., and Dinstein, L., 1973: Textural features for image classification, IEEE Trans. Sys. Man. Cybern., SMC-3, 610-621.

Harrison, E. F., Minnis, P., Barkstrom, B. R., Ramanathan, V., Cess, R. D., and Gibson, G., 1990: Seasonal variation of cloud radiative forcing derived from the Earth Radiation Budget Experiment, J. Geophys. Res., 95, 2021-2034.

Jalickee, J.B., and Ropolewski, ,C. F., 1979: An objective analysis of the boundary-layer thermodynamic structure during GATE, Mon. Wea. Rev., 107, 68-76.

Kida, S., 1991: Log-stable distribution and intermittency of turbulence, J. Phys. Soc. Jpn., 60, pp. 5-8.

Lovejoy.S., D. Schertzer, P. Silas, Y. Tessier and D. Lavallée, 1992: The unified scaling model of atmospheric dynamics and systematic analysis of scale invariance in cloud radiances:, To be publish in to Annales Geophysicae.

Parikh, J., 1977: A comparative study of cloud classification techniques, Rem. Sens. of Envir., 6, 67-81.

Richards, J. A., 1986: Remote Sensing Digital Image Analysis, pp. 281. Springer-Verlag, Berlin, 1986.

Schertzer, D., S. Lovejoy, 1987a: Singularités anisotropes, et divergence de moments en cascades multiplicatifs. Annales Math. du Que. 11, 139.

Schertzer, D., S. Lovejoy, 1987b: Physically based rain and cloud modeling by anisotropic, multiplicative turbulent cascades. J. Geophys. Res. 92, 9693.

Schertzer, D., S. Lovejoy, 1991: Nonlinear geodynamical variability: Multiple singularities, universality and observables. Scaling, fractals and non-linear variability in geophysics, D. Schertzer, S. Lovejoy eds., Kluwer, pp. 41-82.

Schmitt, F., D. Lavallée, D. Schertzer and S. Lovejoy, 1992a: Empirical determination of universal multifractal exponents in turbulent velocity fields. Phys. Rev. Lett.,68, 305-307.

Schmitt, F., S. Lovejoy, D. Schertzer, D. Lavallée and C. Hooge, 1992b: Turbulence and Universal Multifractals III: First estimates of multifractal indices for velocity and temperature fields. *C. R. Acad. des Sci. Paris*, (in press).

Sengupta, S.K., Welch, R. M., Navar, M. S., Berendes, T. A., and Chen, D. W., 1990: Cumulus cloud field morphology and spatial patterns derived from high spatial resolution Landsat imagery. J. Appl. Meteor., 29, 1245-1267.

Tessier, Y., Lovejoy, S. and D., Schertzer, 1992 Universal multifractal in rain and clouds: theory and observatio. J. Appl. Meteor., (in press).

Tournadre, J. and Gautier, C., 1989: Automated cloud field analysis based on spectral and textural signatures. In Deepak, A., Fleming, H.E., and Theon, J.S., eds., Advances in Remote Sensing Retrieval Methods, pp. 391-410. Deepak Publishing, Hampton, 1989.

Welch, R.M., Kuo, K.S., Wielicki, B.A., Sengupta, S.K. and Parker, L., 1988 a: Marine stratocumulus cloud fields off the coast of southern California observed using LANDSAT imagery. Part I: Structural characteristics, J. App. Meteor., 27, 341-362.

Welch, R. M., Sengupta, S.K. and Kuo, K.S., 1988 b: Marine stratocumulus cloud fields off the coast of southern California observed using LANDSAT imagery. Part II: Textural analysis, J. App. Meteor., 27, 363-378.

Welsh, R. M., Sengupta, S. K., Goroch, A. K., Rabindra, P., Rangaraj, N., and Navar, M. S., 1992: Polar cloud and surface classification using AVHRR imagery: An intercomparison of methods. J. Appl. Meteor., 31, 405-420.

Welsh, R. M., and Wielicki, B. A., 1986: Cumulus cloud field properties derived using Landsat digital data. J. Climate Appl. Meteor., 25, 261-276.

Wielicki, B. A. and Parker, L., 1991: On the determination of cloud cover from satellite sensors: the effect of sensor spatial resolution, Submitted to J. Geophys. Res., 1991.

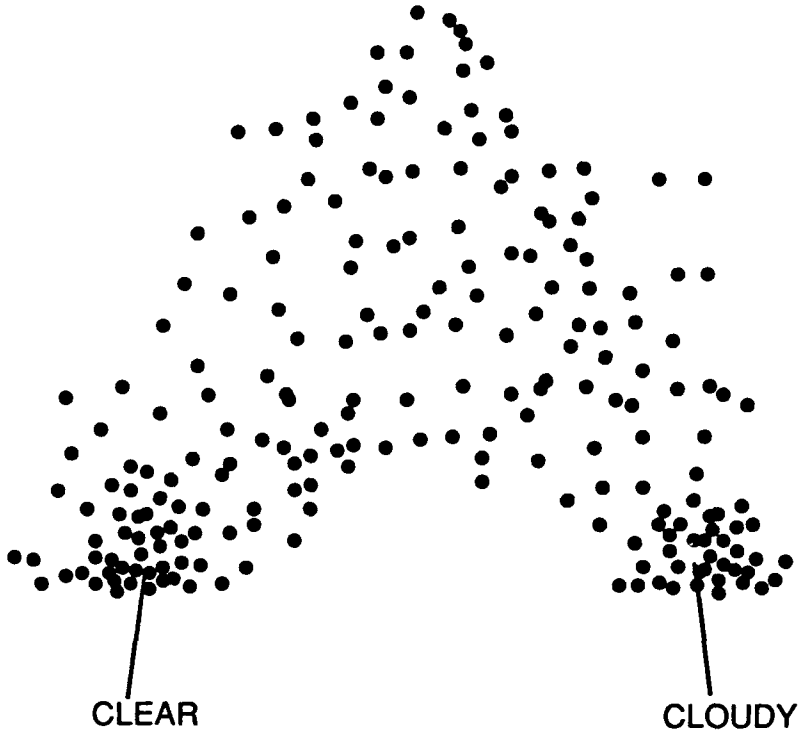

Fig. II.1: Schematic diagram of the 2 dimensional parameter space, typical for the spatial coherence method.

2-10-86 AVHRR Channel 1 (Visible)

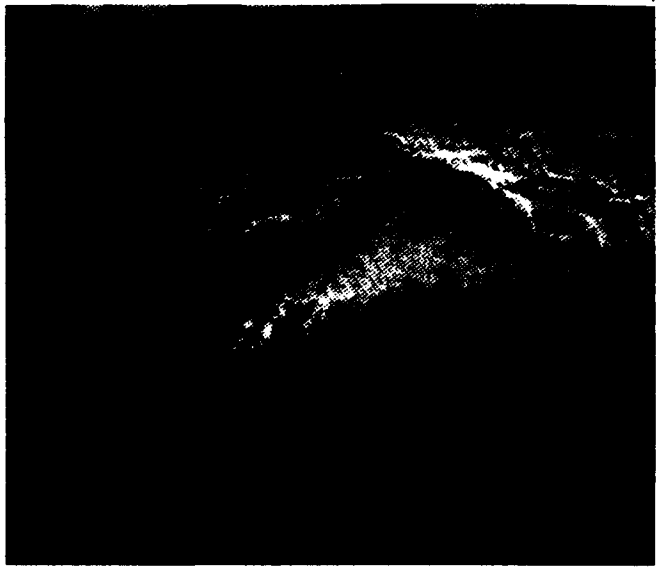

2-10-86 AVHRR Channel 4 (IR)

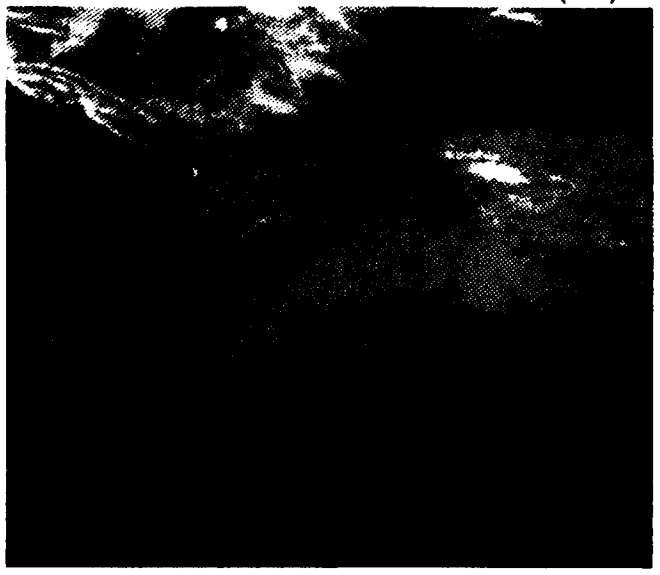

2-11-86 AVHRR Channel 1 (Visible)

2-11-86 AVHRR Channel 4 (IR)

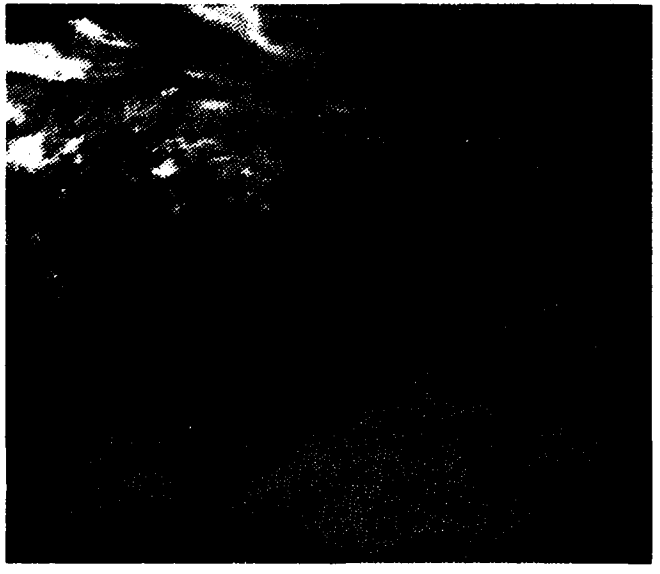

Figure III.1 : FASINEX AVHRR visible and infrared images for 2-10-86 and 2-11-86

2-12-86 AVHRR Channel 1 (Visible)

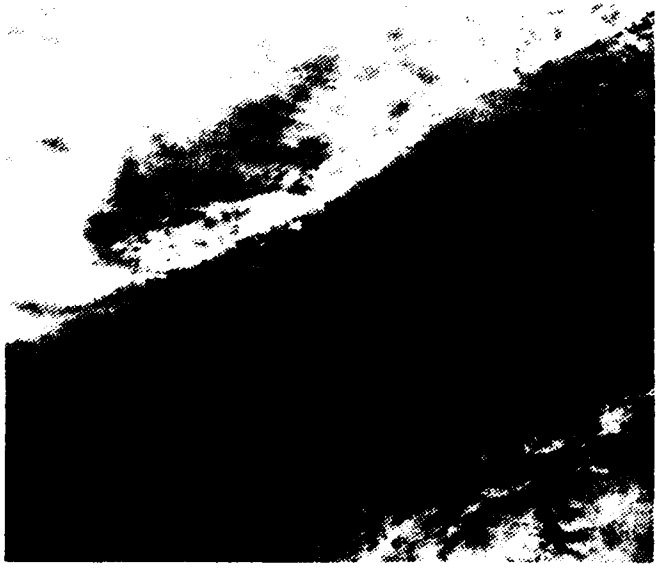

2-12-86 AVHRR Channel 4 (IR)

2-14-86 AVHRR Channel 1 (Visible)

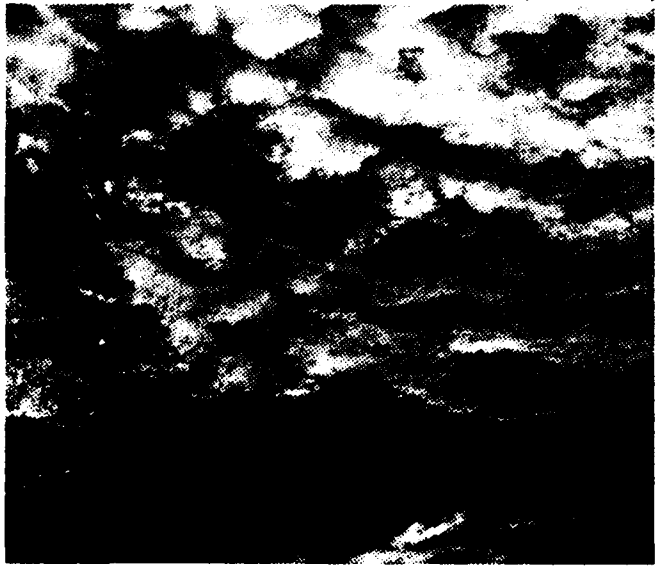

2-14-86 AVHRR Channel 4 (IR)

Figure III.1 : FASINEX AVHRR visible and infrared images for 2-12-86 and 2-14-86

2-15-86 AVHRR Channel 1 (Visible)

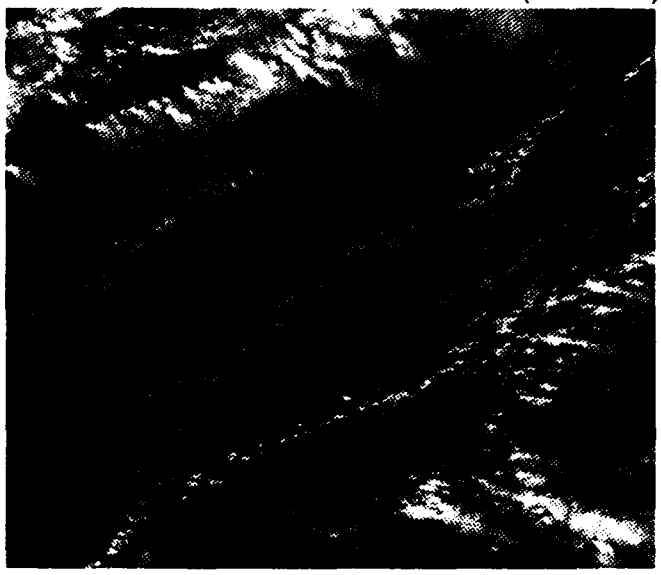

2-15-86 AVHRR Channel 4 (IR)

2-16-86 AVHRR Channel 1 (Visible)

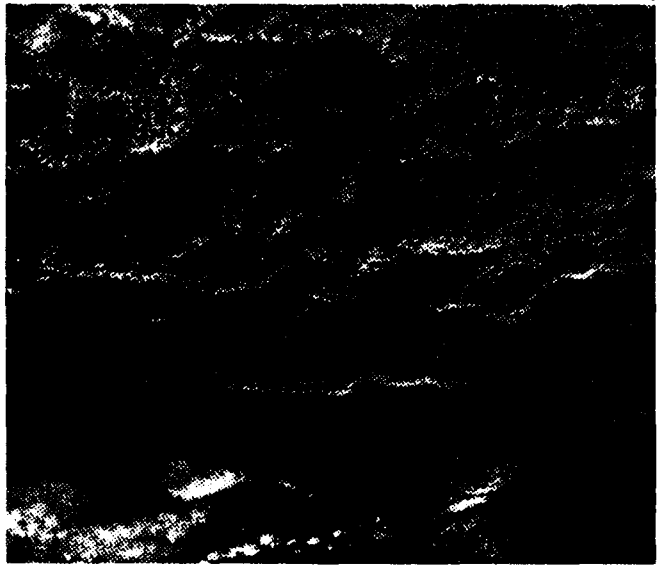

2-16-86 AVHRR Channel 4 (IR)

Figure III.1 :FASINEX AVHRR visible and infrared images for 2-15-86 and 2-16-86

2-17-86 AVHRR Channel 1 (Visible)

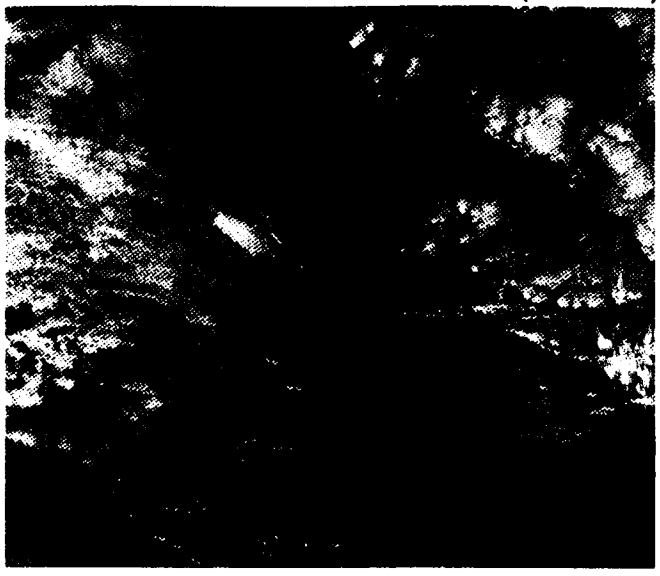

2-17-86 AVHRR Channel 4 (IR)

2-18-86 AVHRR Channel 1 (Visible)

2-18-86 AVHRR Channel 4 (IR)

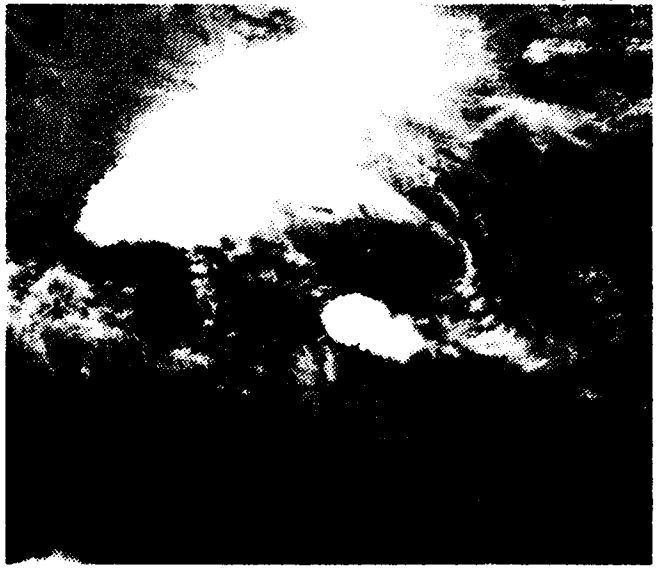

Figure III.1 : FASINEX AVHRR visible and infrared images for 2-17-86 and 2-18-86

2-19-86 AVHRR Channel 1 (Visible)

2-19-86 AVHRR Channel 4 (IR)

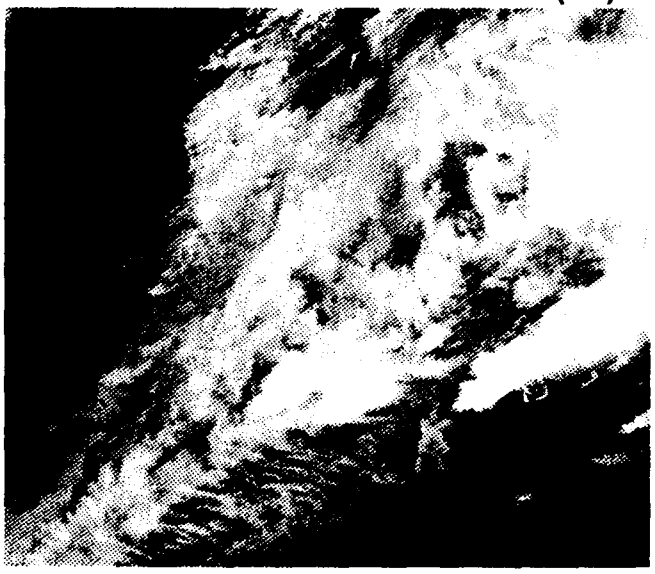

2-20-86 AVHRR Channel 1 (Visible)

2-20-86 AVHRR Channel 4 (IR)

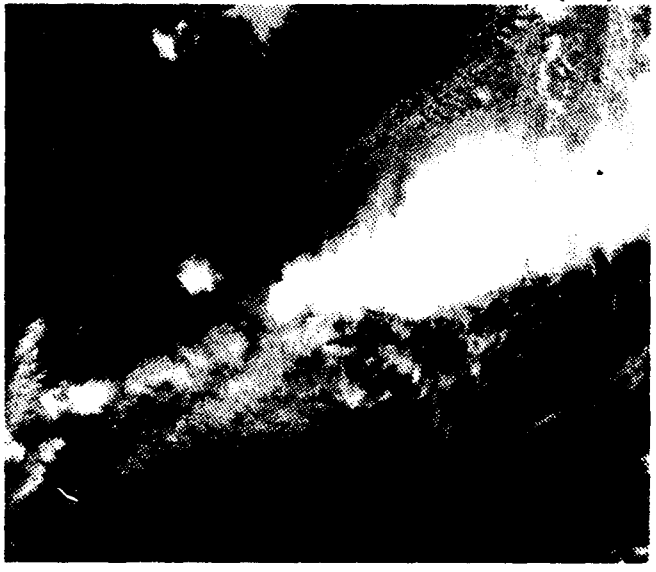

Figure III.1 : FASINEX AVHRR visible and infrared images for 2-19-86 and 2-20-86

2-24-86 AVHRR Channel 1 (Visible)

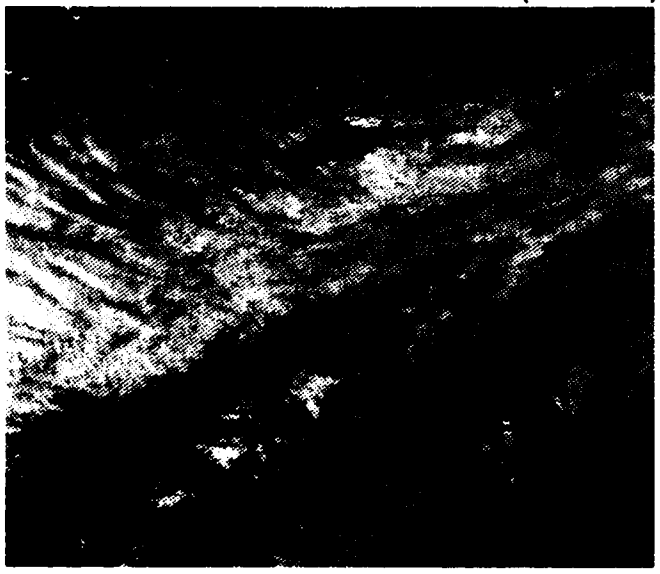

2-24-86 AVHRR Channel 4 (IR)

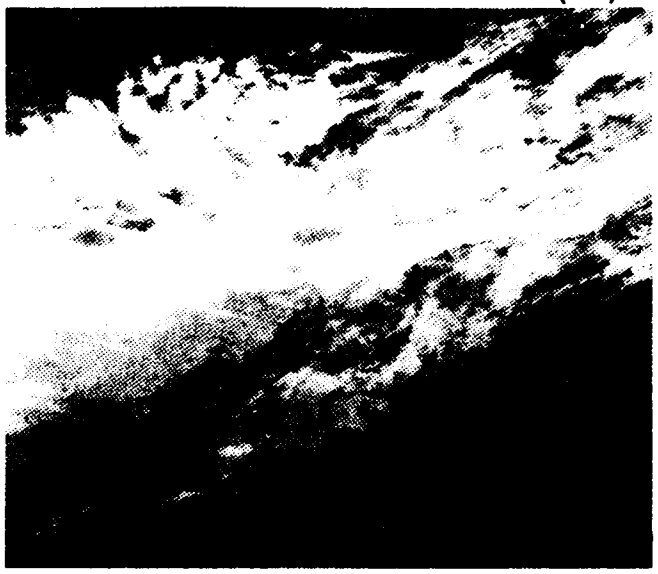

2-25-86 AVHRR Channel 1 (Visible)

2-25-86 AVHRR Channel 4 (IR)

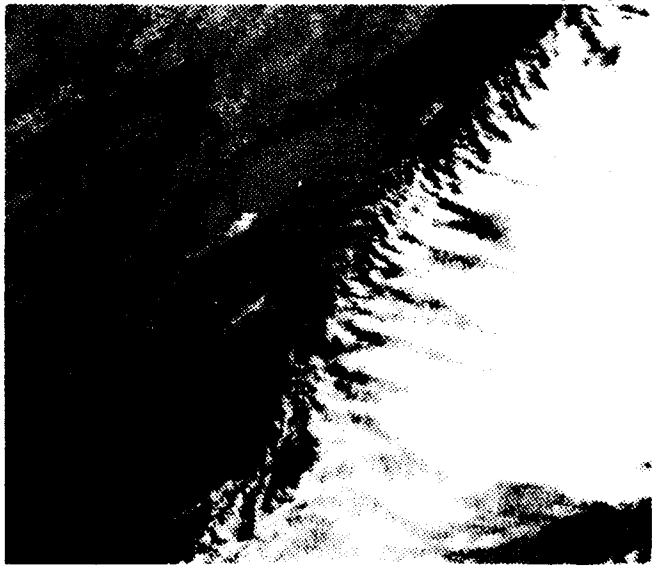

Figure III.1 : FASINEX AVHRR visible and infrared images for 2-24-86 and 2-25-86

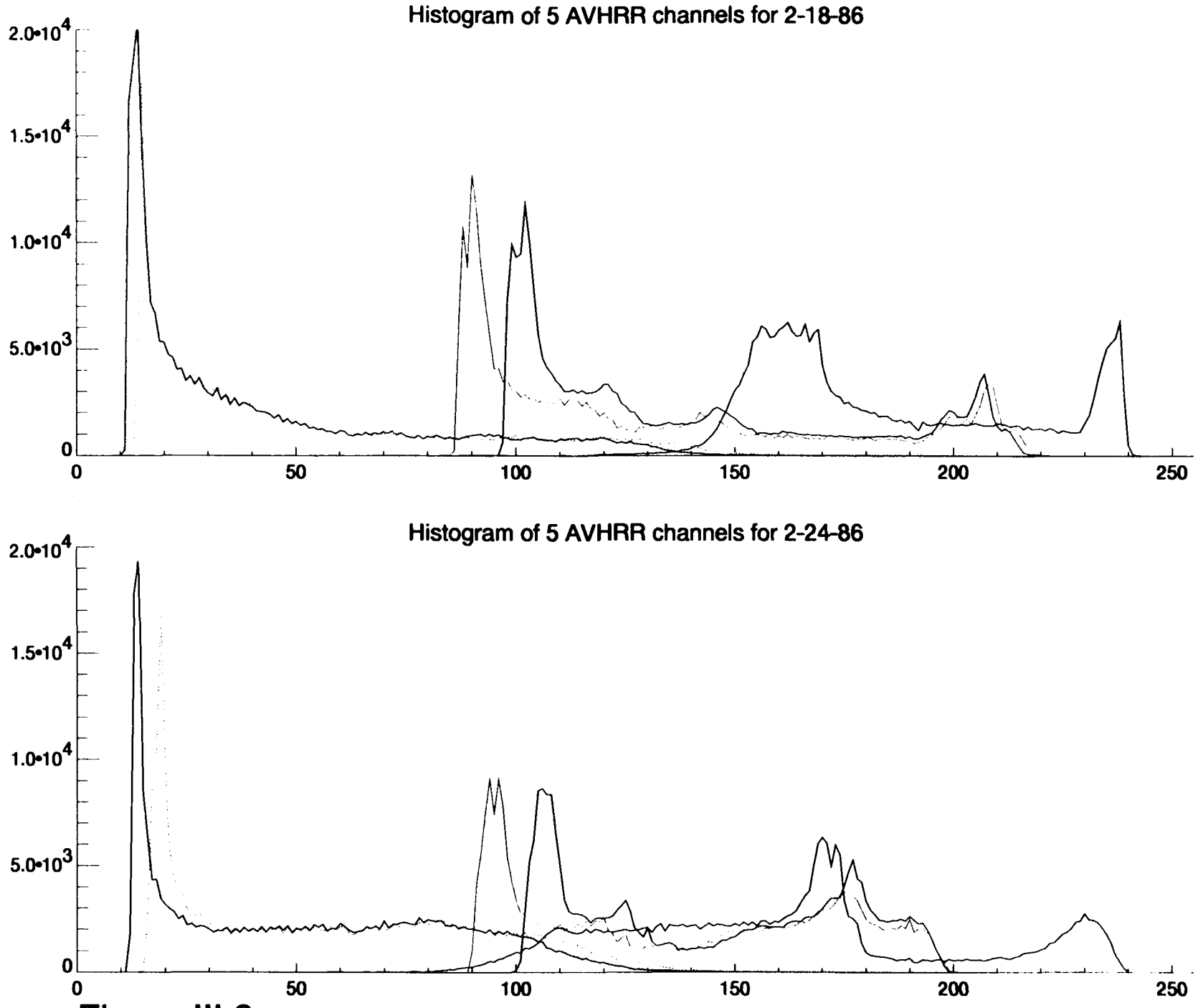

Figure III.2 : AVHRR histograms, purple = channel 1, orange = channel 2, green = channel 3, blue = channel 4, red = channel 5.

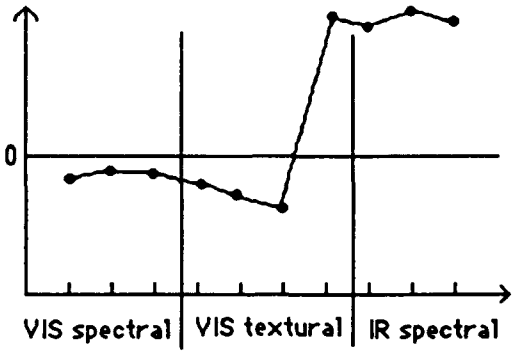

Fig. IV.1: TSF profile for clear sky.

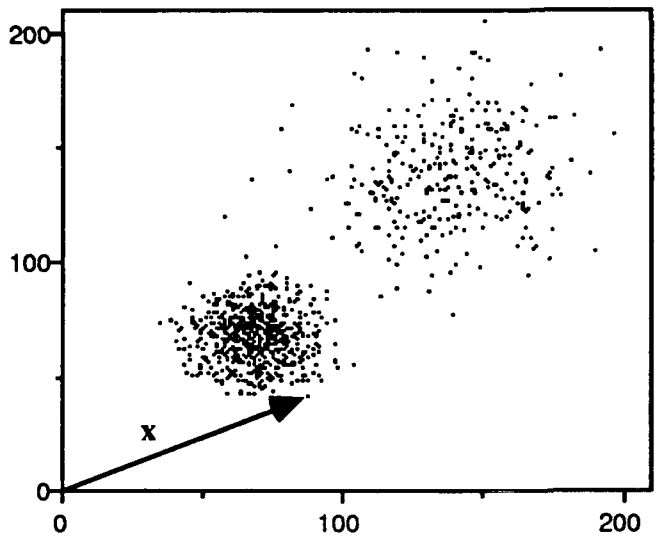

Fig. V.1: Illustration of a two-dimensional parameter space used by Autoclass III to performed classification. The two clusters have both isotropic gaussian (or normal) distributions.

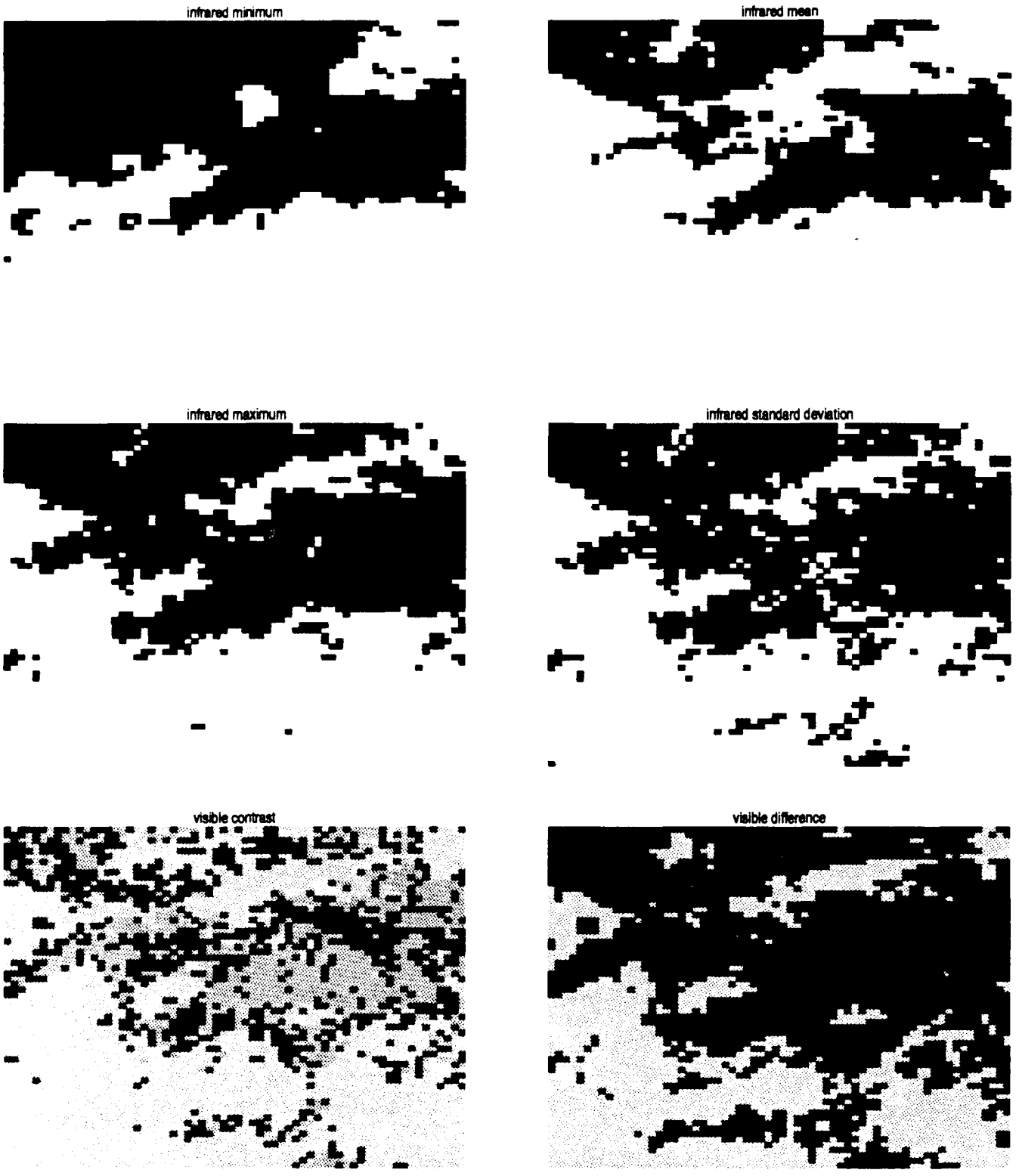

Figure V.2: Examples of single parameter classifications for 2-10-86. Spectral colors low to high are; blue, yellow, light green and dark green. Textural colors low to high are; tan, red, pink and purple.

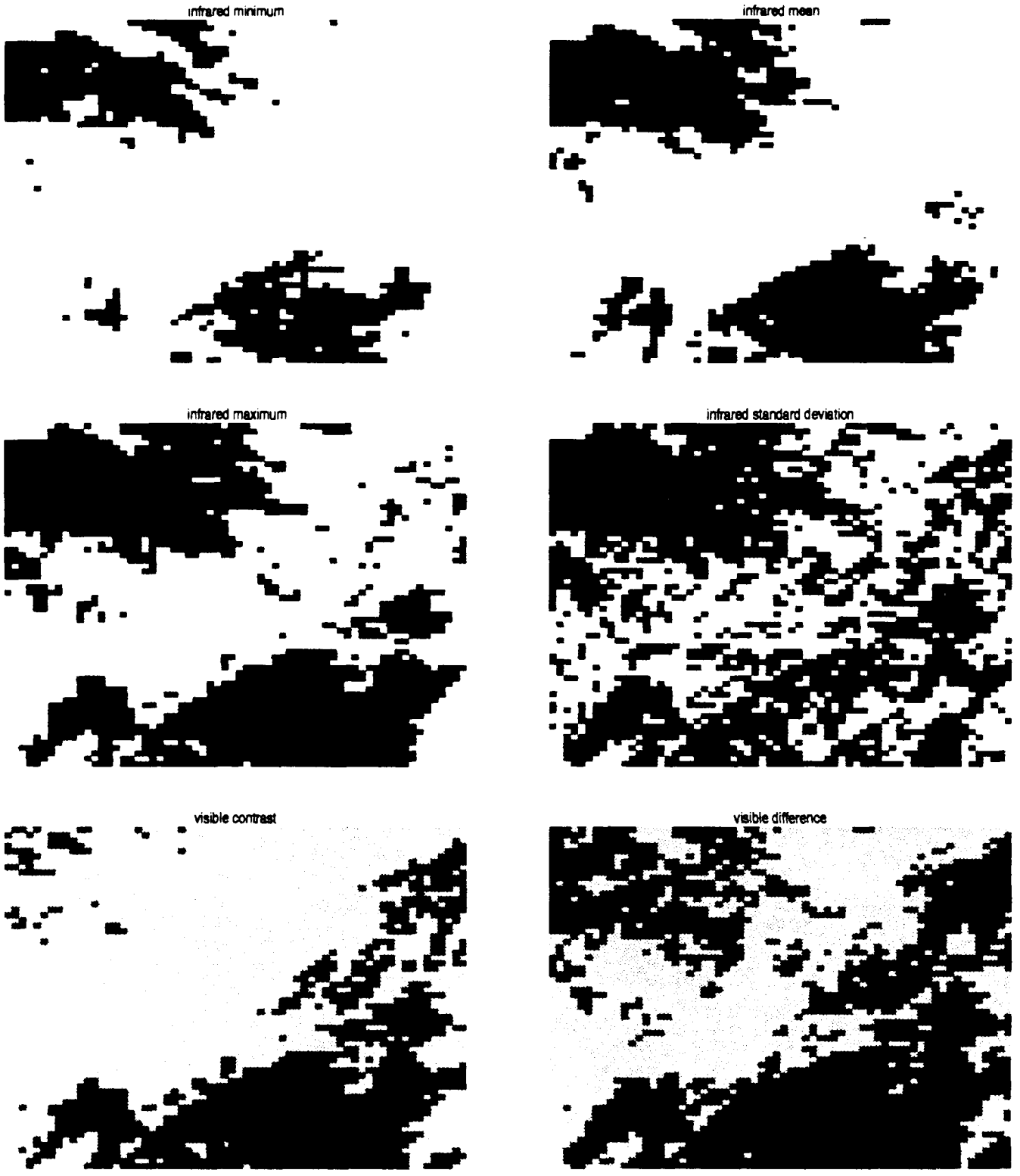

Figure V.2: Examples of single parameter classifications for 2-11-86. Spectral colors low to high are; blue, yellow, light green and dark green. Textural colors low to high are; tan, red, pink and purple.

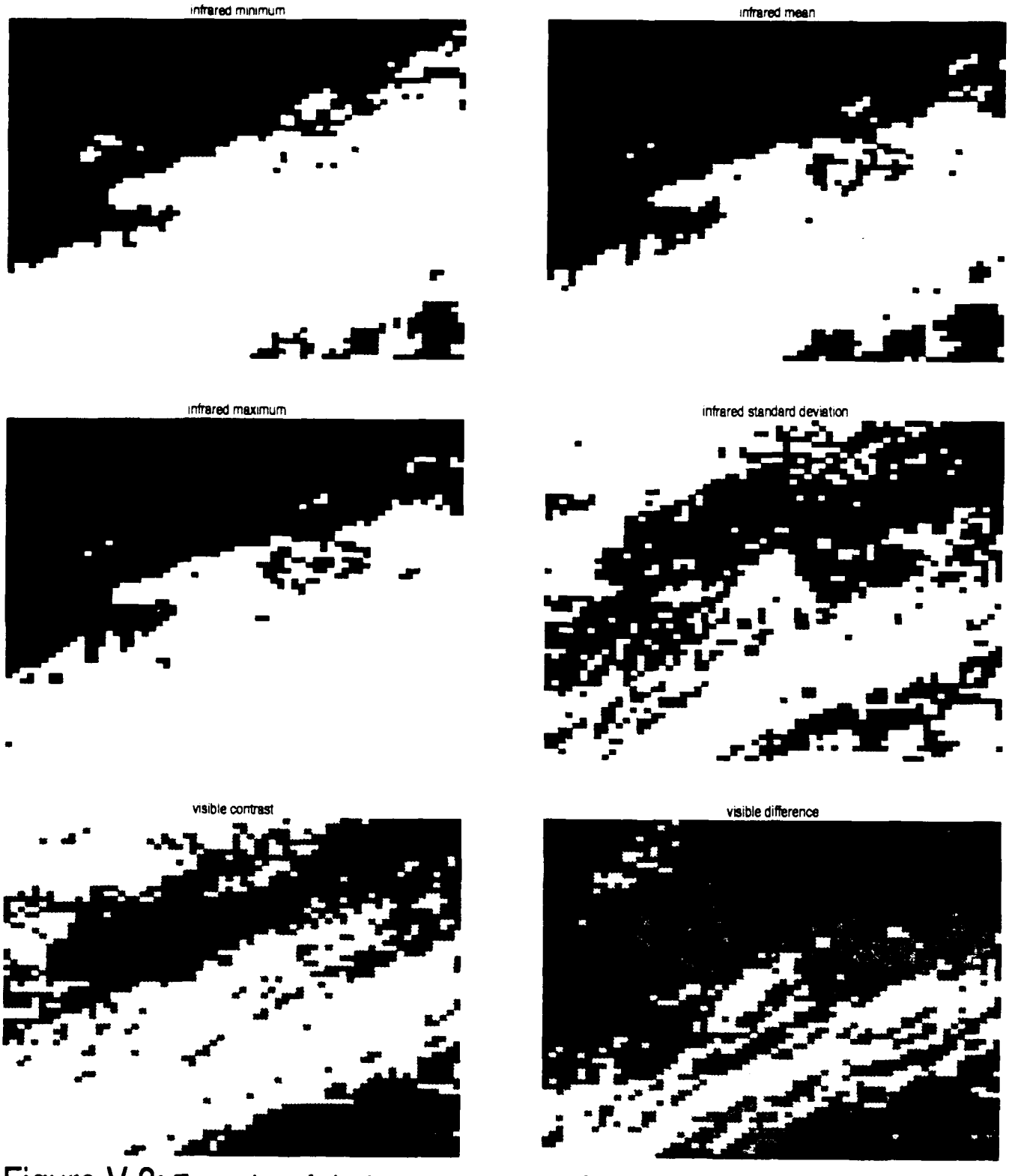

Figure V.2: Examples of single parameter classifications for 2-12-86. Spectral colors low to high are; blue, yellow, light green and dark green. Textural colors low to high are; tan, red, pink and purple.

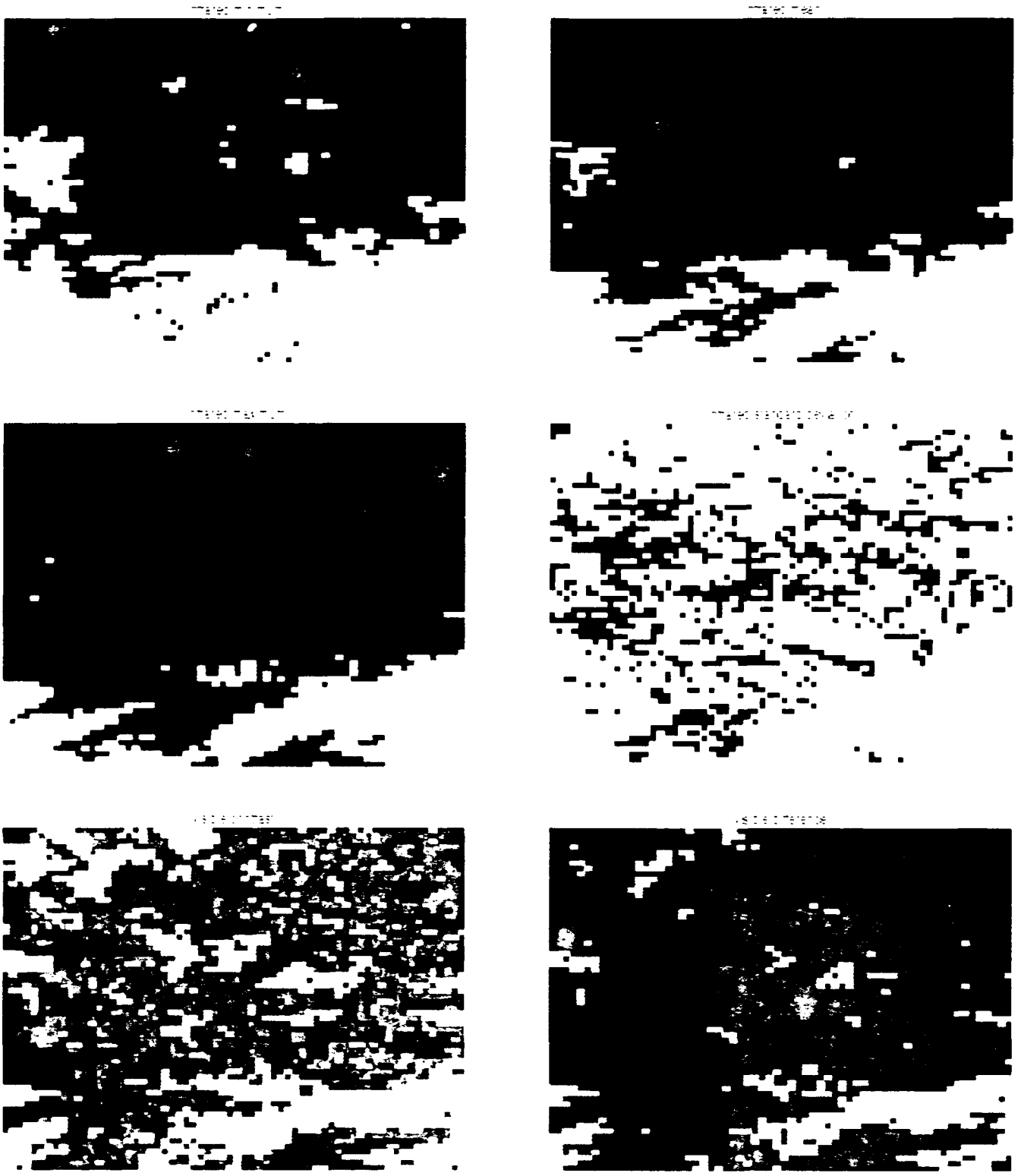

Figure V.2: Examples of single parameter classifications for 2-14-86. Spectral colors low to high are: blue, yellow, light green and dark green. Textural colors low to high are: tan, red, pink and purple.

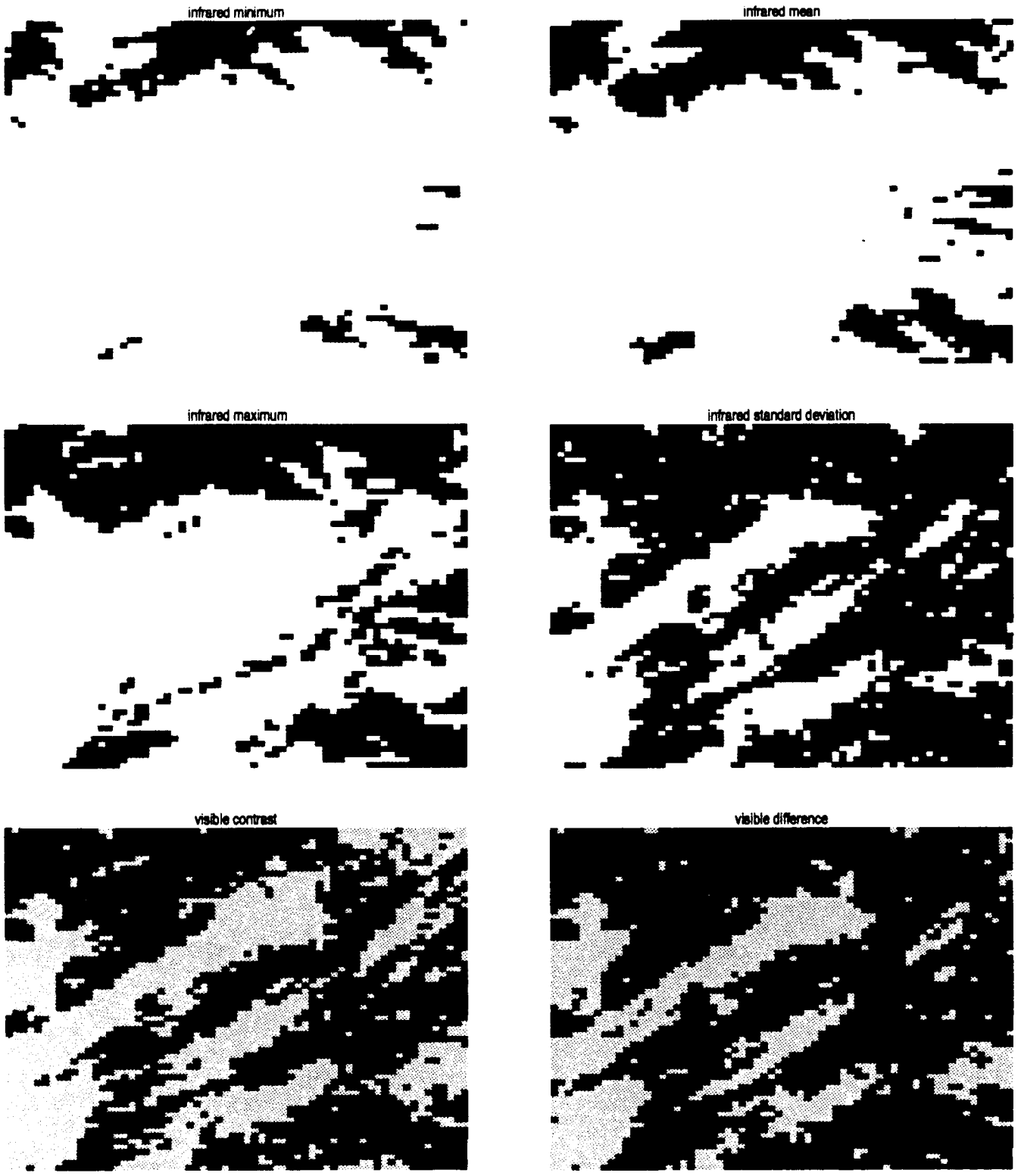

Figure V.2: Examples of single parameter classifications for 2-15-86. Spectral colors low to high are; blue, yellow, light green and dark green. Textural colors low to high are; tan, red, pink and purple.

infrared minimum

Best number of classes = 1,
Implies a random field.

infrared mean

Best number of classes = 1,
Implies a random field.

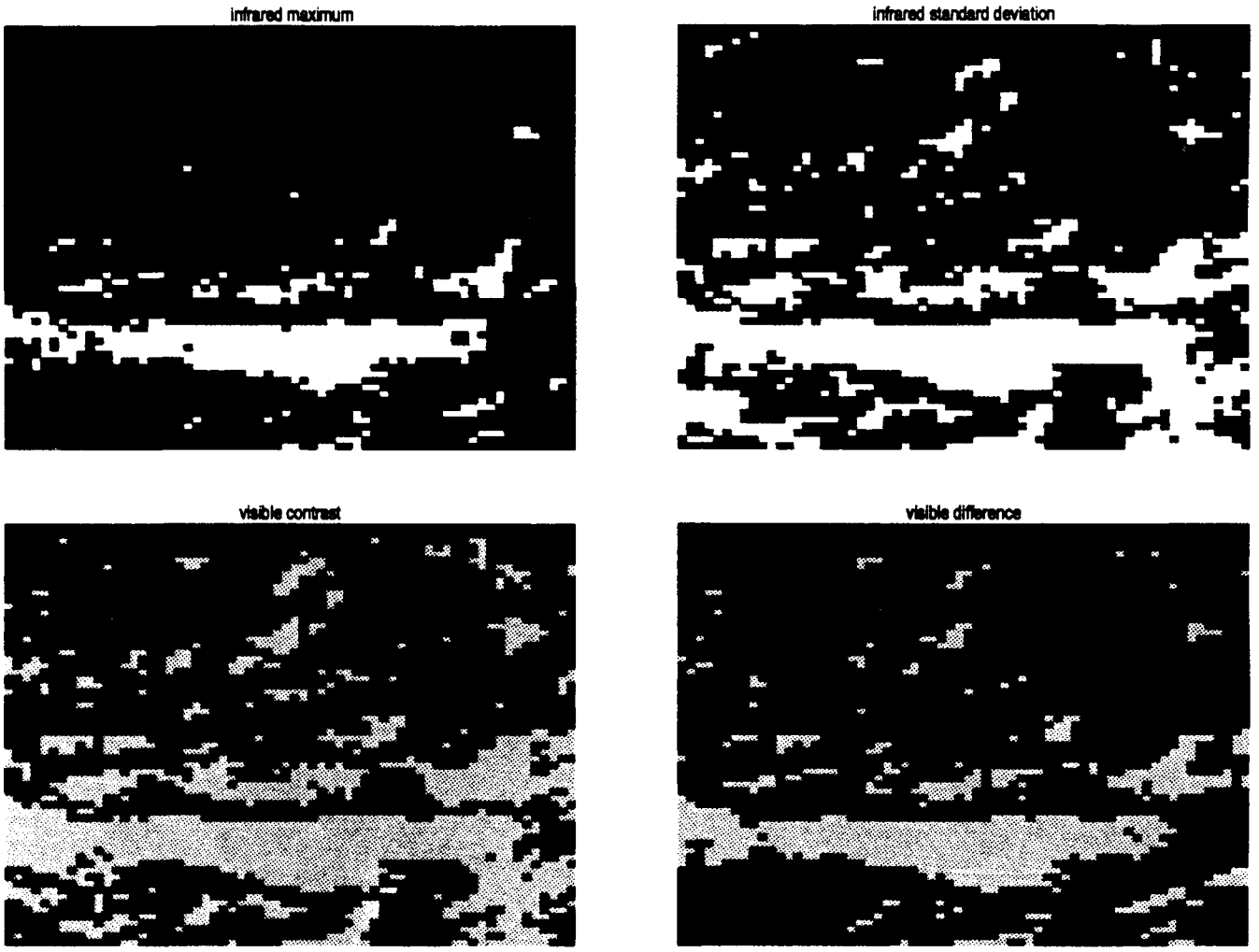

Figure V.2: Examples of single parameter classifications for 2-16-86. Spectral colors low to high are; blue, yellow, light green and dark green. Textural colors low to high are; tan, red, pink and purple.

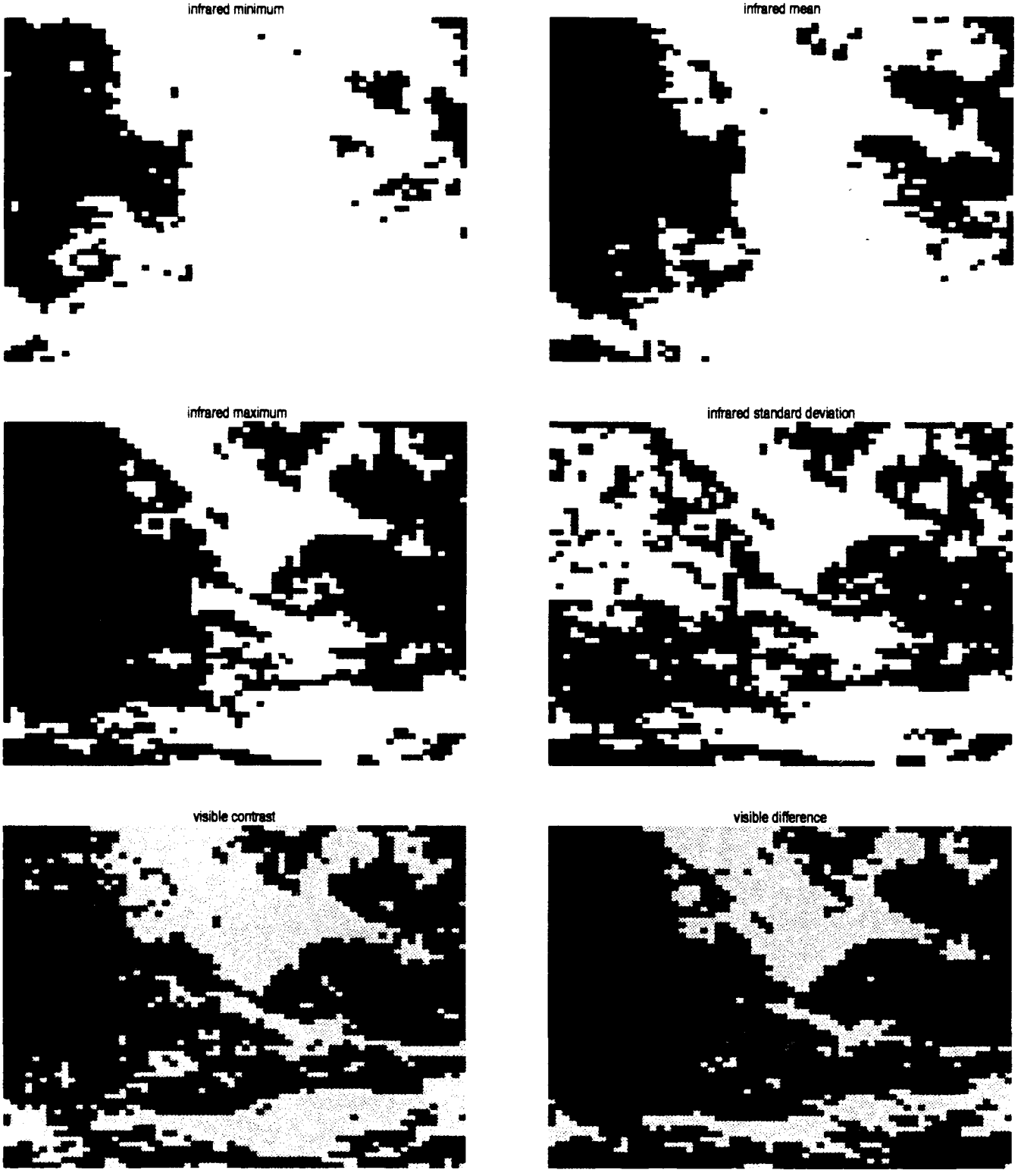

Figure V.2: Examples of single parameter classifications for 2-17-86. Spectral colors low to high are; blue, yellow, light green and dark green. Textural colors low to high are; tan, red, pink and purple.

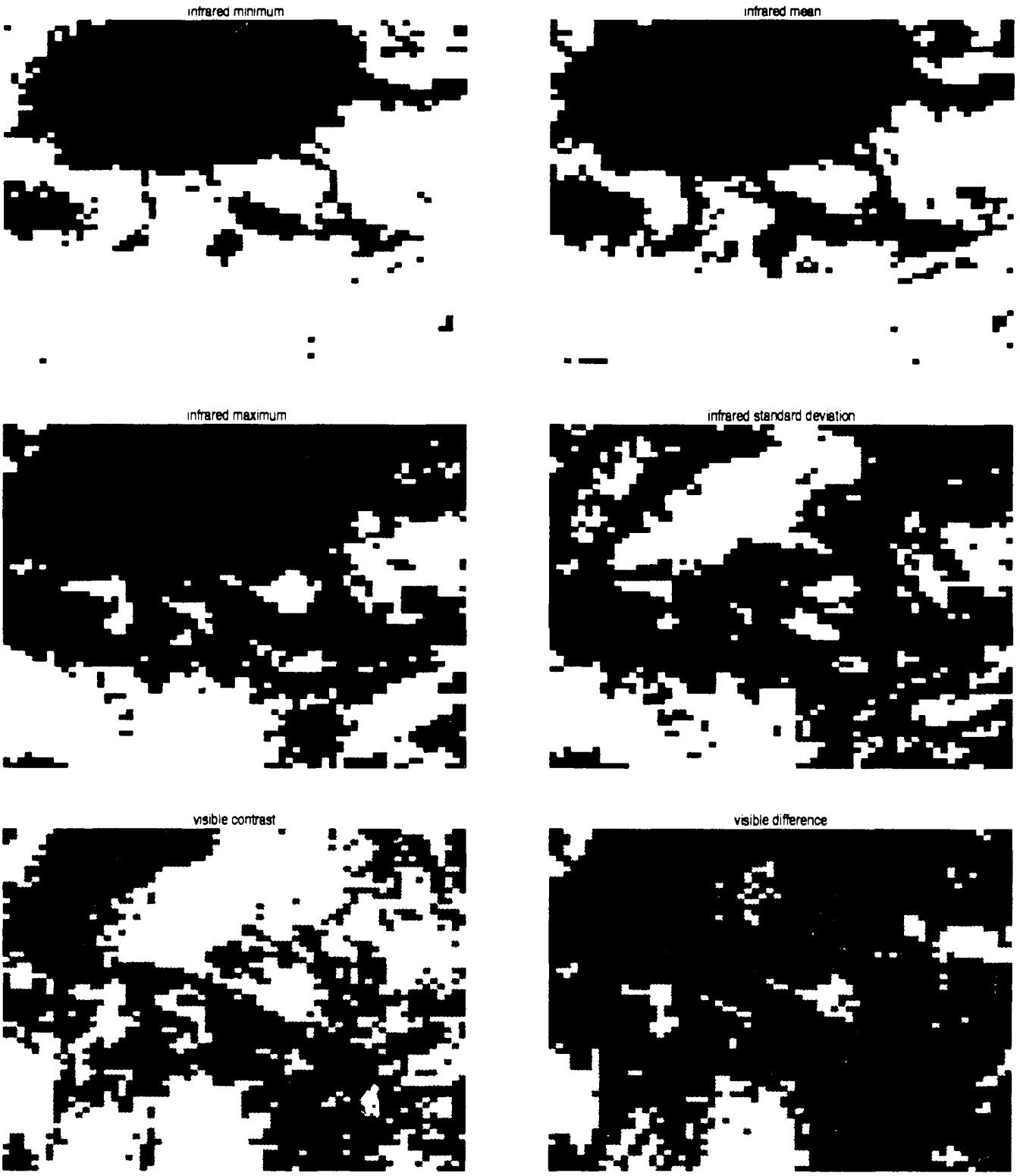

Figure V.2: Examples of single parameter classifications for 2-18-86. Spectral colors low to high are; blue, yellow, light green and dark green. Textural colors low to high are; tan, red, pink and purple.

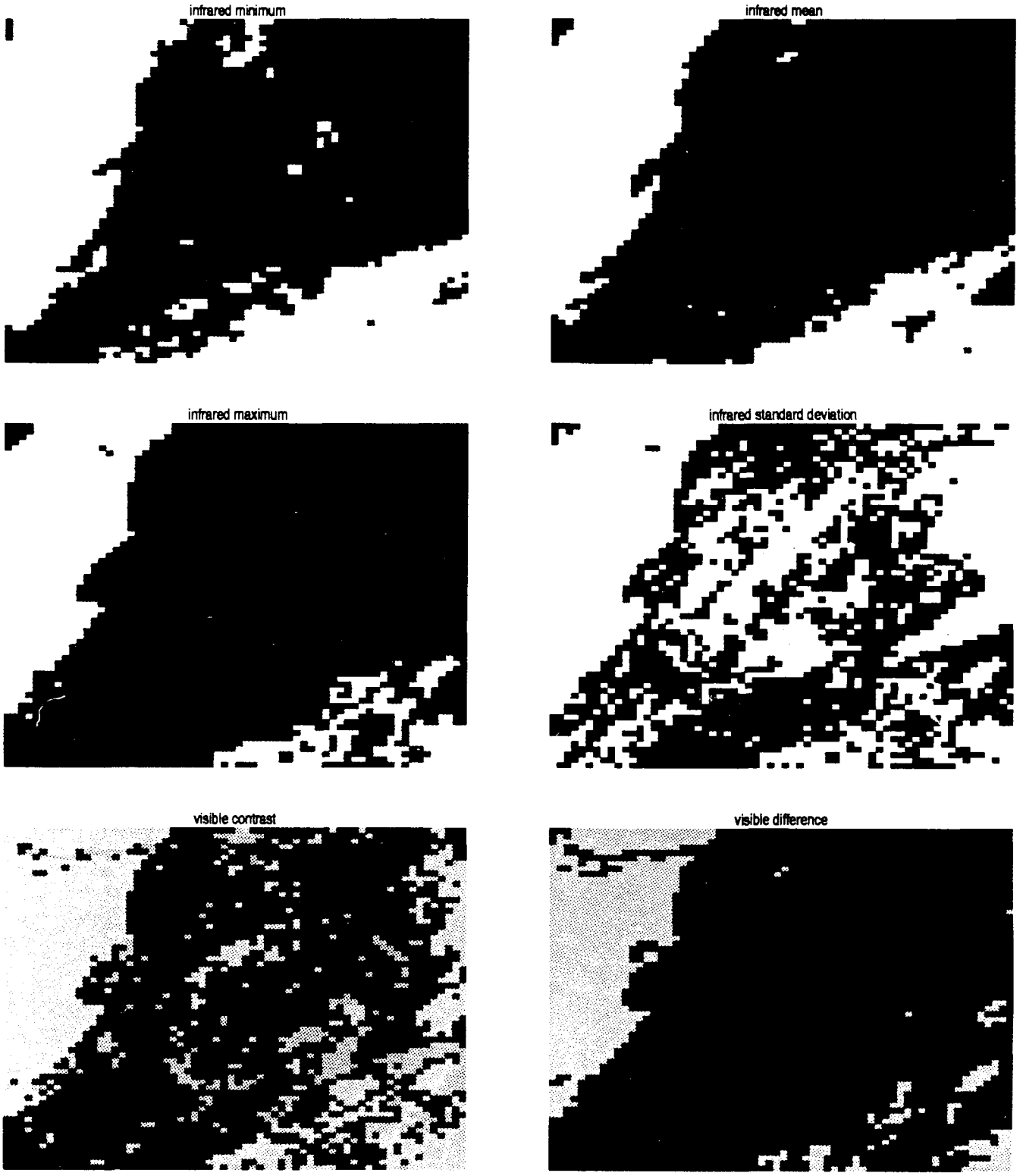

Figure V.2: Examples of single parameter classifications for 2-19-66. Spectral colors low to high are; blue, yellow, light green and dark green. Textural colors low to high are; tan, red, pink and purple.

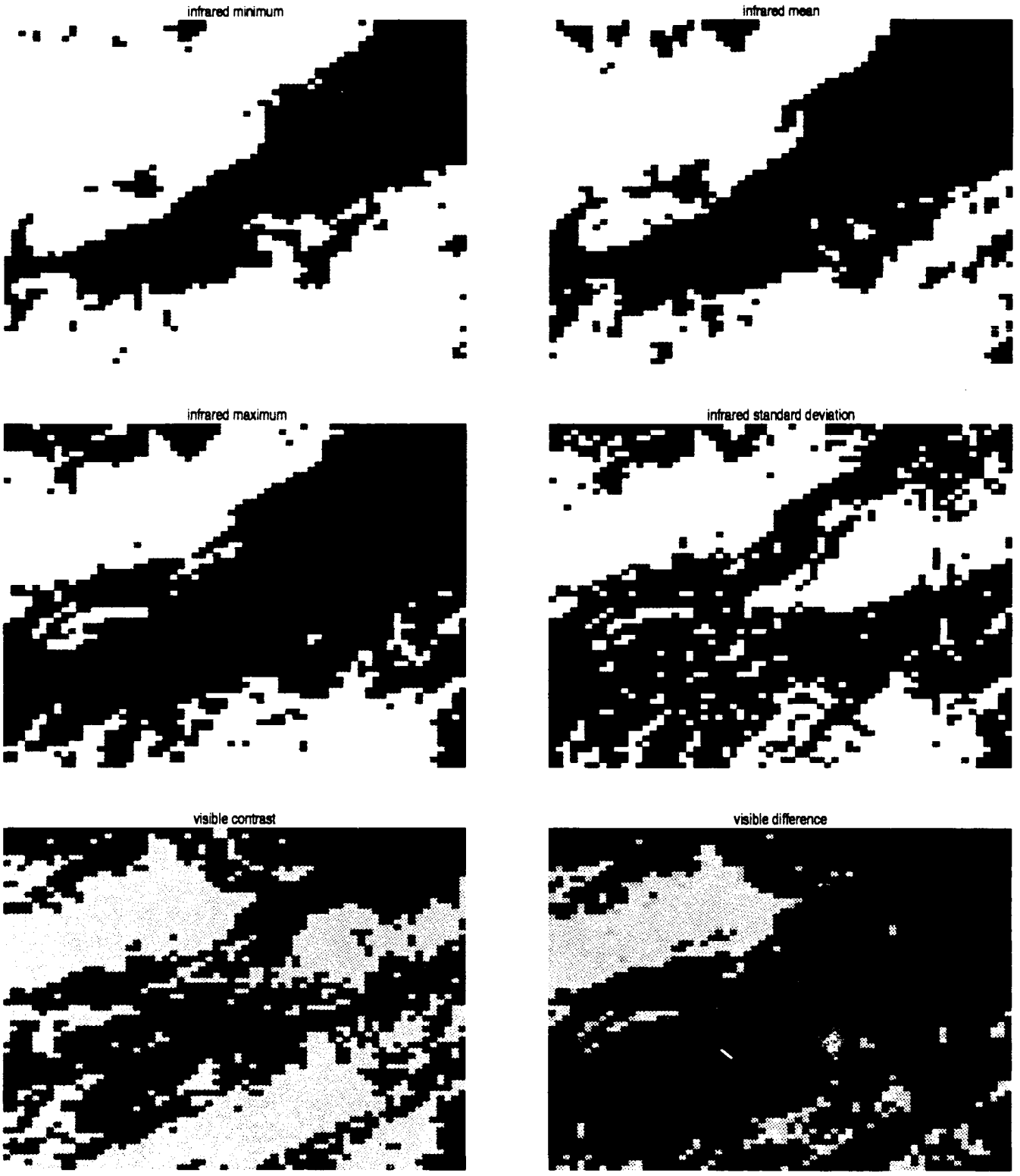

Figure V.2: Examples of single parameter classifications for 2-20-86. Spectral colors low to high are; blue, yellow, light green and dark green. Textural colors low to high are; tan, red, pink and purple.

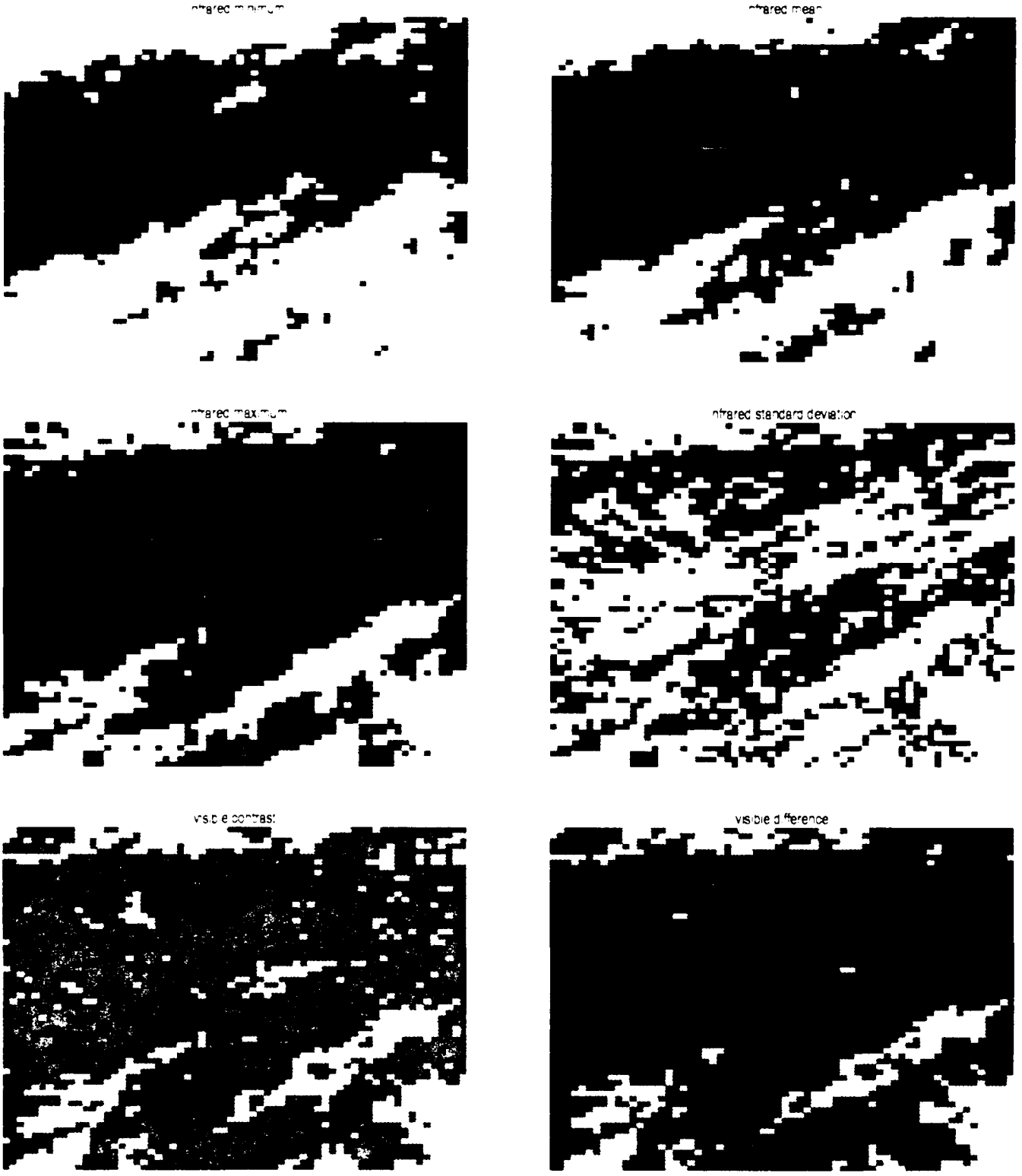

Figure V.2: Examples of single parameter classifications for 2-24-86. Spectral colors low to high are; blue, yellow, light green and dark green. Textural colors low to high are; tan, red, pink and purple.

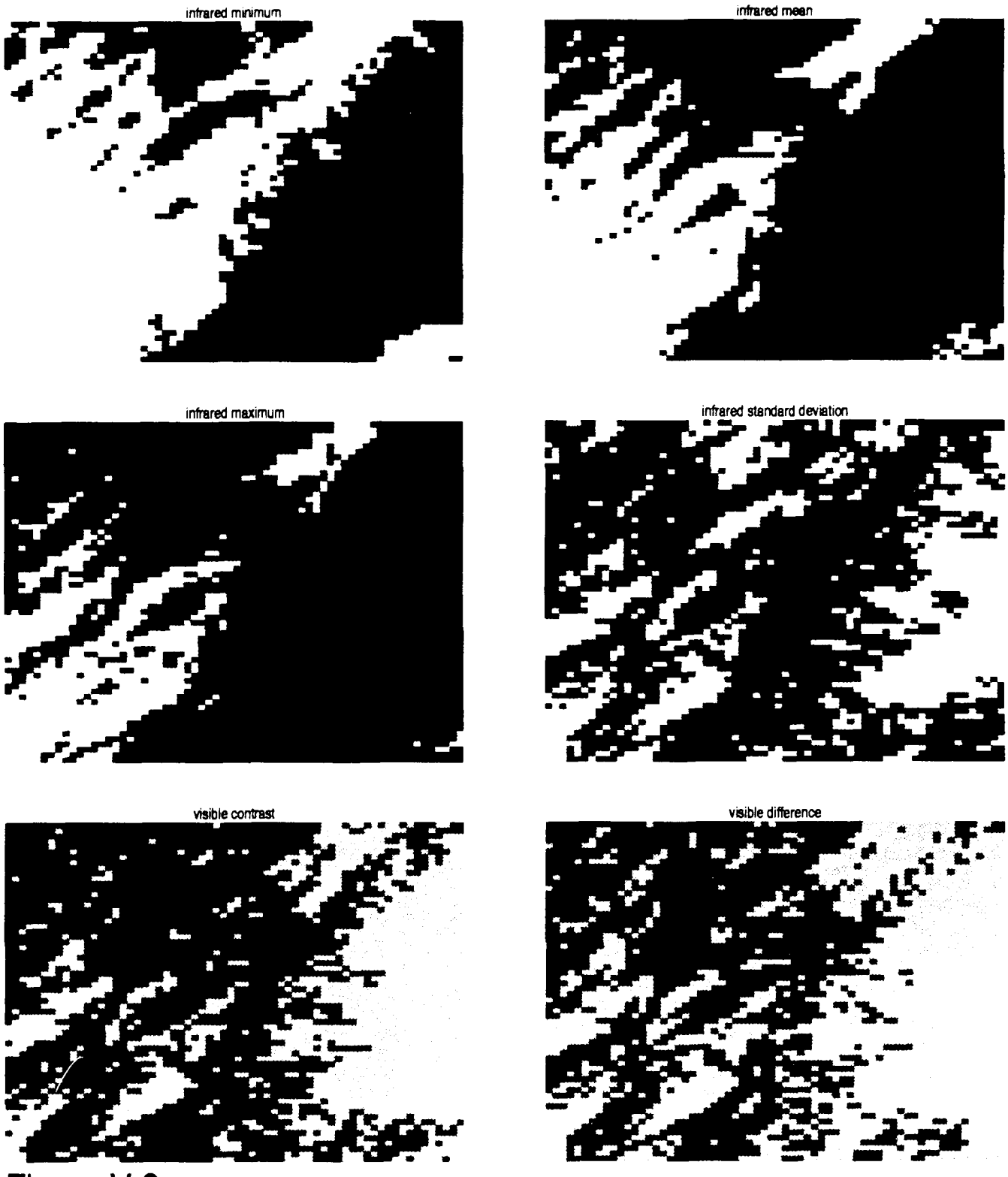

Figure V.2: Examples of single parameter classifications for 2-25-86. Spectral colors low to high are; blue, yellow, light green and dark green. Textural colors low to high are; tan, red, pink and purple.

visible minimum

Best number of classes = 1,
implies a random field.

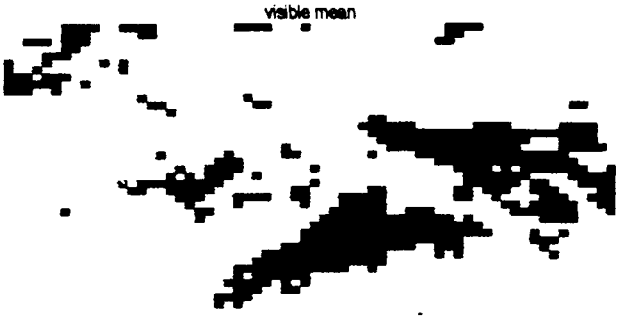

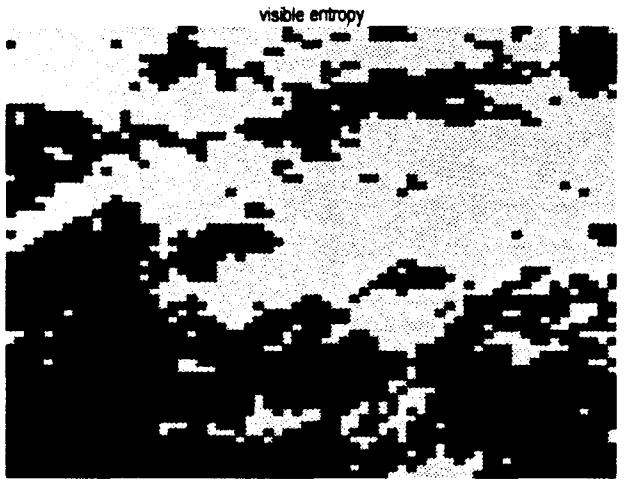

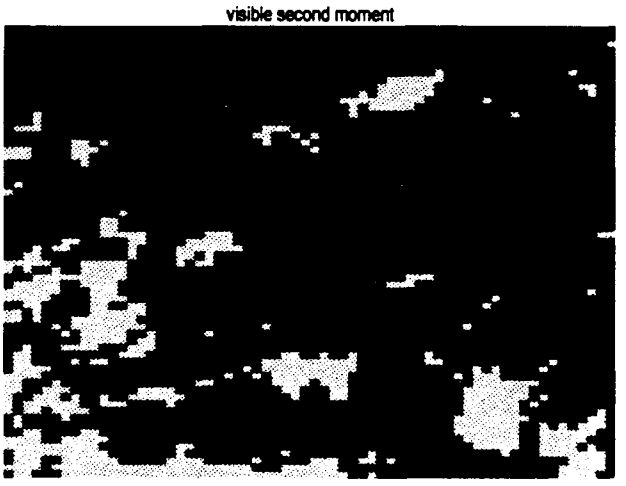

Figure V.3: Examples of single parameter classifications for 2-10-86. Spectral colors low to high are; blue, yellow, light green and dark green. Textural colors low to high are; tan, red, pink and purple.

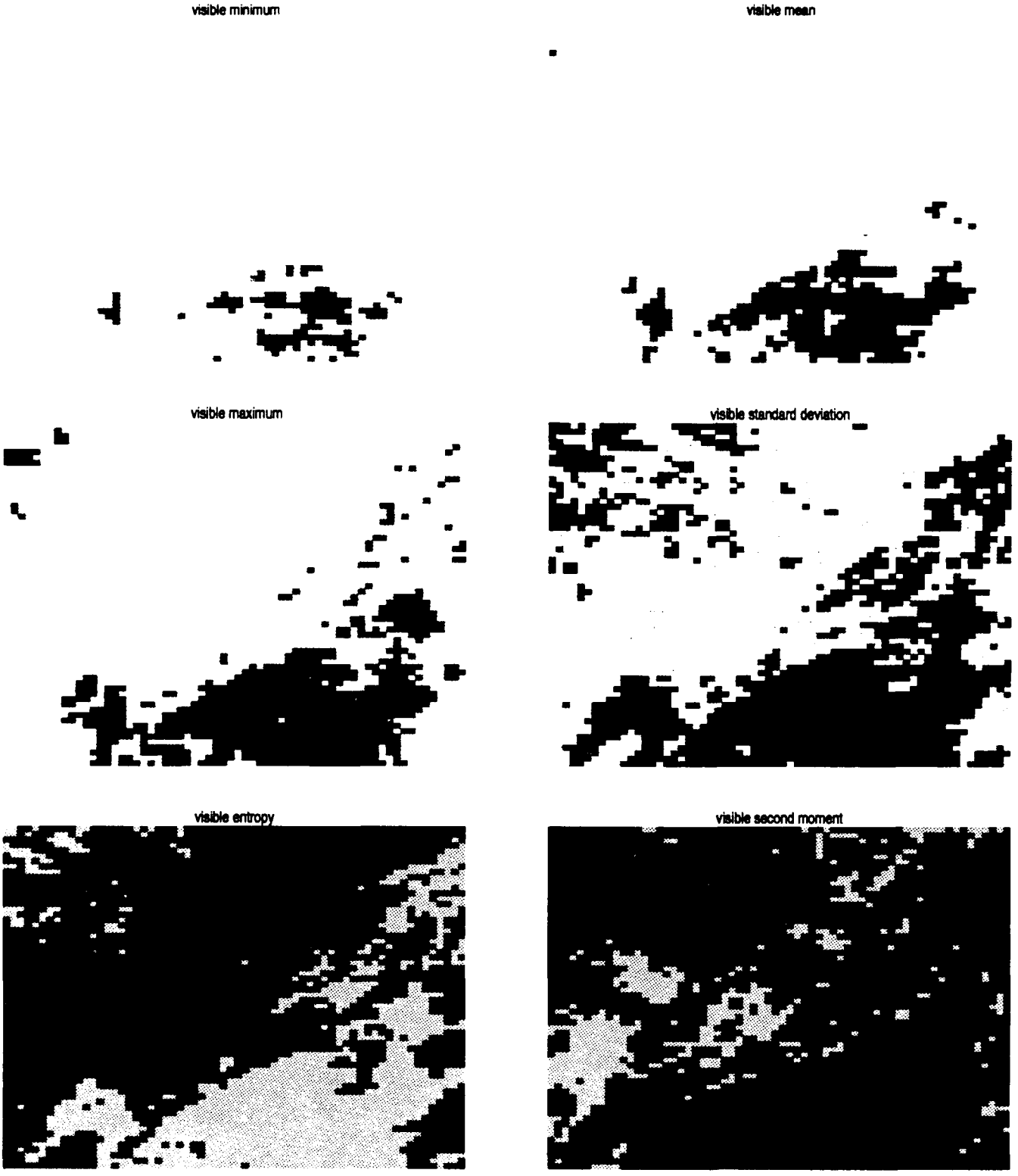

Figure V.3 : Examples of single parameter classifications for 2-11-86.
Spectral colors low to high are; blue, yellow, light green and dark green.
Textural colors low to high are; tan, red, pink and purple.

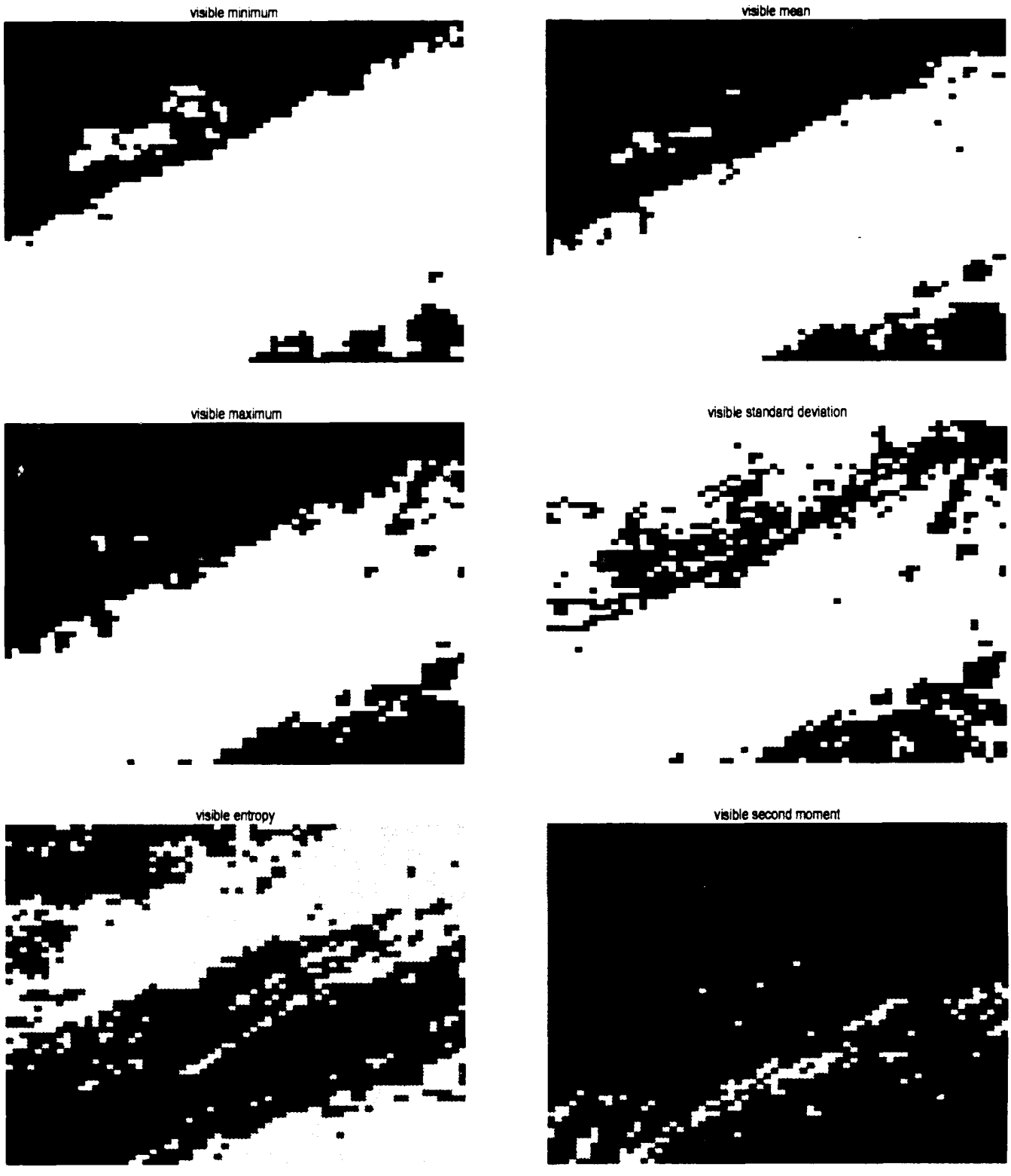

Figure V.3 : Examples of single parameter classifications for 2-12-86. Spectral colors low to high are; blue, yellow, light green and dark green. Textural colors low to high are; tan, red, pink and purple.

visible minimum

Best number of classes = 1,
Implies a random field.

visible mean

Best number of classes = 1,
Implies a random field.

visible maximum

Best number of classes = 1,
Implies a random field.

visible standard deviation

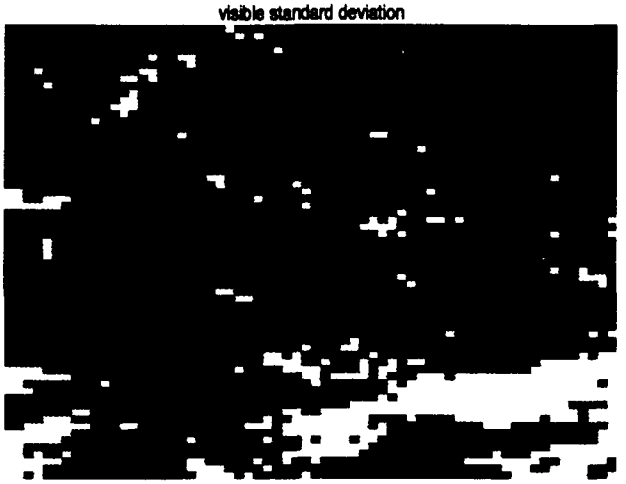

visible entropy

Best number of classes = 1,
Implies a random field.

visible second moment

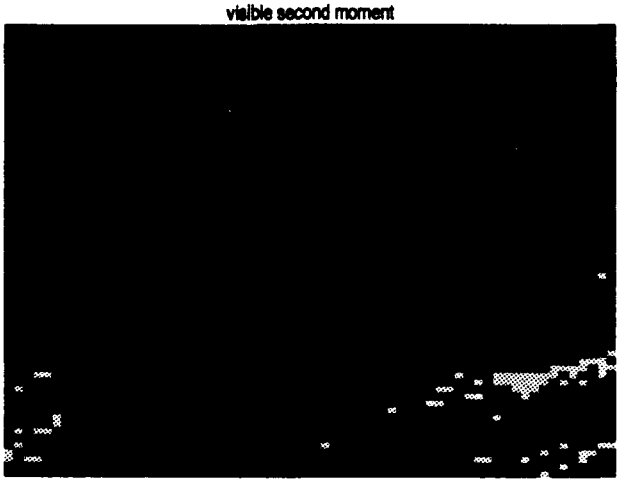

Figure V.3 : Examples of single parameter classifications for 2-14-86. Spectral colors low to high are; blue, yellow, light green and dark green. Textural colors low to high are; tan, red, pink and purple.

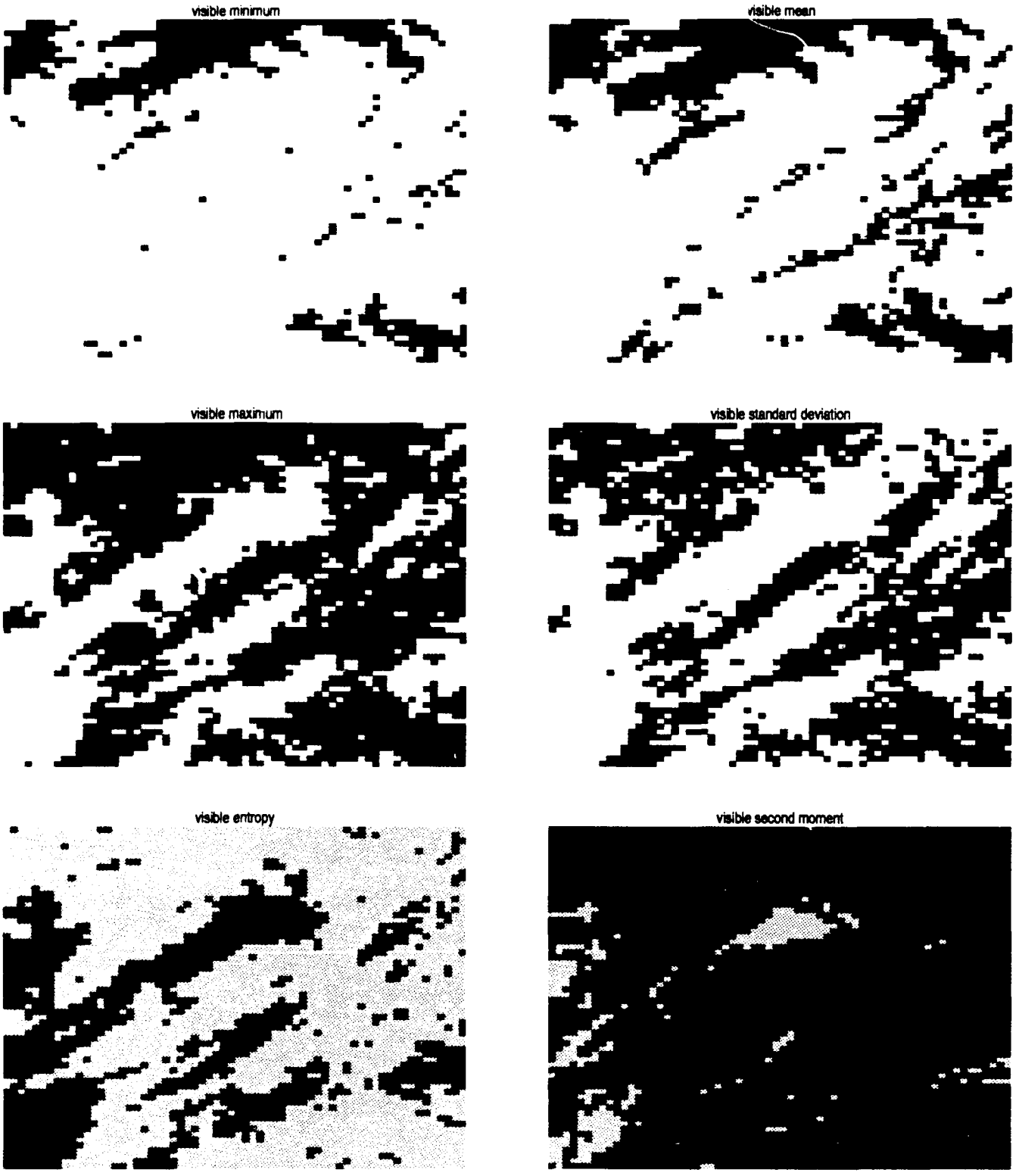

Figure V.3 : Examples of single parameter classifications for 2-15-86. Spectral colors low to high are; blue, yellow, light green and dark green. Textural colors low to high are; tan, red, pink and purple.

visible minimum

Best number of classes = 1,
Implies a random field.

visible mean

Best number of classes = 1,
Implies a random field.

visible maximum

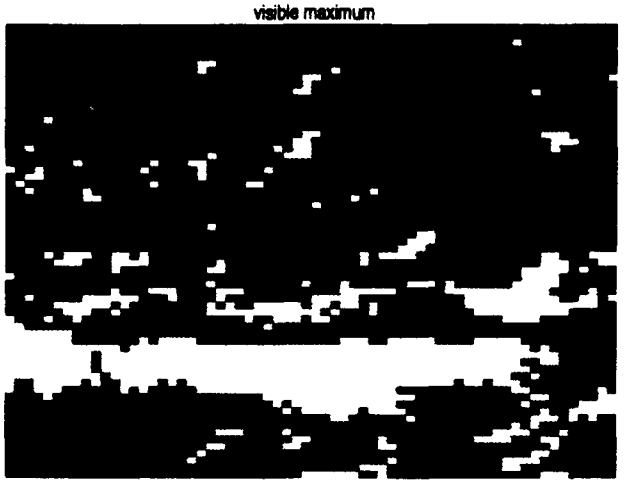

visible standard deviation

visible entropy

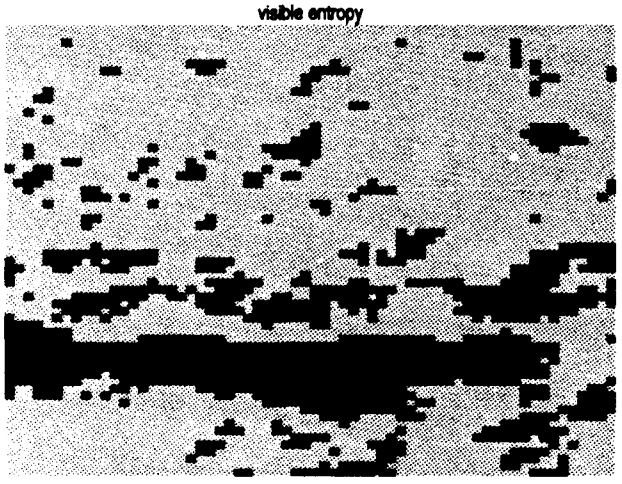

visible second moment

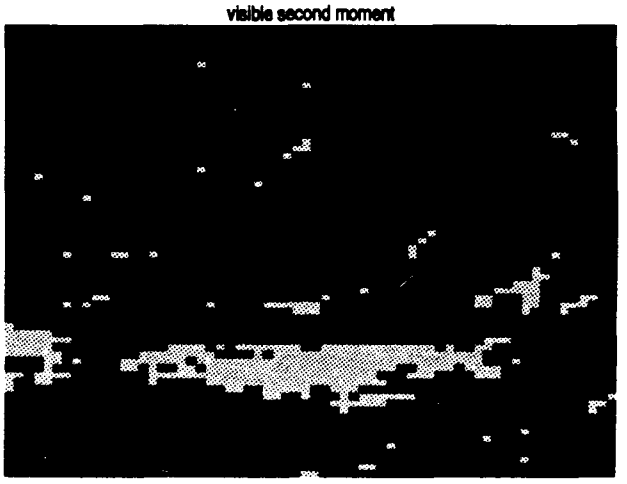

Figure V.3 : Examples of single parameter classifications for 2-16-86.
Spectral colors low to high are; blue, yellow, light green and dark green.
Textural colors low to high are; tan, red, pink and purple.

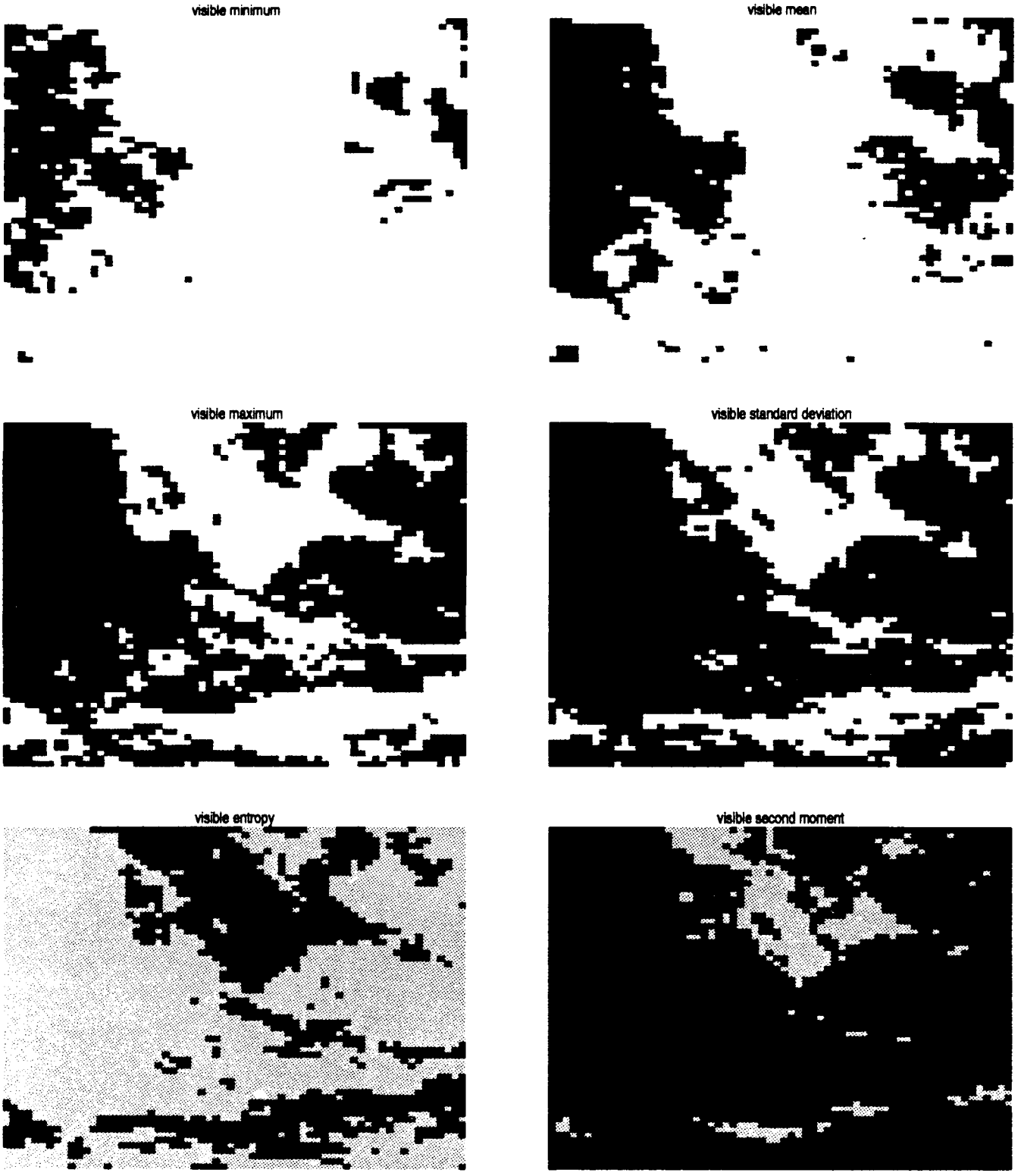

Figure V.3 : Examples of single parameter classifications for 2-17-86. Spectral colors low to high are; blue, yellow, light green and dark green. Textural colors low to high are; tan, red, pink and purple.

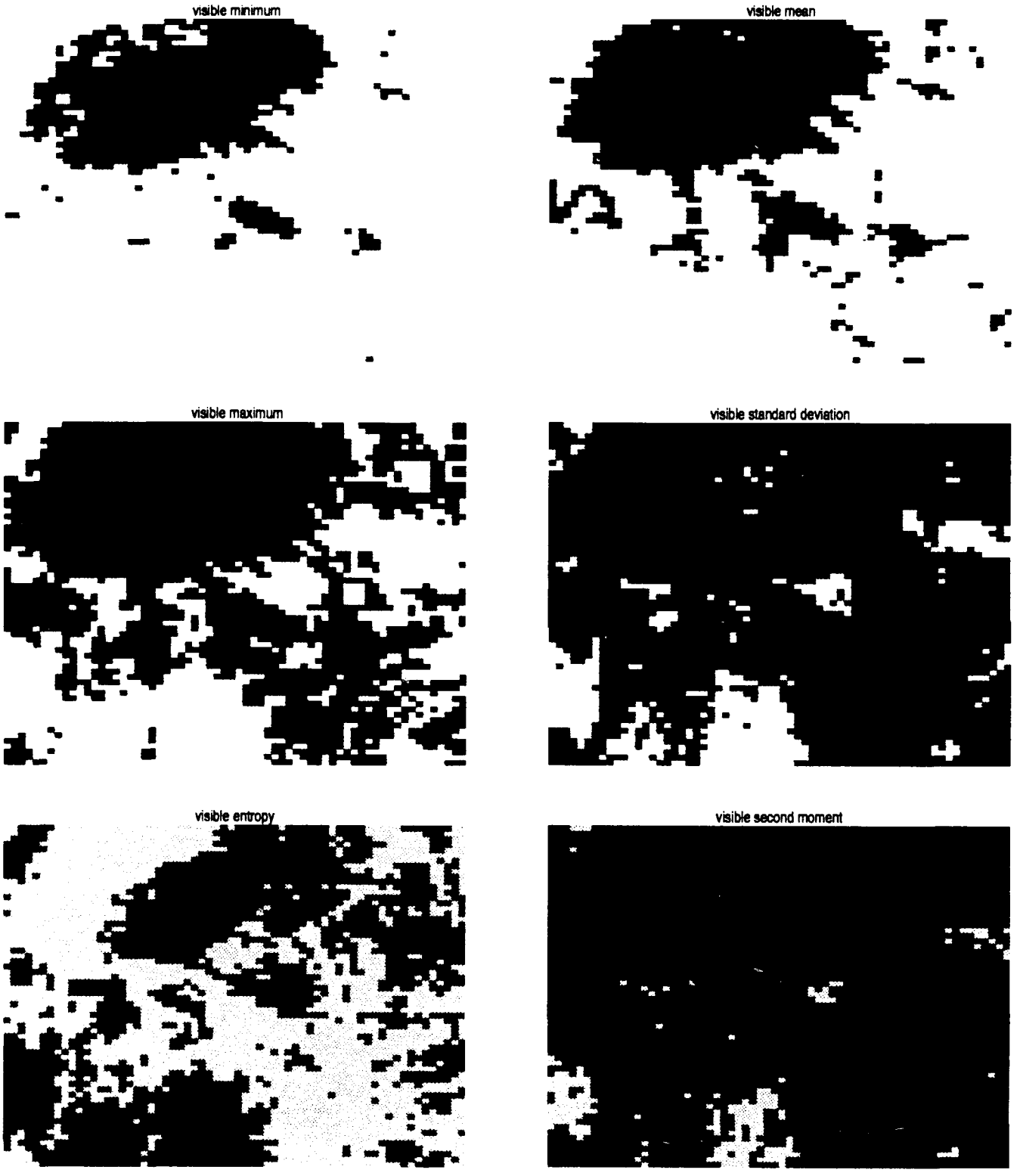

Figure V.3 : Examples of single parameter classifications for 2-18-86. Spectral colors low to high are; blue, yellow, light green and dark green. Textural colors low to high are; tan, red, pink and purple.

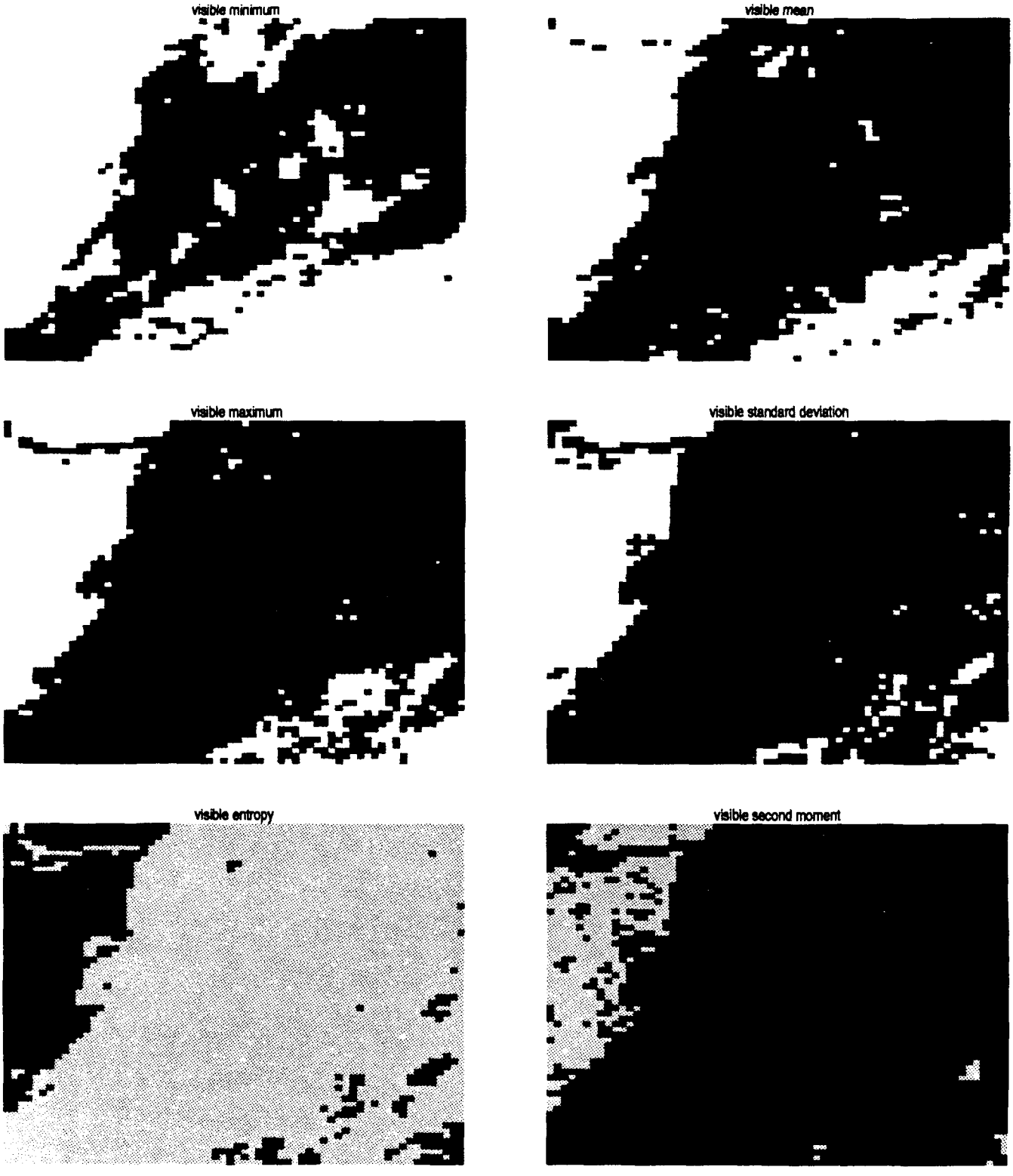

Figure V.3 : Examples of single parameter classifications for 2-19-86.
Spectral colors low to high are; blue, yellow, light green and dark green.
Textural colors low to high are; tan, red, pink and purple.

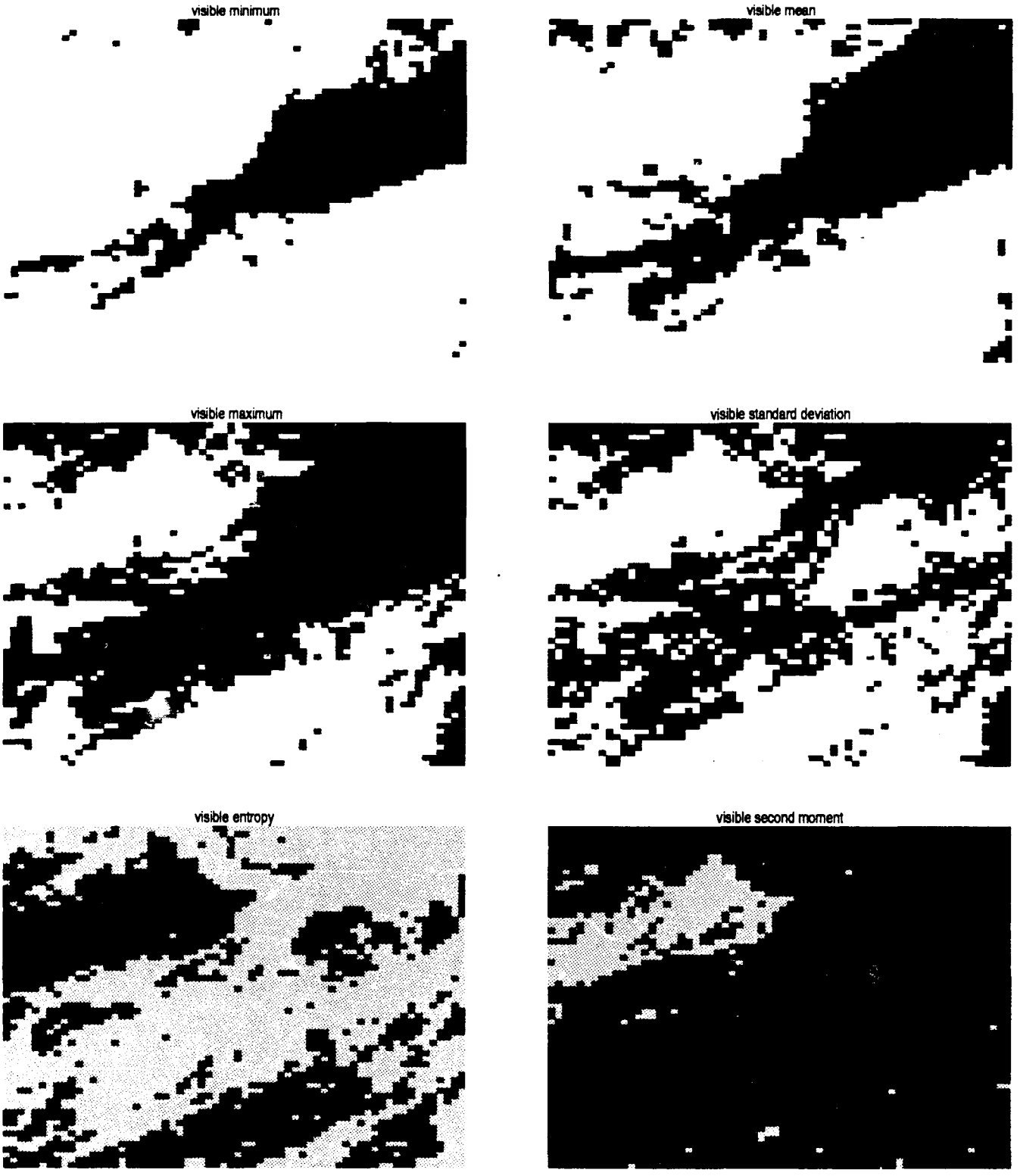

Figure V.3 : Examples of single parameter classifications for 2-20-86. Spectral colors low to high are; blue, yellow, light green and dark green. Textural colors low to high are; tan, red, pink and purple.

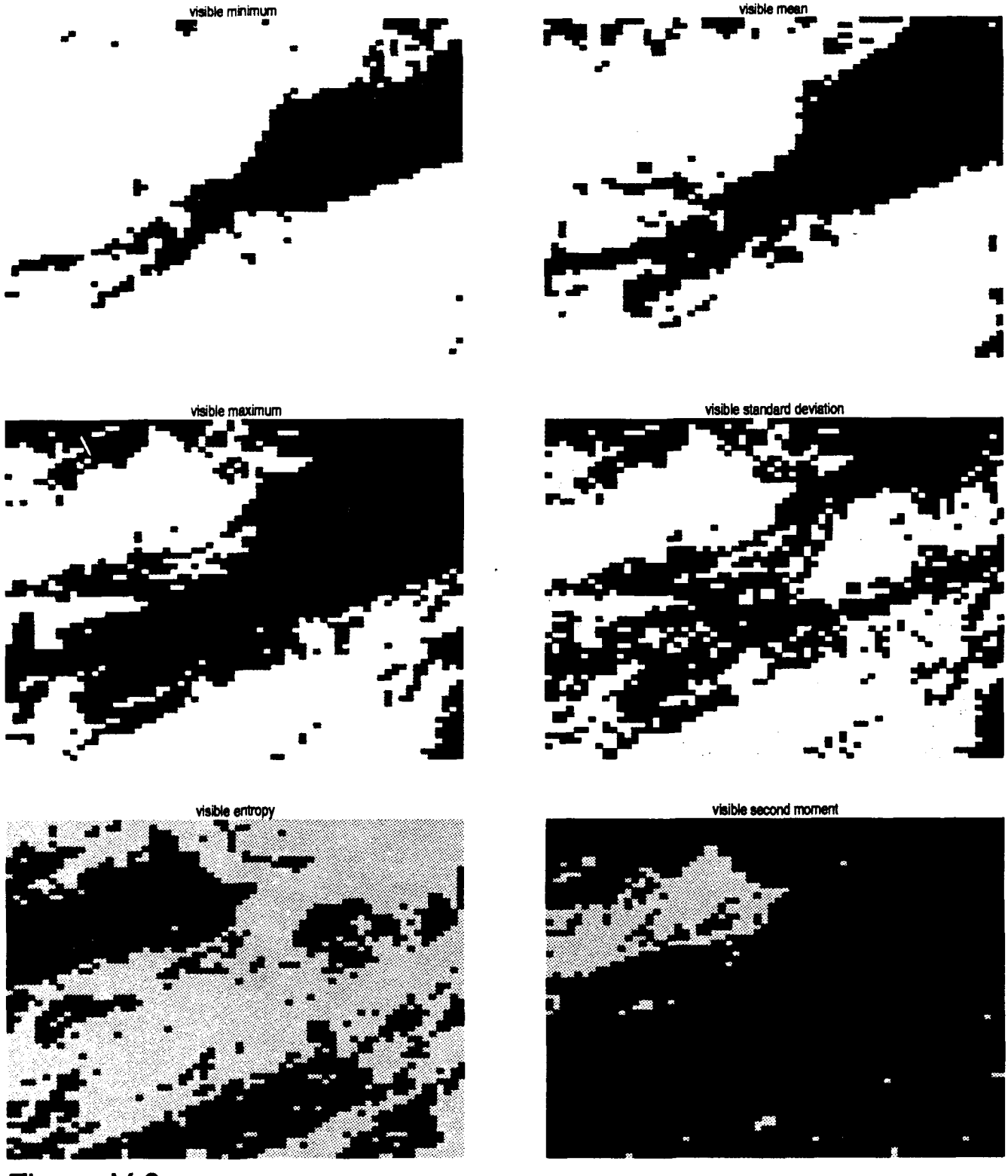

Figure V.3 : Examples of single parameter classifications for 2-20-86.
Spectral colors low to high are; blue, yellow, light green and dark green.
Textural colors low to high are; tan, red, pink and purple.

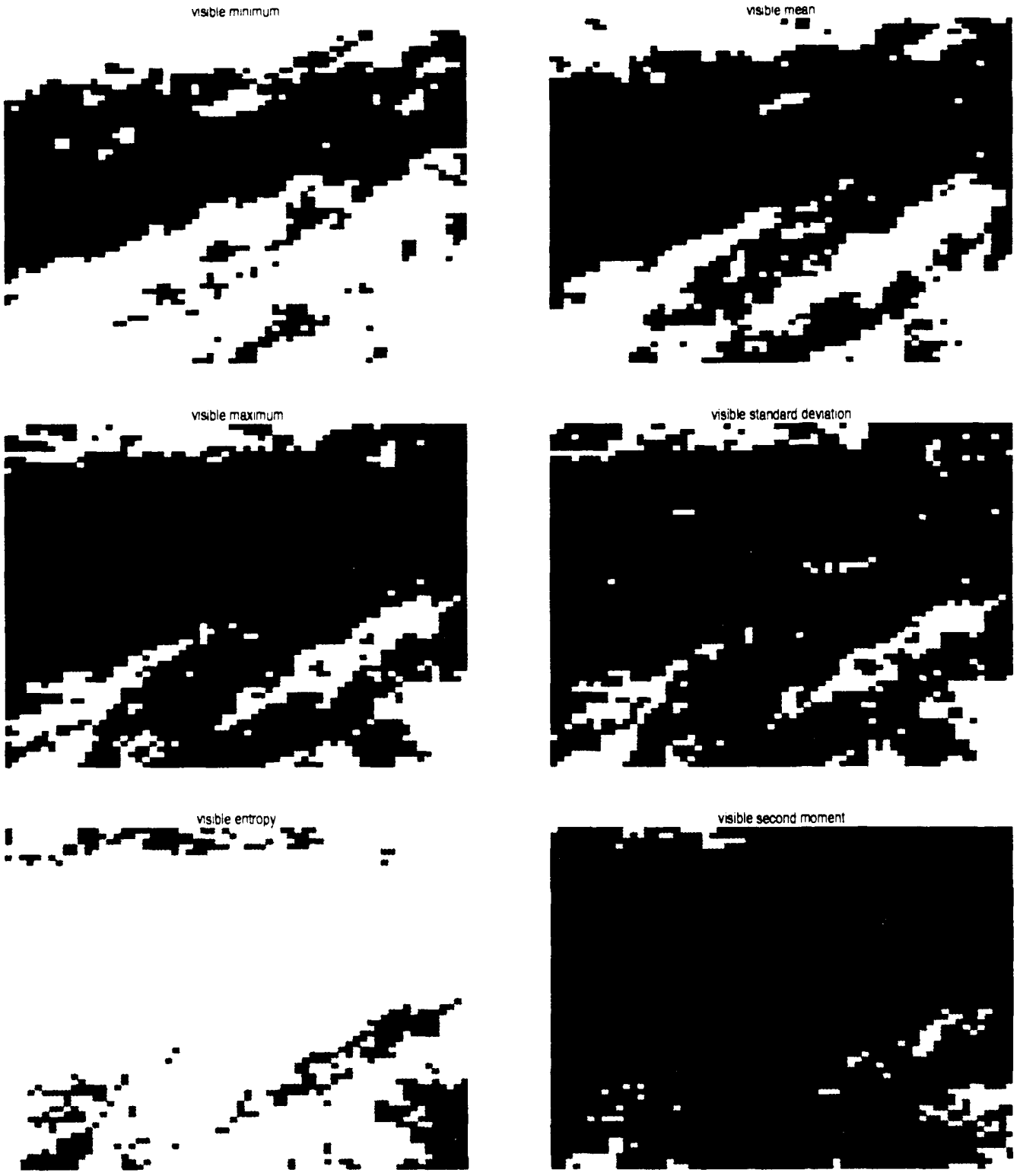

Figure V.3 : Examples of single parameter classifications for 2-24-86. Spectral colors low to high are; blue, yellow, light green and dark green. Textural colors low to high are; tan, red, pink and purple.

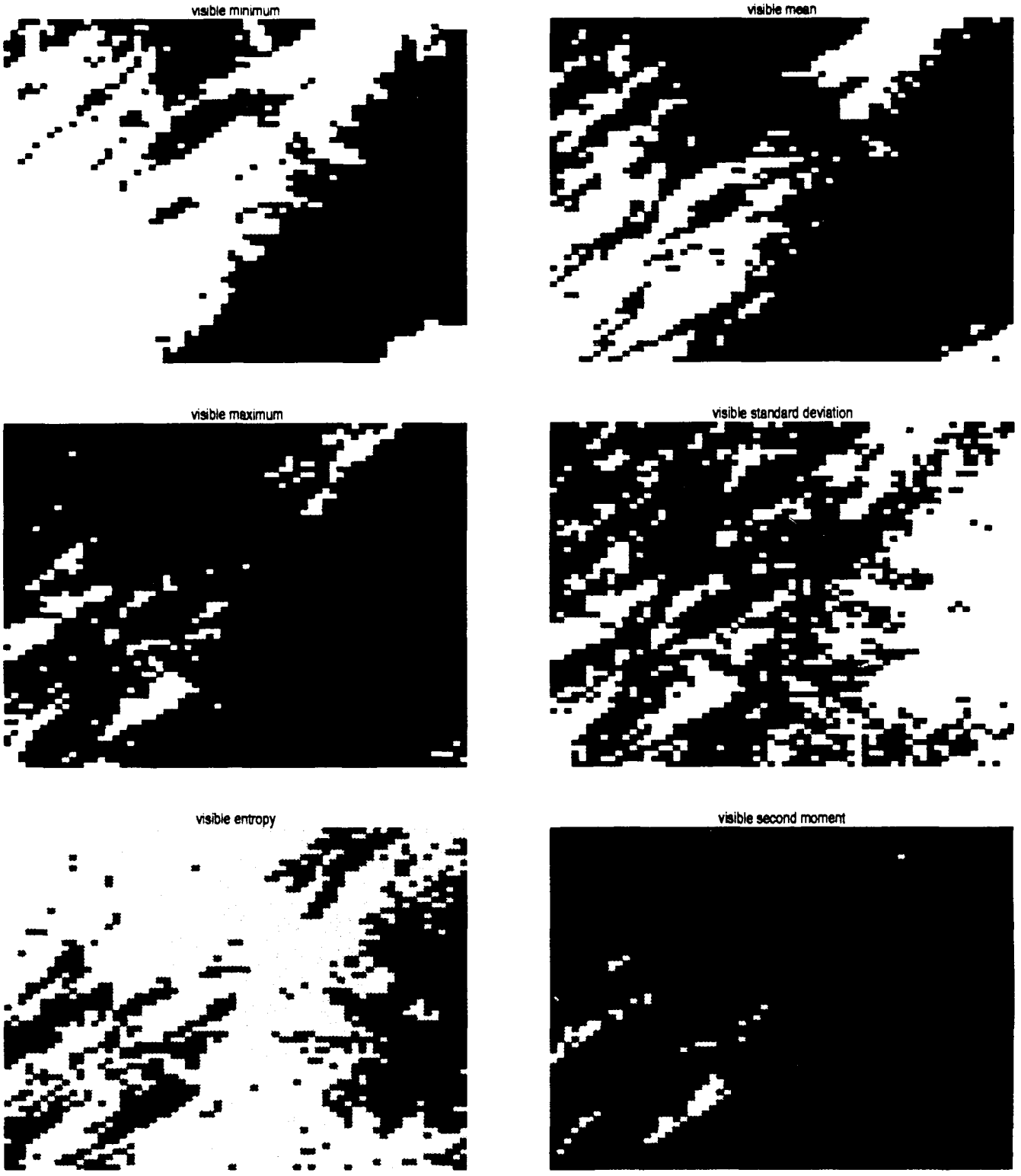

Figure V.3 : Examples of single parameter classifications for 2-25-86. Spectral colors low to high are; blue, yellow, light green and dark green. Textural colors low to high are; tan, red, pink and purple.

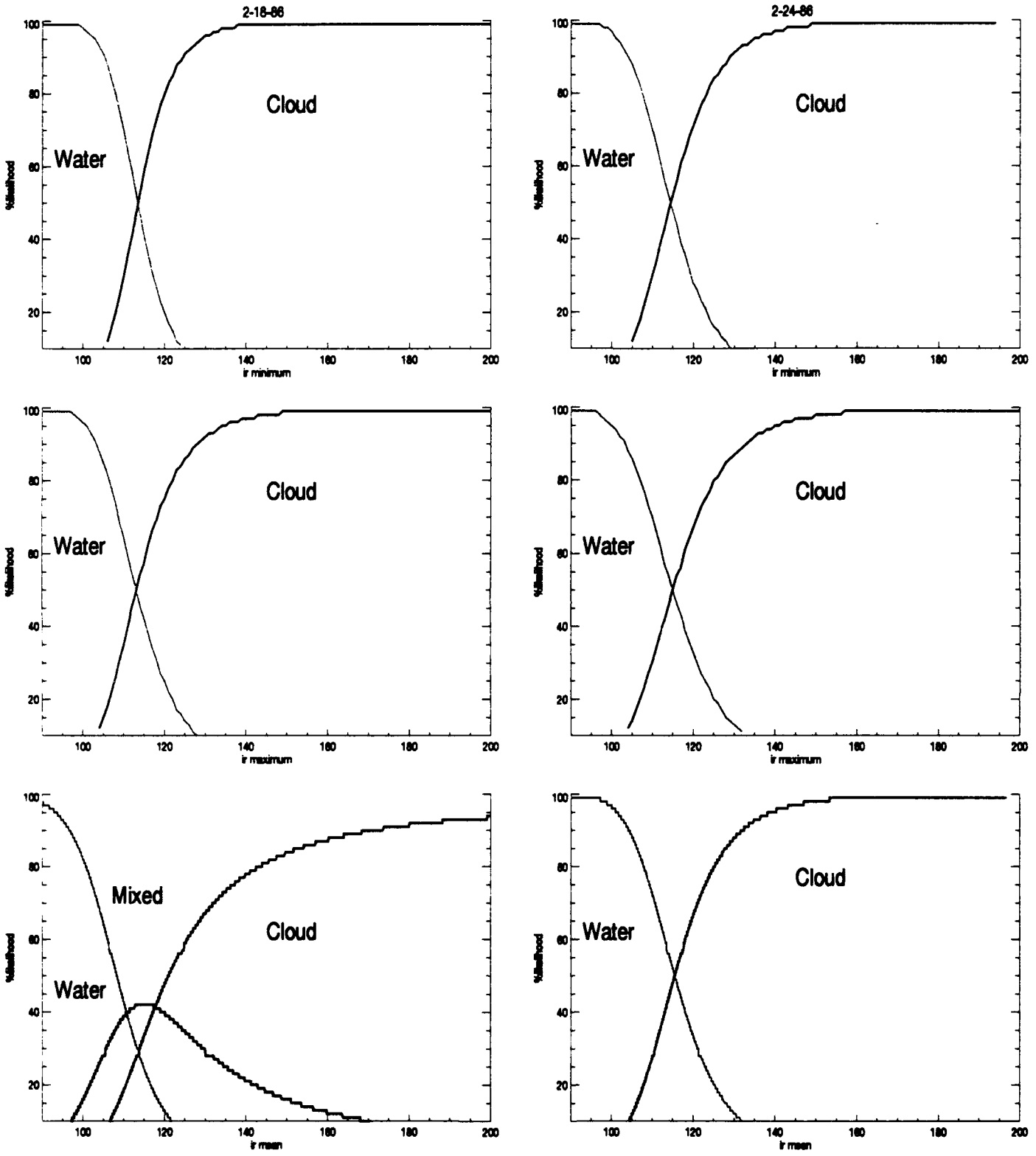

Figure V.4 : Three IR spectral parameter V diagrams for 2-18-86 and 2-24-86, used to estimate cloud fraction. Blue = water, red = clouds, purple = mixed.

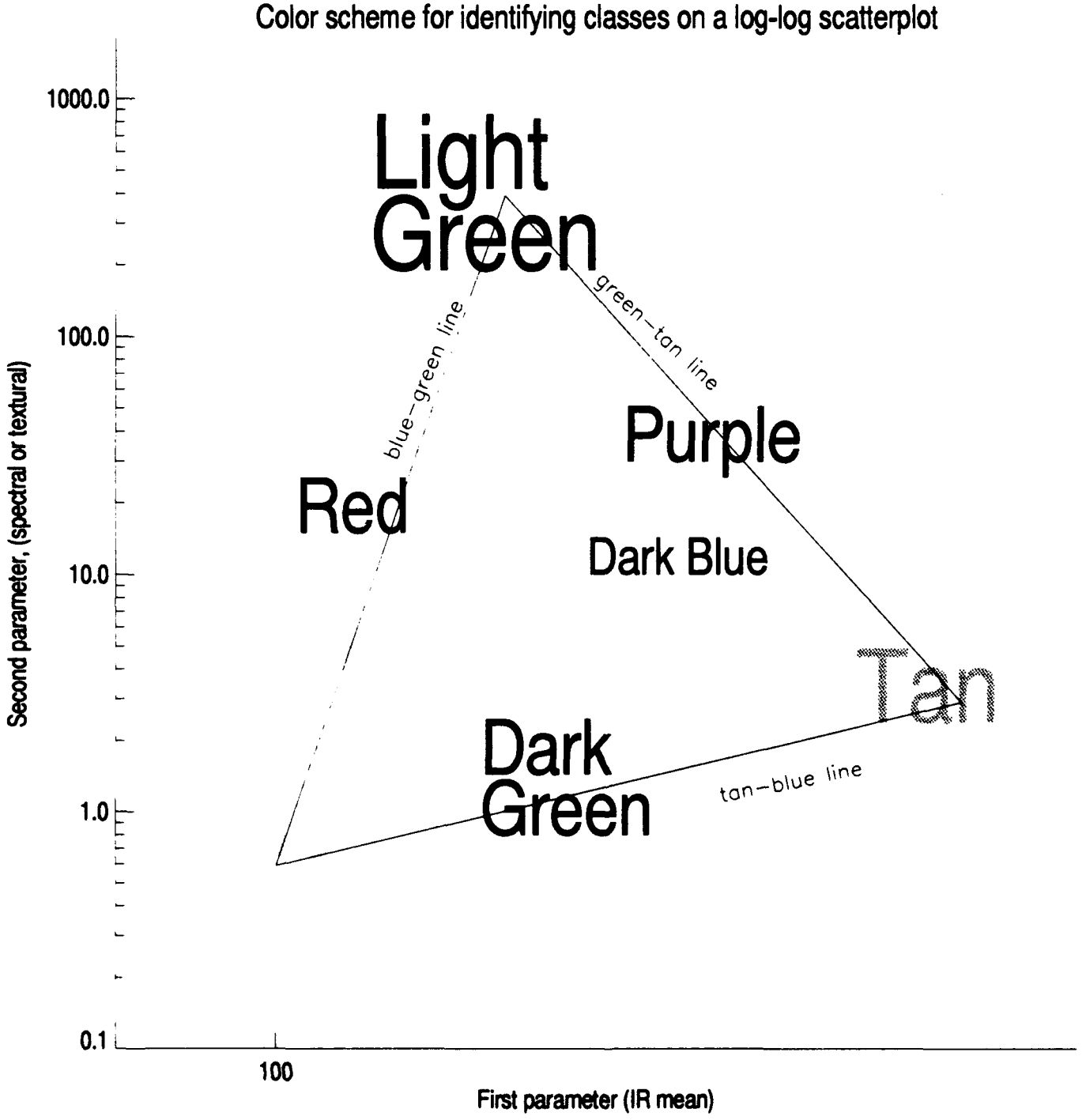

Figure V.5 :Schematic diagram indicating basic coloring scheme for two parameter spaces. (For physical interpretation see text and Table V.7)

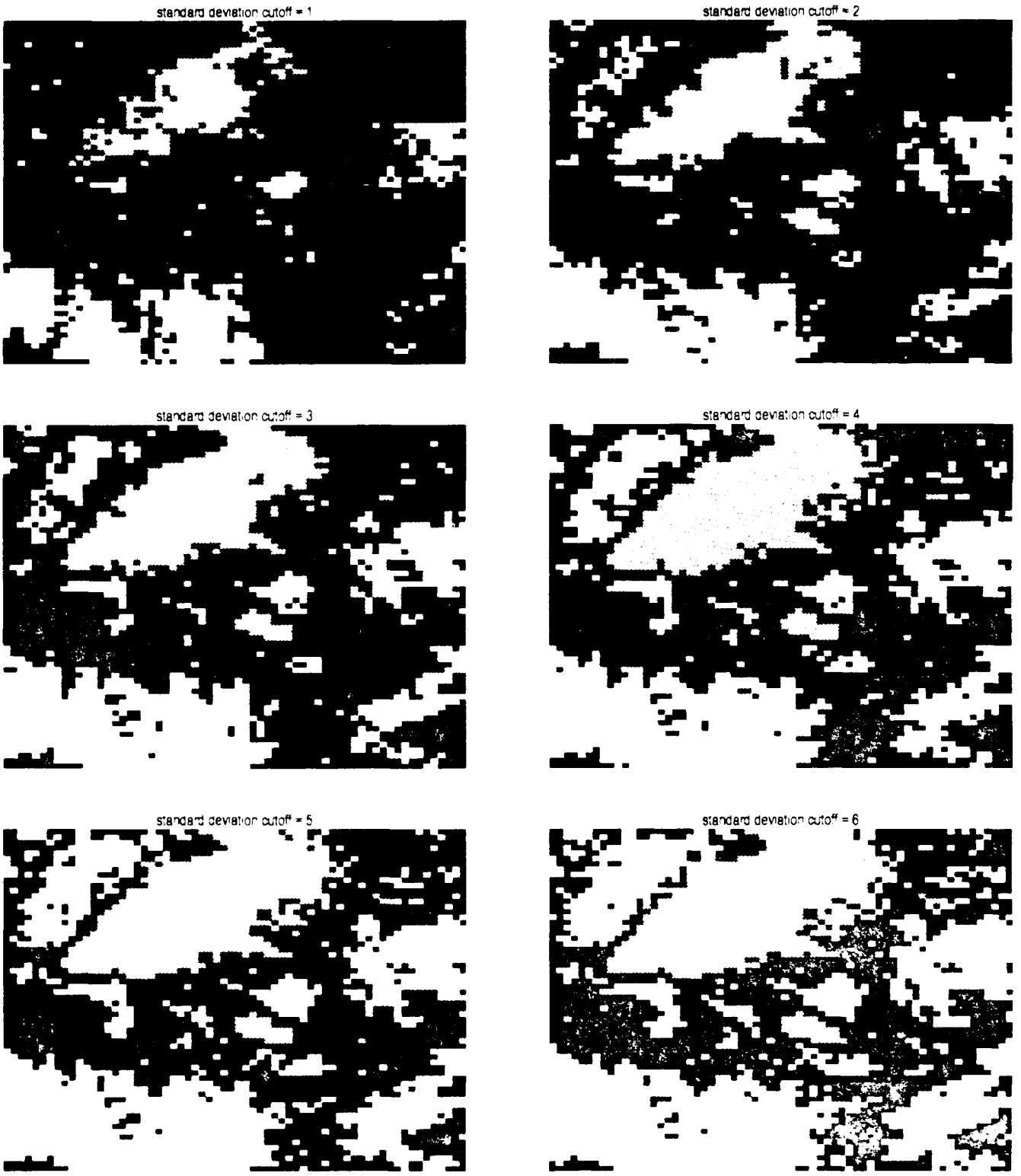

Figure V.6 : Spatial coherence method for 2-18-86 with standard deviation threshold set to 1,2,3,4,5 and 6

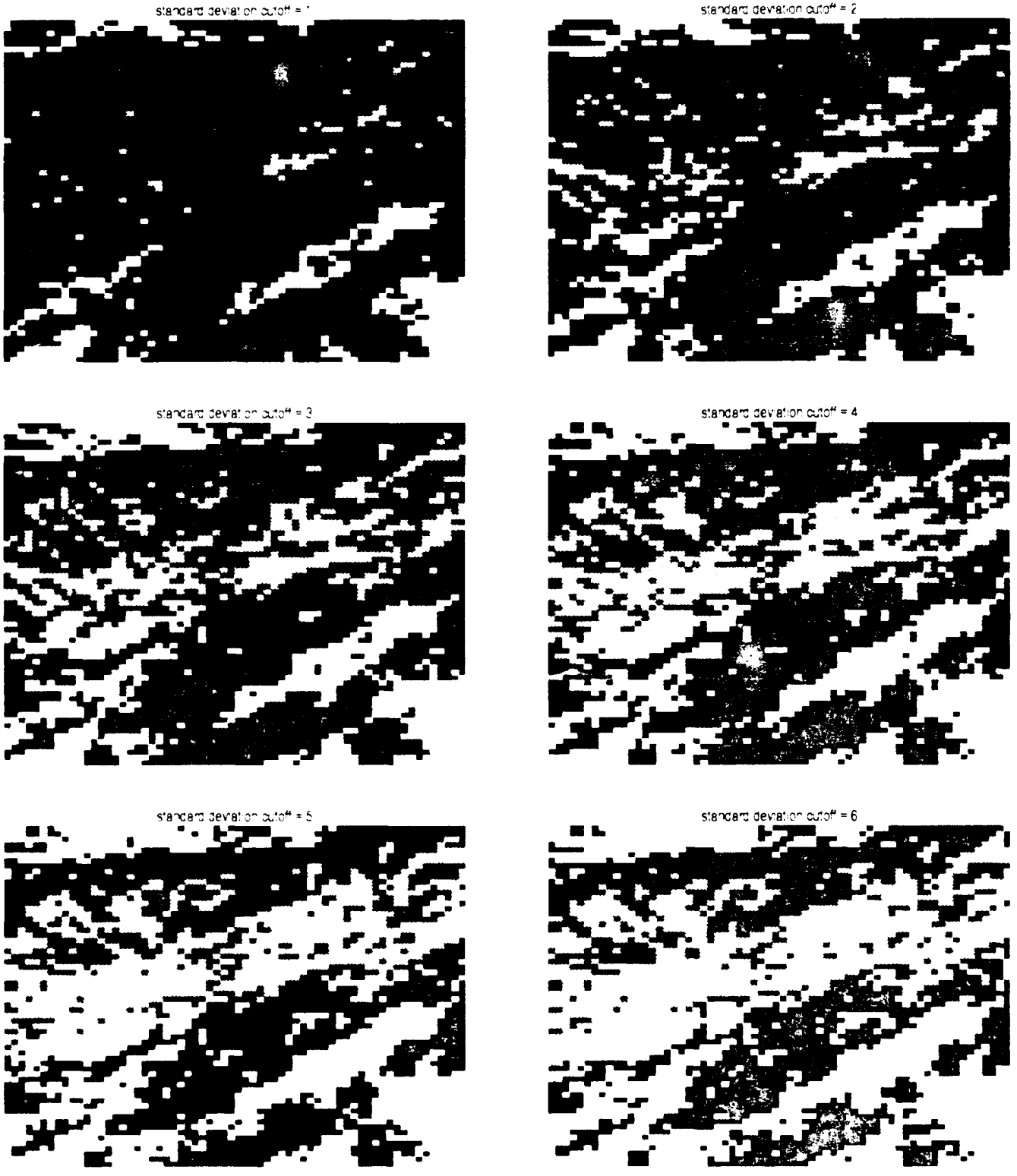

Figure V.6 : Spatial coherence method for 2-24-86 with standard deviation threshold set to 1,2,3,4,5 and 6

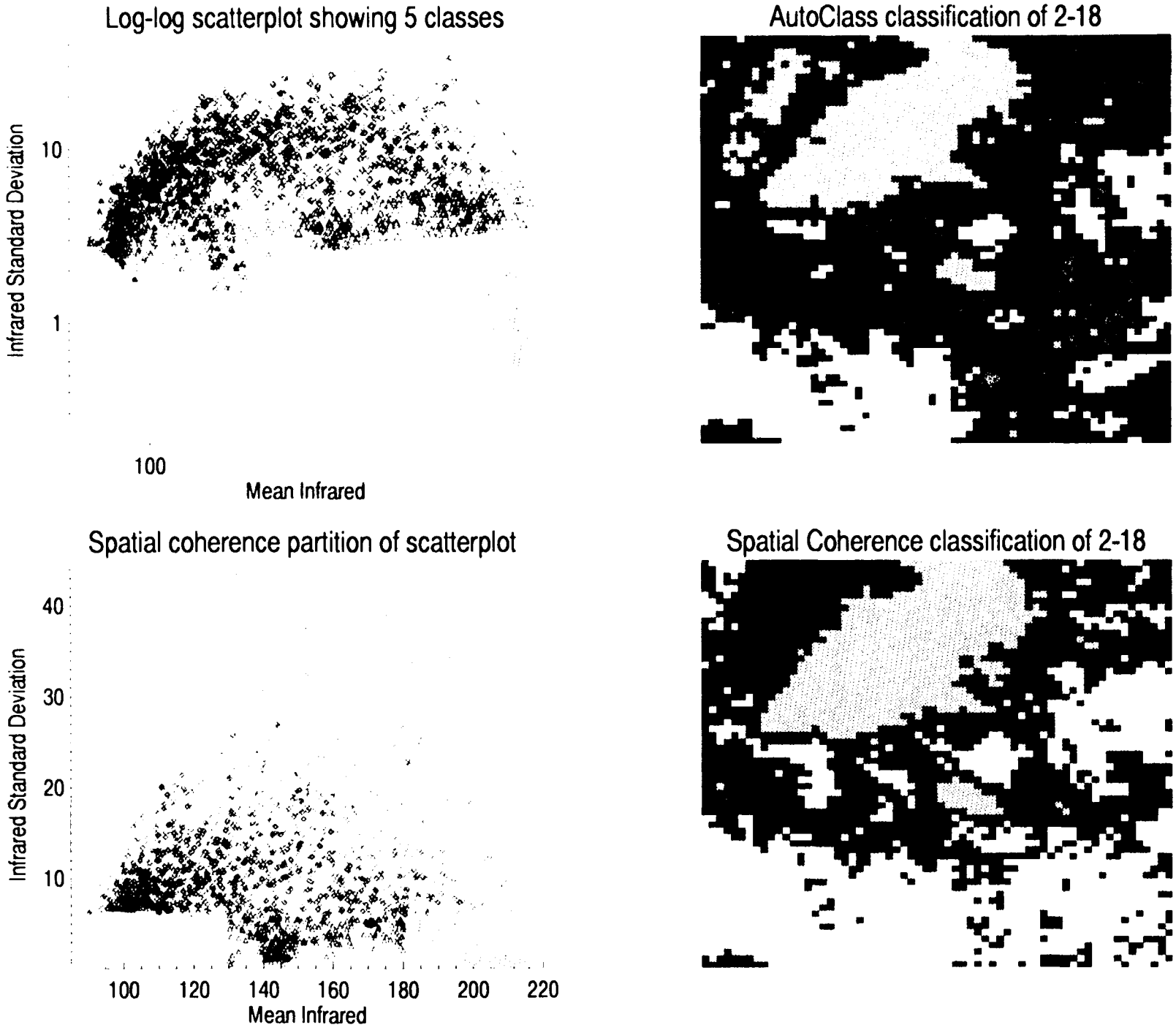

Figure IV.7. Comparison of spatial coherence method with Autoclass for 2-18-86

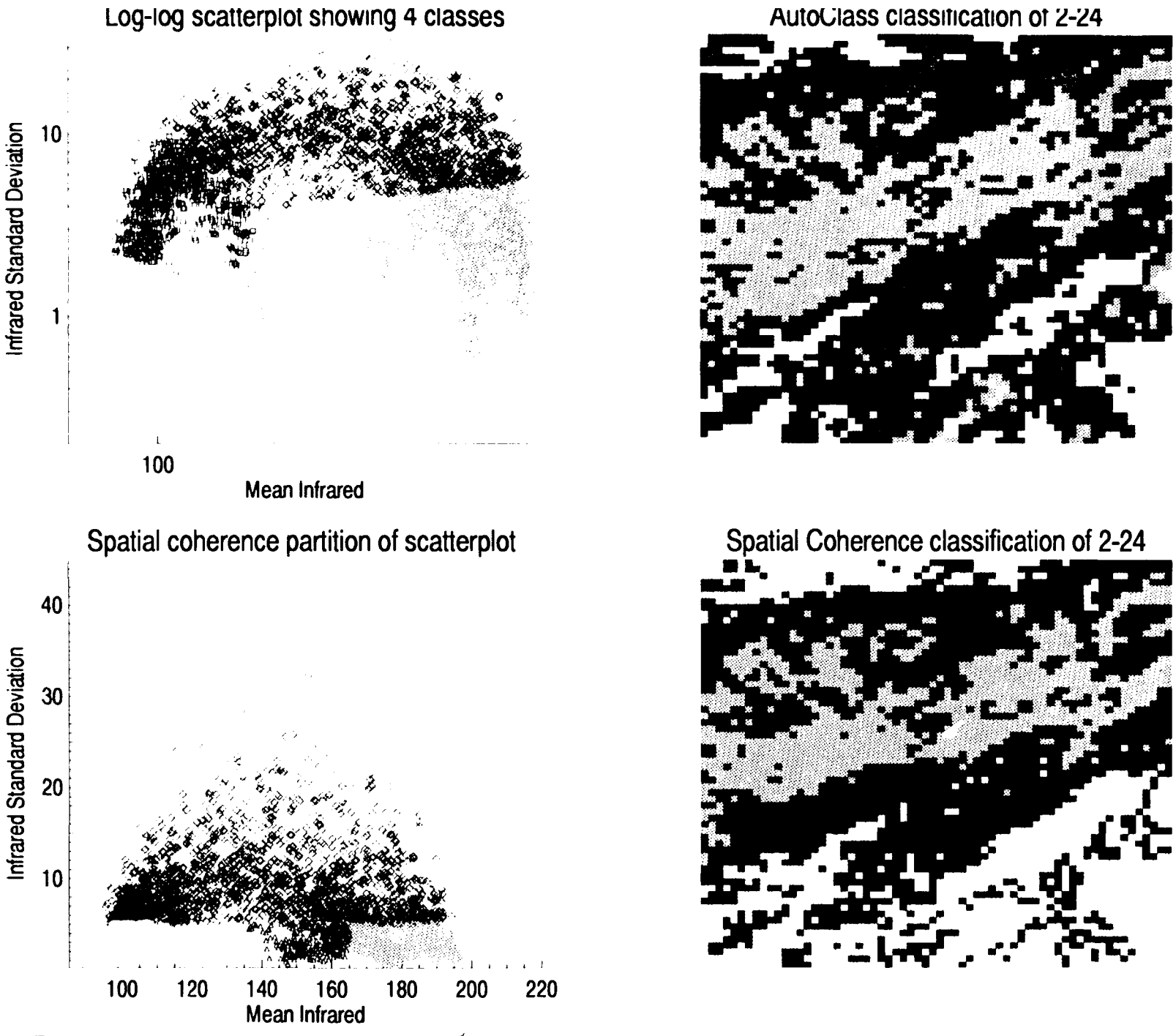

Figure V.7. Comparison of spatial coherence method with Autoclass for 2-24-86

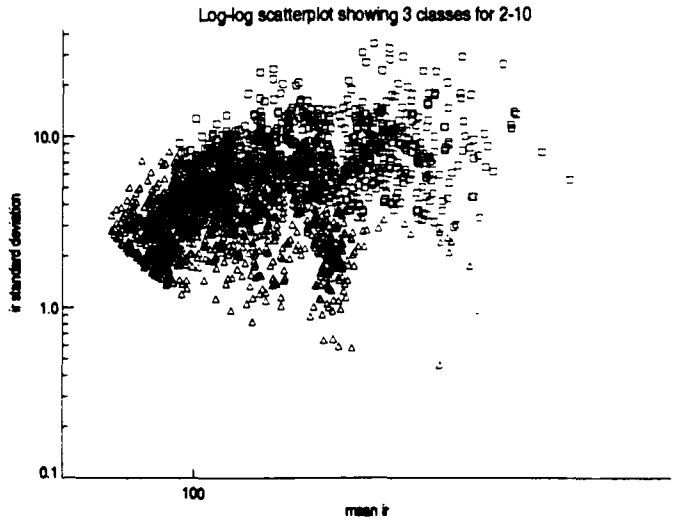

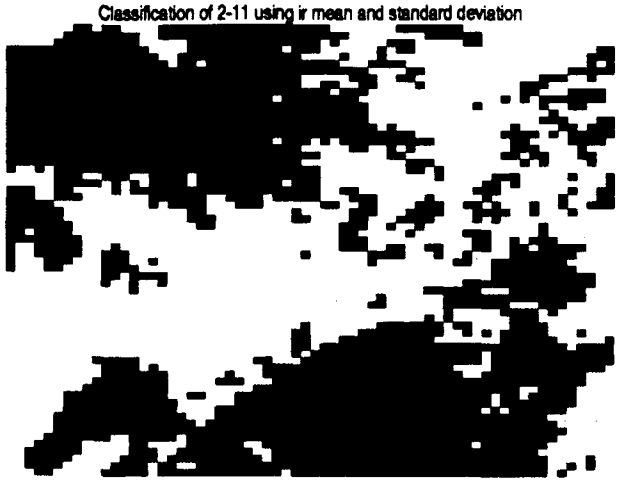

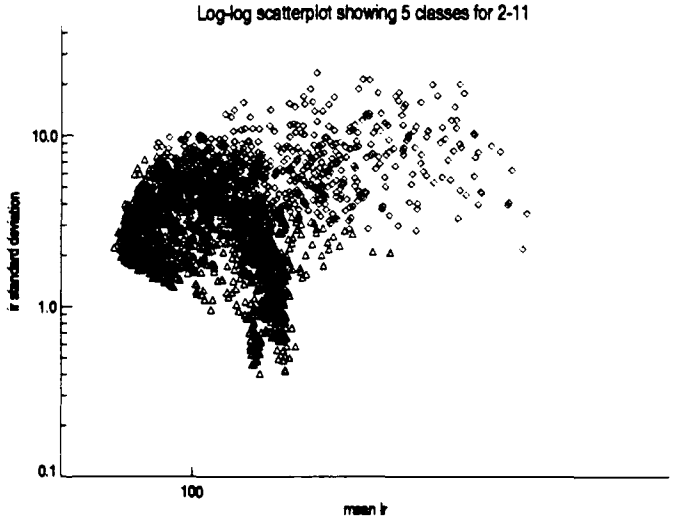

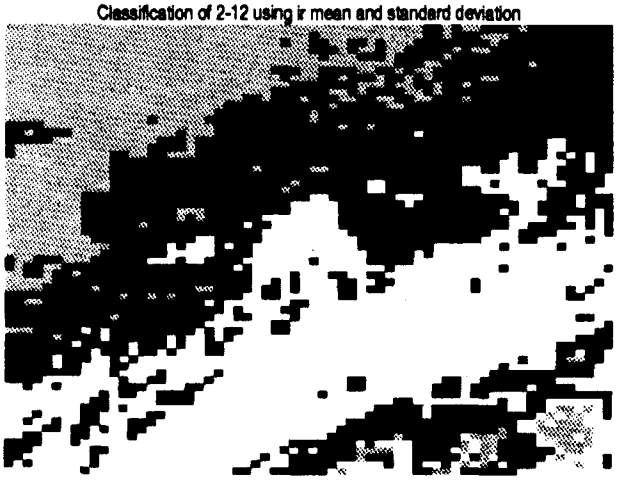

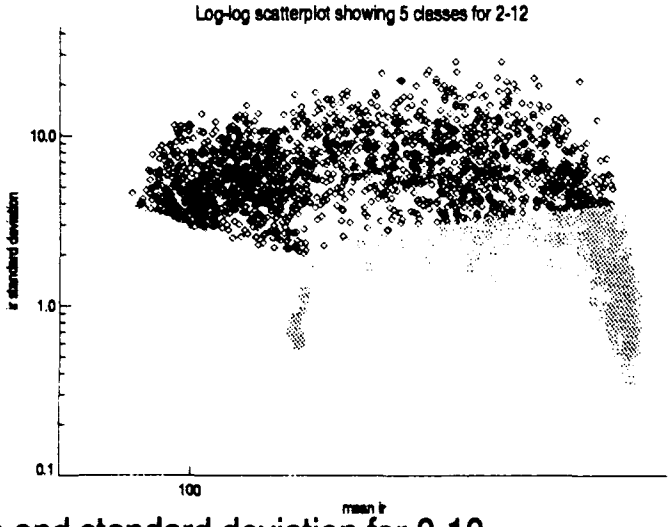

Figure V.8 : Classification using ir mean and standard deviation for 2-10, 2-11 and 2-12. See ajoining scatterplots and Table V.7 for color coding

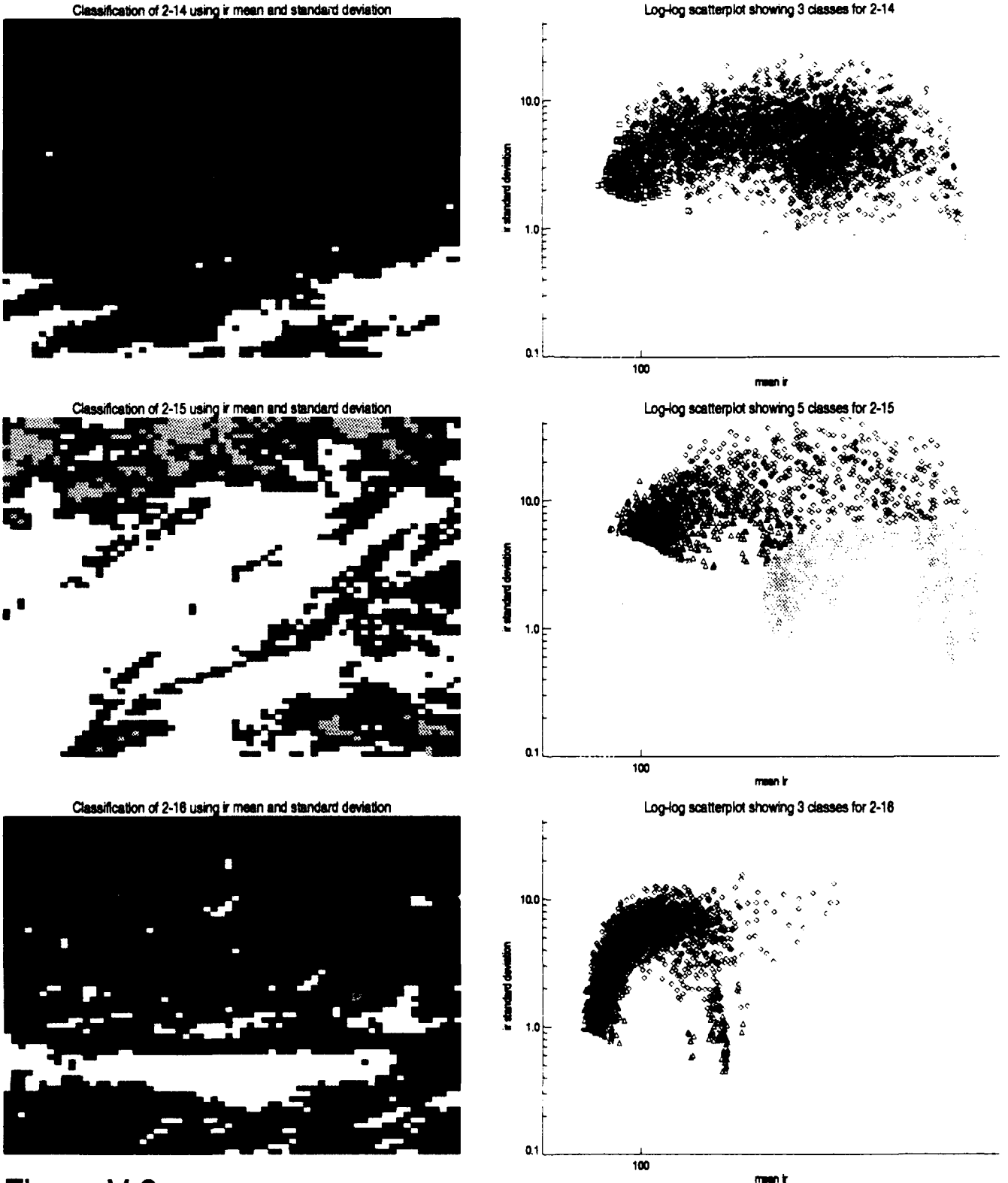

Figure V.8 : Classification using ir mean and standard deviation for 2-14, 2-15 and 2-16. See ajoining scatterplot and Table V.7 for color coding.

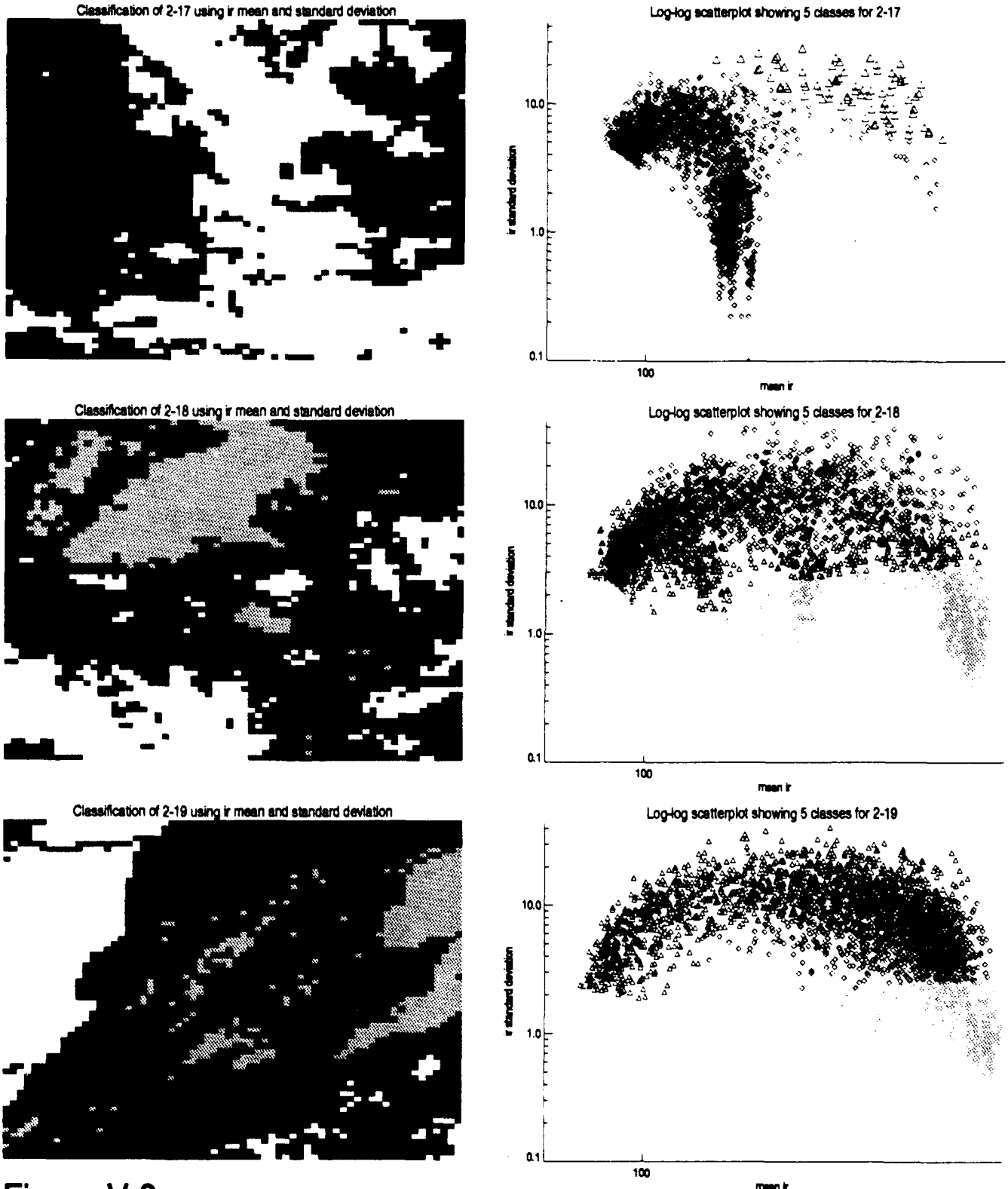

Figure V.8 : Classification using ir mean and standard deviation for 2-17, 2-18 and 2-19. See ajoining scatterplot and Table V.7 for color coding.

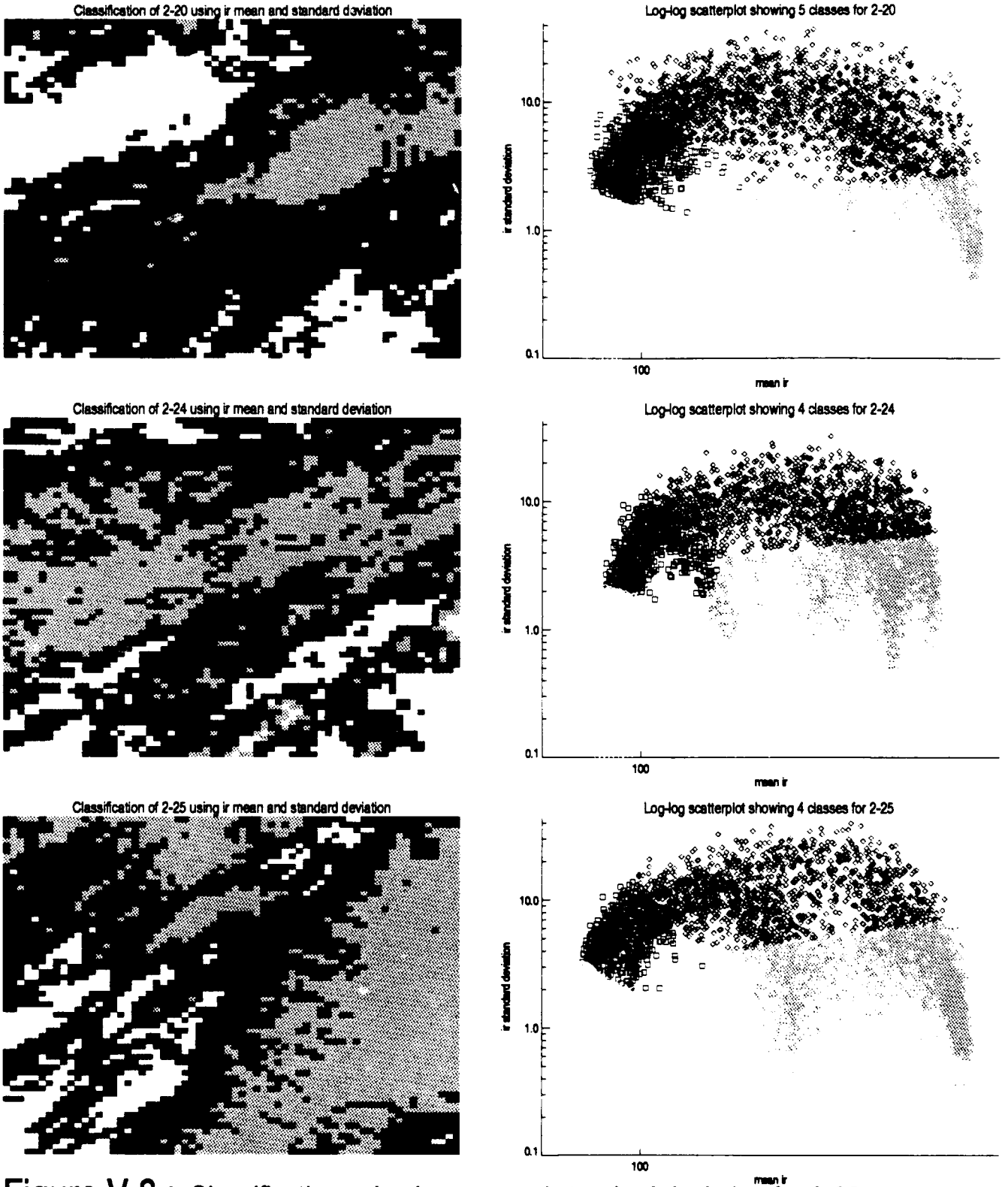

Figure V.8 : Classification using ir mean and standard deviation for 2-20, 2-24 and 2-25. See ajoining scatterplot and Table V.7 for color coding.

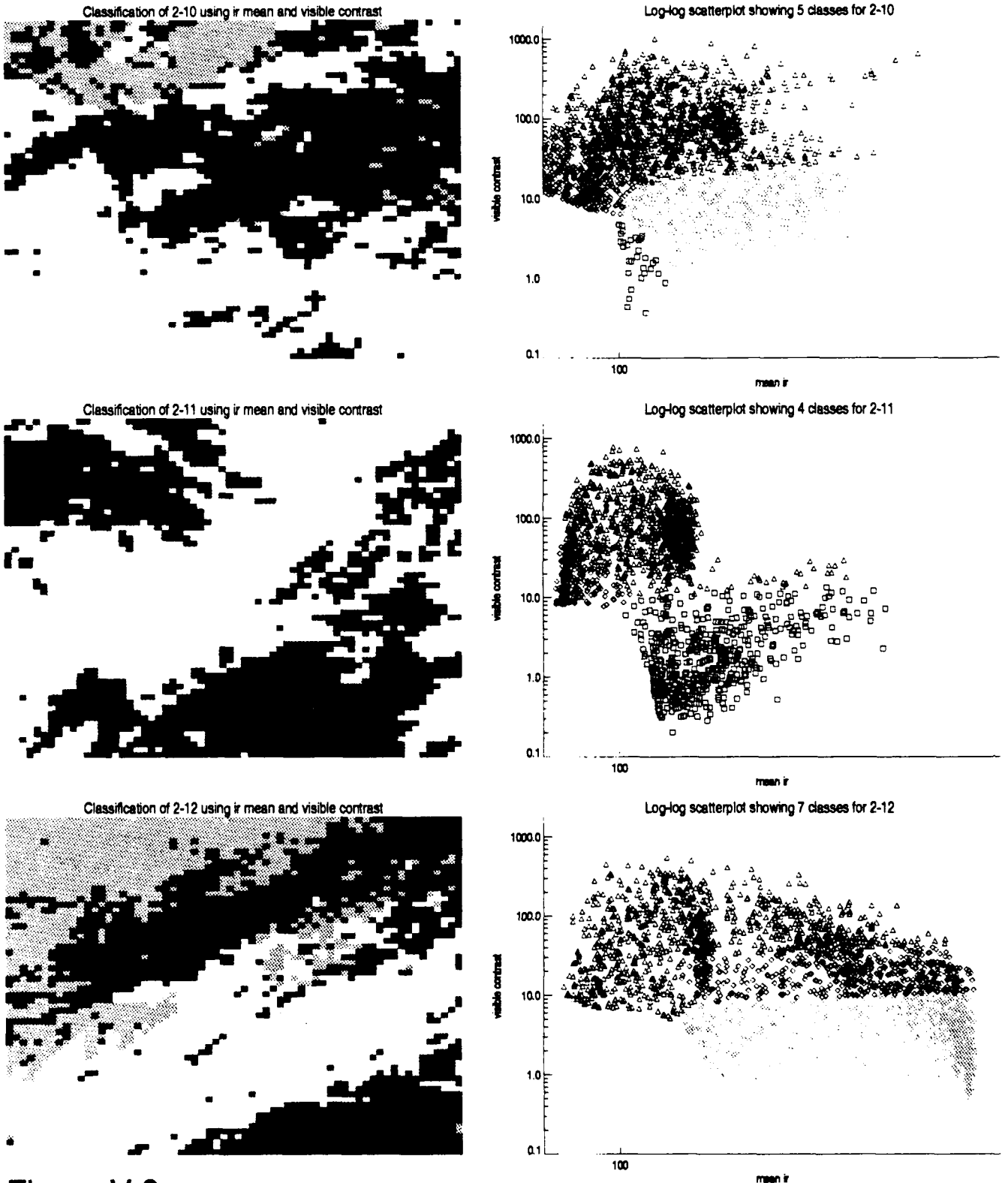

Figure V.9 : Classification using ir mean and visible contrast for 2-10, 2-11, and 2-12. See ajoining scatterplot and Table V.7 for color coding.

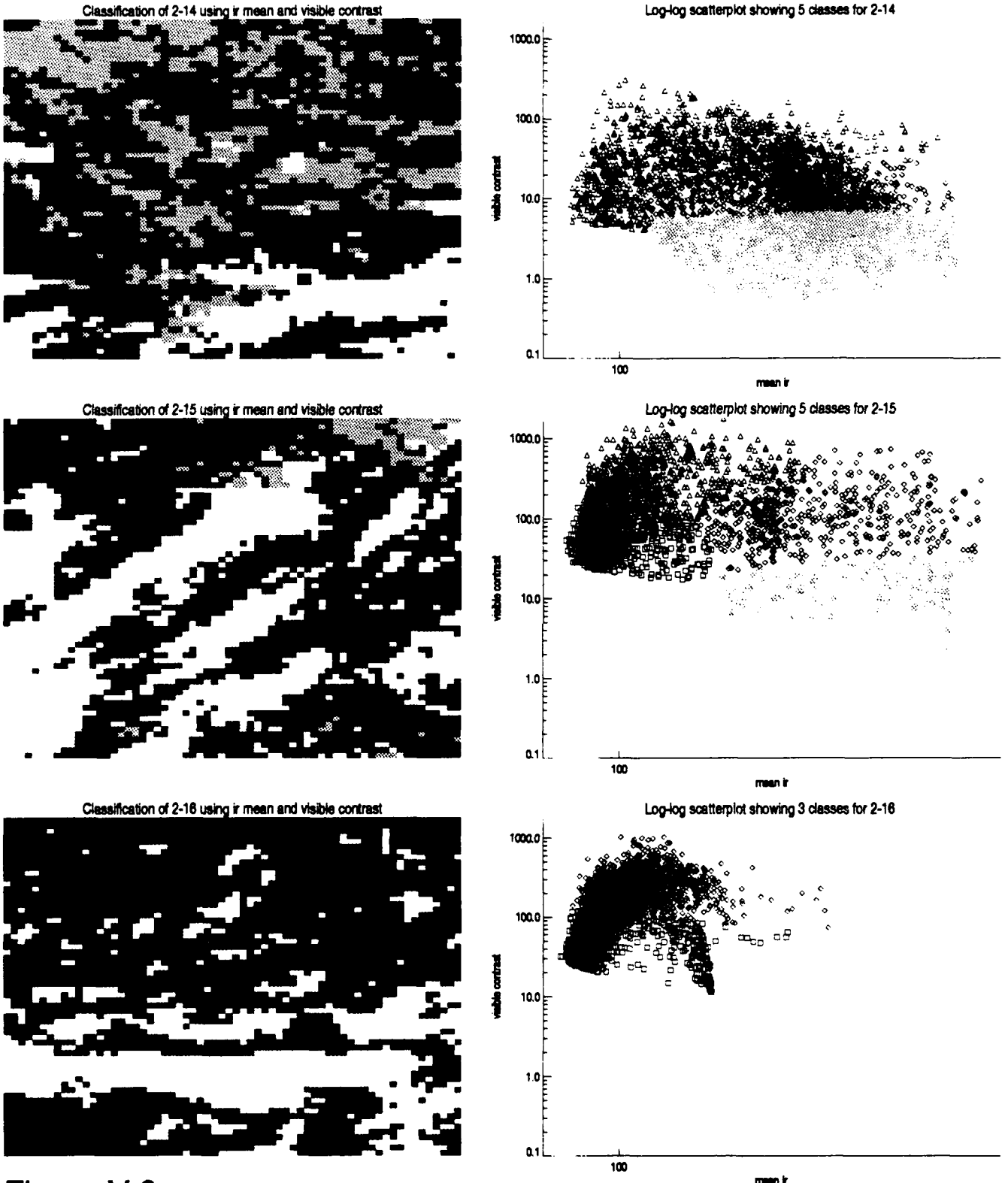

Figure V.9 : Classification using ir mean and visible contrast for 2-14, 2-15, and 2-16. See ajoining scatterplot and Table V.7 for color coding.

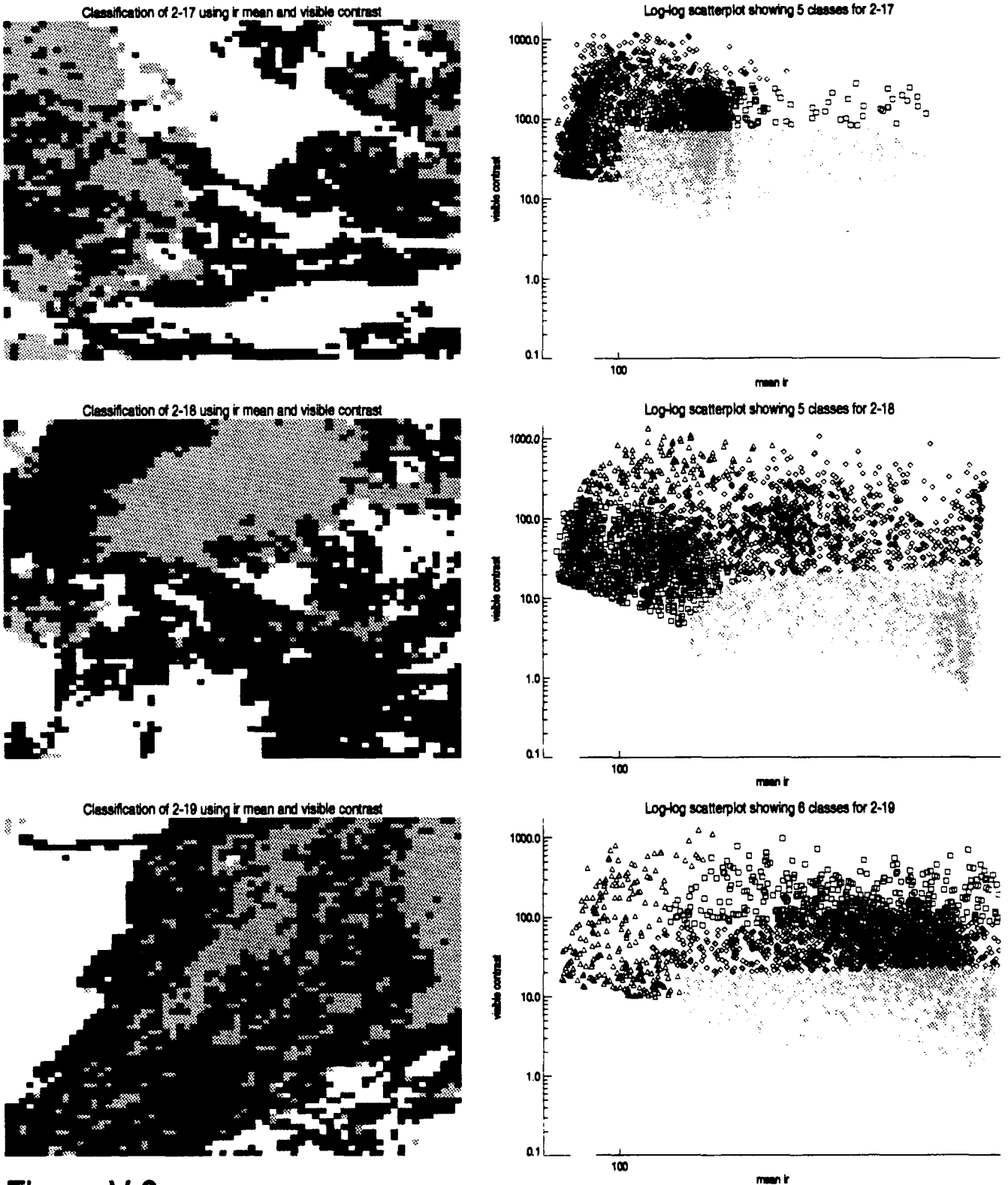

Figure V.9 : Classification using ir mean and visible contrast for 2-17, 2-18, and 2-19. See ajoining scatterplot and Table V.7 for color coding.

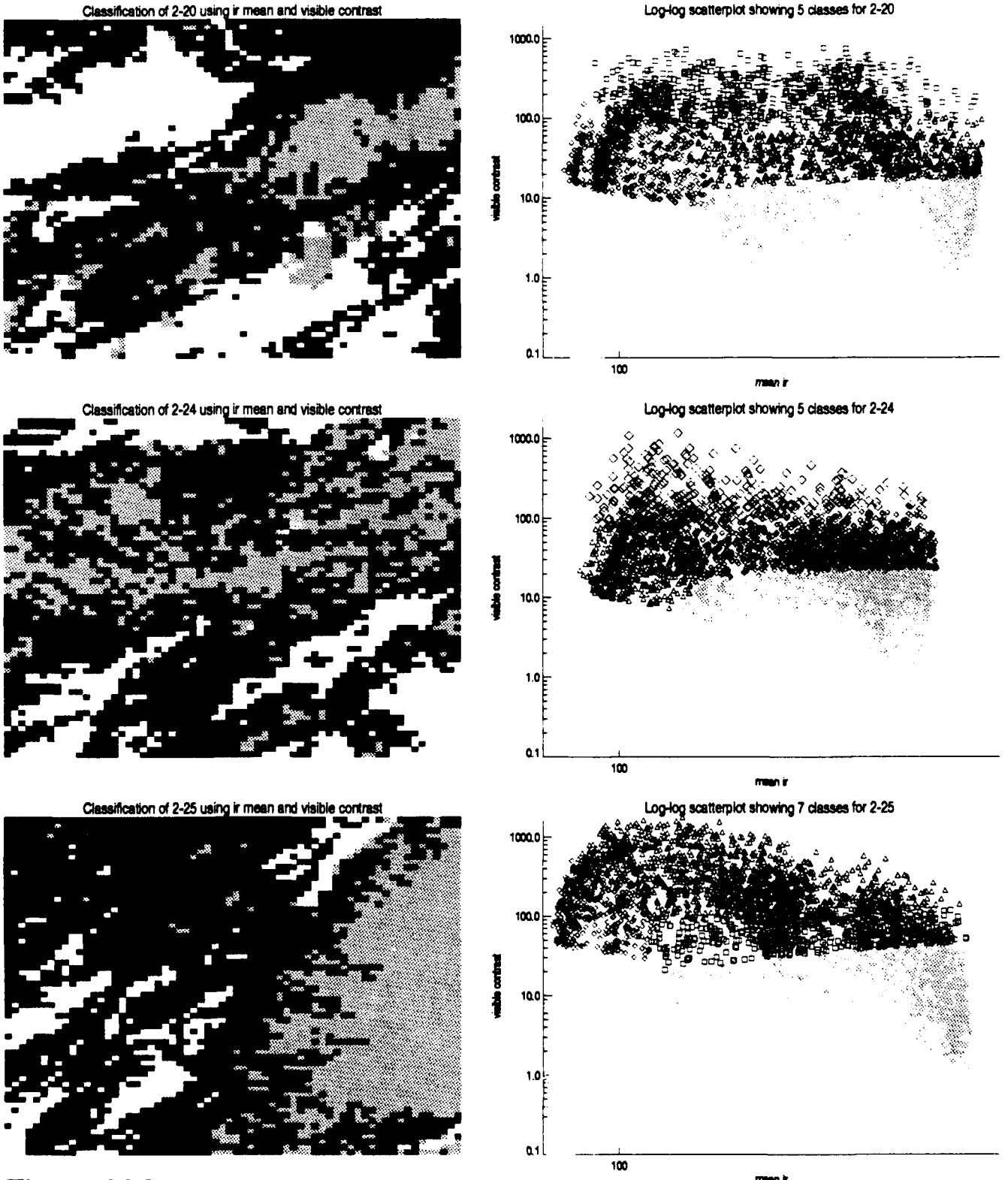

Figure V.9 : Classification using ir mean and visible contrast for 2-20, 2-24, and 2-25. See ajoining scatterplot and Table V.7 for color coding.

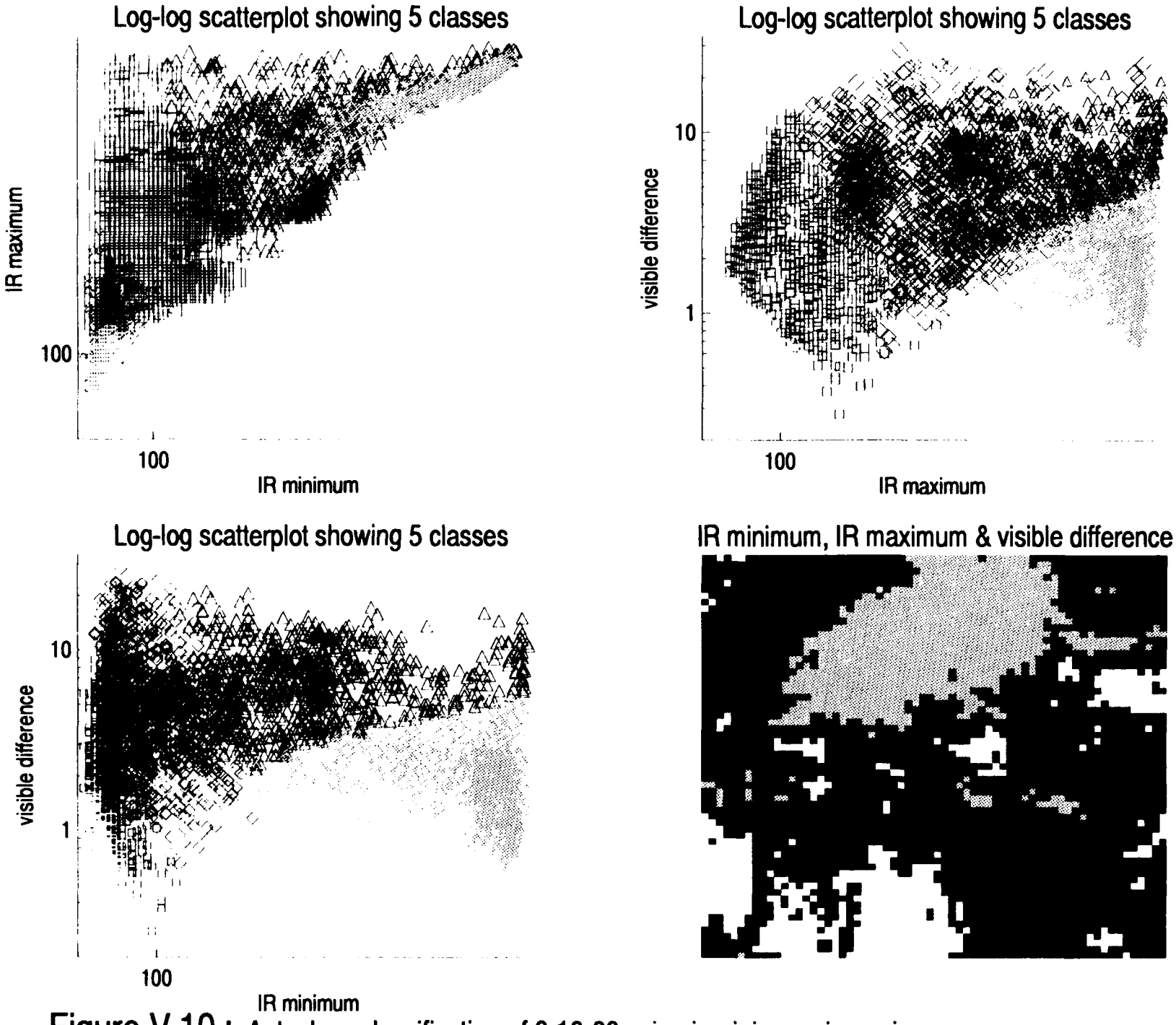

Figure V.10 : Autoclass classification of 2-18-86 using ir minimum, ir maximun and visible difference with three 2-dimensional projected scatterplots.

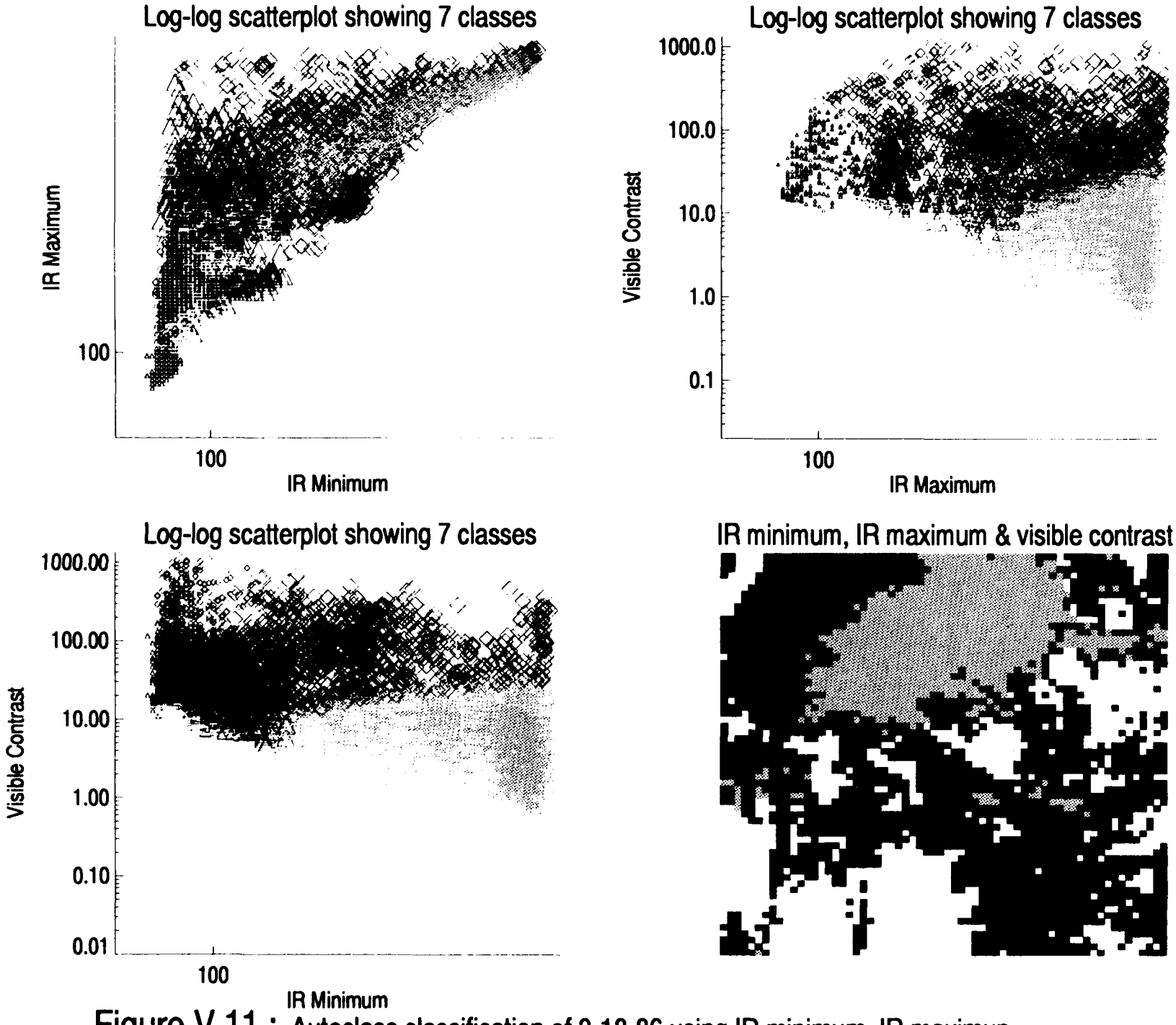

Figure V.11 : Autoclass classification of 2-18-86 using IR minimum, IR maximun and visible contrast with three 2-dimensional projected scatterplots.

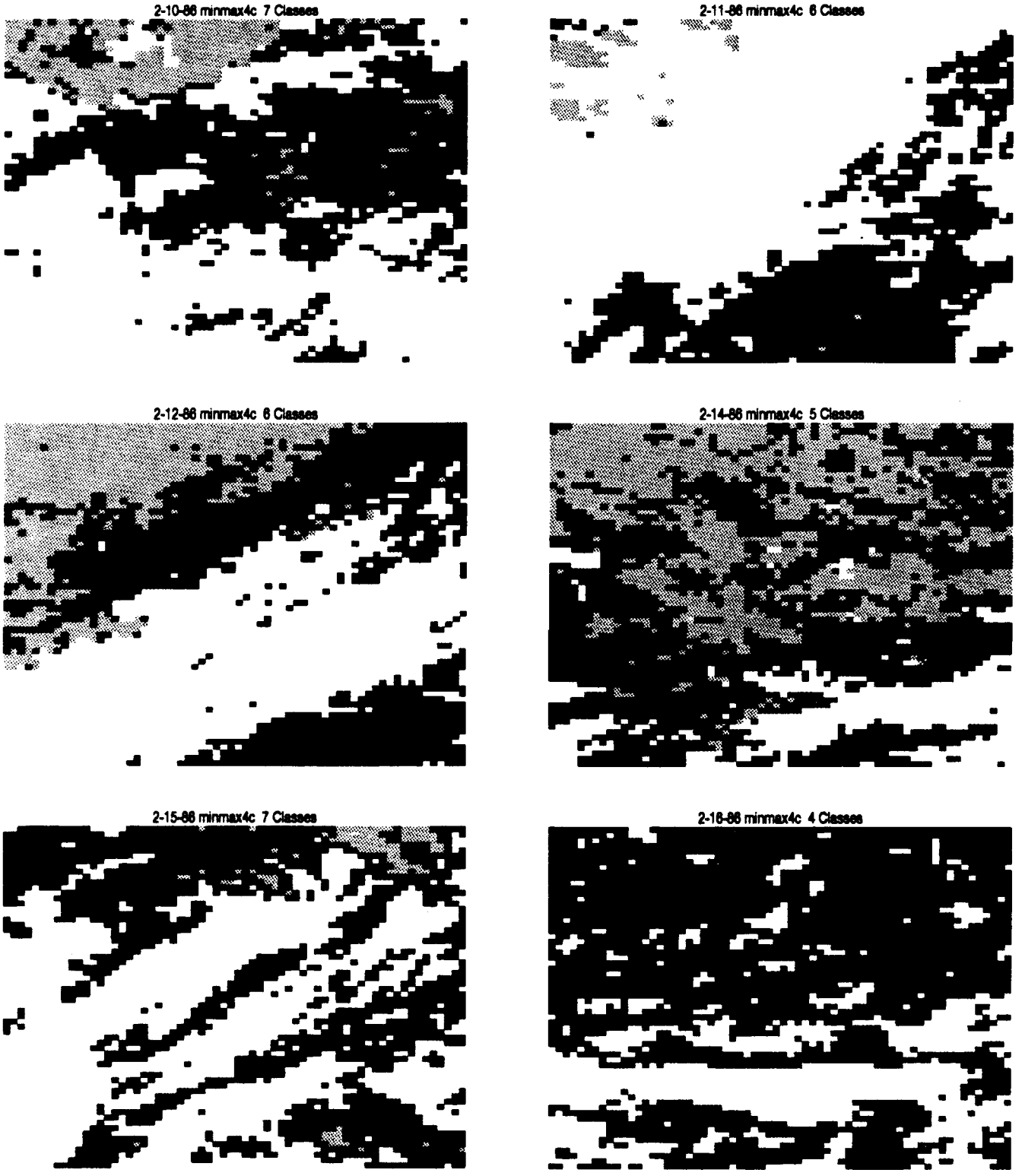

Figure V.12 : Autoclass classification of 2-10, 2-11, 2-12, 2-14, 2-15 and 2-16 using IR minimum, IR maximun and visible contrast.

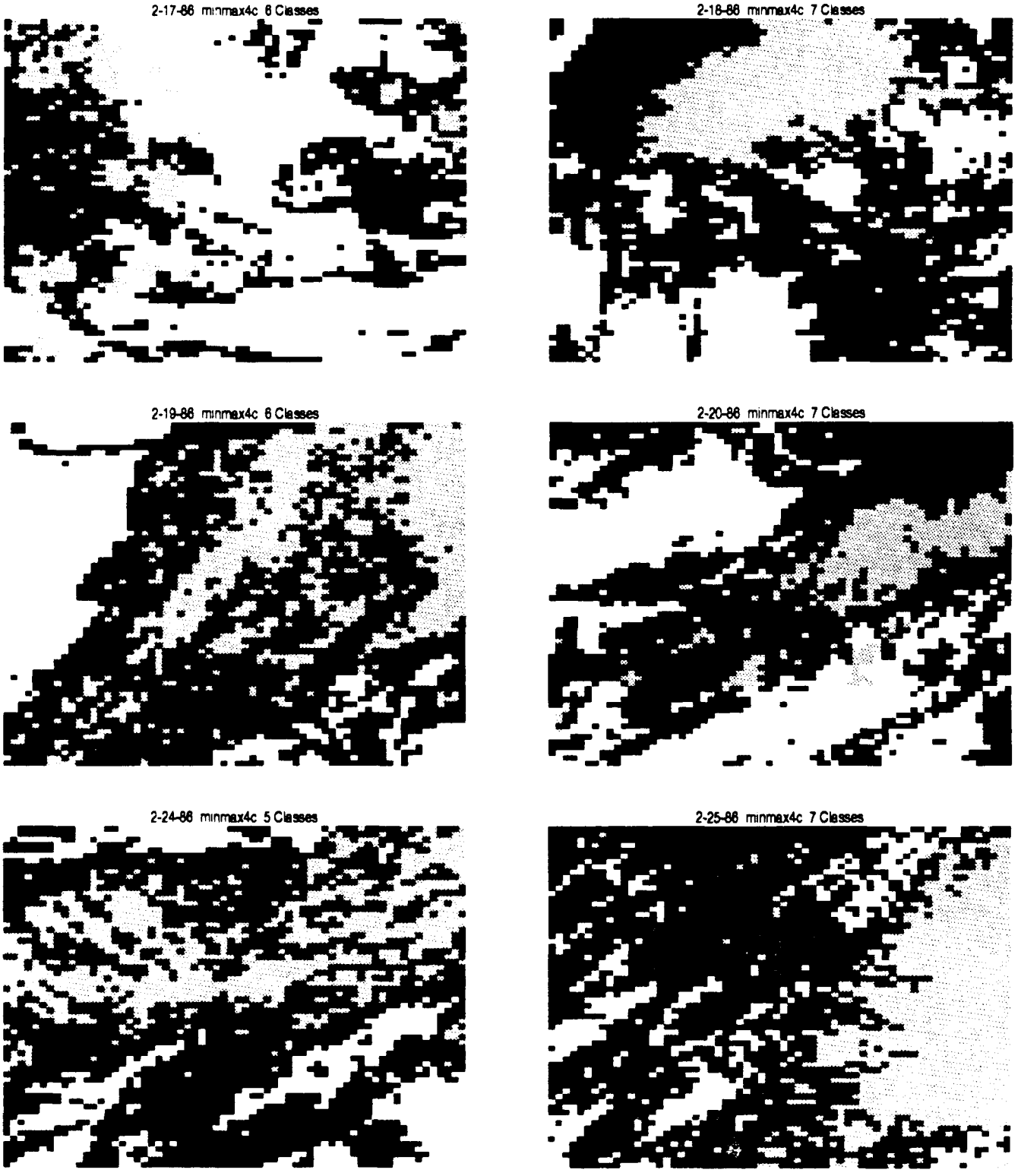

Figure V.12 :Autoclass classification of 2-17, 2-18, 2-19, 2-20, 2-24 and 2-25 using IR minimum, IR maximun and visible contrast.

CAPTIONS FOR FIGURES IN CHAPTER VI

Figure VI.1: Energy spectra corresponding to the visible images contained in channel 1 (512×512 pixels). For purpose of comparison, the spectra are superimposed and displaced from their true energy values (energy in arbitrary units). The spectra are ordered chronologically starting from the lower end of the graph. Each spectrum is displaced by two orders of magnitude from the last so that while the first spectrum (lower end of the graph) is not displaced at all from its true energy values. The energy of the second spectrum is off by two orders of magnitude, the third spectrum off by four orders of magnitude and so on.

Figure VI.2: Same as fig. VI.1 but for the infrared images of channel 4.

Figure VI.3: Comparison of the ensemble averaged energy spectra of channel 1 (solid line) and channel 4 (dotted line).

Figure VI.4.a,b,c,d: Log-log plots of the statistical moment versus ρ for image 2-14-86 for $\theta = 0, 45, 90$ and 135, respectively.

Figure VI.5.a,b,c,d: Log-log plots of the statistical moment versus ρ for image 2-24-86 for $\theta = 0, 45, 90$ and 135, respectively.

Figure VI.6.a,b,c,d: Log-log plots of the statistical moment versus ρ for the statistical average of 13 images for $\theta = 0, 45, 90$ and 135, respectively.

Figure VI.7: Plots of the scaling exponent versus q^{th} order of the statistical moment for $\theta = 0, 45, 90$ and 135 for 2-14-86.

Figure VI.8: Plots of the scaling exponent versus q^{th} order of the statistical moment for $\theta = 0, 45, 90$ and 135 for 2-24-86.

Figure VI.9: Plots of the scaling exponent versus q^{th} order of the statistical moment for $\theta = 0, 45, 90$ and 135 for the statistical average of 13 images.

Figure VI.10a,b,c,d: Plots of log(statistical moment) versus log(superpixel size) for *Difference*, *Contrast*, *Entropy* and *Angular Second Moment*, respectively for image 2-14-86 and $\theta = 0$.

Figure VI.11a,b,c,d: Plots of log(statistical moment) versus log(superpixel size) for *Difference*, *Contrast*, *Entropy* and *Angular Second Moment*, respectively for image 2-14-86 and $\theta = 45$.

Figure VI.12a,b,c,d: Plots of log(statistical moment) versus log(superpixel size) for *Difference*, *Contrast*, *Entropy* and *Angular Second Moment*, respectively for image 2-14-86 and $\theta = 90$.

Figure VI.13a,b,c,d: Plots of log(statistical moment) versus log(superpixel size) for *Difference*, *Contrast*, *Entropy* and *Angular Second Moment*, respectively for image 2-14-86 and $\theta = 135$.

Figure VI.14a,b,c,d: Plots of log(statistical moment) versus log(superpixel size) for *Difference*, *Contrast*, *Entropy* and *Angular Second Moment*, respectively for image 2-24-86 and $\theta = 0$.

Figure VI.15a,b,c,d: Plots of log(statistical moment) versus log(superpixel size) for *Difference*, *Contrast*, *Entropy* and *Angular Second Moment*, respectively for image 2-24-86 and $\theta = 45$.

Figure VI.16a,b,c,d: Plots of log(statistical moment) versus log(superpixel size) for *Difference*, *Contrast*, *Entropy* and *Angular Second Moment*, respectively for image 2-24-86 and $\theta = 90$.

Figure VI.17a,b,c,d: Plots of log(statistical moment) versus log(superpixel size) for *Difference*, *Contrast*, *Entropy* and *Angular Second Moment*, respectively for image 2-24-86 and $\theta = 135$.

Figure VI.18a,b,c,d: Plots of log(statistical moment) versus log(superpixel size) for *Difference*, *Contrast*, *Entropy* and *Angular Second Moment*, respectively for simulated multifractal field and $\theta = 0$.

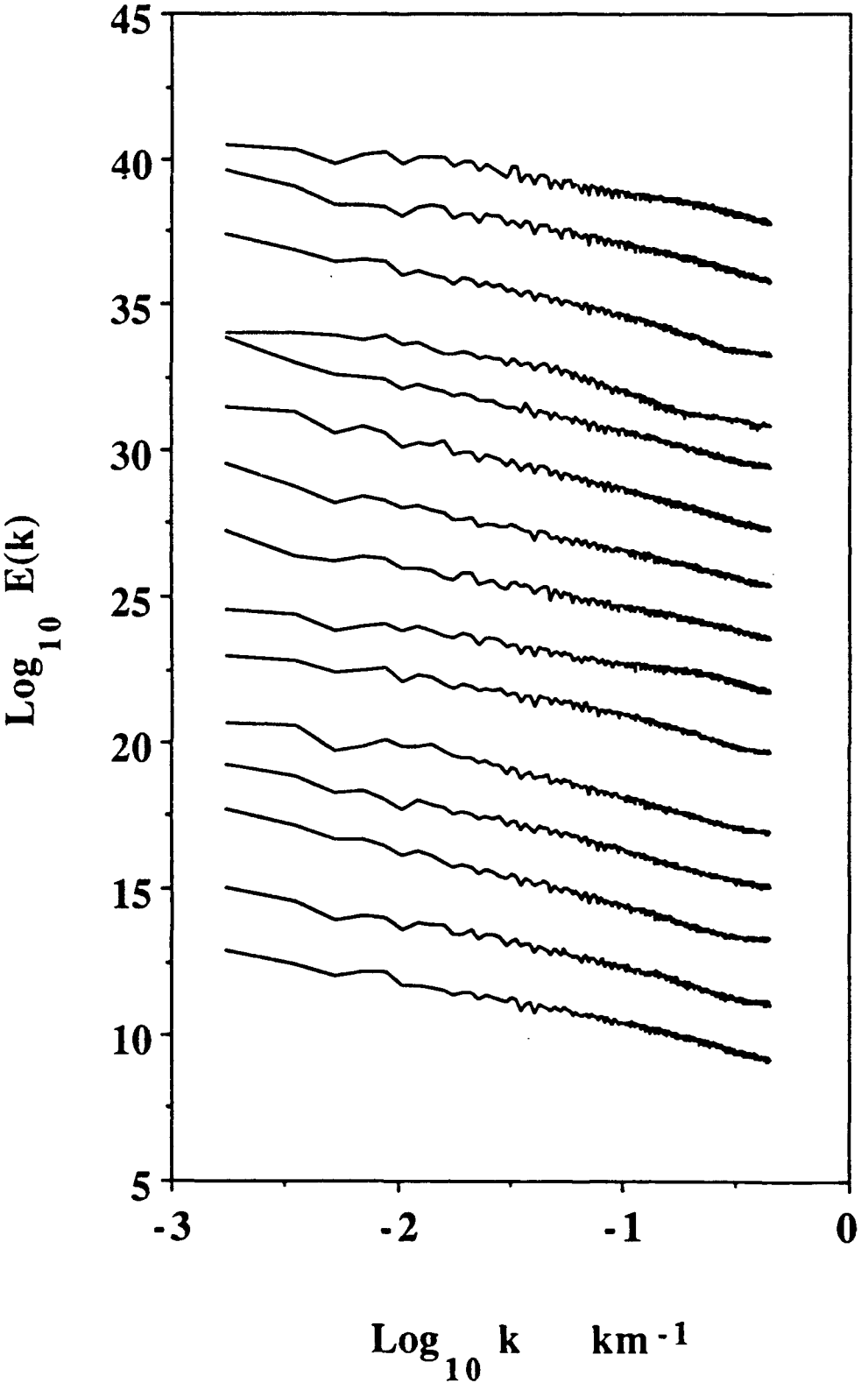

Figure VI.1

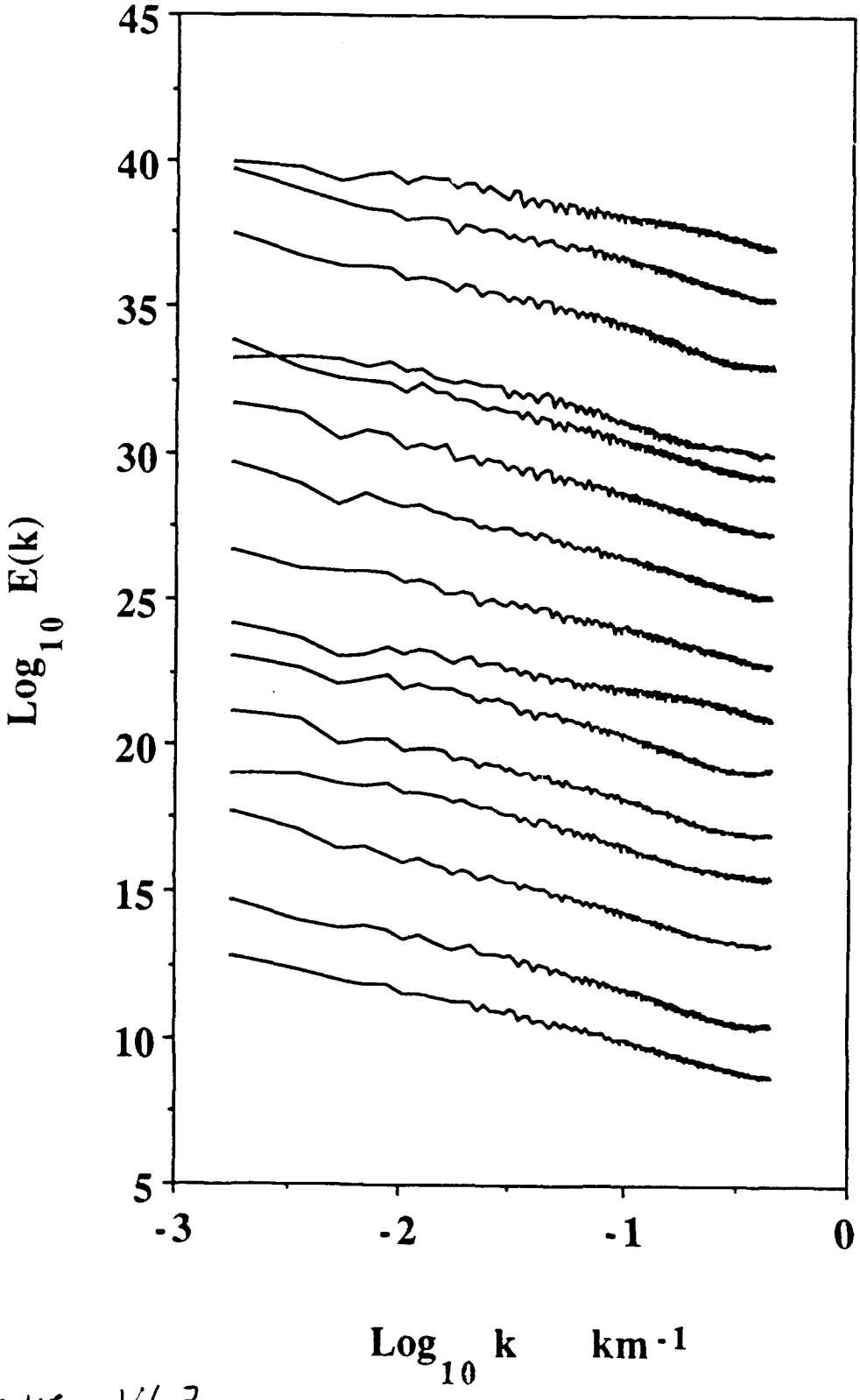

Figure VI.2

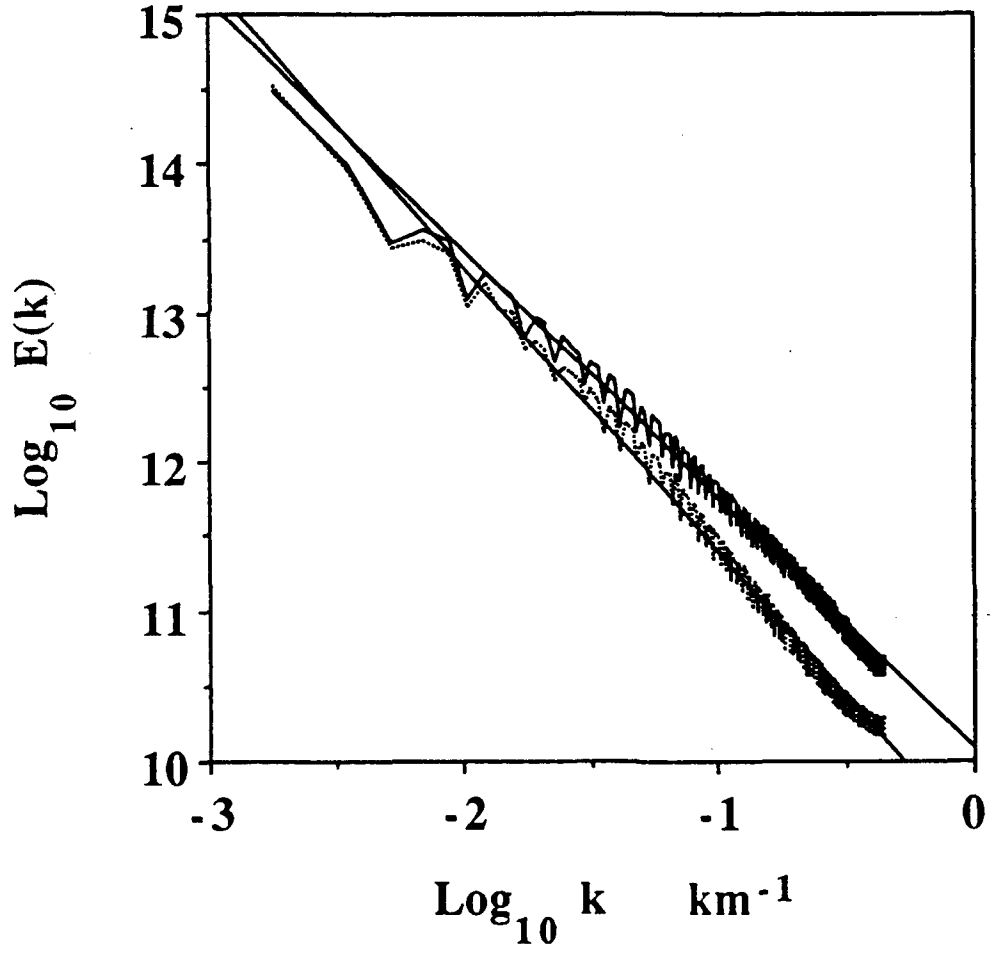

Figure VI.3

2-14-86, Angle=0

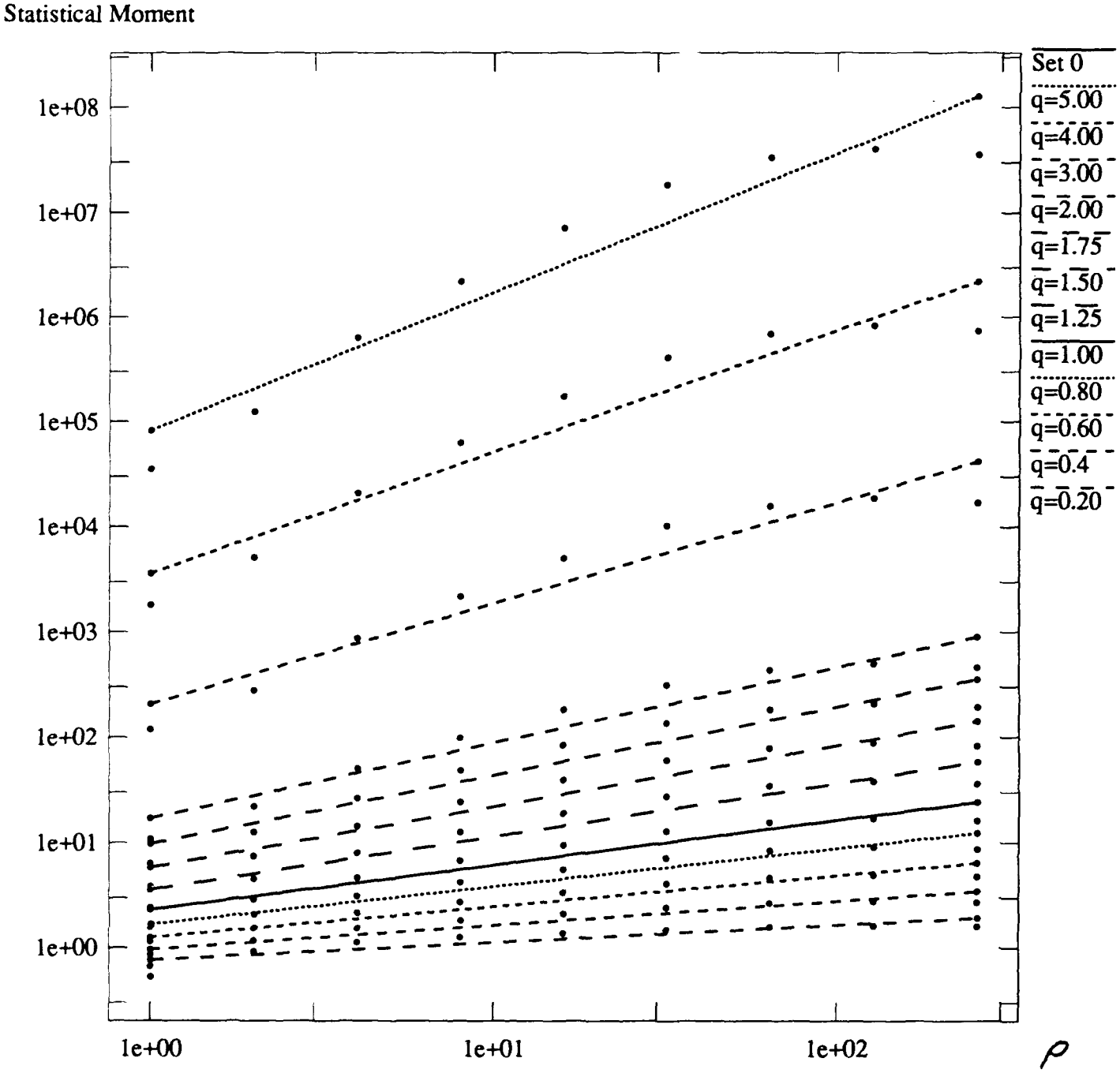

Figure VI.4.a

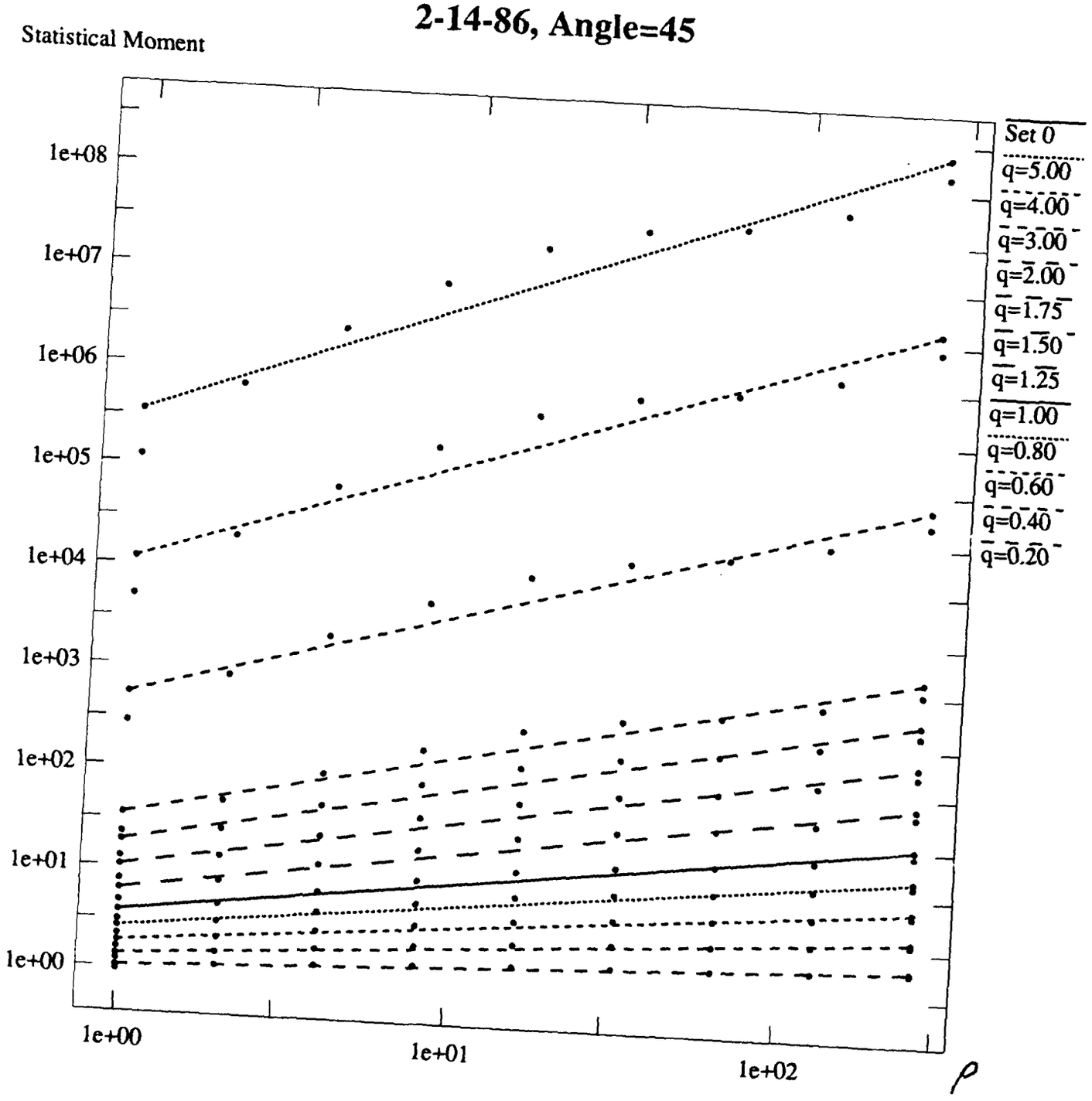
2-14-86, Angle=45
Statistical Moment
1e+08
1e+07
1e+06
1e+05
1e+04
1e+03
1e+02
1e+01
1e+00
1e+00
1e+01
1e+02
ρ
Set 0
q=5.00
q=4.00
q=3.00
q=2.00
q=1.75
q=1.50
q=1.25
q=1.00
q=0.80
q=0.60
q=0.40
q=0.20

Figure VI.4.b

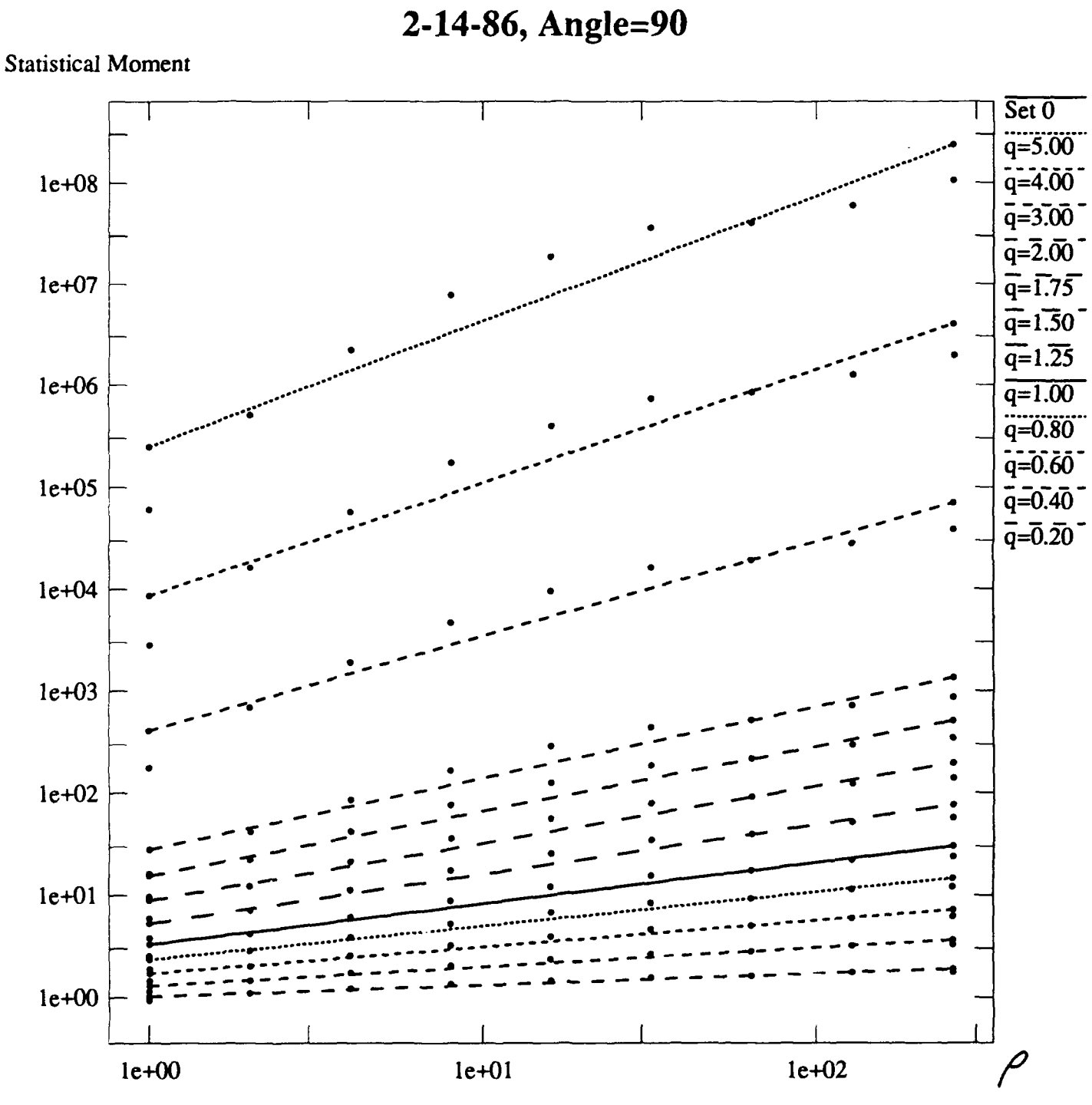
2-14-86, Angle=90
Statistical Moment
1e+08
1e+07
1e+06
1e+05
1e+04
1e+03
1e+02
1e+01
1e+00
1e+00
1e+01
1e+02
ρ
Set 0
q=5.00
q=4.00
q=3.00
q=2.00
q=1.75
q=1.50
q=1.25
q=1.00
q=0.80
q=0.60
q=0.40
q=0.20

Figure VI.4.c

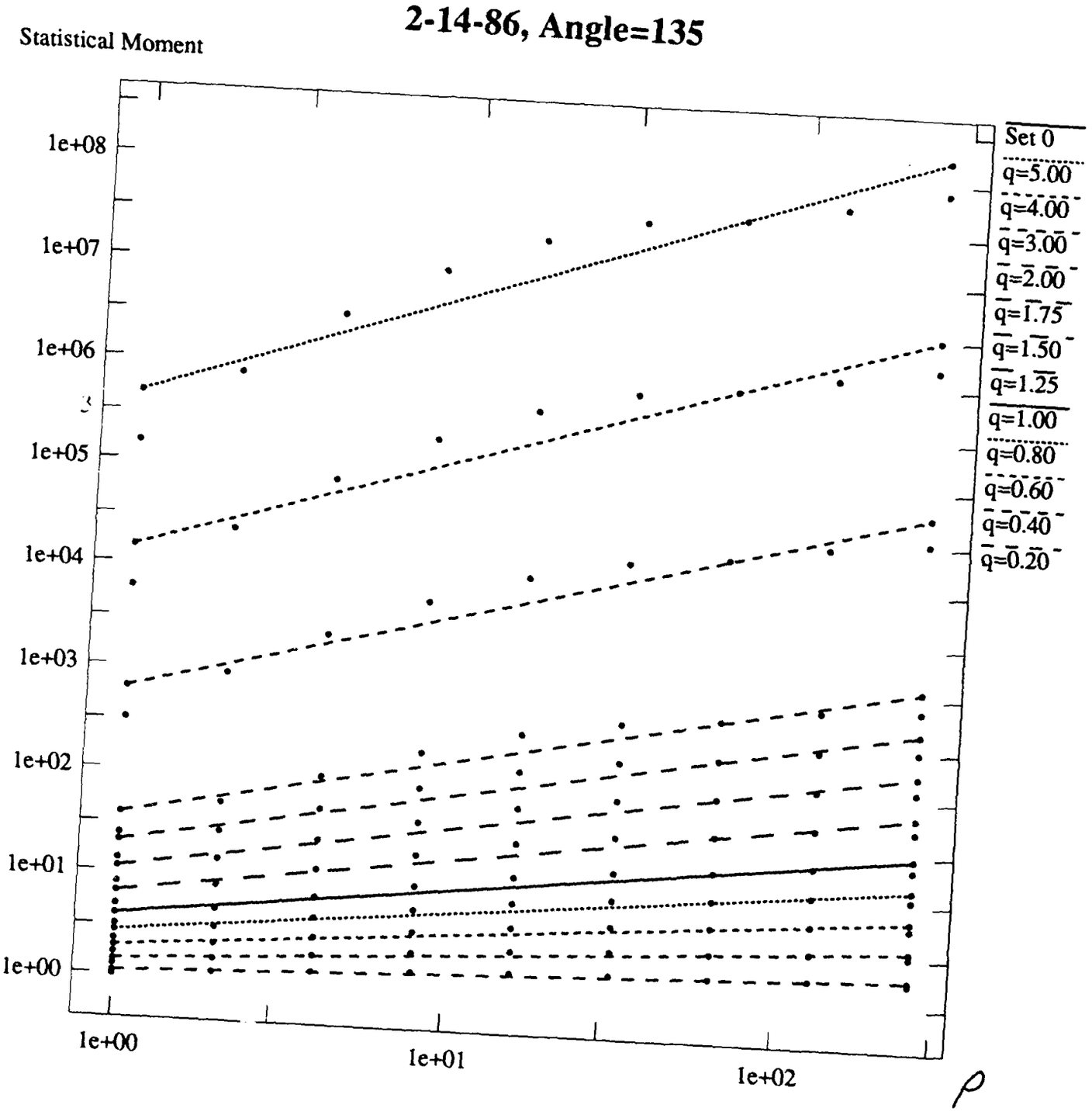
2-14-86, Angle=135
Statistical Moment
1e+08
1e+07
1e+06
1e+05
1e+04
1e+03
1e+02
1e+01
1e+00
1e+00
1e+01
1e+02
p
Set 0
q=5.00
q=4.00
q=3.00
q=2.00
q=1.75
q=1.50
q=1.25
q=1.00
q=0.80
q=0.60
q=0.40
q=0.20

Figure VI.4.d

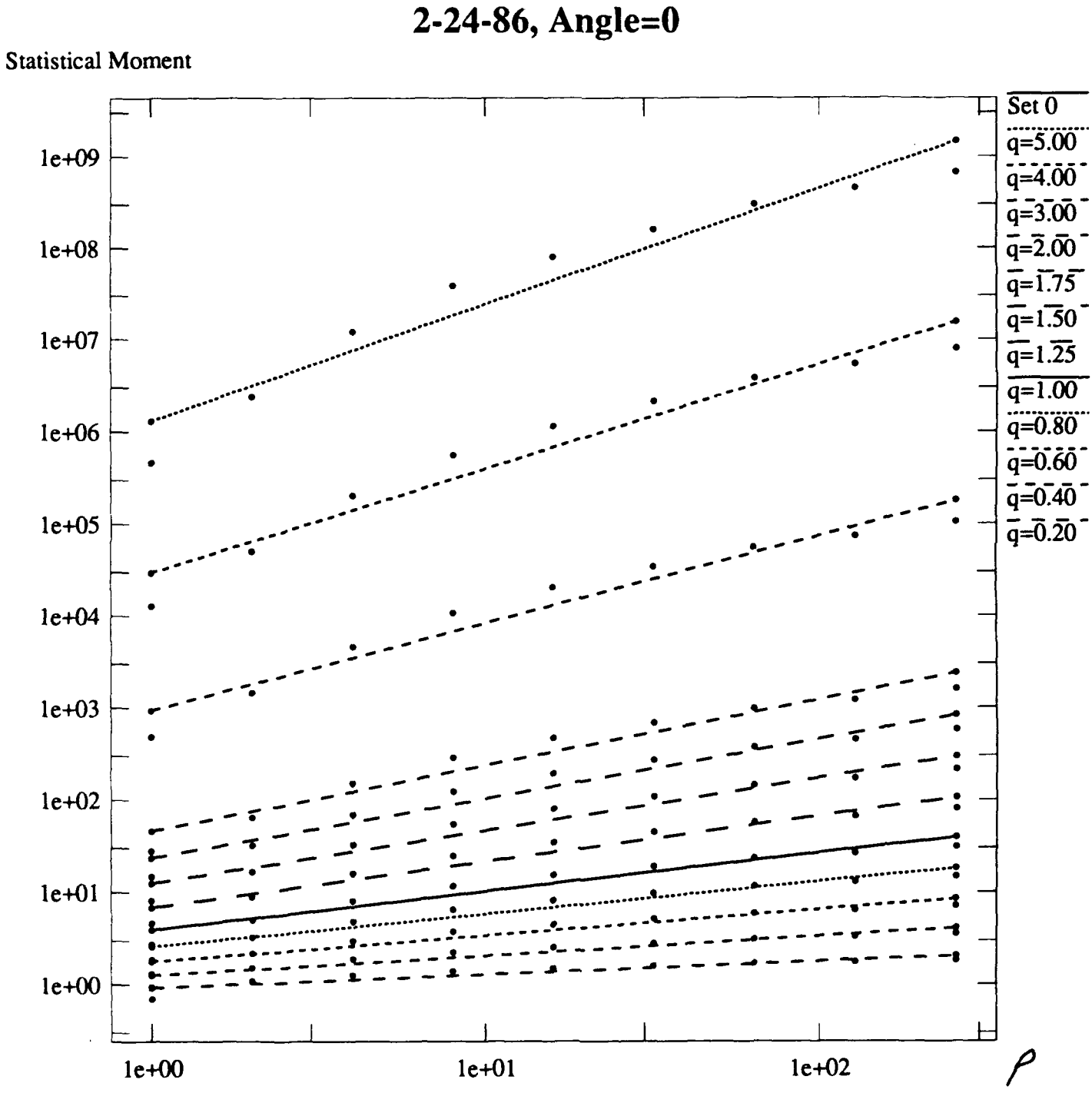
2-24-86, Angle=0
Statistical Moment
1e+09
1e+08
1e+07
1e+06
1e+05
1e+04
1e+03
1e+02
1e+01
1e+00
1e+00
1e+01
1e+02
p
Set 0
q=5.00
q=4.00
q=3.00
q=2.00
q=1.75
q=1.50
q=1.25
q=1.00
q=0.80
q=0.60
q=0.40
q=0.20

Figure VI.5.a

2-24-86, Angle=45

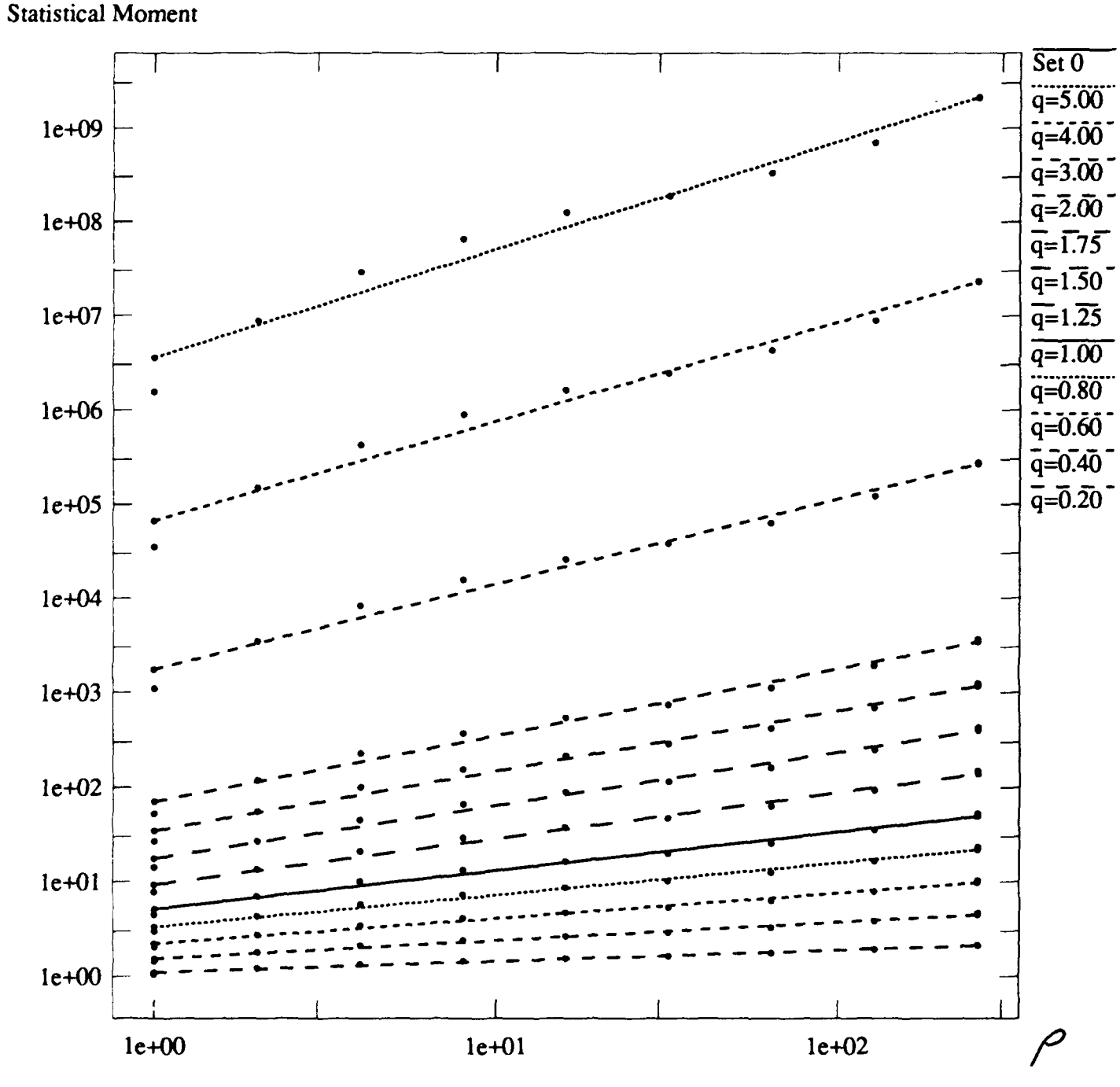

Figure VI.5.b

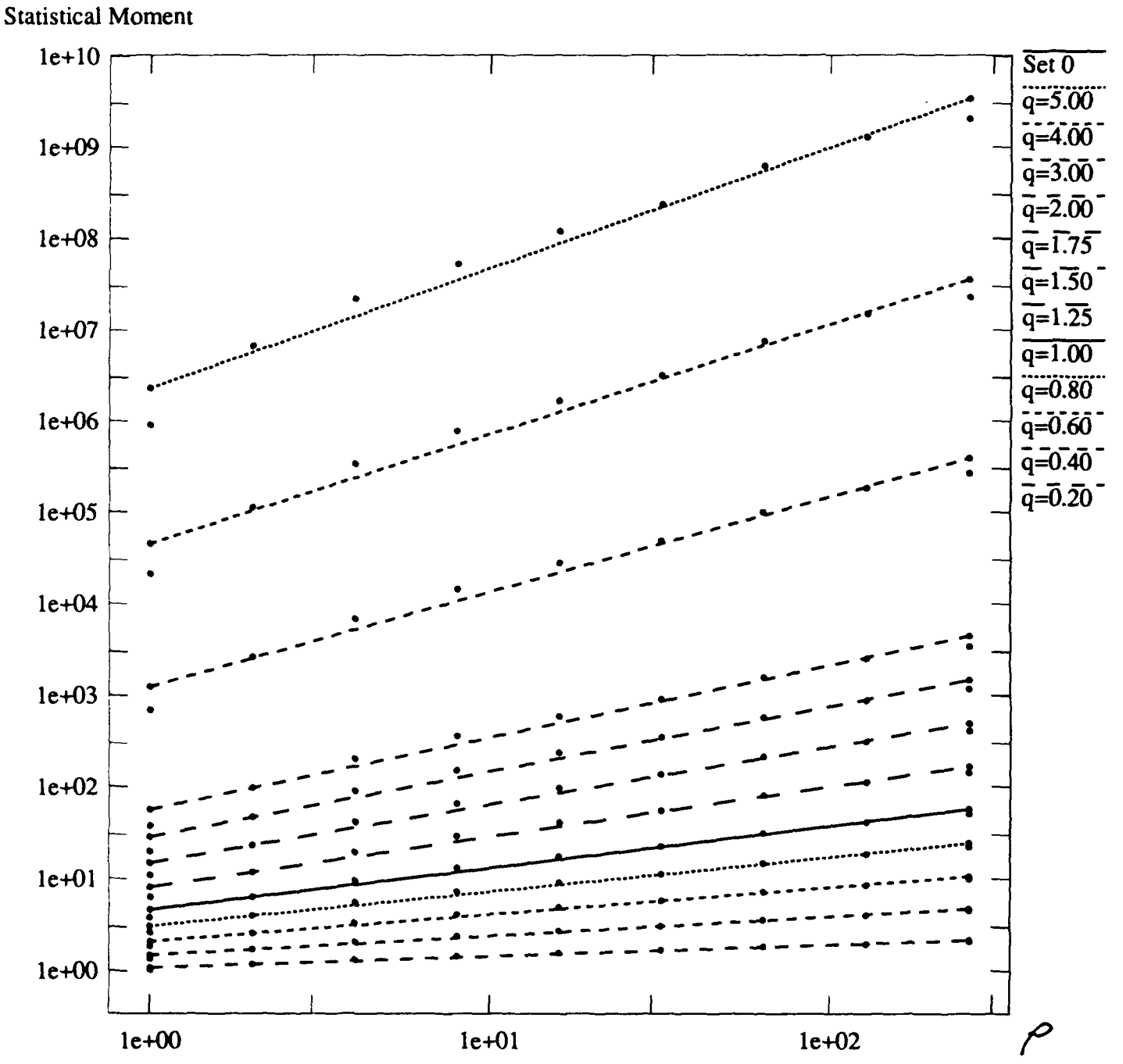
2-24-86, Angle=90
Statistical Moment
1e+10
1e+09
1e+08
1e+07
1e+06
1e+05
1e+04
1e+03
1e+02
1e+01
1e+00
1e+00
1e+01
1e+02
p
Set 0
q=5.00
q=4.00
q=3.00
q=2.00
q=1.75
q=1.50
q=1.25
q=1.00
q=0.80
q=0.60
q=0.40
q=0.20

igure V1.5.c

2-24-86, Angle=135

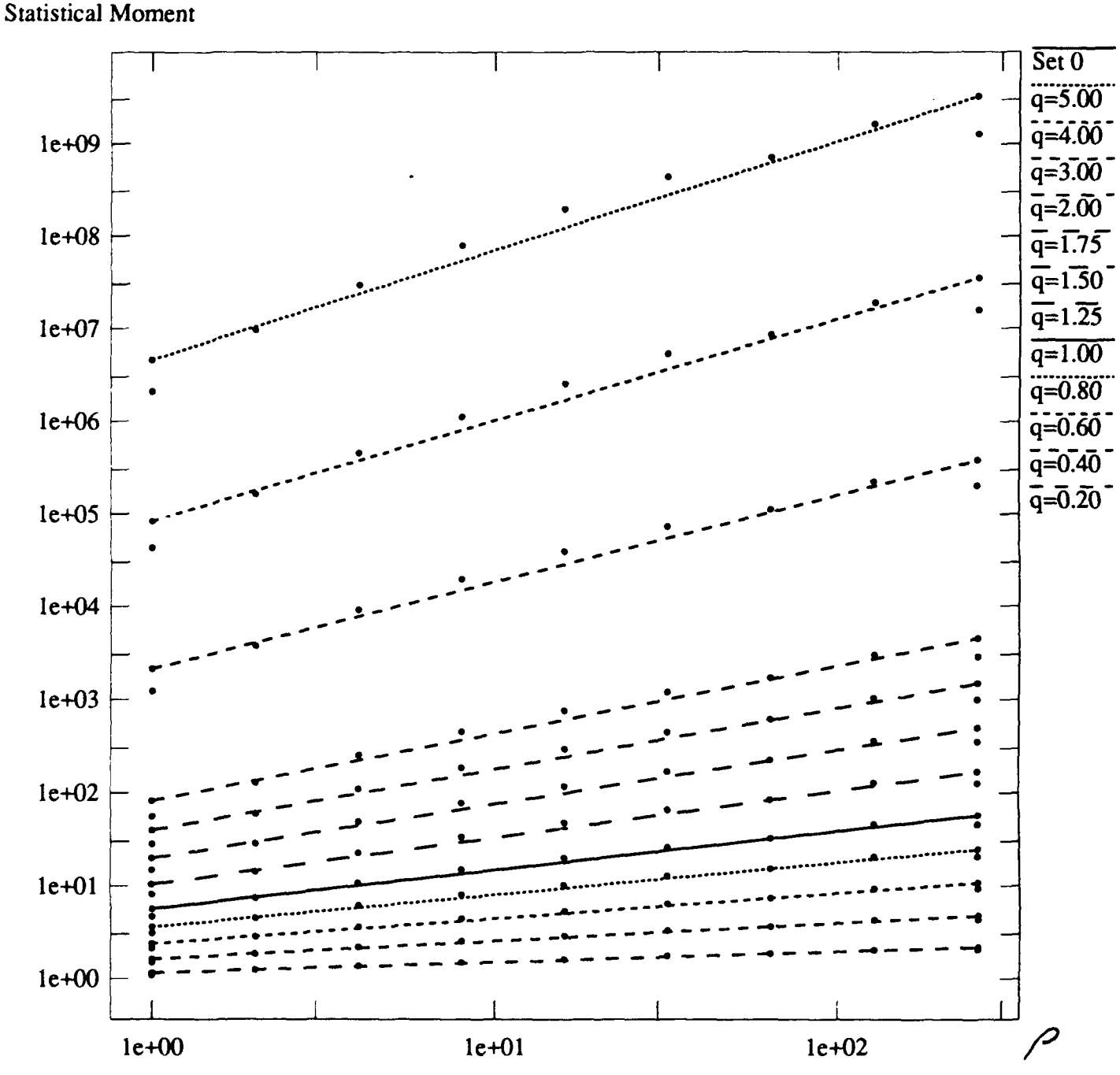

Figure VI.5.d

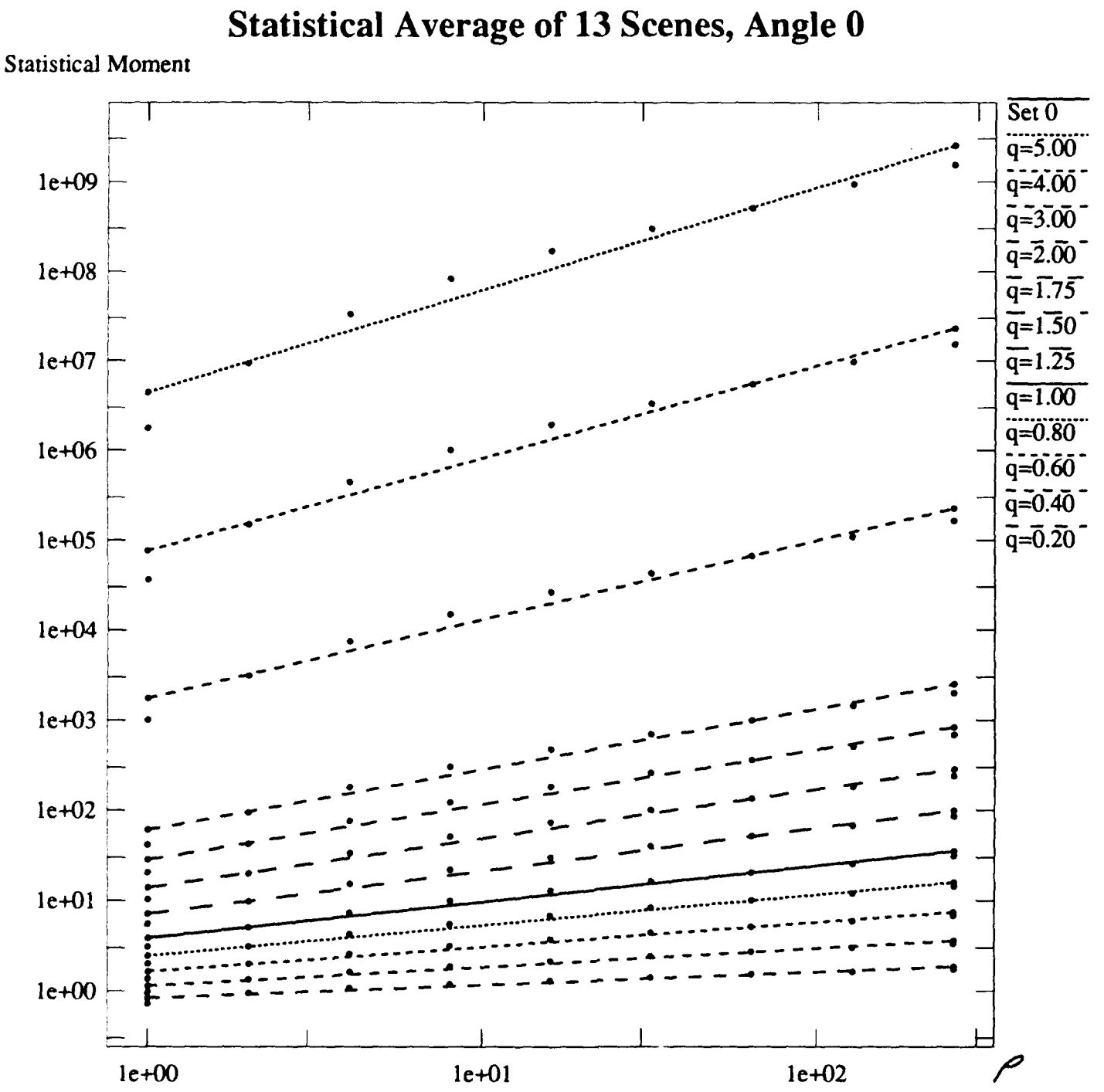
Statistical Average of 13 Scenes, Angle 0
Statistical Moment
1e+09
1e+08
1e+07
1e+06
1e+05
1e+04
1e+03
1e+02
1e+01
1e+00
1e+00
1e+01
1e+02
p
Set 0
q=5.00
q=4.00
q=3.00
q=2.00
q=1.75
q=1.50
q=1.25
q=1.00
q=0.80
q=0.60
q=0.40
q=0.20

Figure VI.6.a

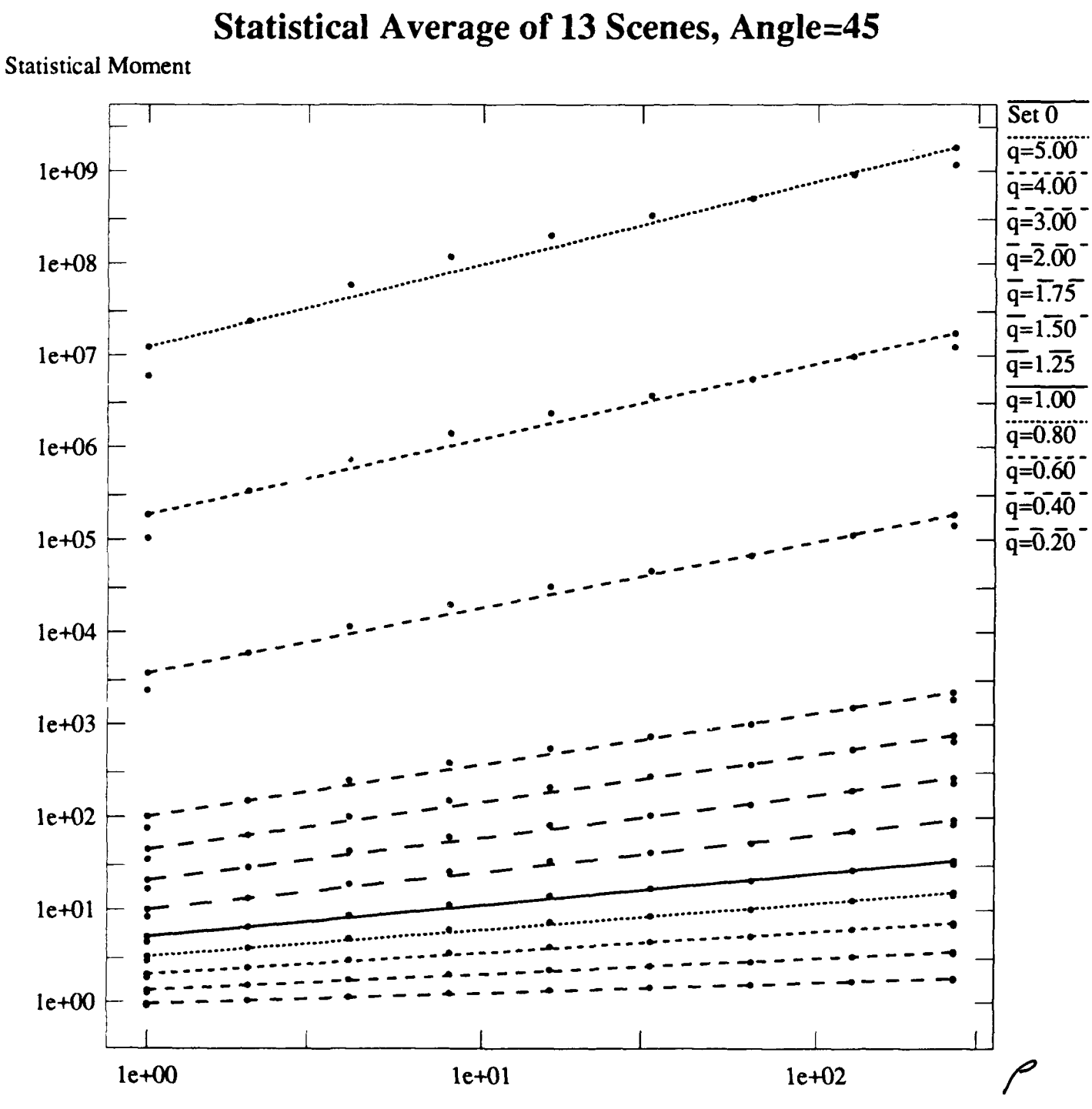
Statistical Average of 13 Scenes, Angle=45
Statistical Moment
1e+09
1e+08
1e+07
1e+06
1e+05
1e+04
1e+03
1e+02
1e+01
1e+00
1e+00
1e+01
1e+02
ρ
Set 0
q=5.00
q=4.00
q=3.00
q=2.00
q=1.75
q=1.50
q=1.25
q=1.00
q=0.80
q=0.60
q=0.40
q=0.20

gure VI.6.b

Statistical Average of 13 Scenes, Angle=90

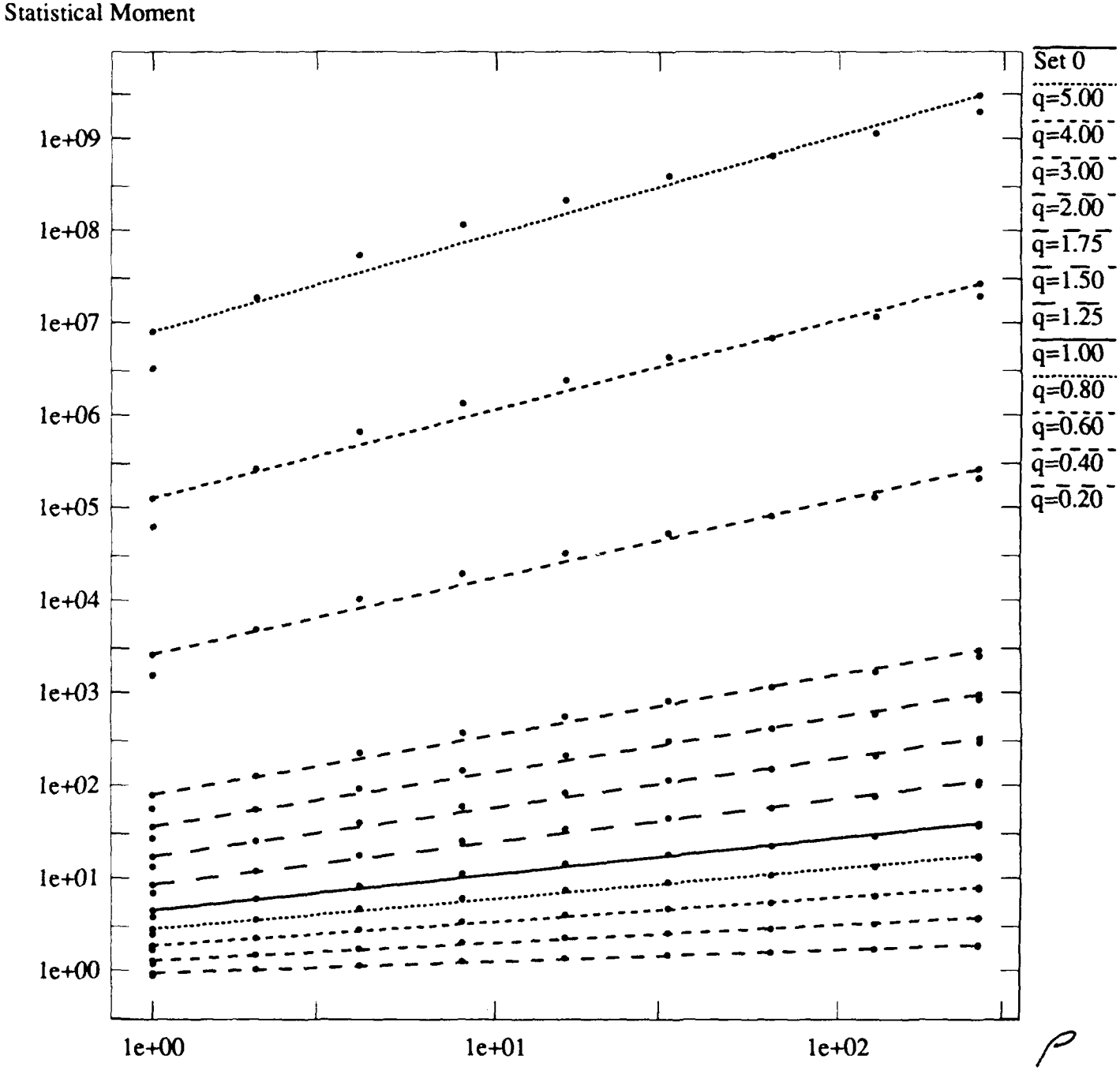

igure VI.6.e

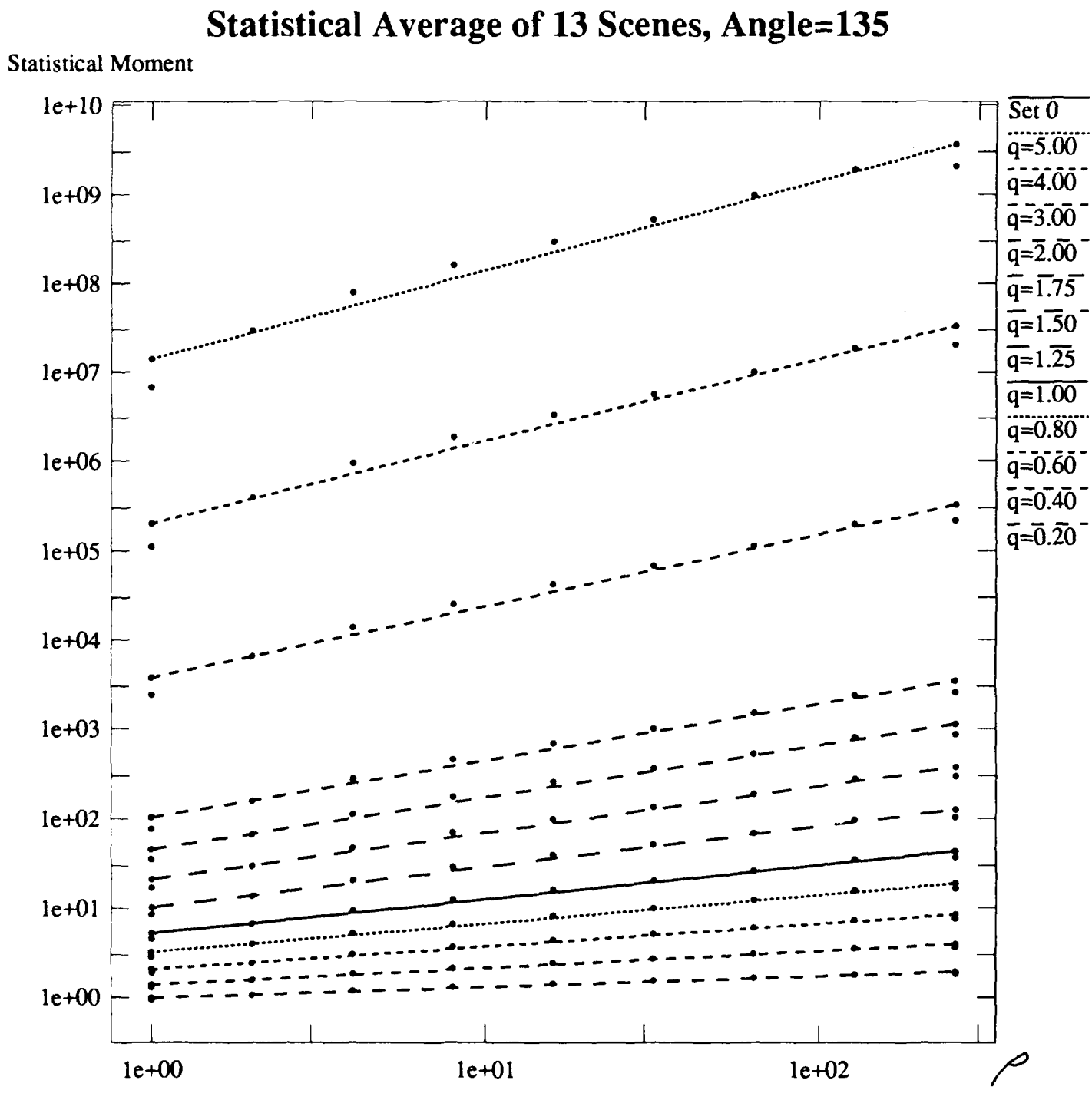
Statistical Average of 13 Scenes, Angle=135
Statistical Moment
1e+10
1e+09
1e+08
1e+07
1e+06
1e+05
1e+04
1e+03
1e+02
1e+01
1e+00
1e+00
1e+01
1e+02
ρ
Set 0
q=5.00
q=4.00
q=3.00
q=2.00
q=1.75
q=1.50
q=1.25
q=1.00
q=0.80
q=0.60
q=0.40
q=0.20

igure VI.6.d

2-14-86

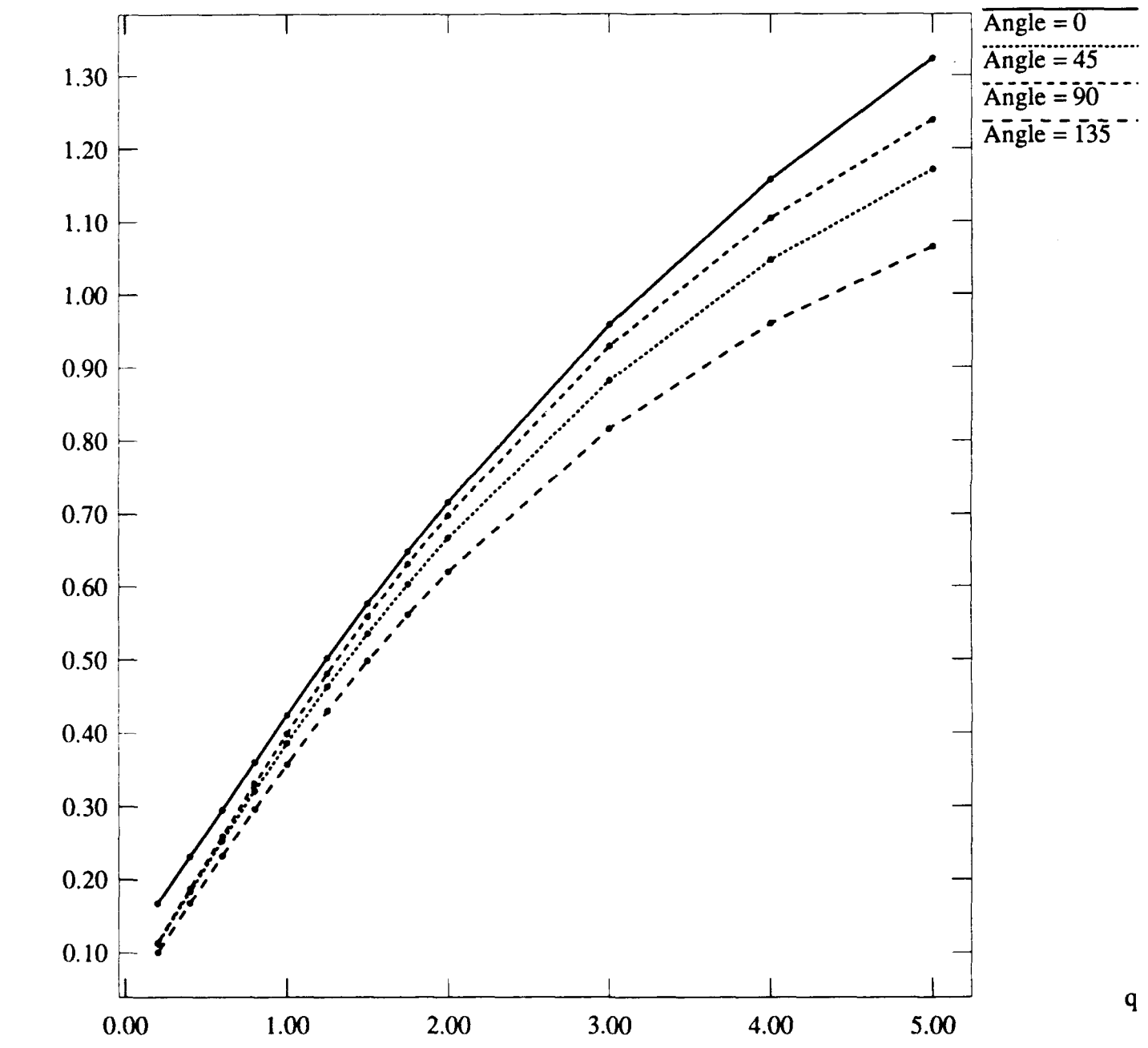

Figure VI.7

2-24-86

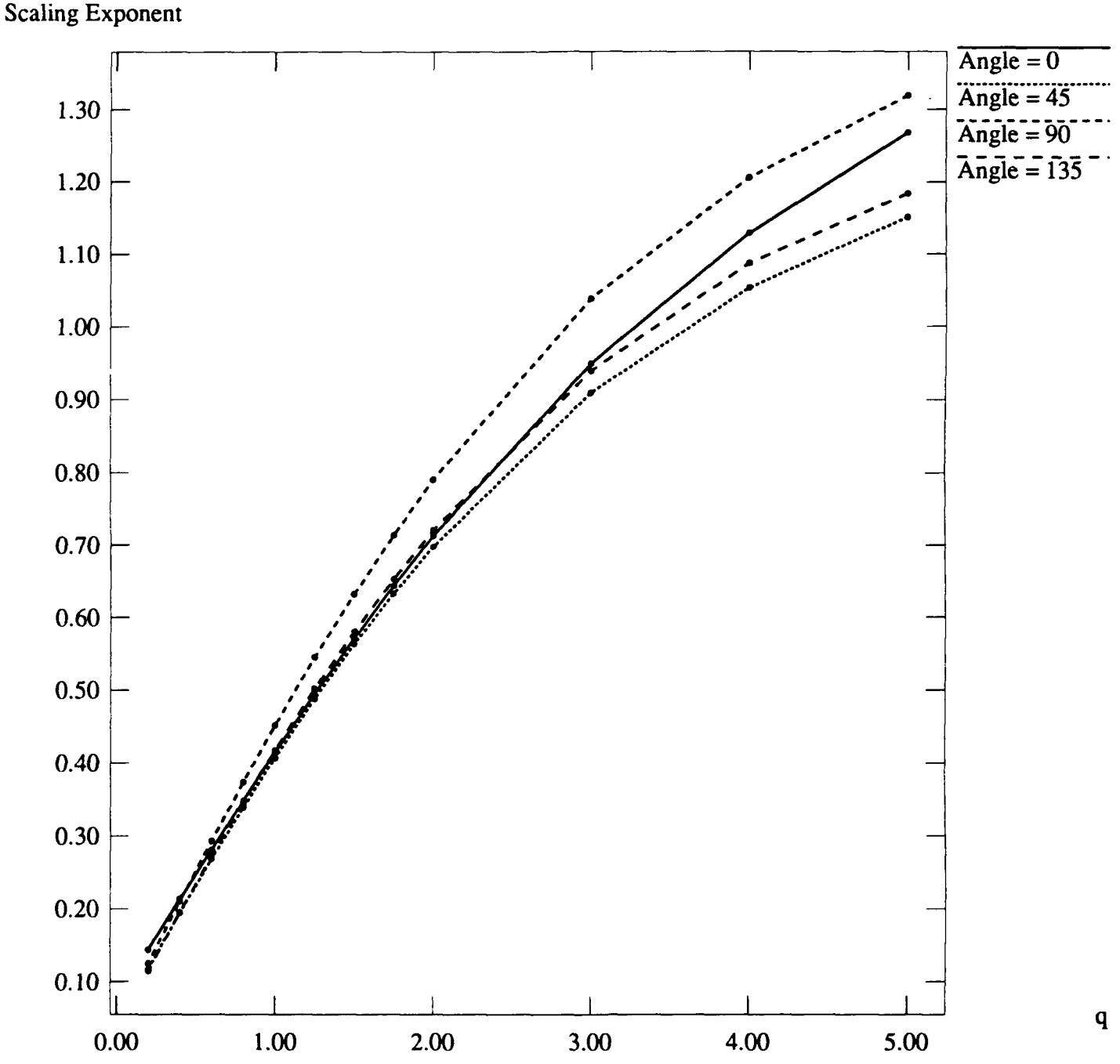

Figure V1.8

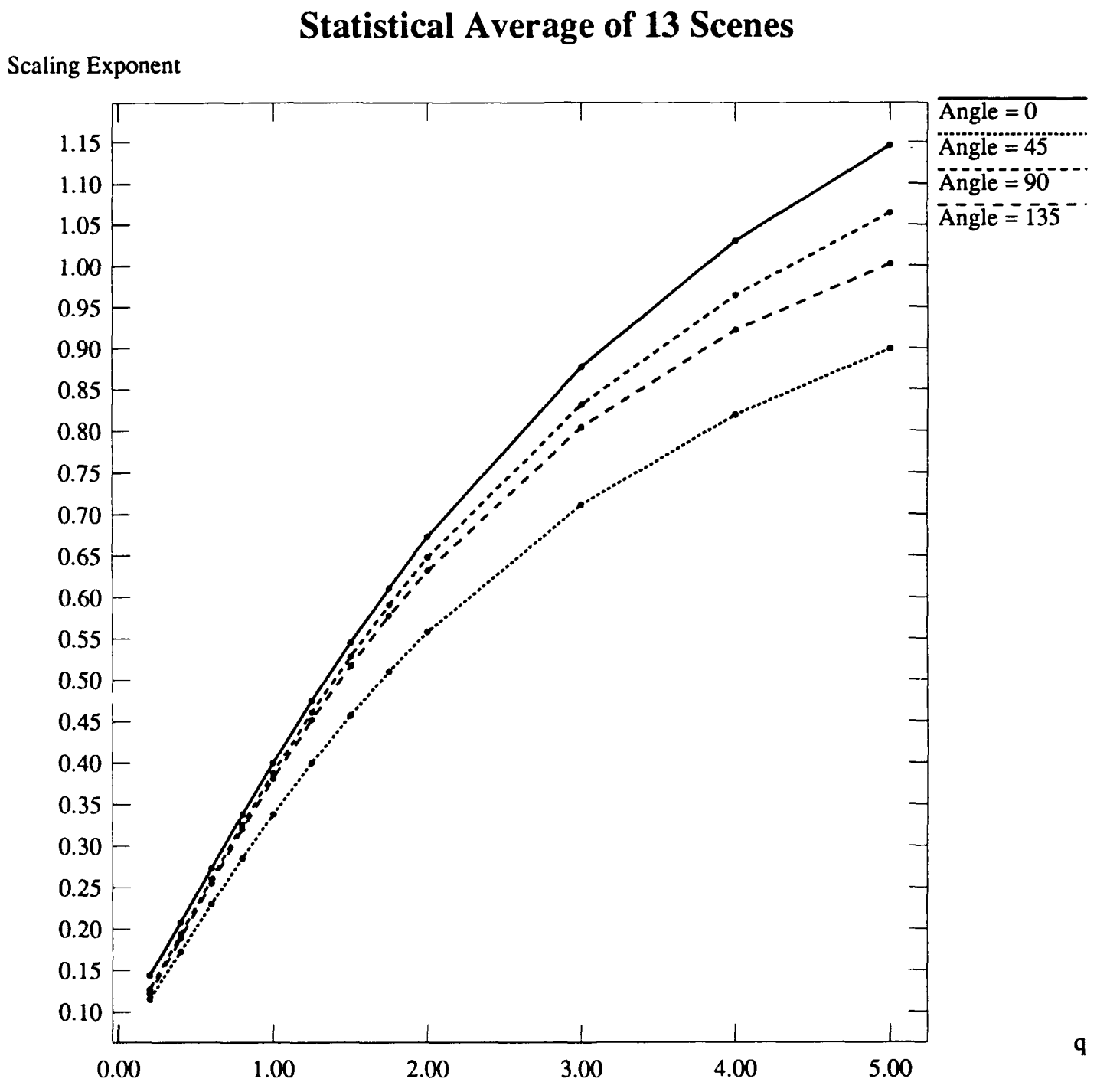
Statistical Average of 13 Scenes
Scaling Exponent
1.15
1.10
1.05
1.00
0.95
0.90
0.85
0.80
0.75
0.70
0.65
0.60
0.55
0.50
0.45
0.40
0.35
0.30
0.25
0.20
0.15
0.10
0.00
1.00
2.00
3.00
4.00
5.00
q
Angle = 0
Angle = 45
Angle = 90
Angle = 135

Figure V1.9

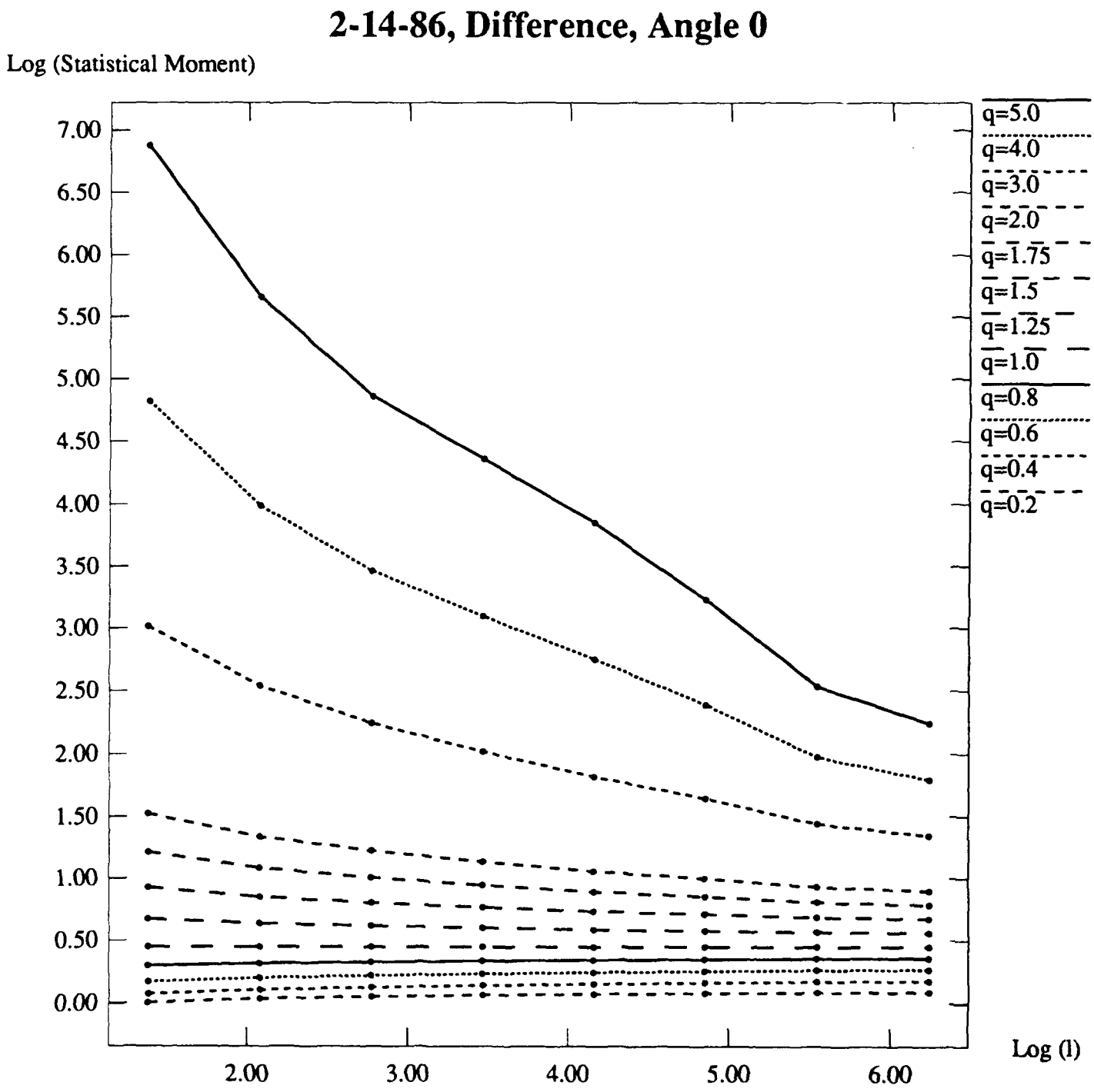

Figure V1.10.a

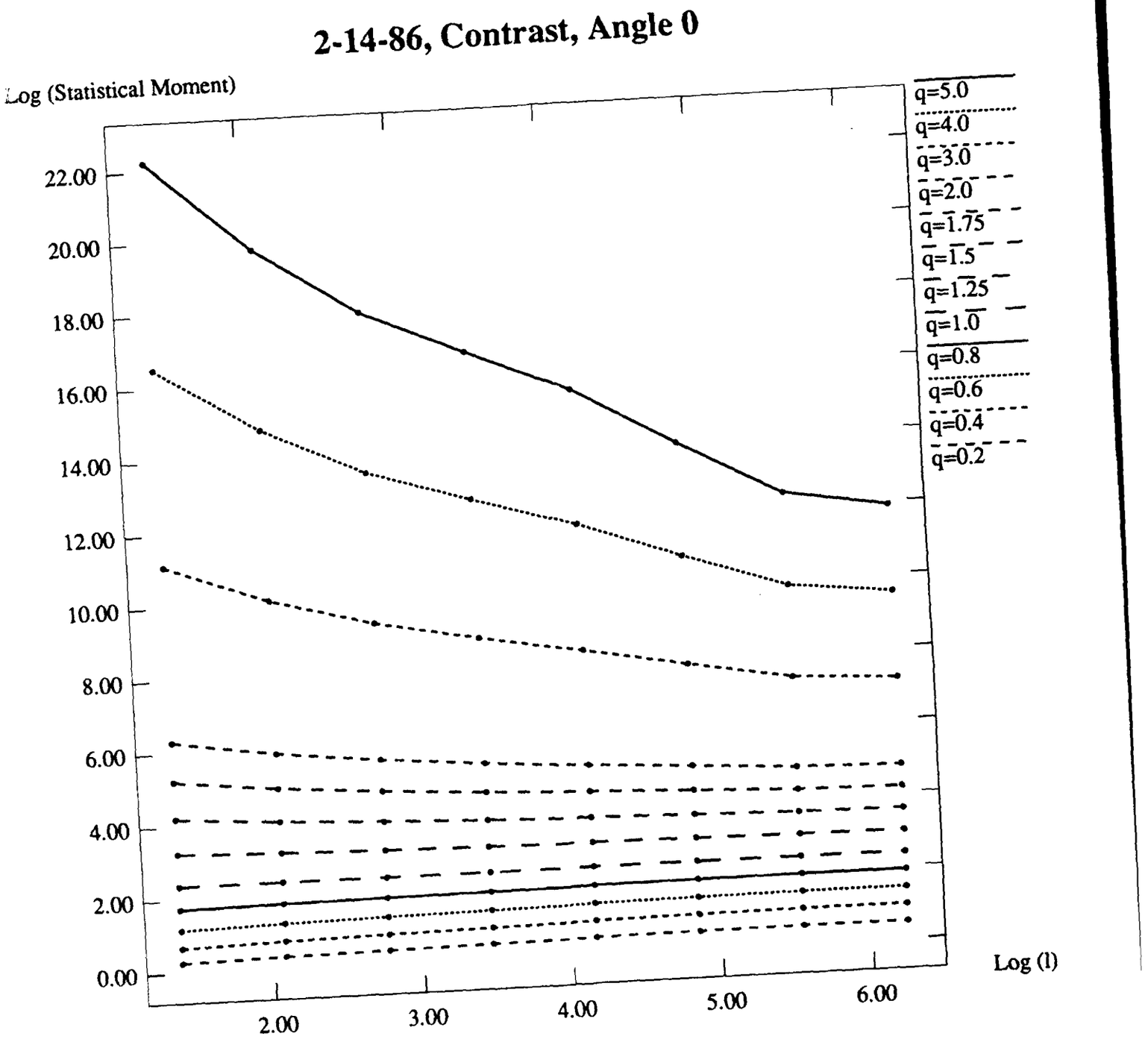

Figure VI.10.b

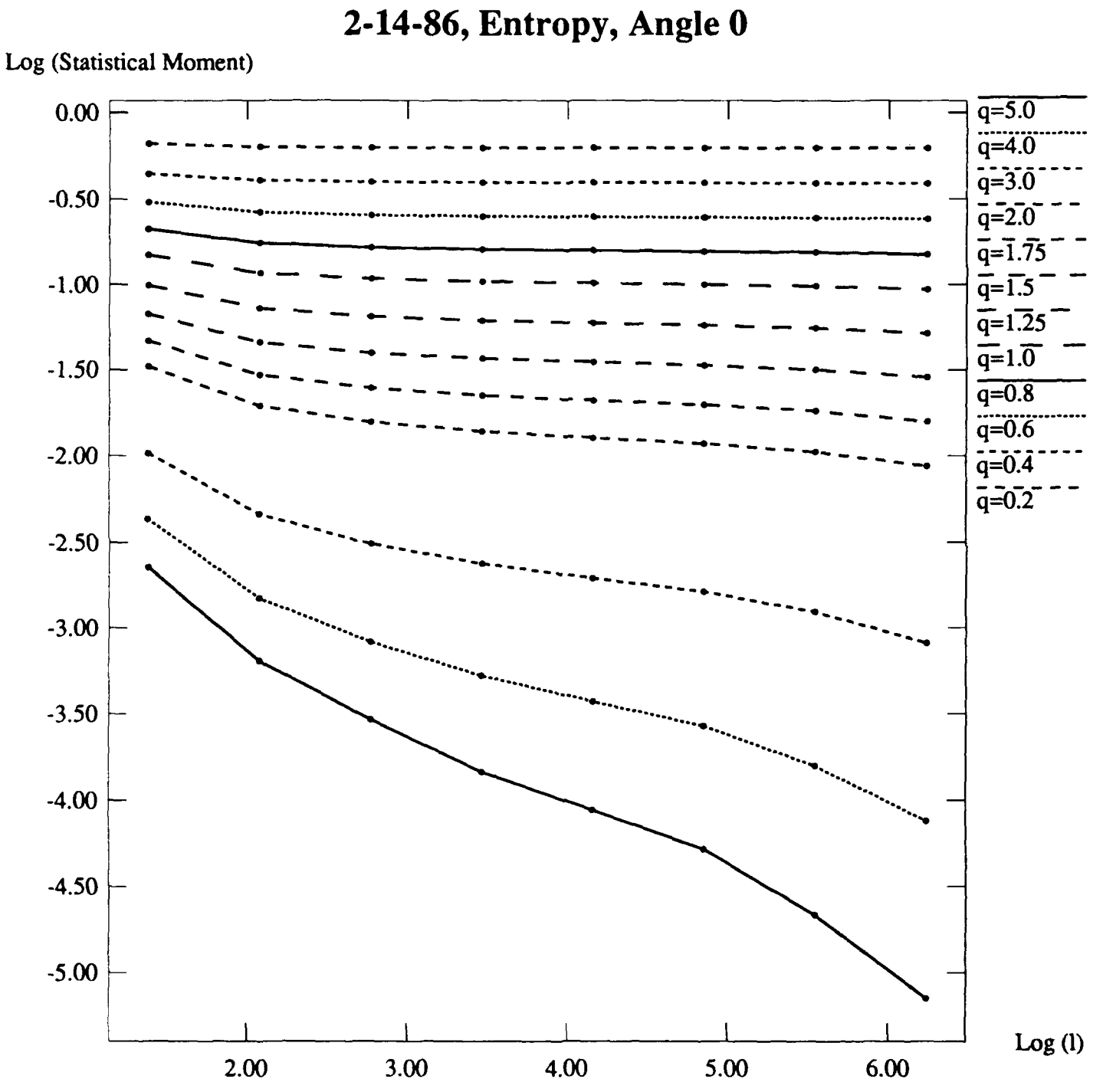

Figure VI.10.c

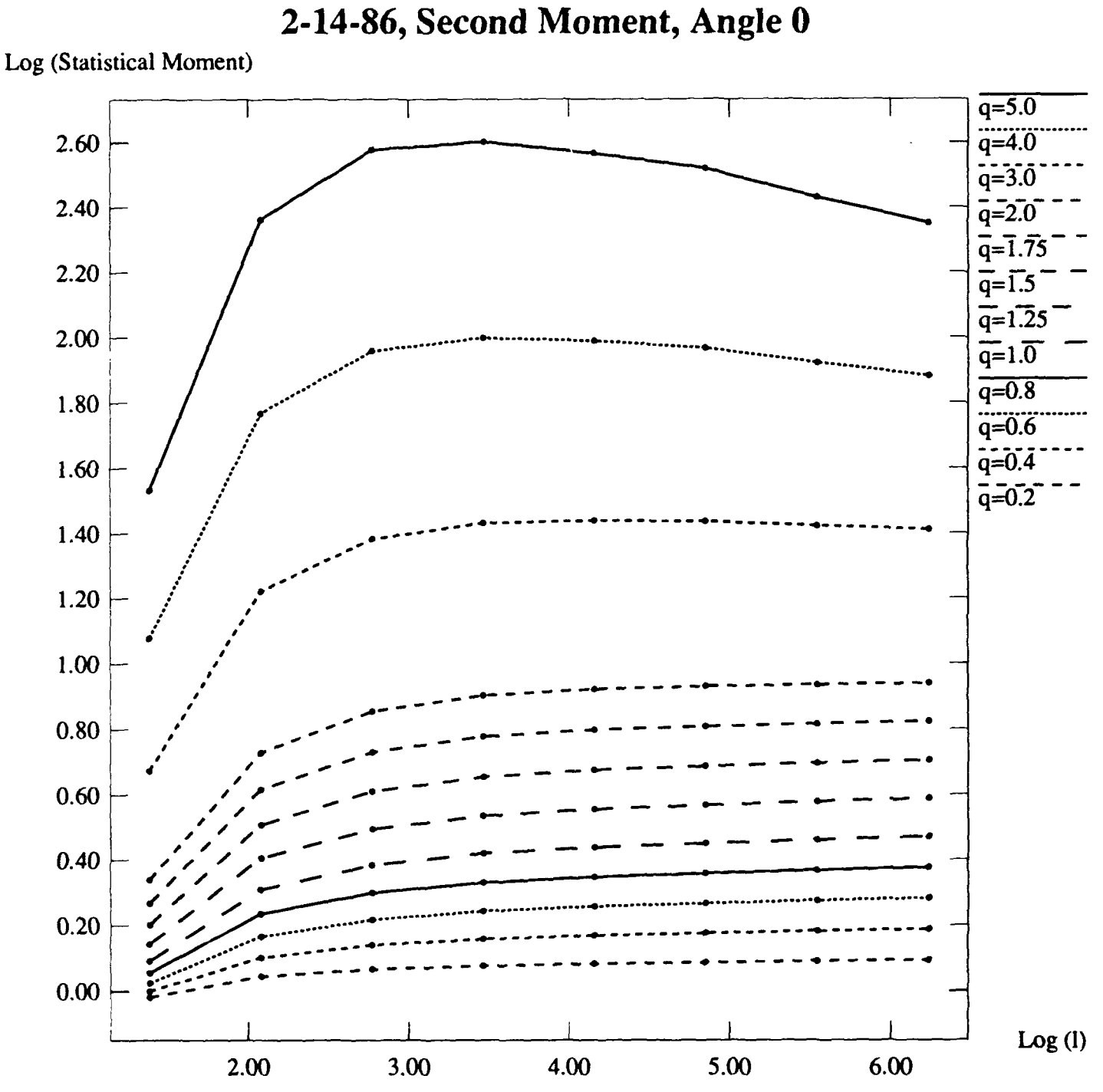

Figure VI.10.d

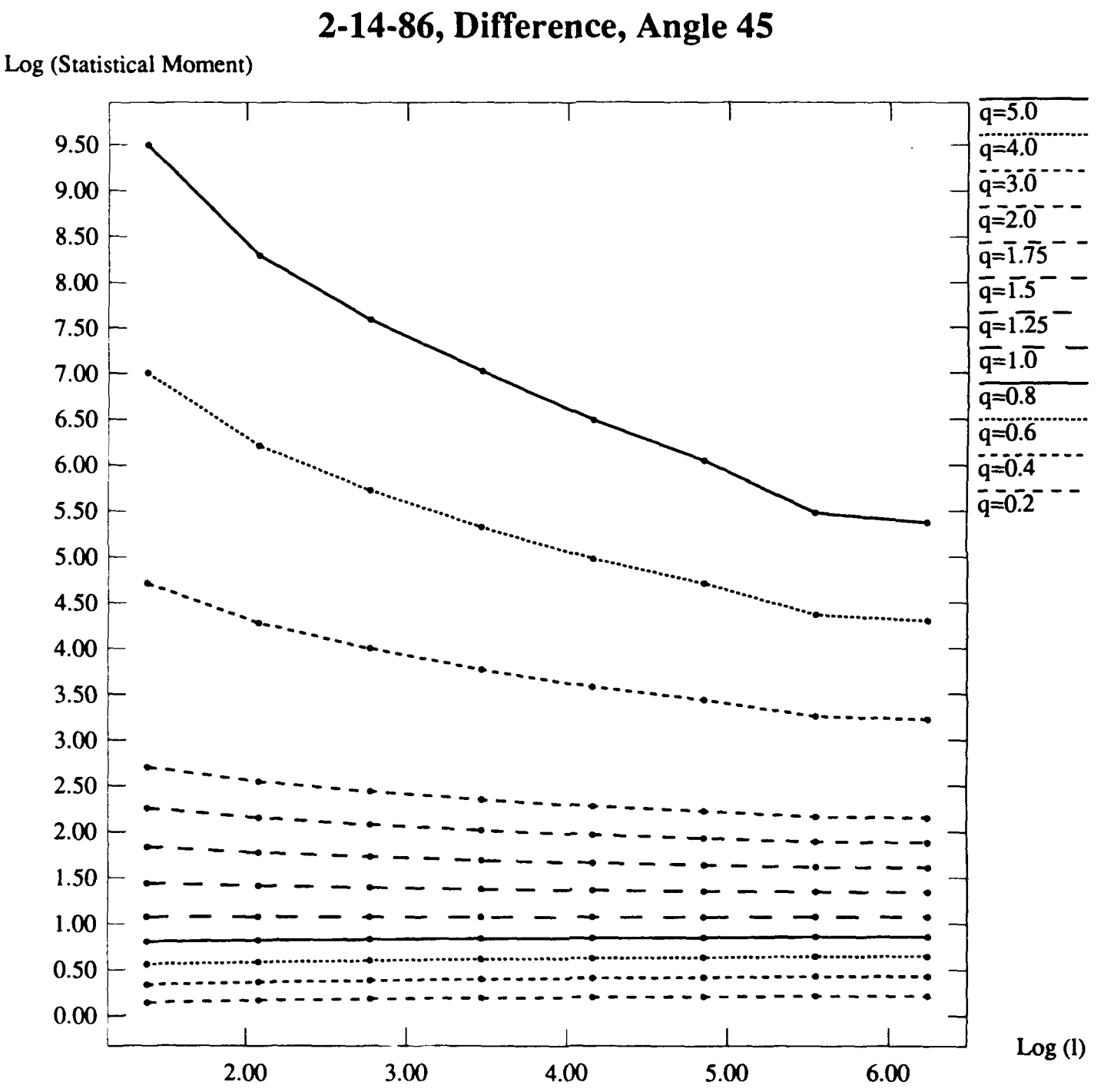

Figure VI.11.a

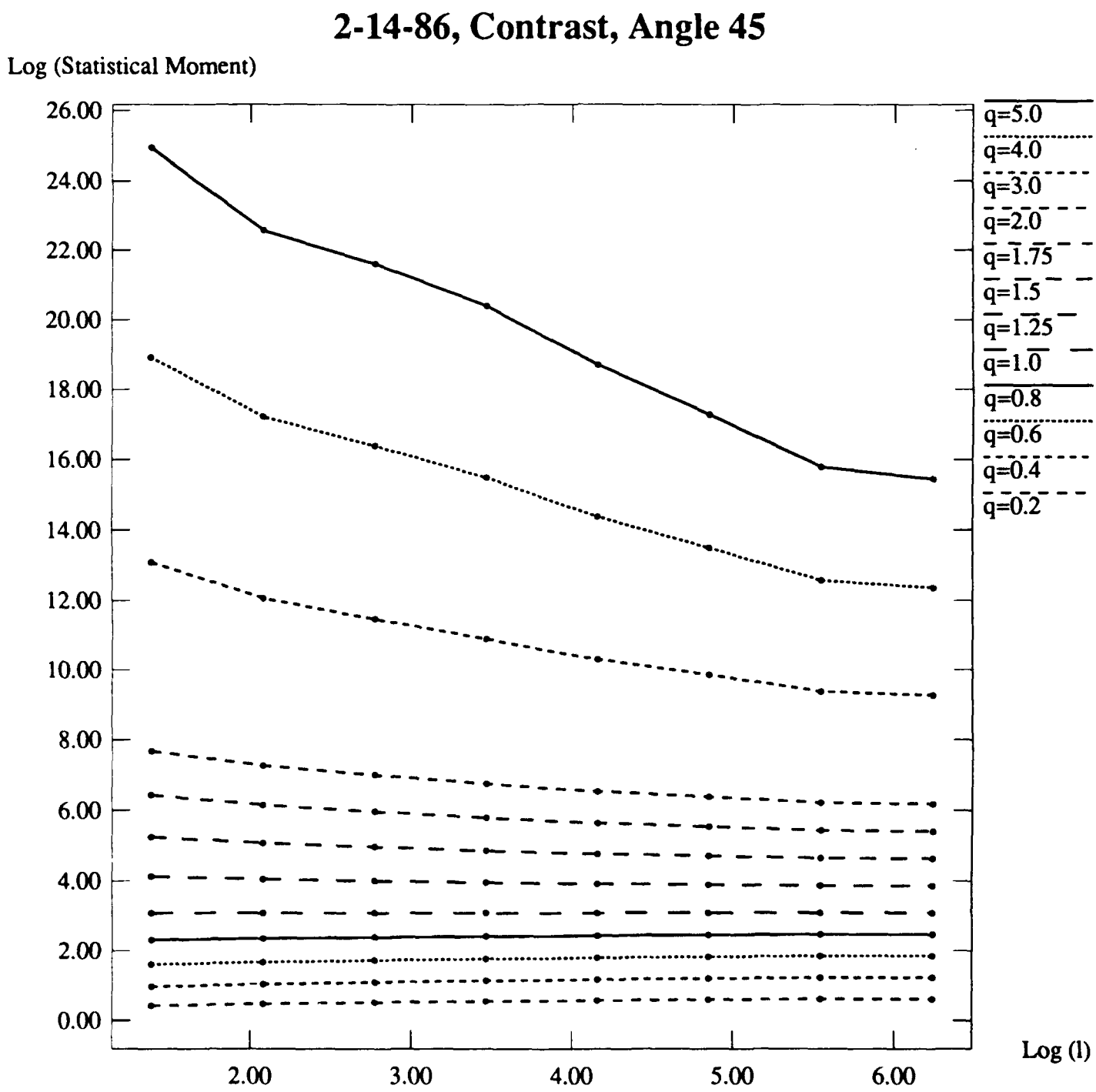

Figure VI.11.b

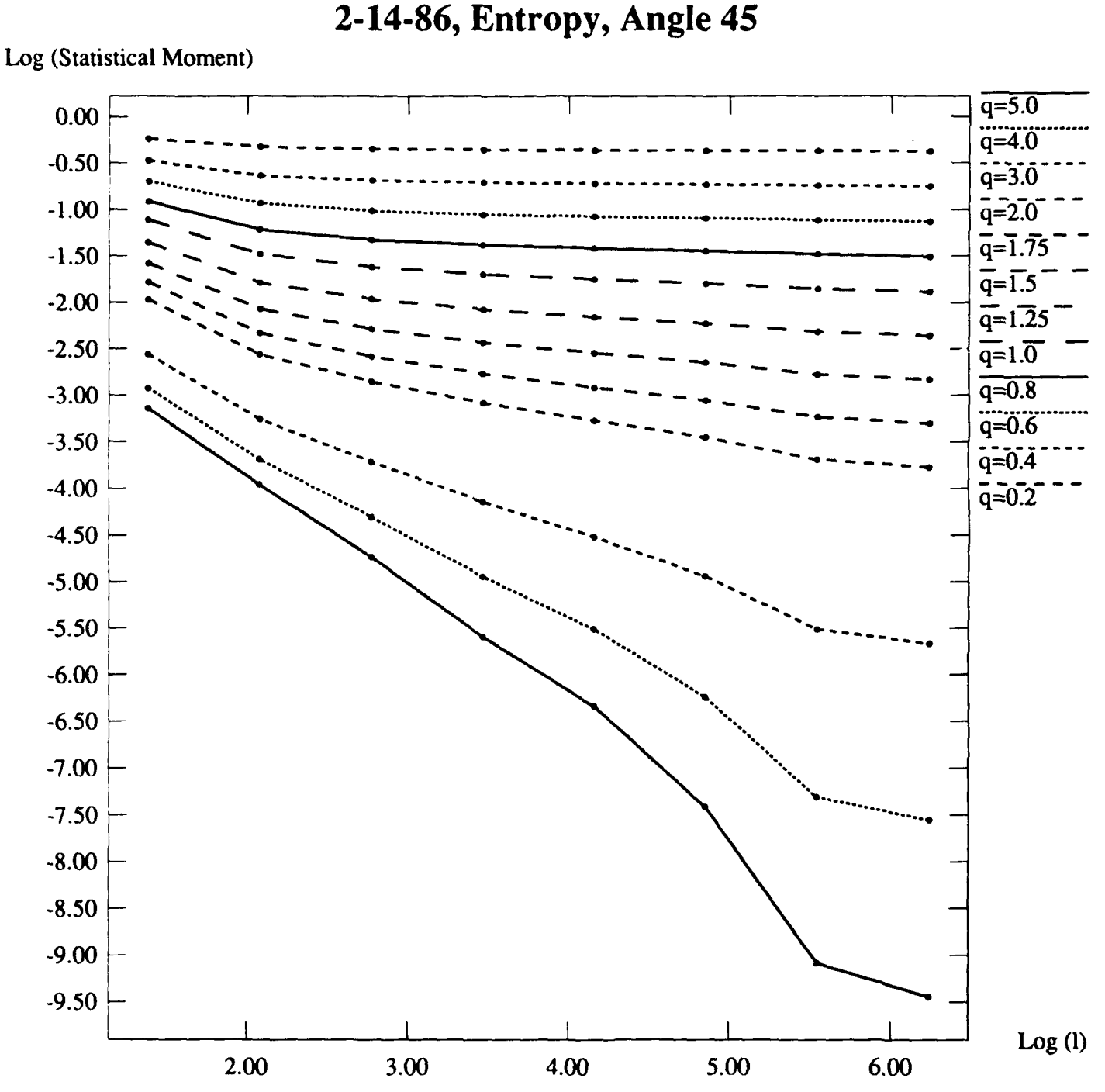

Figure VI.11.c

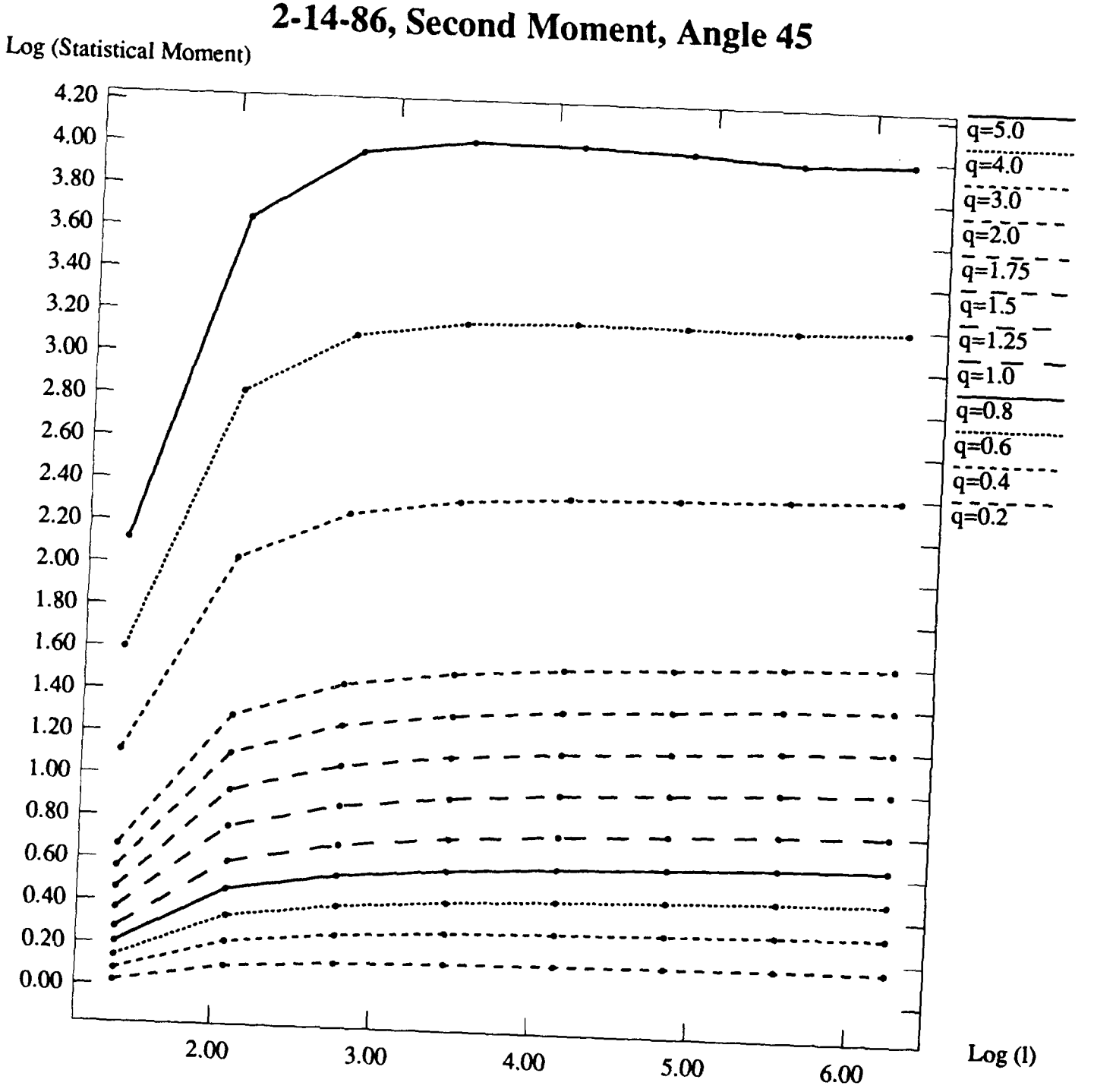

Figure VI.11.d

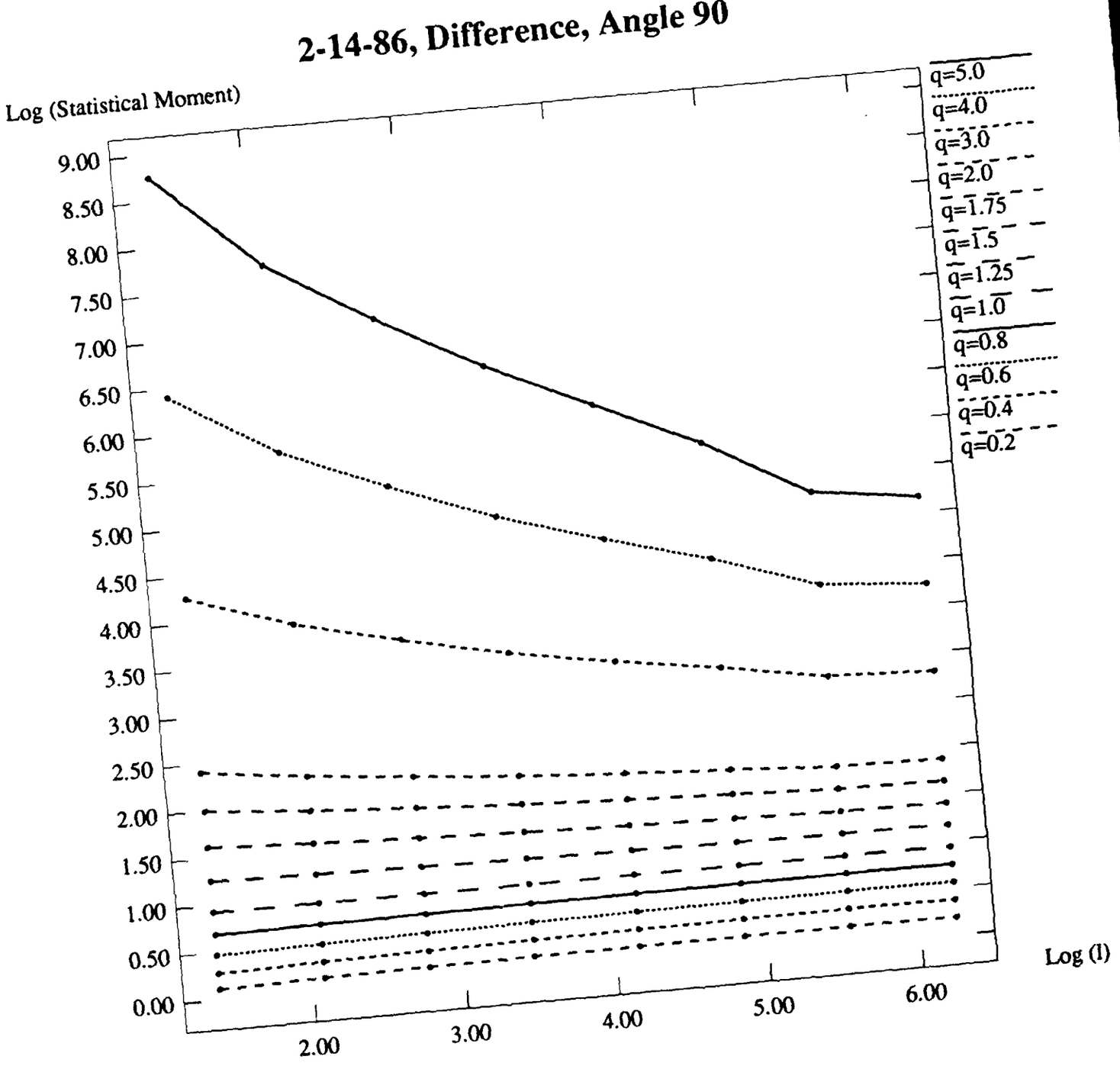

Figure V1.12.a

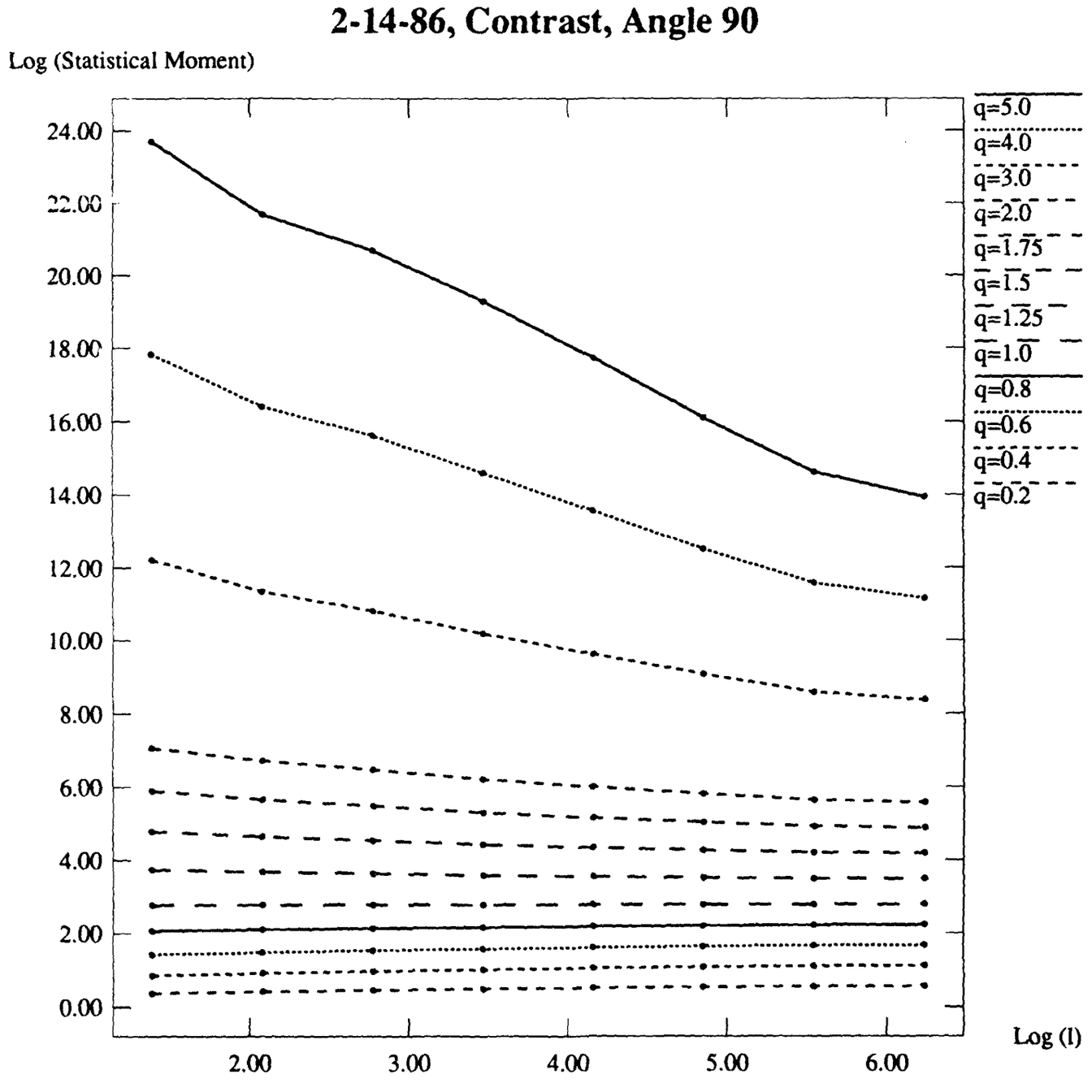

Figure VI.12.b

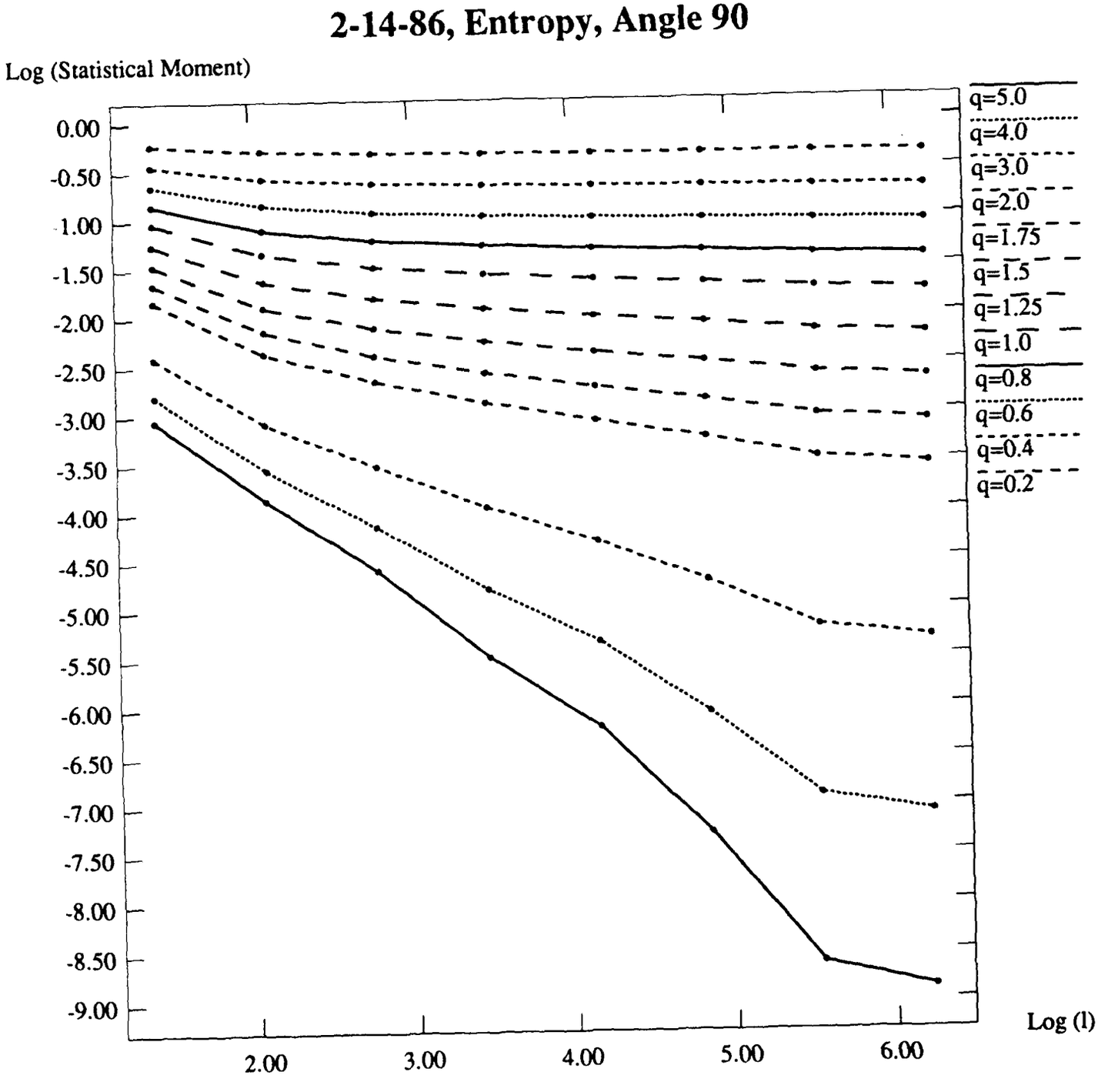

Figure VI.12.c

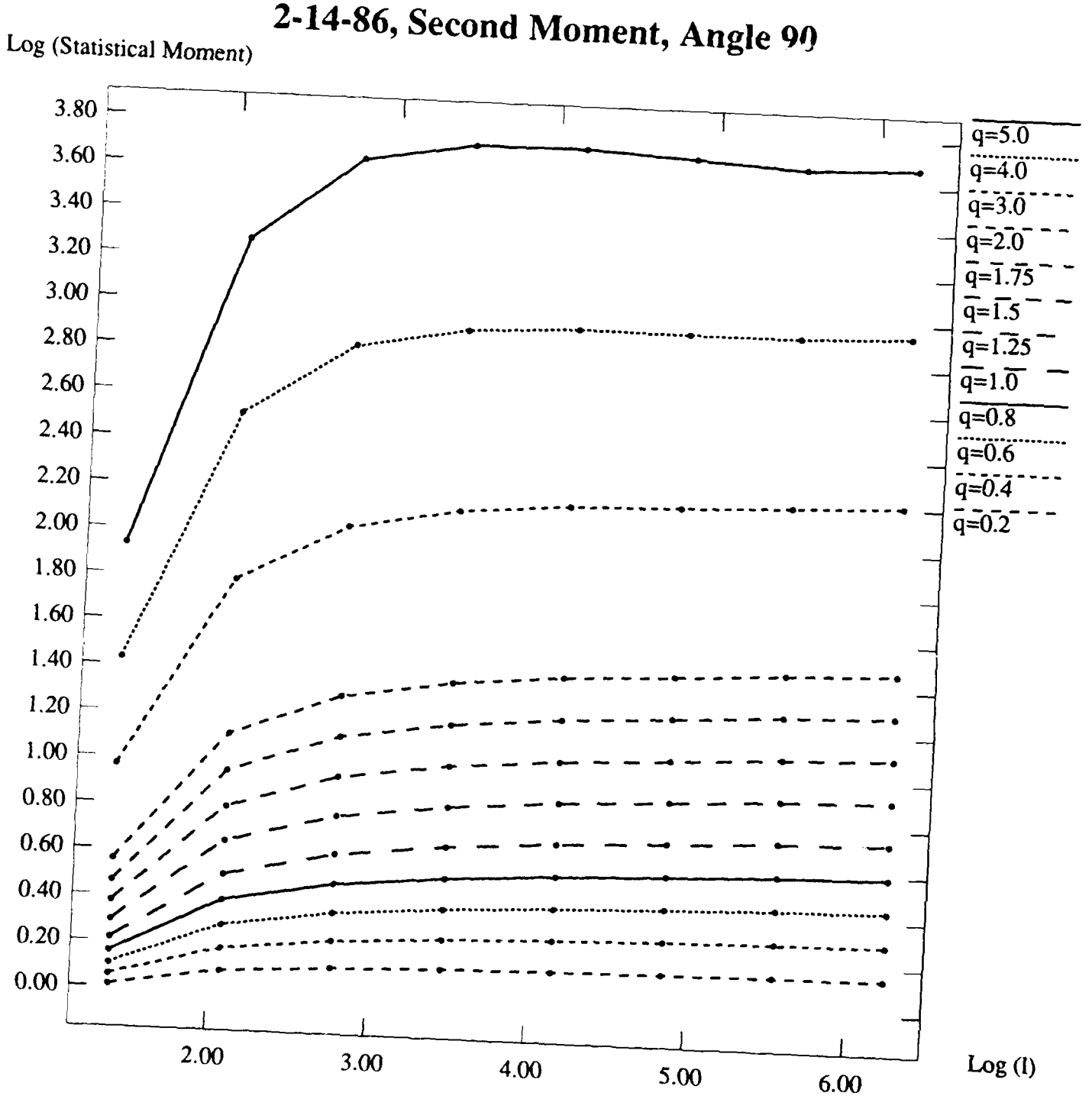
2-14-86, Second Moment, Angle 90
Log (Statistical Moment)
3.80
3.60
3.40
3.20
3.00
2.80
2.60
2.40
2.20
2.00
1.80
1.60
1.40
1.20
1.00
0.80
0.60
0.40
0.20
0.00
2.00
3.00
4.00
5.00
6.00
Log (l)
q=5.0
q=4.0
q=3.0
q=2.0
q=1.75
q=1.5
q=1.25
q=1.0
q=0.8
q=0.6
q=0.4
q=0.2

igure V1.12.d

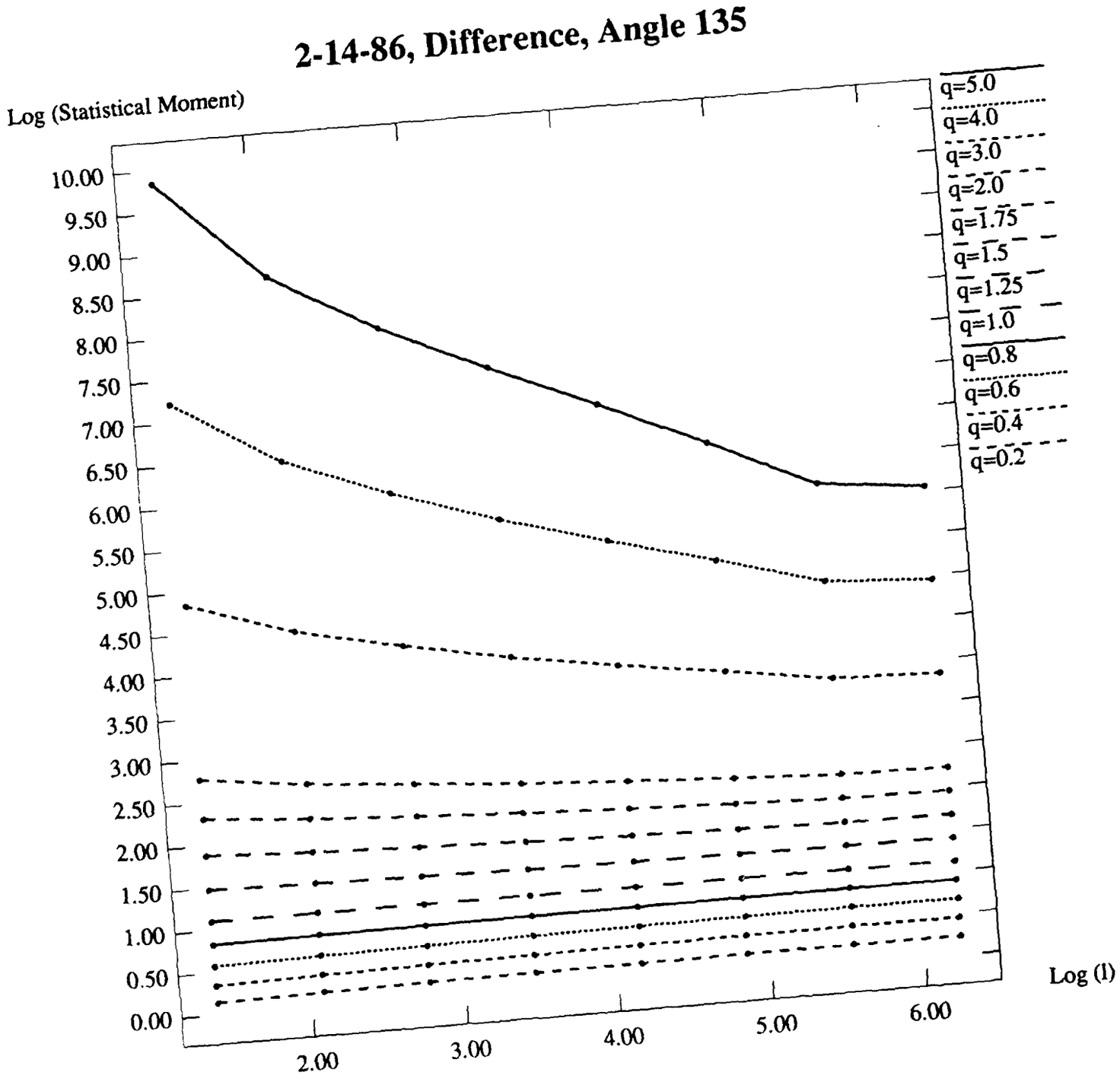

Figure V1.13.a

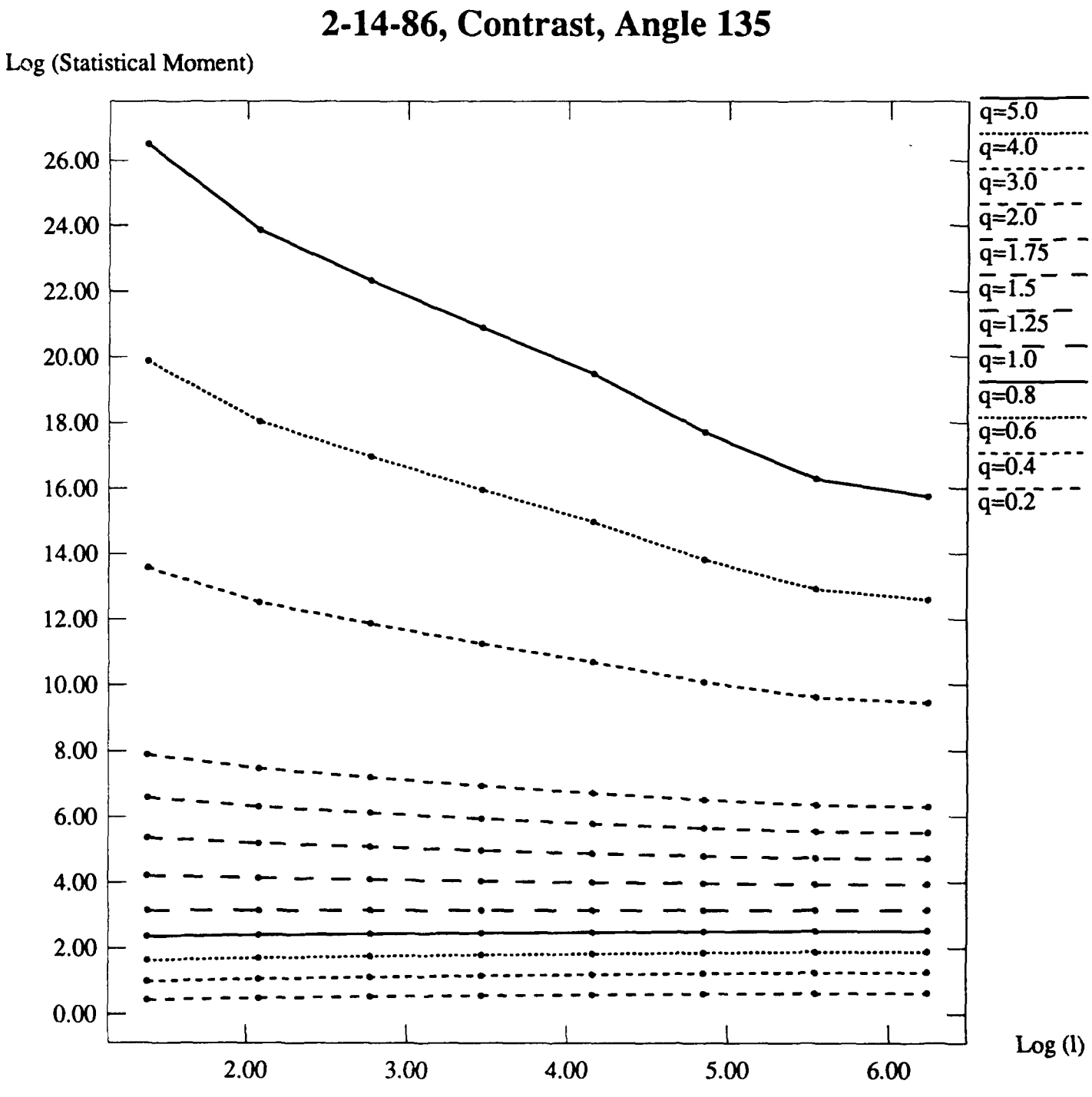

Figure VI.13.b

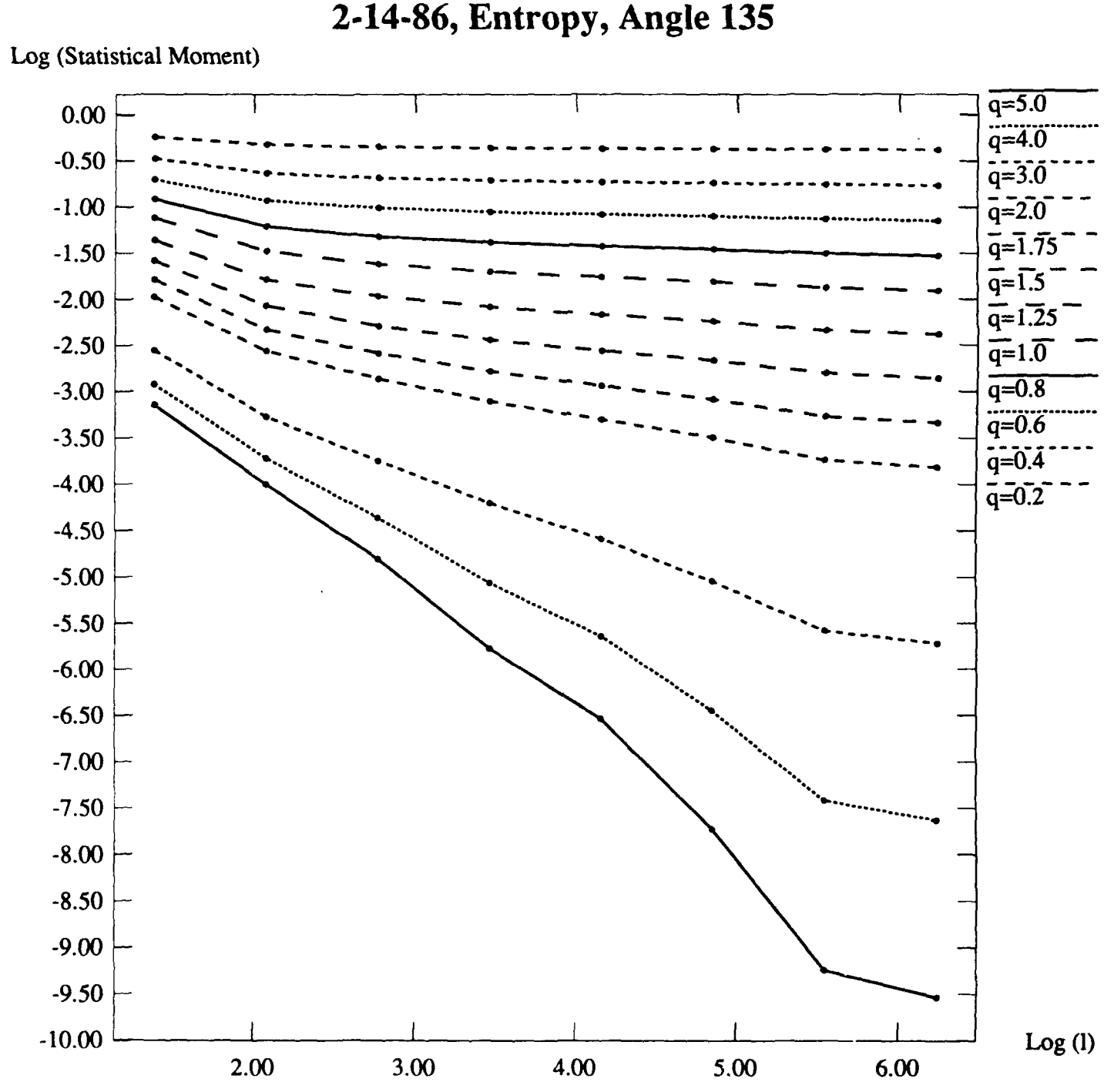

Figure VI.13.C

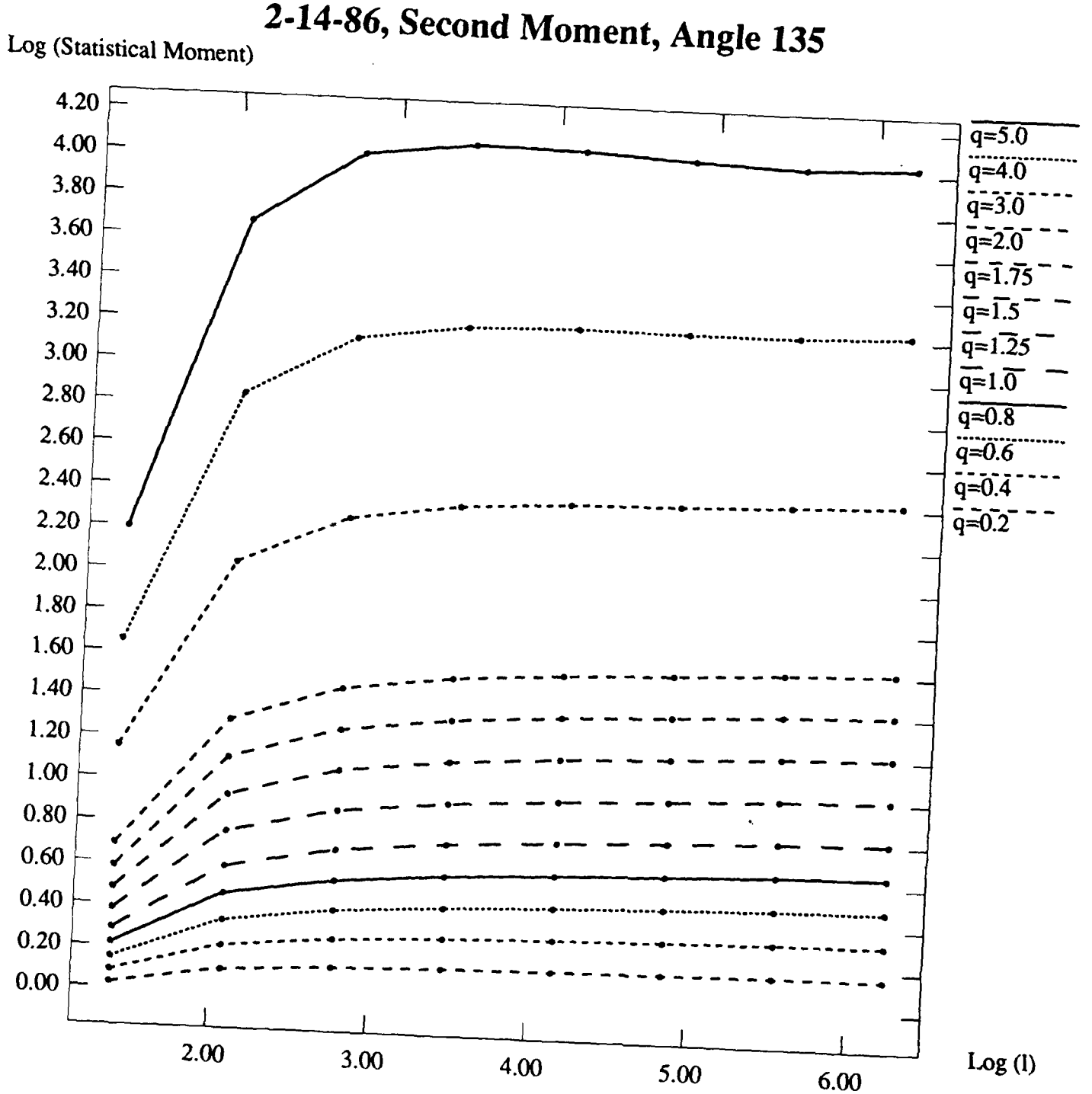

Figure VI.13.d

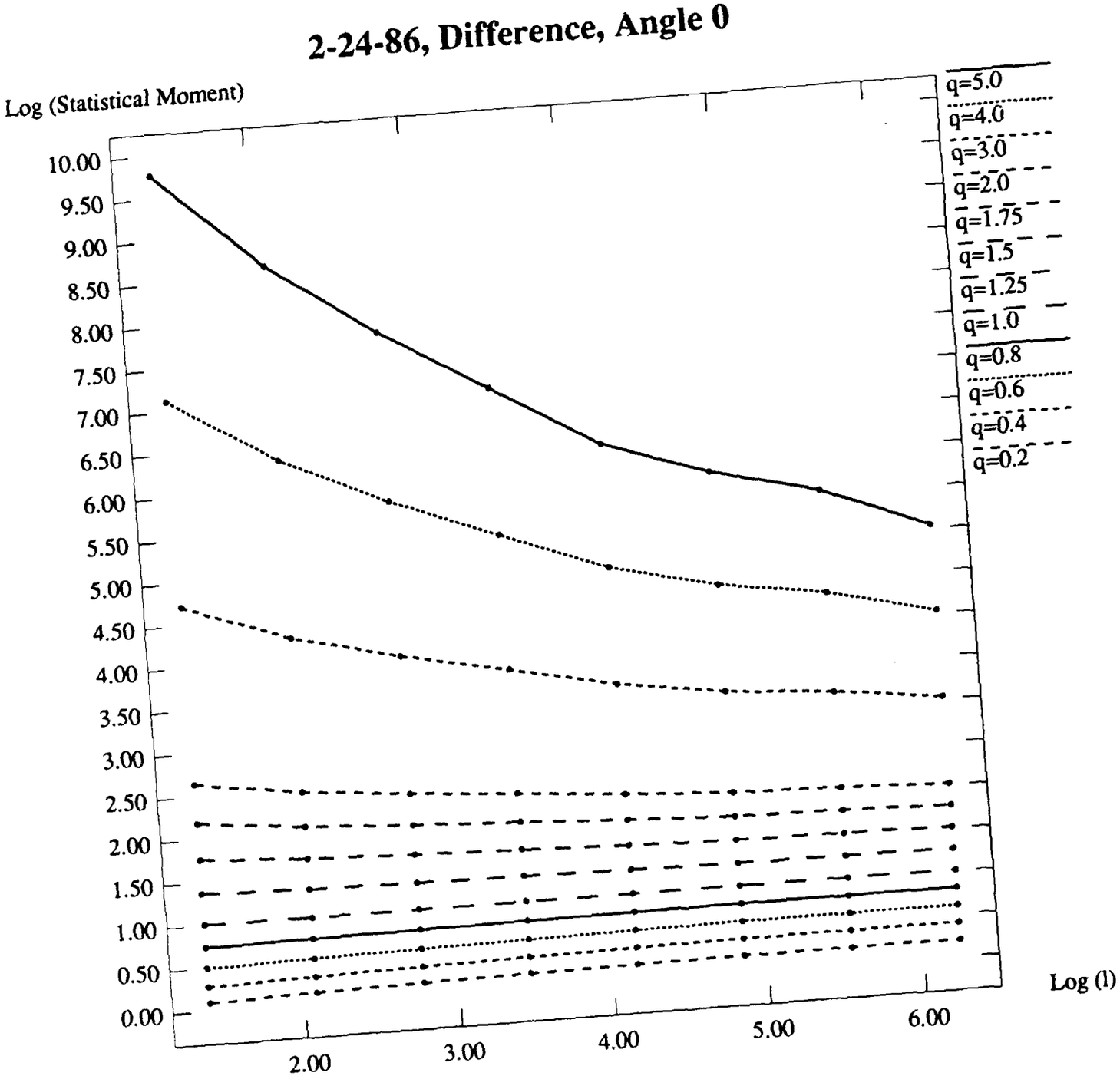

Figure VI.14.a

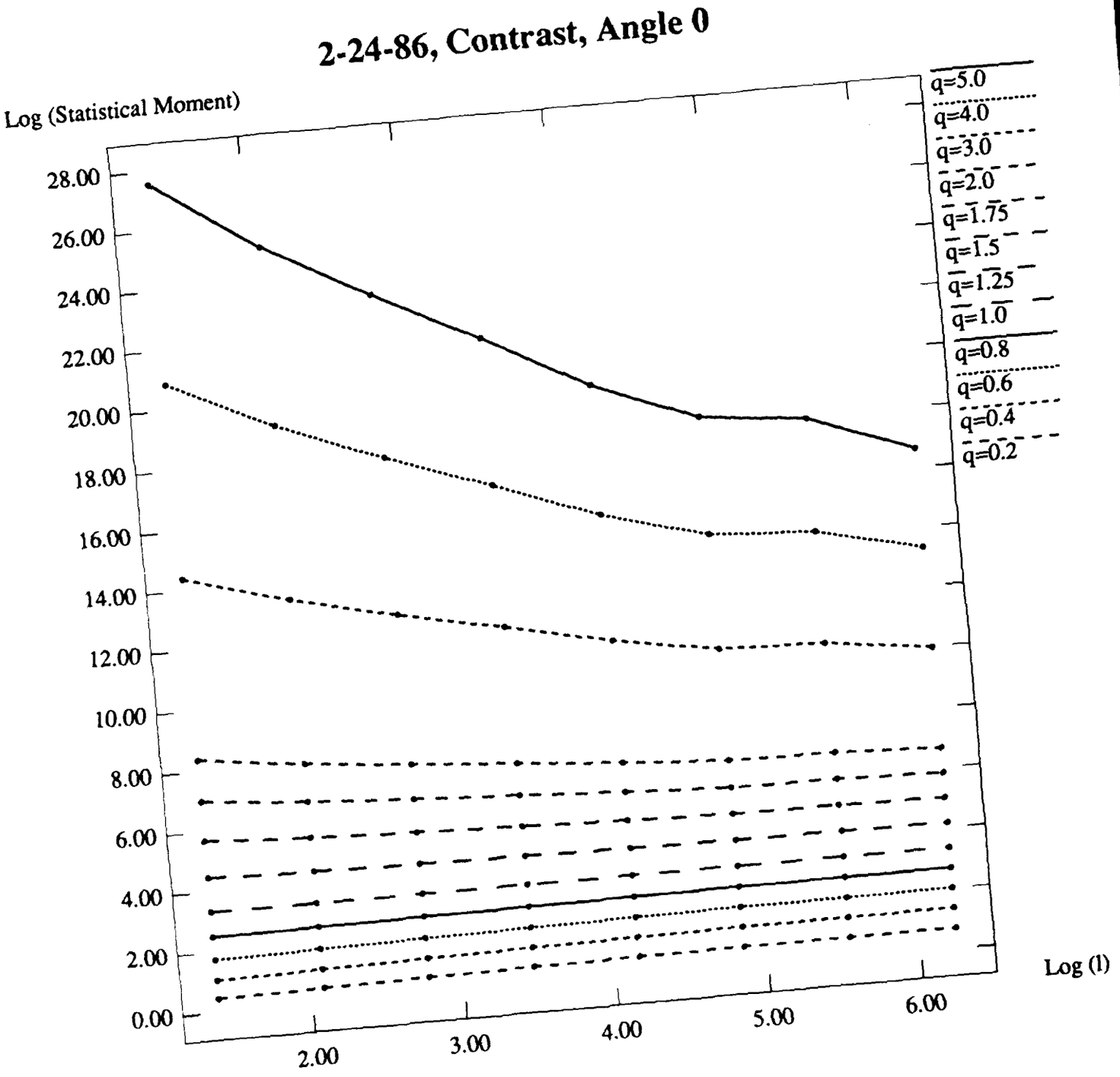

Figure V1.14.b

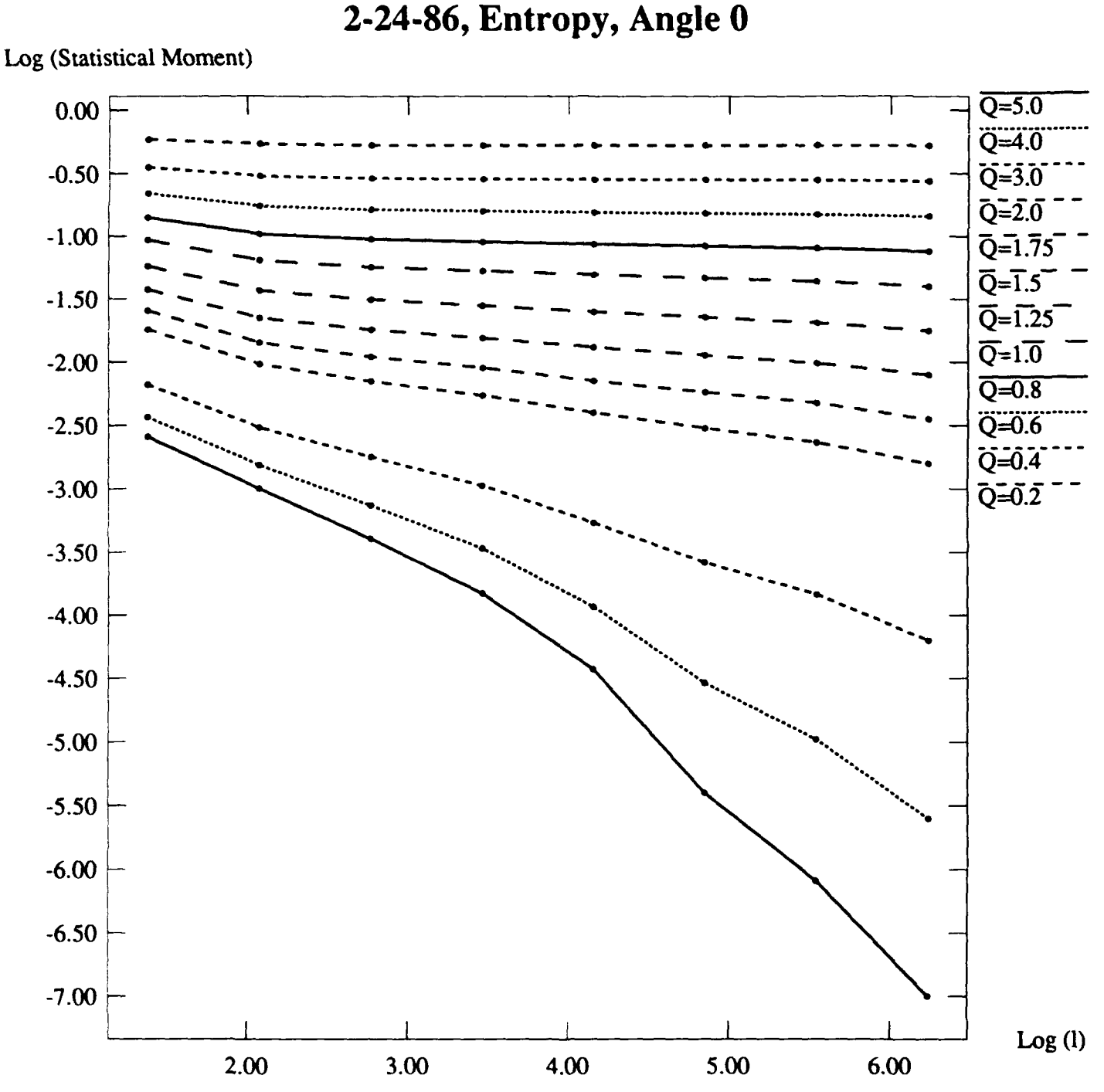

Figure V1.14.c

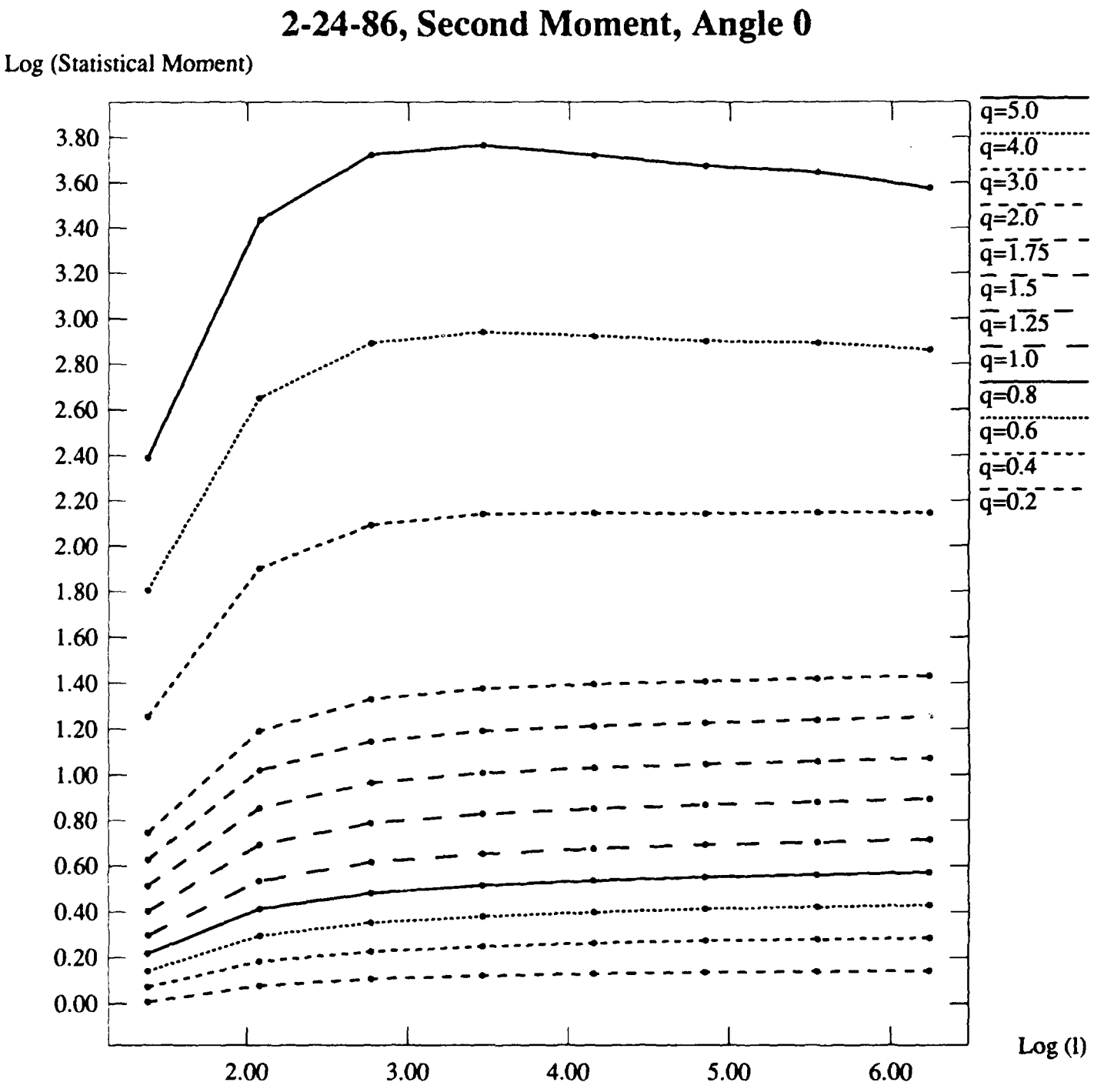

Figure V1.14.d

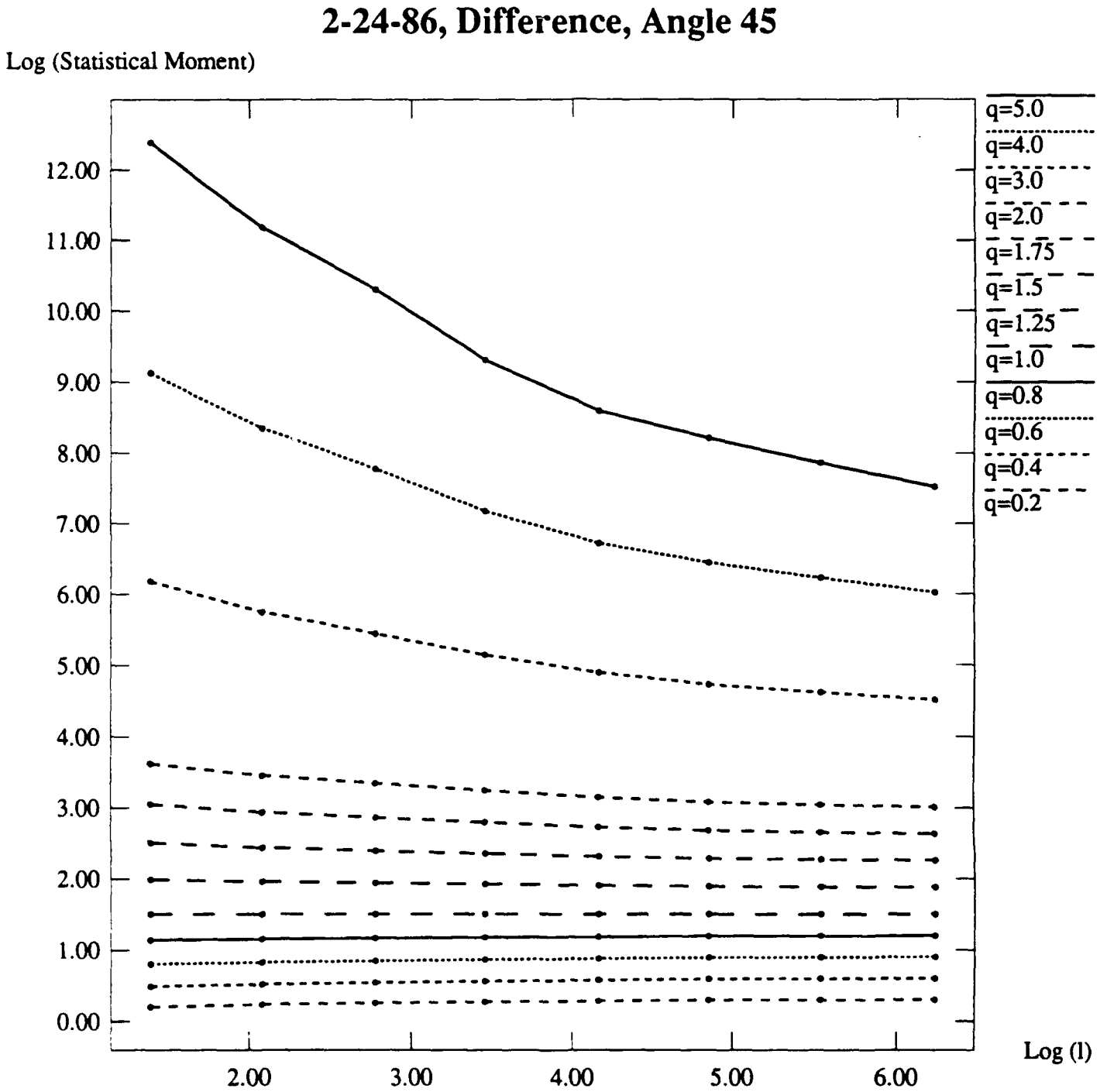

Figure VI.15.a

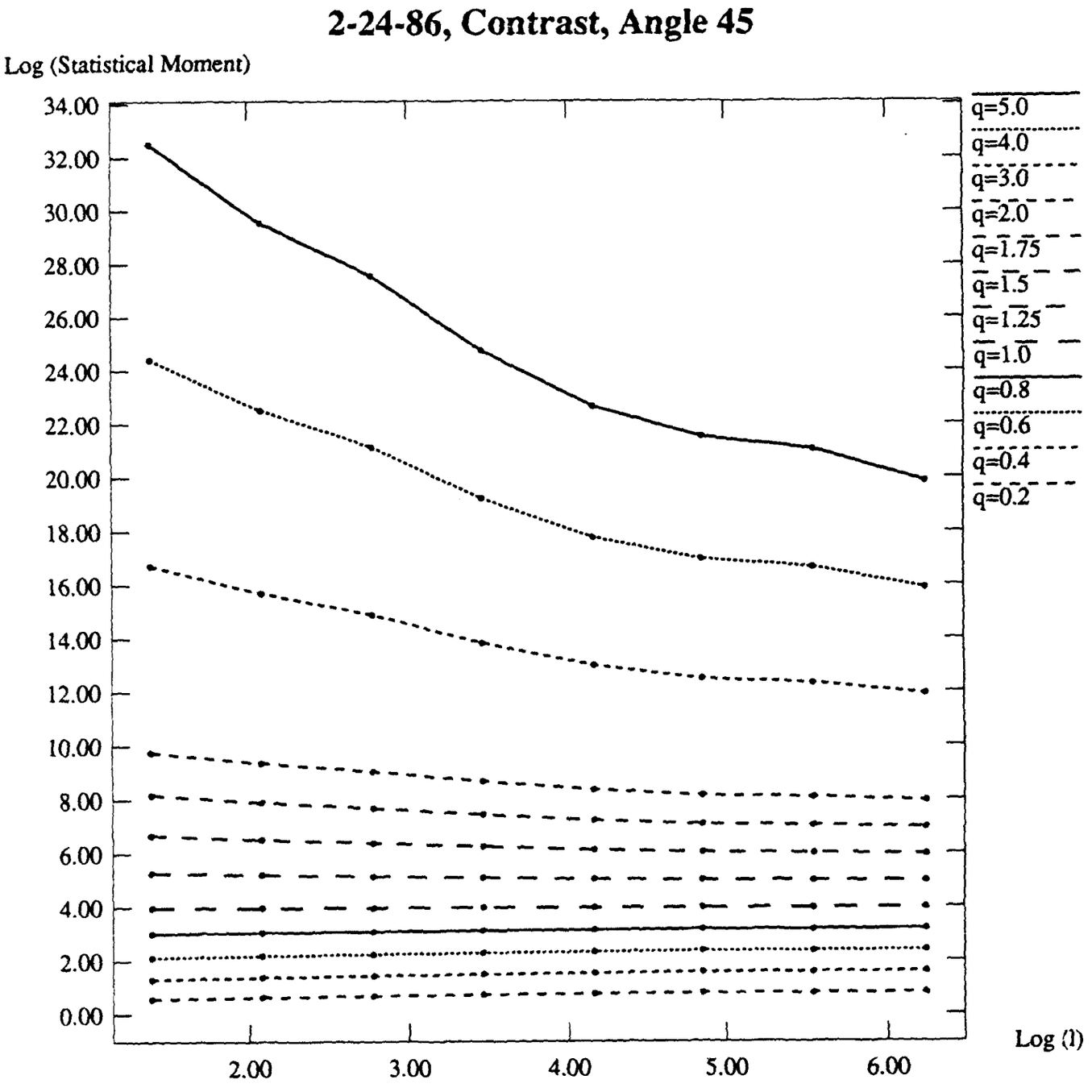

Figure VI.15.b

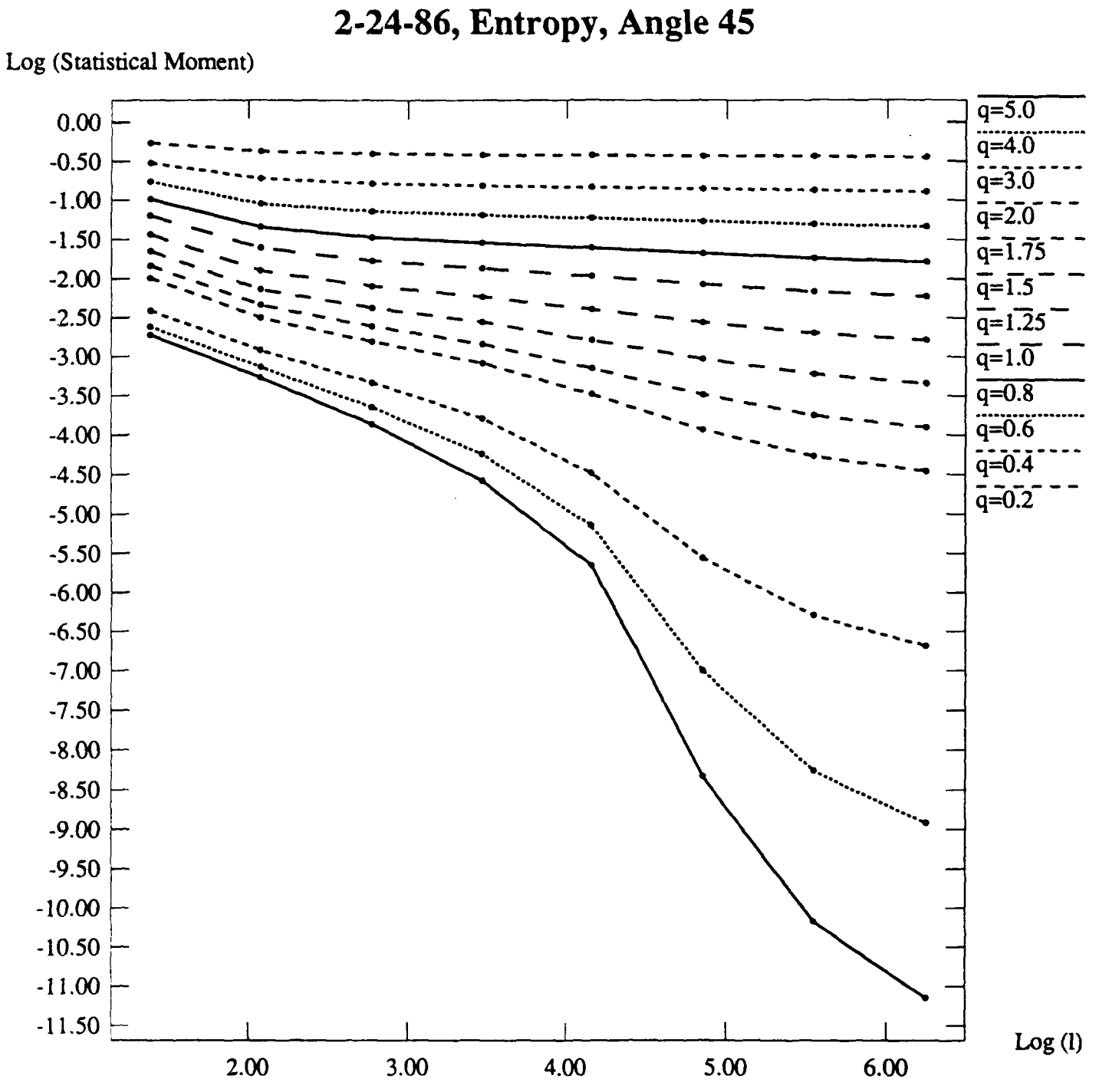

Figure VI.15.c

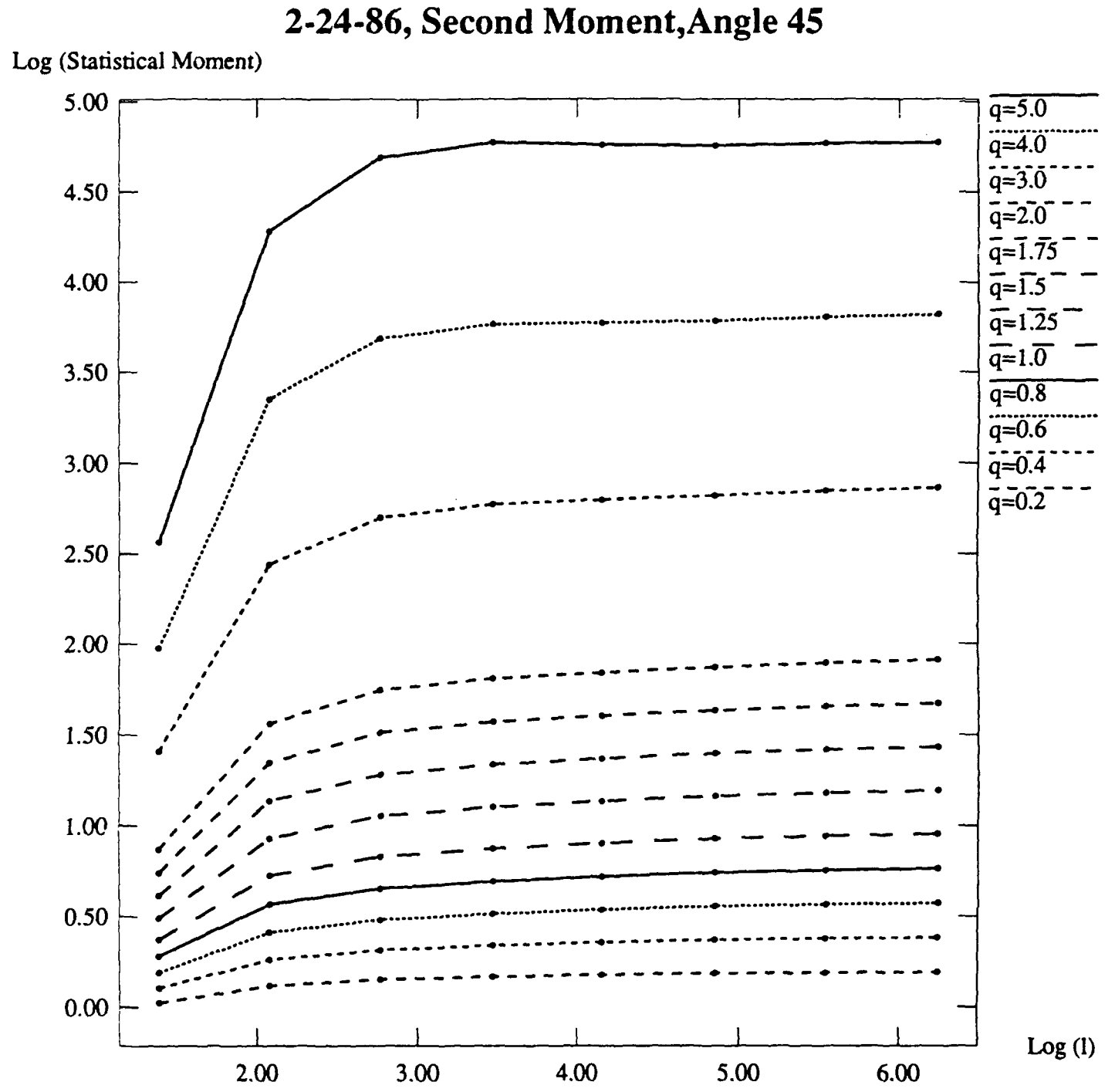
2-24-86, Second Moment,Angle 45
Log (Statistical Moment)
5.00
4.50
4.00
3.50
3.00
2.50
2.00
1.50
1.00
0.50
0.00
2.00
3.00
4.00
5.00
6.00
Log (l)
q=5.0
q=4.0
q=3.0
q=2.0
q=1.75
q=1.5
q=1.25
q=1.0
q=0.8
q=0.6
q=0.4
q=0.2

igure VI.15.d

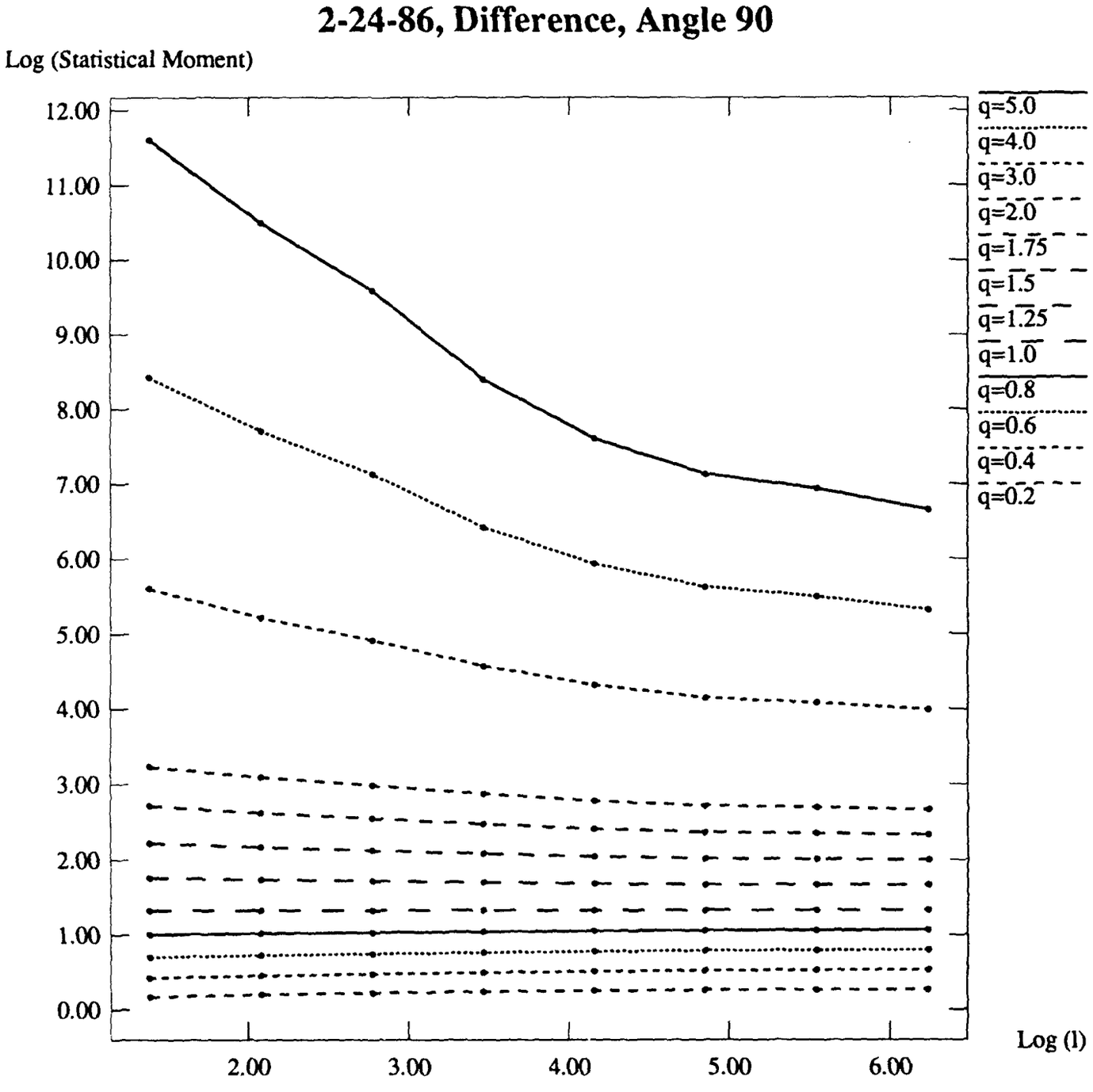

Figure VI.16.a

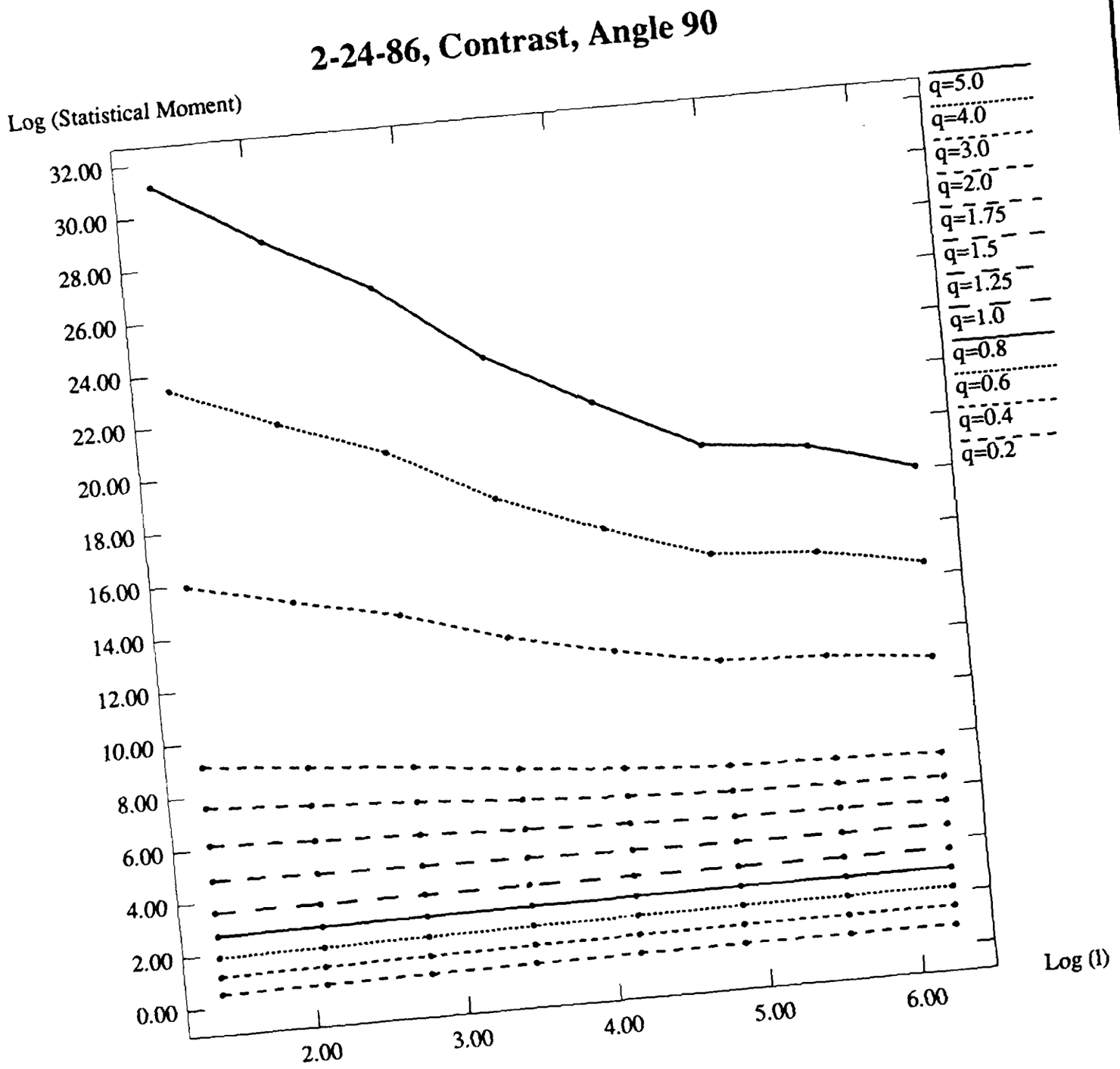

Figure V1.16.b

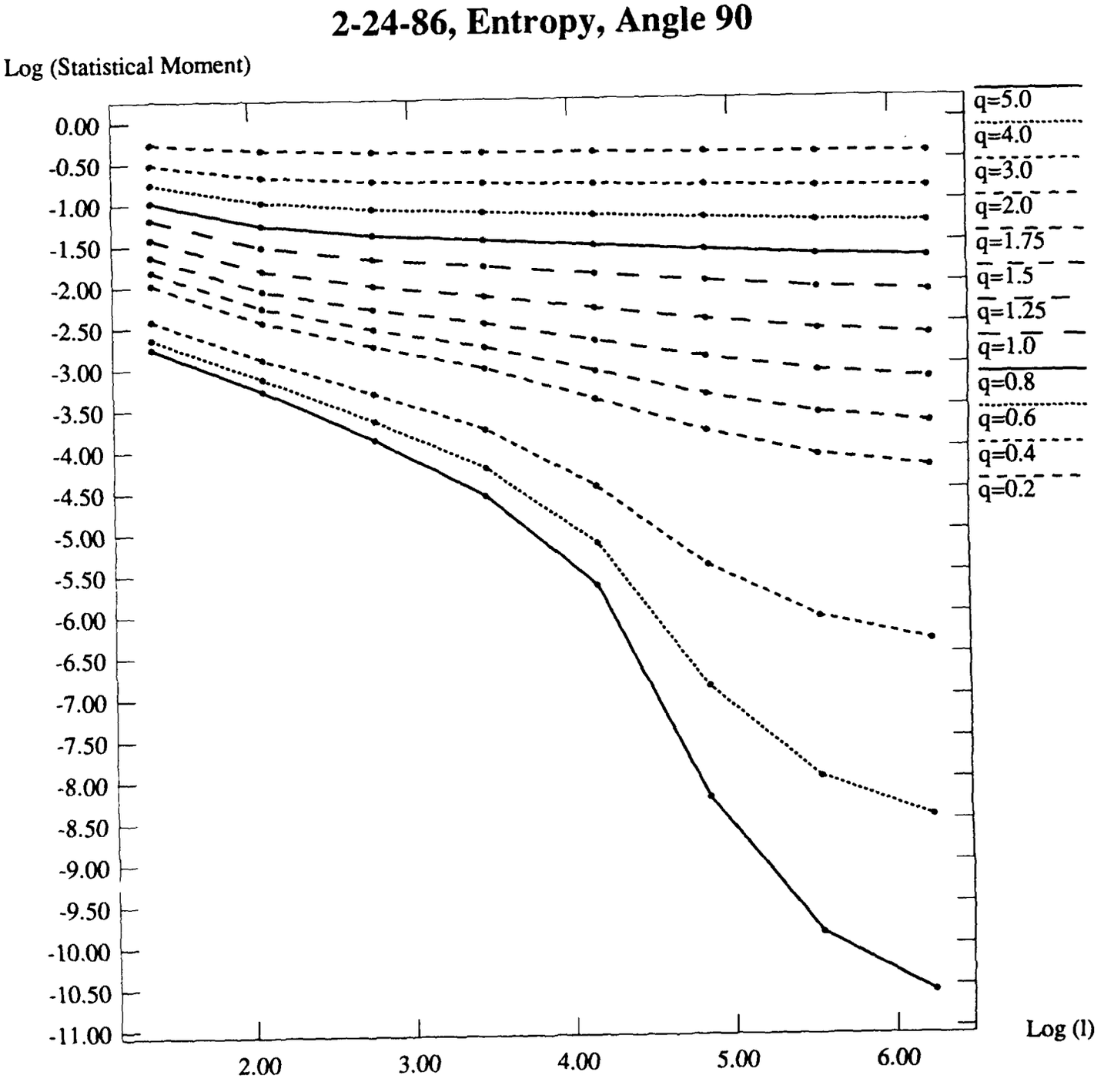

Figure VI.16.c

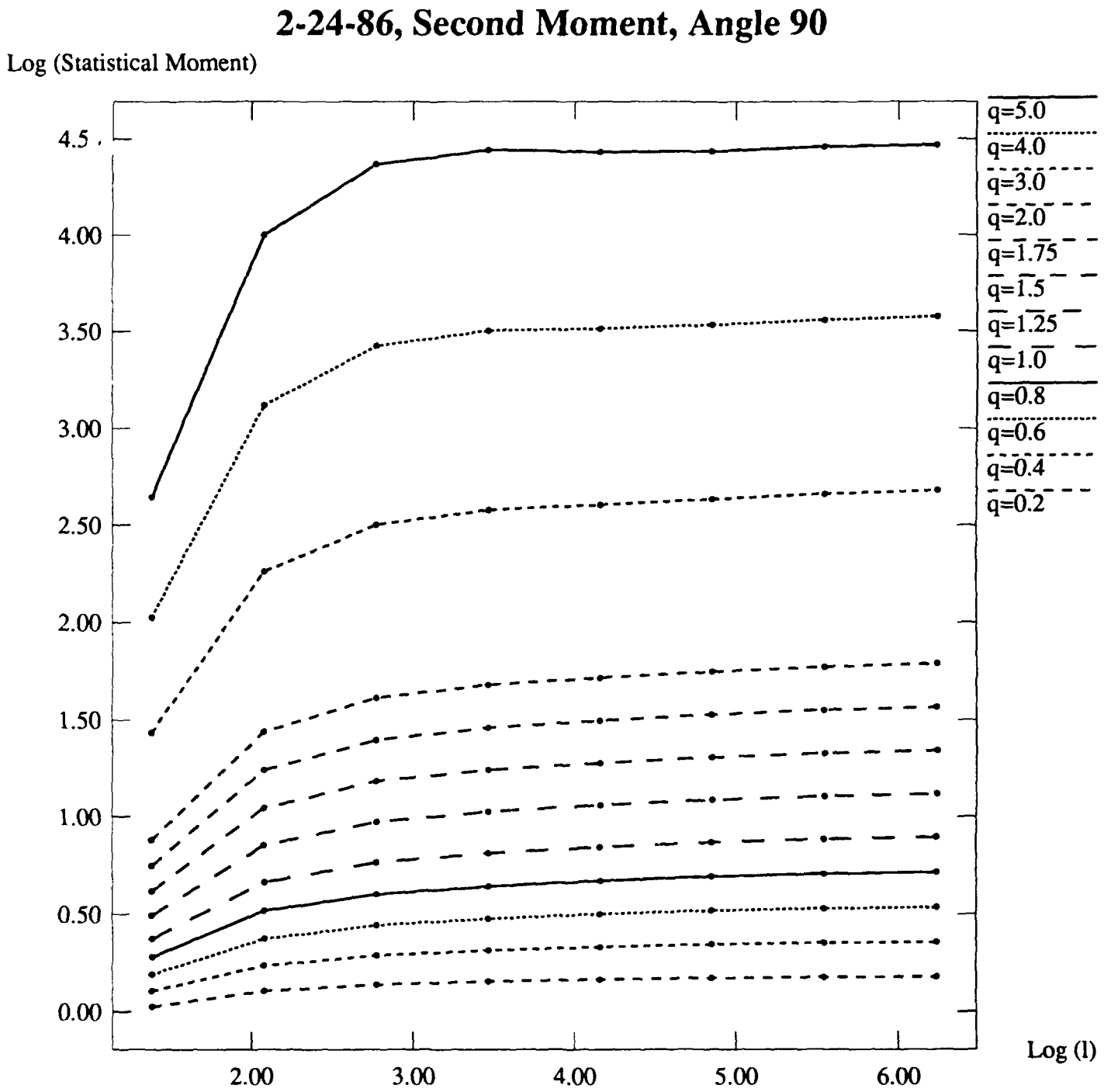

Figure VI.16.d

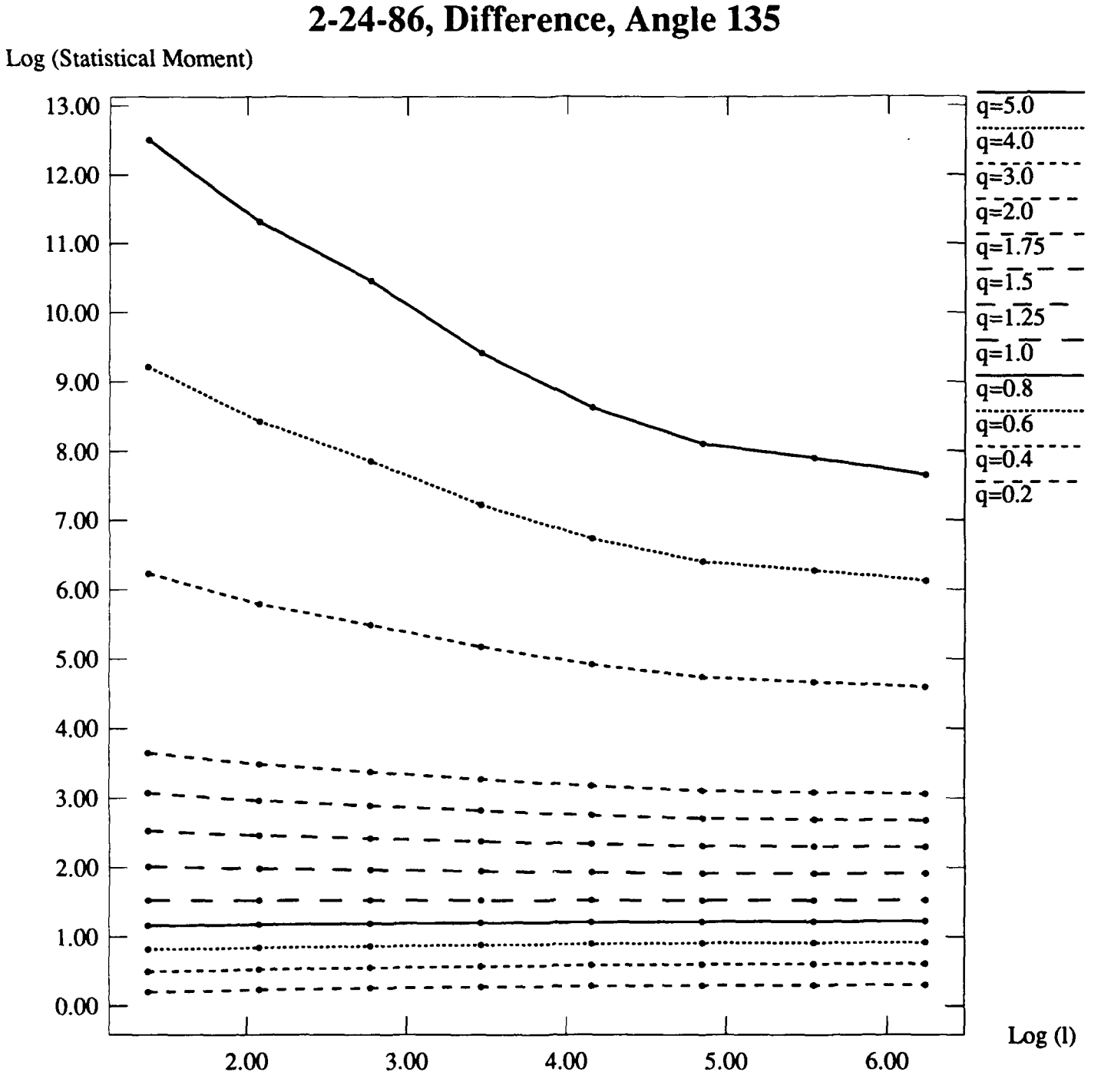

Figure VI.17.a

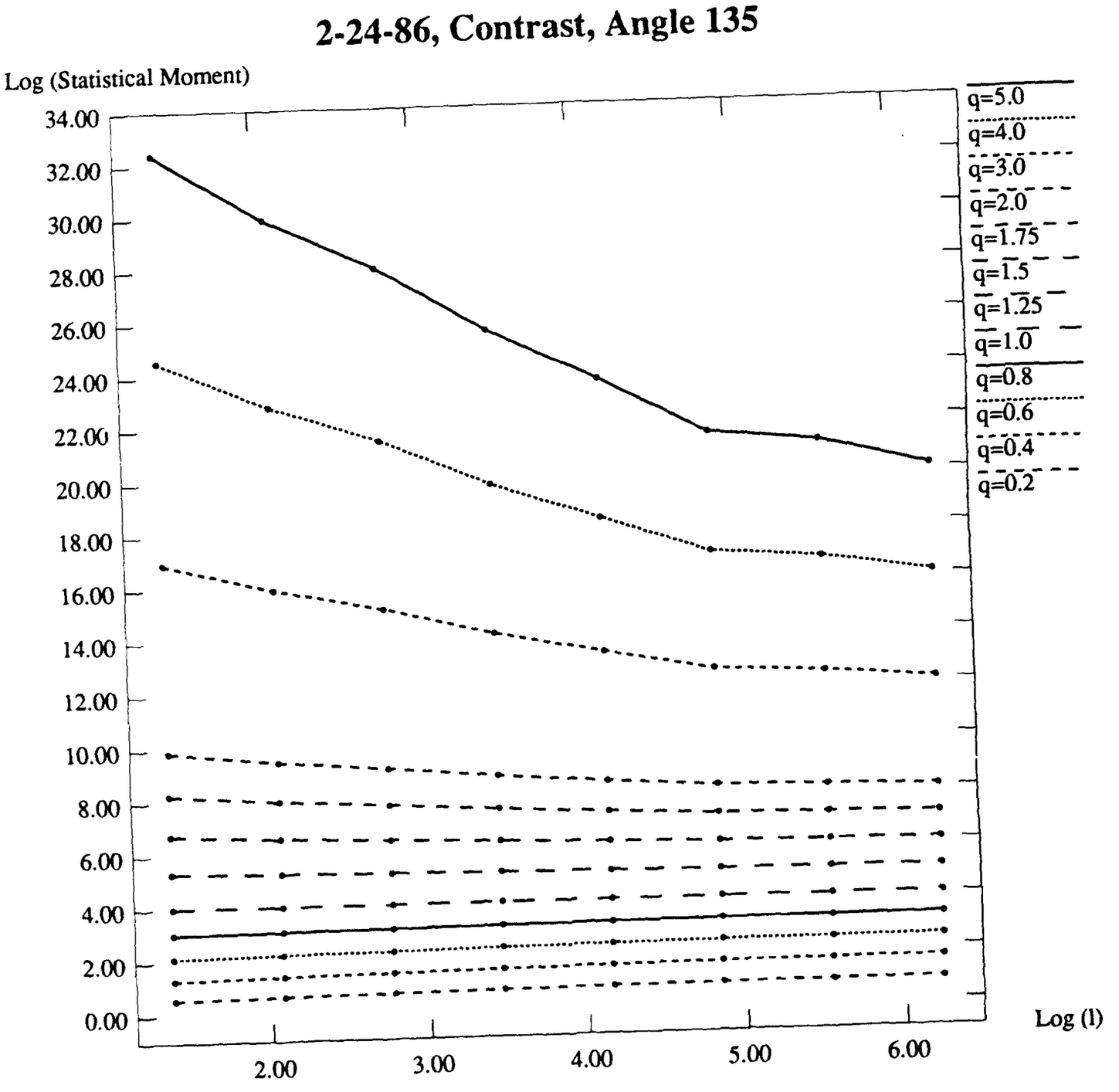

Figure VI.17.b

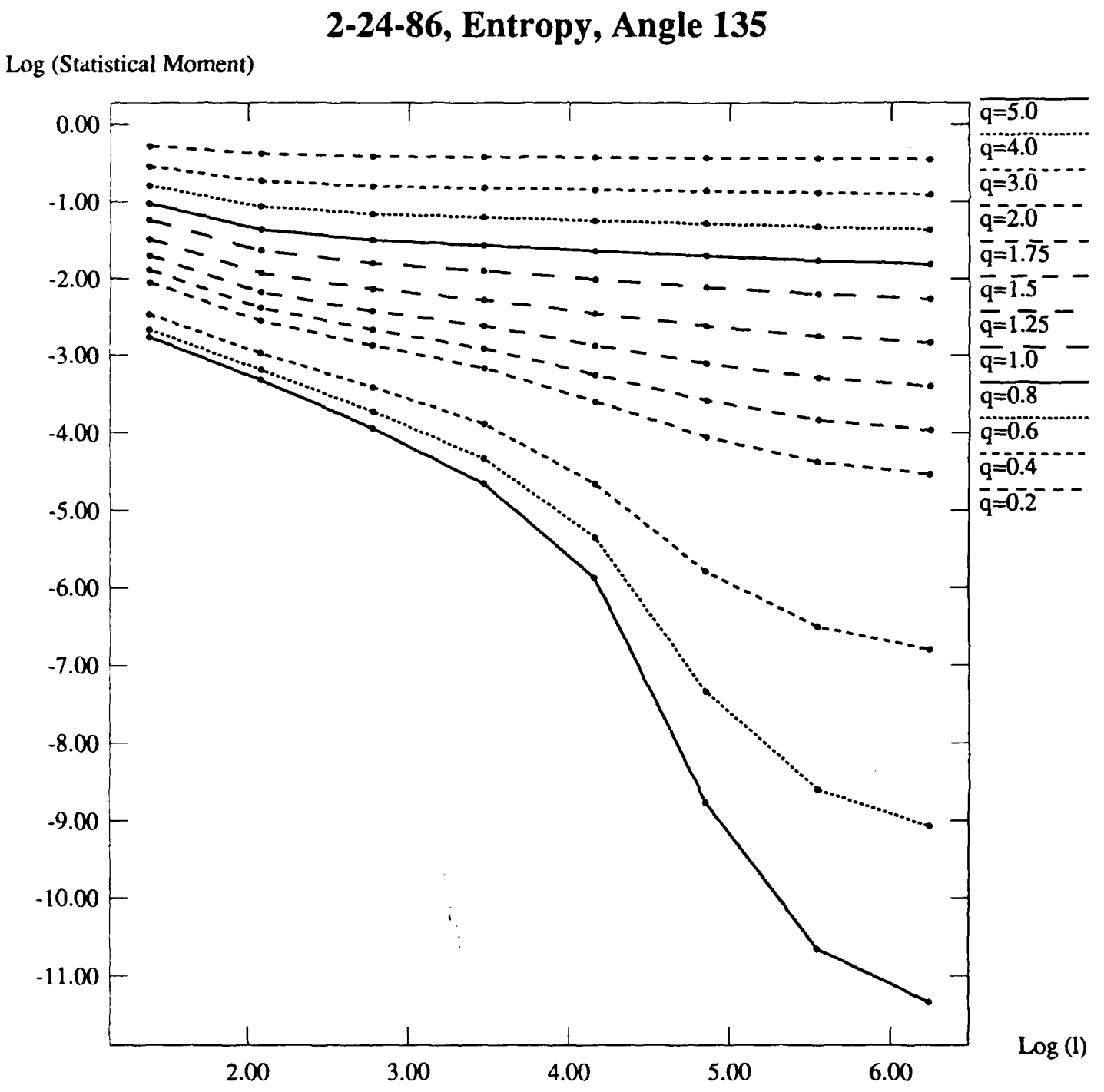

Figure VI.17.c

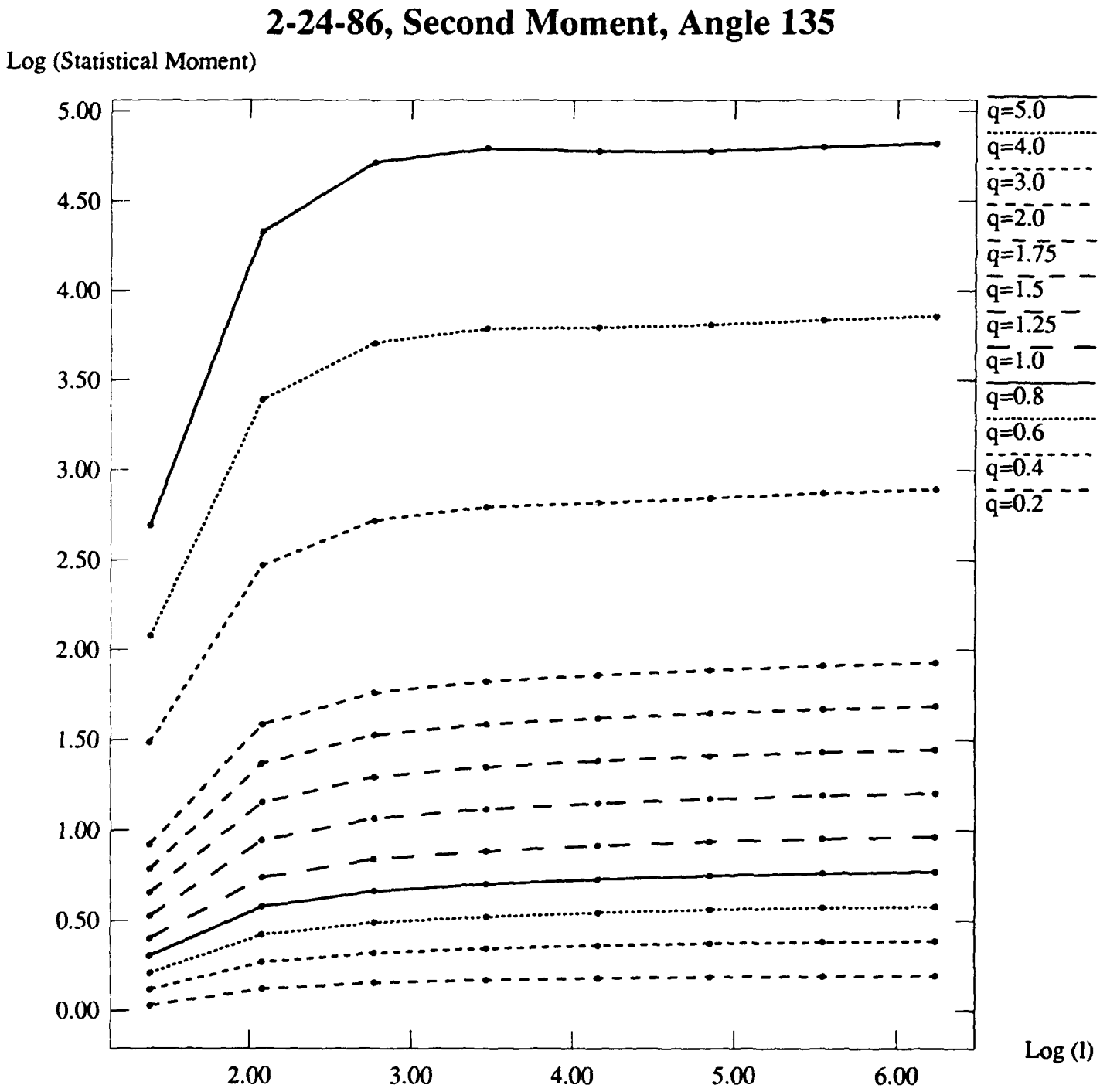

Figure V1.17.d

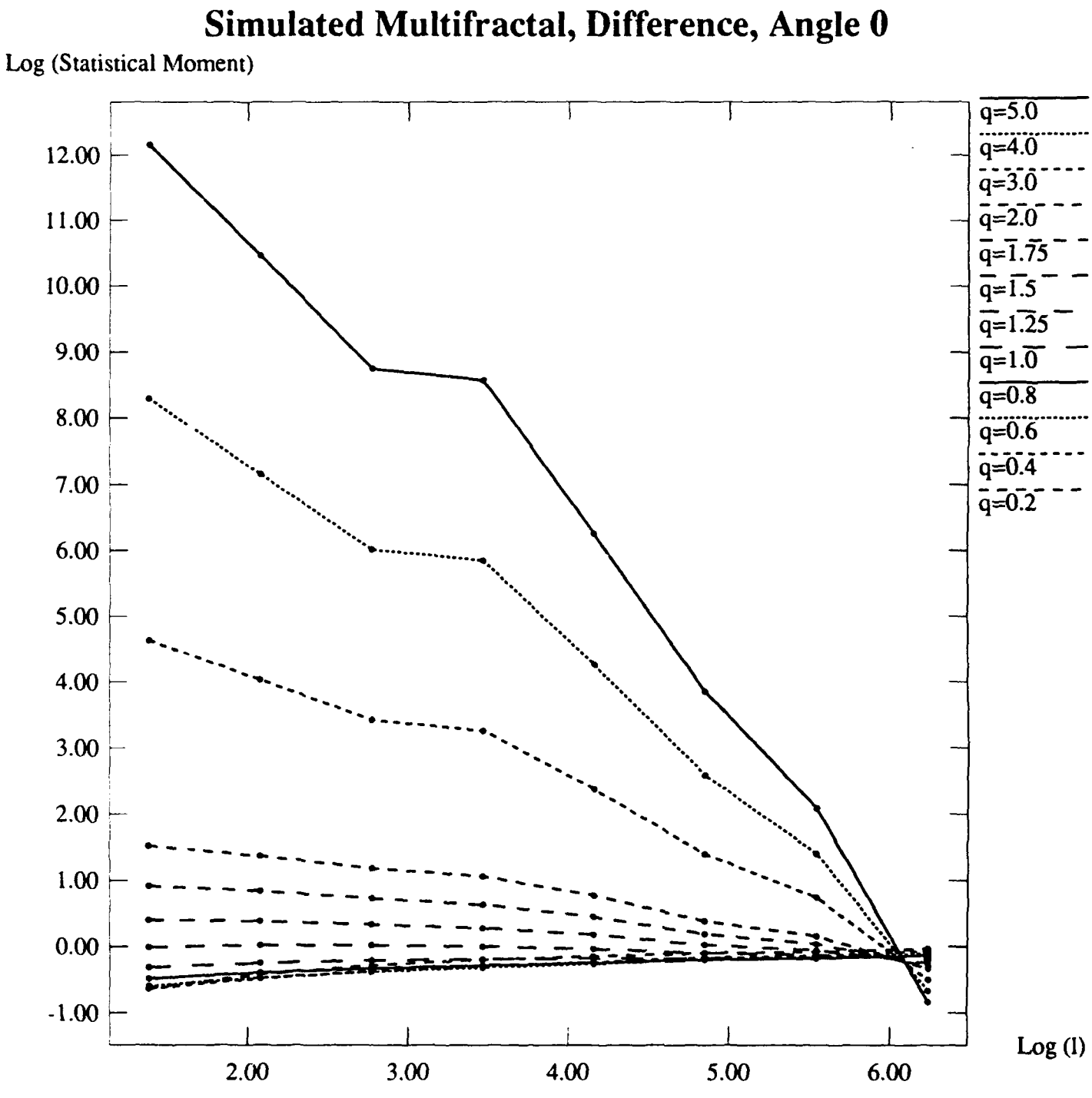

Figure VI.18.a

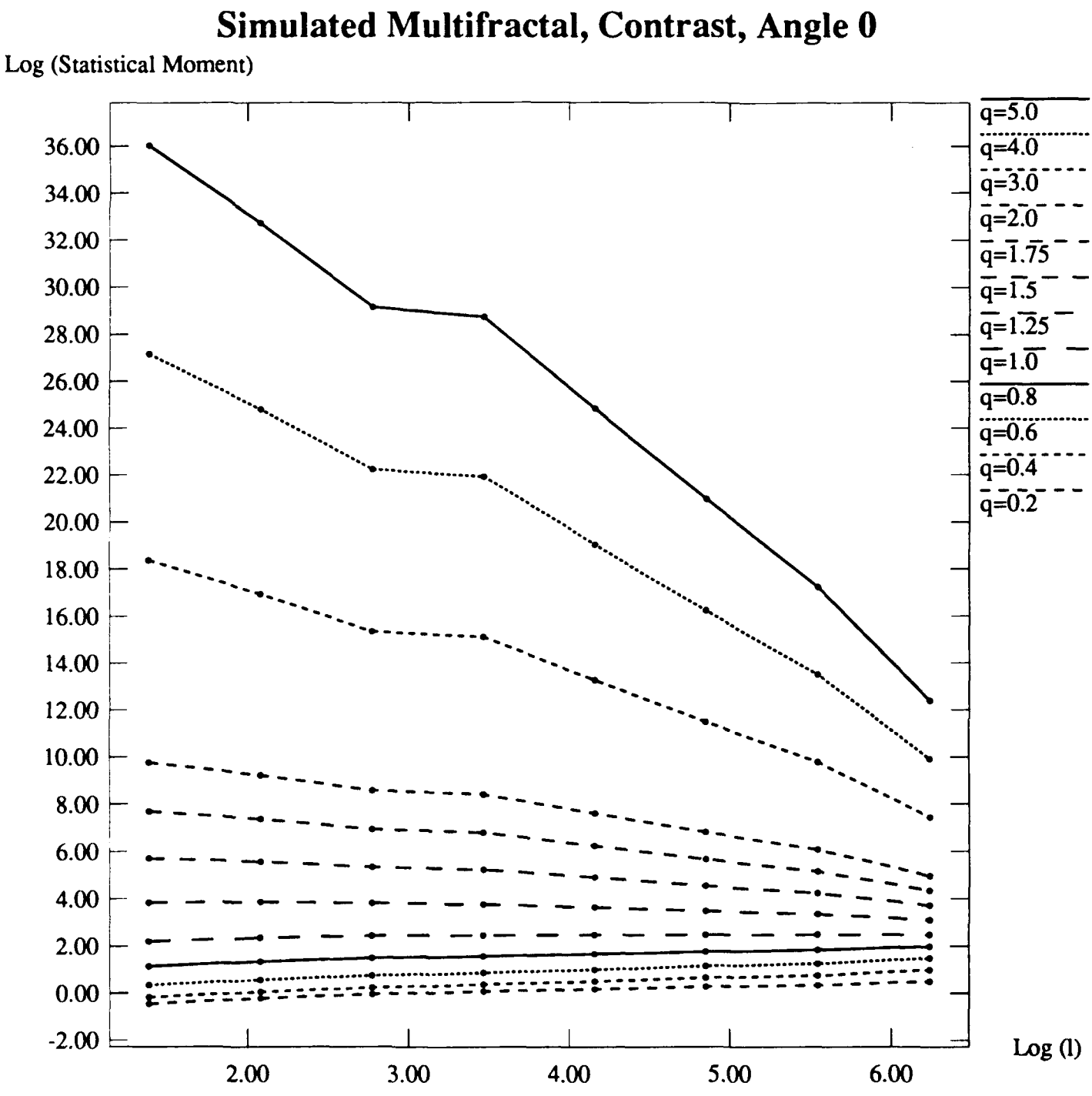

Figure VI.18.b

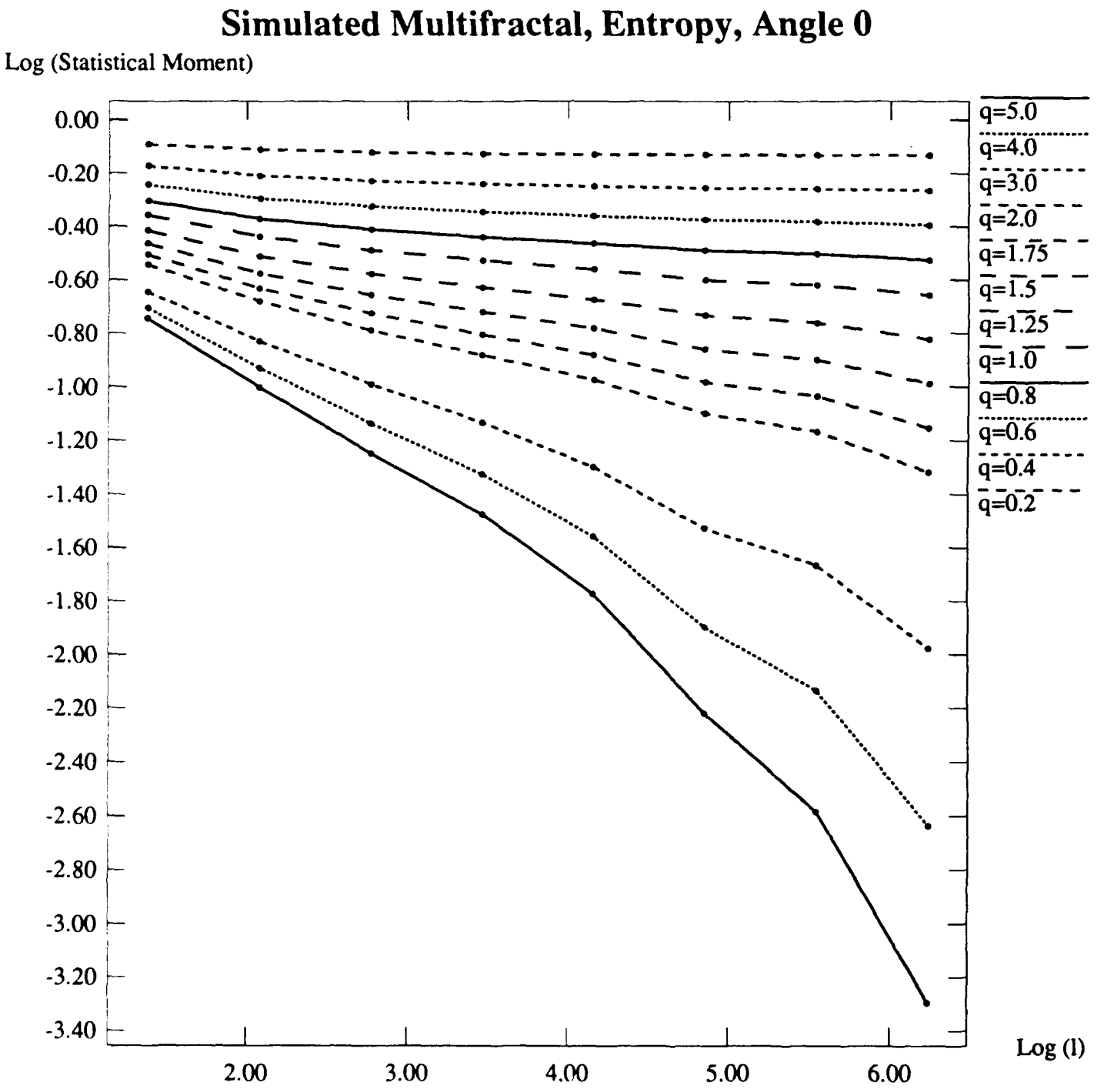

Figure VI.18.c

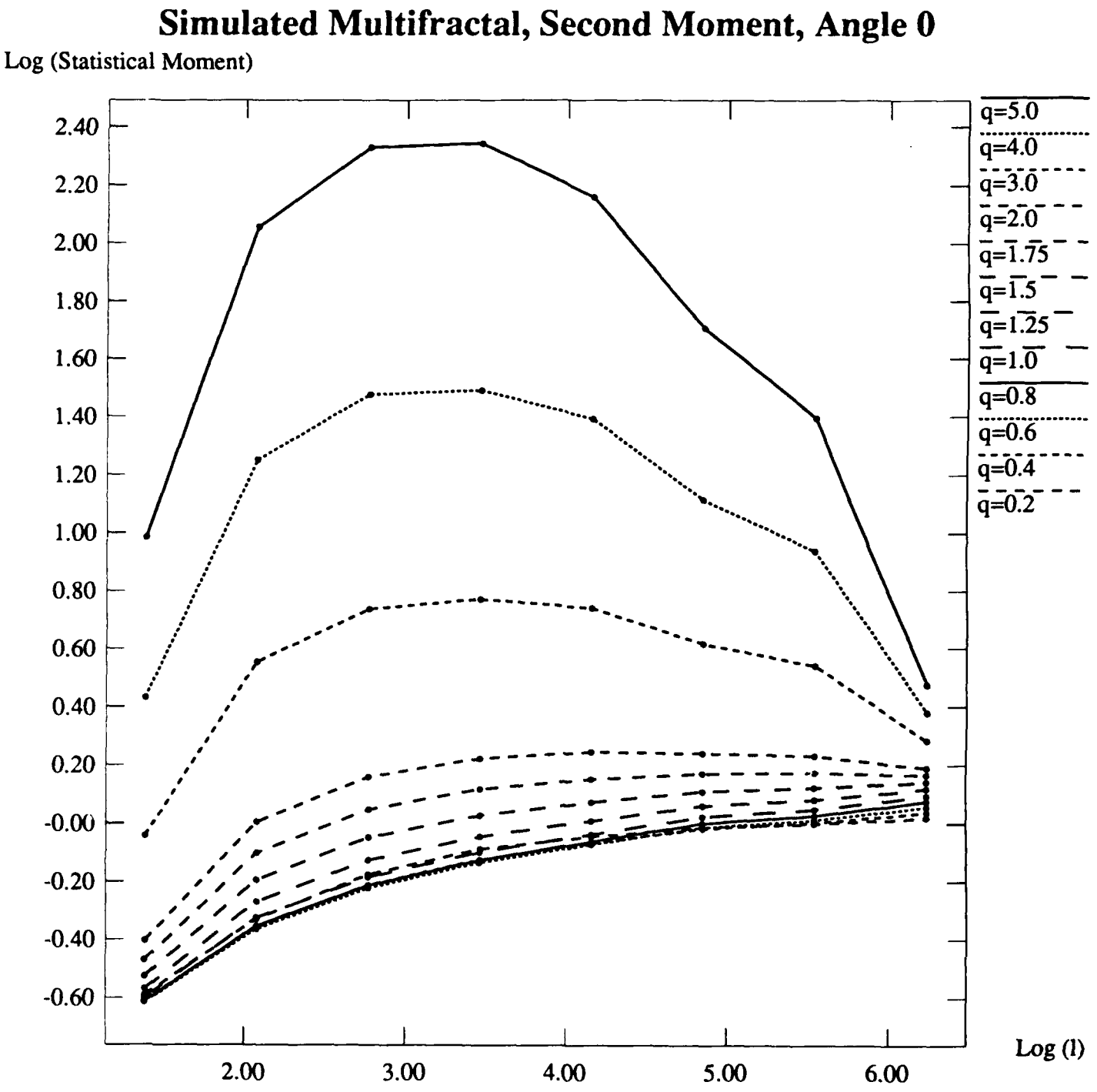

Figure VI.18.d